UNIVERSIDAD COMPLUTENSE DE MADRID

FACULTAD DE CIENCIAS FÍSICAS

TESIS DOCTORAL

A search for Heavy Neutral Leptons with masses up to 150 MeV and studies on scintillation light detection in SBND

Búsqueda de Leptones Neutros Pesados con masas hasta 150 MeV y estudio de la detección de luz de centelleo en SBND

MEMORIA PARA OPTAR AL GRADO DE DOCTOR

PRESENTADA POR

Rodrigo Álvarez Garrote

DIRECTORES

Inés Gil Botella
José Ignacio Crespo Anadón

A search for Heavy Neutral Leptons with masses up to 150 MeV and studies on scintillation light detection in SBND

Búsqueda de Leptones Neutros Pesados con masas hasta 150 MeV y estudio de la detección de luz de centelleo en SBND

Memoria de investigación presentada por:

Rodrigo Álvarez Garrote

para optar al grado de Doctor

Dirigida por:

Dra. Inés Gil Botella
Dr. José Ignacio Crespo Anadón

Universidad Complutense de Madrid
Facultad de Ciencias Físicas
Programa de doctorado en física

Agradecimientos

Mi madre me enseñó desde pequeño que es de bien nacido ser agradecido. Durante estos cuatro años he tenido la oportunidad de viajar y conocer otras culturas y países, guardando recuerdos que me acompañarán siempre. También he tenido la suerte de encontrar en este camino personas maravillosas, y compañeros sin los que completar esta tesis hubiera sido imposible. A todos vosotros, gracias.

En primer lugar, quiero agradecer a Inés y José su dedicación. Me habéis enseñado a cuestionarme todo, y la paciencia y tesón para encontrar poco a poco las respuestas. Gracias por no dejar de creer en mi, y por darme la oportunidad de trabajar aprendiendo y descubriendo cosas. Gracias también a Clara, Carmen, Antonio, Iván, Enrique, Aritz y toda la gente del grupo de neutrinos donde me sentí uno más desde el primer día.

Un lugar de trabajo no es solo una mesa y un ordenador (gracias Diana por los patitos de colores). A Jose Soto le debo buena parte de lo que sé de LArSoft y todos esos trucos que nadie más conoce, también me pegaste esa costumbre de comer el menú del CIEMAT en menos de diez minutos. Gracias a la vieja guardia de estudiantes: Juan, Lourdes, Jaime, Irene, Carmen??. Desde cómo disecar una mandarina a hacer rafting, también me enseñasteis las dobles comisiones de servicio y otras magias negras. David, siempre nos quedará Benasque. Pepe, te aprecio aunque te guste Madame Bovary. Ludo, no estamos mayores, tenemos *experiencia*. Gracias Nicola por chivarme tu receta de Ravioli. Y a todas las nuevas hornadas (Diego, Alejo, Elvira, Dani, Oliver y los nuevos peques) gracias por el soplo de aire fresco. Antonio, espero que puedas perdonarme. Cecilia, mi gymbro, gracias por mancharme el abrigo. Gracias Iñaki, por estar ahí desde que nos conocimos en el máster, y por programar el Sico web. A mis neutrinos les guardo un cariño especial, Andrés, gracias por descubrirnos al padre Kotas. Laura, eres una persona maravillosa, gracias por los karaokes de media tarde. Sergio, gracias por escuchar mis desahogos de camino al bus y enseñarme la *verdadera* carbonara. Jorge, espero que te lleves un buen recuerdo, y que sigas bailando mucho.

Illinois is as flat as it can get, however, my journey there was a bumpy ride. Henry, you were the first thing I saw through the window that cold morning of April. Gustavo, Antonio, Alex, Dorm 2 was not the same after you left. My first stay wouldn't make sense without the real SBND: Lan, Lane, Lynn, Moon, Bear and Fran; you made me feel at home in another continent. Thanks Rob for storming Dorm 15 with me. 2024 was even colder, but I met the sweetest Brazilian girls. Essa sopa me devolveu a vida, Isabella. Obrigado pelos passos de baile, Camila. Rohan, thanks for all the rides. Jiaoyang thanks for teaching me how to make sushi. Namitha you are crazy, Prague was crazy.

Gracias Vilja y Nadia por compartir ese primer año post-covid y enseñarme a preparar avena. Gracias María, sin tu consejo y Overleaf Premium, este manuscrito nunca se habría compilado. A mis vragasbundos, os invitaré al próximo meeting de conserjes. Tuve mucha suerte de encontrarme en la universidad con gente como Dani, Andrea, Rubén, Diego, Esther..., y tantos otros que pasearon conmigo por la facultad. Alberto, Carlos, Pedro, Laura, Lorena gracias por soportarme todos estos años. Dani, siempre es divertido pelear la pole. Sergio, gracias por sacarme de casa siempre que estoy triste y llevarme a las barras, y por ser el mejor amigo que uno puede tener.

Sin mi familia nada de esto tendría sentido. Durante mis veranos en Peleas de Abajo empecé a ver estrellas y cogerle el gusanillo a la física. Montar cabañas, andar en bici, sentirme libre. Elvira, Jesús, Inma, gracias por darme tanta verdura, aunque costara. Mamá, papá, me habéis dado todo lo que tengo, gracias por quererme tanto. Nuria, gracias por dar siempre la cara por mí. Esteban, Dominique, gracias por acogerme desde el principio. No puedo acabar estos agradecimientos sin ti, Iris. Gracias por compartir tu vida y formar un hogar conmigo. Tú ves lo mejor de mí y me animas a seguir cuando no me quedan fuerzas. Sé que me querrás aunque me quede calva y toda arrugada.

Este proyecto ha sido financiado con la ayuda PID2023-147949NB-C51 por el Ministerio Español de Ciencia, Innovación y Universidades (MI-CIU/ AEI/ 10.13039/ 501100011033/ FEDER, UE).

Contents

Agradecimientos i

Abstract vi

Resumen ix

1 Neutrino physics 1
- 1.1 The discovery of the neutrino . . . 1
- 1.2 Neutrinos in the Standard Model of Particle Physics . . . 2
- 1.3 Beyond the Standard Model: the neutrino mass problem . . . 5
- 1.4 Neutrino oscillations . . . 7
  - 1.4.1 Open problems in neutrino physics . . . 9
- 1.5 Sterile neutrinos . . . 11
  - 1.5.1 Experimental hints . . . 11
- 1.6 Heavy neutral leptons . . . 13

2 SBND in the SBN program 16
- 2.1 The Short-Baseline Neutrino program . . . 16
- 2.2 The Booster Neutrino Beam . . . 19
- 2.3 The LArTPC Technology . . . 21
  - 2.3.1 Charge production and transport in a LArTPC . . . 24
  - 2.3.2 Light production and propagation in a LArTPC . . . 29
- 2.4 SBND: the Short-Baseline Near Detector . . . 30
  - 2.4.1 Charge readout system . . . 31
  - 2.4.2 Cosmic Ray Tagger system . . . 34
  - 2.4.3 Photon Detection System . . . 36
  - 2.4.4 Trigger and DAQ system . . . 38

3 Characterization of SBND X-ARAPUCA photodetectors 41
- 3.1 Introduction . . . 41
- 3.2 Experimental setup at CIEMAT . . . 45
- 3.3 Calibration . . . 49
  - 3.3.1 Gain measurement . . . 49
  - 3.3.2 Crosstalk measurement . . . 52
  - 3.3.3 Linearity study . . . 54
- 3.4 VUV photon detection efficiency . . . 55
- 3.5 Visible photon detection efficiency . . . 61

3.5.1 Angular dependence . . . 62

4 Light simulation and reconstruction in SBND 65
4.1 Light simulation . . . 65
4.1.1 Light production and propagation . . . 66
4.1.2 Photon detector simulation . . . 69
4.2 Light reconstruction . . . 73
4.2.1 Signal processing . . . 74
4.2.1.1 Hit finding . . . 76
4.2.2 Signal clustering . . . 78
4.3 Light reconstruction efficiency . . . 80
4.3.1 Calorimetry resolution . . . 81
4.3.2 Detected light yield . . . 82
4.3.3 Position resolution . . . 83
4.3.4 Timing resolution . . . 86

5 Heavy neutral lepton signal and background simulation 92
5.1 Signal simulation . . . 92
5.1.1 HNL production . . . 94
5.1.2 HNL propagation . . . 95
5.1.3 HNL decay . . . 97
5.1.4 HNL decay product kinematics . . . 100
5.2 Background simulation . . . 103

6 Detector simulation, reconstruction and selection of HNL candidates 107
6.1 General overview . . . 107
6.2 TPC simulation . . . 108
6.3 TPC reconstruction . . . 110
6.3.1 Pandora pattern recognition . . . 111
6.4 CRT simulation . . . 114
6.5 CRT Reconstruction . . . 115
6.6 High-level reconstruction . . . 116
6.6.1 Beam flash matching . . . 116
6.6.2 Particle identification . . . 117
6.6.3 CRT-TPC Matching . . . 118
6.6.4 CRUMBS . . . 119
6.7 HNL event selection . . . 120
6.7.1 Preselection . . . 120
6.7.2 $N \to e^+e^-\nu$ selection . . . 123
6.7.3 Results . . . 127
6.7.4 Future prospects: studies with truth variables . . . 131

7 SBND sensitivity to HNLs decaying into electron-positron-neutrino 133
7.1 Uncertainty treatment . . . 133
7.2 Limit setting . . . 135
7.2.1 Likelihood-based tests . . . 136
7.2.2 CL_s Method . . . 137
7.3 Results . . . 138

7.3.1 Comparison with other experiments 141

Conclusions **143**

Bibliography **146**

List of Figures **163**

List of Tables **170**

A Analytical toy-model for the VUV PDE study **172**

B Monte Carlo samples produced for the HNL analysis **175**
B.1 Signal samples 175
B.2 Background samples 176

C XGBoost BDT model **179**

D Arrival time distributions in the conservative selection **180**

E Arrival time distributions in the aggressive selection **183**

F Arrival time distributions in the smeared true selection **186**

Abstract

Introduction Neutrino physics is one of today's most promising fields in particle physics. The discovery of neutrino oscillations is an evidence of their mass not being null. However, the Standard Model of elementary particles (SM) does not contain a mechanism that generates them, so we have to search beyond the SM to find answers. Other unknowns remain open, such as the amount of CP symmetry violated in the lepton sector that could help explain the differences between matter and antimatter that formed the present universe. Nor is it understood why these particles are so light, more than six orders of magnitude below the next fermion, the electron. A possible explanation is the existence of heavier neutrino mass states usually referred as heavy neutral leptons (HNLs).

One of the most advanced technologies for detecting neutrino interactions is the liquid argon time projection chamber (LArTPC). LArTPC detectors form a 3D image of the ionized electrons in the interaction, producing a detailed description of each neutrino event. Argon is also a prolific scintillator (40k photons/MeV) with light signals indicating the interaction time. The Short-Baseline Near Detector (SBND), a 112-active mass LArTPC at Fermilab, will measure millions of neutrino interactions from the Booster Neutrino Beam (BNB). As the near (L=110 m) detector of the Short-Baseline neutrino program, SBND will search for a fourth light neutrino ($\sim$ eV) in the coming years. This hypothesis could explain the anomalous data observed in the LSND and MiniBooNE experiments.

Objectives The thesis has two objectives. First, the study of the generation and detection of argon scintillation light with X-ARAPUCA sensors at SBND. This new technology that traps the incoming photons in a highly reflective box with silicon photomultipliers, composes the far detector light system of the DUNE experiment. SBND has 192 X-ARAPUCA sensors with hardware configurations that have not been tested before. The second is to perform a sensitivity study for HNLs produced in kaon two-body decays in the BNB and decaying to an electron-positron pair and a neutrino inside SBND in

the low mass range < 150 MeV. The first exclusion limits of SBND to HNLs decaying into this channel are estimated.

Methodology A dedicated cryogenic setup was developed at CIEMAT to characterize the response of X-ARAPUCA sensors to argon scintillation light (produced with a ^{241}Am source) and visible light (produced with a 420 nm laser). Two SBND X-ARAPUCAs were tested in liquid argon using four Hamamatsu VUV4 SiPMs of known photon detection efficiency (PDE) as reference sensors. From the measured data the PDE of both X-ARAPUCAs to visible and vacuum ultraviolet (VUV) light as well as their linear behavior and the correlated crosstalk noise are determined.

To estimate the performance of the X-ARAPUCA system at SBND, MC simulations in LArSoft using Geant4 have been carried out including the measured values of PDE and crosstalk at CIEMAT. Also, the simulated response of the X-ARAPUCAs was updated with a more realistic bipolar signal, which includes the readout electronics effects. The simulated data sample included neutrinos from the BNB and the muon background from cosmic rays that affect SBND as it is a near-surface detector. Dedicated signal processing, pulse reconstruction and clustering algorithms were developed for the specific signatures of the X-ARAPUCAs.

The studied HNL decay signal $N \to e^+e^-\nu$ consists of two *showers* or electromagnetic cascades with a common vertex. To perform a selection, signal data samples (HNLs) in the mass range of 10 to 150 MeV and background (BNB neutrinos and cosmic muons) were simulated. The signal simulation required incorporating the full BNB flux within the BSM physics generator developed by ICARUS and SBND, MeVPrtl. The effects of anisotropies in the HNL decay were also included. To perform the selection, a full detector response was simulated and the reconstructed variables of the different SBND systems were used. To separate the signals from the background, a dedicated boosted decision tree was trained. Finally, the arrival time at the SBND upstream wall was used as a variable to separate the SM neutrinos from the HNLs, which propagate slower due to their heavier mass.

Results The X-ARAPUCA with Hamamatsu S13360-6050-VE SiPMs and Glass to Power Blue wavelength-shifter bar showed PDE values to the VUV light between 1.99% and 2.29% for over-voltages in the de 2–3 V range. Onsemi MICROFC-30050-SMT and Eljen EJ-286 wavelength-shifter bar X-ARAPUCA's values were between 1.27%–2.20% for over-voltages of 3.25 V and 5.75 V. The efficiency to visible (420 nm) light was extrapolated to the angle of incidence expected at SBND with values in the 0.3%–0.45% range for both X-ARAPUCAs.

From the light signals study, the performance in reconstruction efficiency, energy resolution and spatial reconstruction was found to be comparable with the PMT system. Selecting events with $\leq$ 200 MeV of deposited energy an overall time resolution of 3.05 ± 0.04 ns was achieved, enough to resolve the BNB bunch structure. This allows to perform BSM searches between SM neutrino bunches (background-free regions).

The HNL selection performed obtained a selection efficiency of 12.5% suppressing the SM event background by a factor of more than 10^3. Assuming that no HNL signal was observed, the obtained SBND exclusion limits on the muon coupling $|U_{\mu 4}|^2$ are in the $[3.30 \times 10^{-3}$–$4.32 \times 10^{-7}]$ range for HNLs of masses between 10–150 MeV.

Conclusions The results obtained in this thesis are the first characterization of the X-ARAPUCA light system installed at SBND. Measurements of the photon detection efficiency to the VUV and visible light have been performed, and the results have been implemented in the detector simulation. A complete scintillation light reconstruction of the SBND X-ARAPUCA signals has been developed. Their expected performance using simulated neutrino beam events and cosmic rays has been determined. Both the software tool developed to process and analyze the laboratory data of the X-ARAPUCA, and the signal processing of the SBND waveforms have been transferred to DUNE. A first end-to-end sensitivity study of HNLs in SBND in the mass range $<$ 150 MeV using a full detector simulation is presented. From a fit to the arrival time of HNL candidates with nanosecond resolution, a world leading sensitivity after three years of data was found in the 30–150 MeV mass range.

Resumen

Introducción La física de neutrinos es uno de los campos de investigación más prometedores de la actualidad. El descubrimiento de las oscilaciones de neutrinos es una evidenc ia de su masa. Sin embargo, el Modelo Estándar de partículas elementales (SM) no contiene ningún mecanismo que las genere y por tanto hemos de buscar fuera de él para encontrar respuestas. Otras cuestiones siguen abiertas, como la cantidad de simetría CP violada en el sector leptónico que podría ayudar a explicar las diferencias entre materia y antimateria que formaron el universo actual. Tampoco se entiende por qué estas partículas son tan ligeras, más de seis ordenes de magnitud por debajo del siguiente fermión, el electrón. Una posible explicación es la existencia de estados de masa de neutrinos más pesados (HNLs).

Una de las tecnologías mas avanzadas en la detección de las interacciones de neutrinos son las cámaras de proyección temporal de argón liquido (LArTPCs). En ellas, la imagen 3D de los electrones ionizados en la interacción permite reconstruir con gran precisión los detalles de cada evento. El argón también emite luz de centelleo (40k fotones/MeV) que permiten determinar el instante de la interacción. El Short-Baseline Near Detector (SBND), una LArTPC de 112 toneladas de volumen activo en Fermilab (USA), medirá con gran estadística el flujo de neutrinos producidos por el Booster Neutrino Beam (BNB). Como detector cercano del Short-Baseline neutrino program (L=110 m), SBND pondrá a prueba en los próximos años la hipótesis de la existencia de un cuarto neutrino ligero ($\sim$ 1 eV), que podría explicar los datos anómalos encontrados en los experimentos LSND y MiniBooNE.

Objetivos Esta tesis tiene dos objetivos principales. El primero es el estudio de la generación y detección de la luz de centelleo de argón con los sensores X-ARAPUCA en SBND. Esta nueva tecnología que atrapa los fotones incidentes en una caja altamente reflectante donde son medidos por SiPMs, constituye el sistema de luz de los detectores lejanos del experimento DUNE. SBND cuenta con 192 sensores X-ARAPUCA con configuraciones de hardware que no han sido probadas antes. El segundo objetivo es realizar un estudio de sensibilidad a la detección de HNLs producidos en la desintegración

de kaones a dos cuerpos en el BNB y desintegrandose a un par electrón-positrón y un neutrino dentro de SBND. Además, se han estimado los primeros límites de exclusión de SBND a HNLs desintegrándose en este canal.

Metodología Para caracterizar la respuesta de los sensores X-ARAPUCA a la luz de centelleo de argón y la luz visible se ha diseñado un montaje experimental de argón líquido en el CIEMAT para medir dos X-ARAPUCAs junto con cuatro VUV4 SiPMs de referencia. Con los datos obtenidos se ha podido determinar por primera vez la eficiencia de detección (PDE) de las X-ARAPUCA de SBND a la luz visible (generada con un láser a 420 nm) y ultravioleta de vacío (VUV, producida por partículas alfa de una fuente radioactiva) así como su comportamiento lineal y el ruido correlacionado de crosstalk.

Para estimar las prestaciones del sistema de X-ARAPUCAs en SBND se han realizado simulaciones de MC con Geant4 en LArSoft incluyendo los valores medidos de PDE y crosstalk en el CIEMAT. Así mismo, se actualizó la respuesta simulada de las X-ARAPUCA con una señal bipolar, más realista, que incluye los efectos de la electrónica. Para recuperar la respuesta de centelleo original, se tunearon y desarrollaron algoritmos de reconstrucción que incluyen el filtrado y deconvolución de las señales de luz. La muestra de datos simulados incluía neutrinos del haz BNB y el fondo de muones proveniente de los rayos cósmicos que atraviesan SBND, al estar el detector en superficie.

La señal de la desintegración de HNL estudiada $N \to e^+e^-\nu$ consiste en dos cascadas electromagnéticas con un vértice común. Para realizar una selección se simularon datos de señal (HNLs) en el rango de masas de 10 a 150 MeV y sucesos de fondo (neutrinos del BNB y muones cósmicos). La simulación de la señal requirió incorporar el flujo completo de neutrinos del BNB dentro del generador de física BSM desarrollado por ICARUS y SBND, MeVPrtl. También se incluyeron los efectos de las anisotropías en la desintegración del HNL. Además se simuló la respuesta completa del detector, utilizando variables reconstruidas a partir de las señales de los distintos sistemas de SBND. Para separar las señales del fondo se entrenó un boosted decision tree dedicado. Finalmente, se ha utilizado el tiempo de llegada de la luz de centelleo como variable para separar los neutrinos del SM de los HNLs, que tardan más en propagarse al ser más masivos.

Resultados Las X-ARAPUCAs con SiPMs Hamamatsu S13360-6050-VE y barra wavelength-shifter Glass to Power Blue mostraron valores de PDE a la luz VUV entre 1.99 % y 2.29 % para sobretensiones de 2–3 V, mientras que las X-ARPAUCA Onsemi MICROFC-30050-SMT y barra wavelength-shifter Eljen EJ-286 entre 1.27 %–2.20 % para sobretensiones de 3.25 V a 5.75 V. Se obtuvo una medida de PDE a la luz de 420 nm (el pico del TPB), que extrapolada al angulo de incidencia esperado en SBND dio valores en el rango de 0.3 %–0.45 % para ambas X-ARAPUCAs.

La reconstrucción de las señales de luz a partir de datos simulados mostró resoluciones energéticas y espaciales comparables al sistema de tubos foto-multiplicadores. Seleccionando sucesos de neutrinos que depositaran más de 200 MeV, se obtuvo una resolución temporal del sistema de $3{,}05 \pm 0{,}04$ ns, capaz de resolver la estructura interna del BNB y realizar búsquedas de BSM entre los paquetes de neutrinos del SM.

Las selección de HNLs realizada obtuvo eficiencias de selección entre el 12.5 % y el 25 %, suprimiendo el fondo de eventos del SM en un factor de más de 10^3. Asumiendo que no se observara una señal de HNL, se obtuvieron límites de exclusión de SBND a este tipo de proceso con valores de $|U_{\mu 4}|^2$ en el rango de $[3{,}30 \times 10^{-3}$–$4{,}32 \times 10^{-7}]$ para masas de HNLs entre 10–150 MeV.

Conclusiones Los resultados obtenidos en esta tesis han permitido caracterizar por primera vez el sistema de detección de luz X-ARAPUCA instalado en SBND. Se ha determinado su PDE a la luz ultravioleta y a la luz visible por primera vez. Las medidas realizadas se han incluido en la simulación de SBND. A su vez, se ha desarrollado la reconstrucción de las señales de luz y estimado su rendimiento esperado utilizando eventos simulados de neutrinos provenientes del haz con muones cósmicos. Las herramientas de software desarrolladas para el análisis de datos de laboratorio y proceso de señales en SBND se han transferido a DUNE. Por último, se ha realizado el primer estudio de sensibilidad incluyendo una simulación y reconstrucción completa de SBND a la búsqueda de HNLs en el rango de masas < 150 MeV desintegrándose a un par electrón-positrón y un neutrino dentro de SBND. Los resultados, realizando un ajuste al tiempo de llegada de los candidatos de HNL con resolución de ns, muestran que SBND será capaz de liderar la búsqueda de HNLs en el rango de masas de 30-150 MeV tras tres años de toma de datos.

Chapter 1

Neutrino physics

Neutrinos are one of the most intriguing elementary particles in modern particle physics. For many decades, they were thought to be massless. They can propagate through the Earth or escape the dense core of a collapsing star. Their almost-inert nature makes the study of their properties difficult. As of today, the mechanism that generates the neutrino masses lies outside our current understanding of the subatomic worlds. In this chapter, the current knowledge of their physical properties is outlined. First, an historical review of their discovery is given in Section 1.1. The description of neutrinos within the Standard Model of Particle Physics is described in Section 1.2. The experimental evidence of the neutrino masses and the current three-neutrino oscillation paradigm are reviewed in Sections 1.3 and 1.4. The experimental anomalies found in neutrino oscillations and theoretical reasons motivating the existence of more neutrino states are summarized in Section 1.5. Lastly, an introduction to the heavy neutral lepton models is presented in Section 1.6.

1.1 The discovery of the neutrino

The existence of neutrinos was first postulated by Wolfgang Pauli [1] in 1930 to explain the continuous spectra observed in beta decays and ensure spin conservation [2]. As a weakly interacting particle with no electric charge, neutrinos can escape the detectors carrying away energy and momentum, leaving no visible traces. This led to the famous quote:

> *I have done a terrible thing: I have postulated a particle that cannot be detected.*

attributed to Pauli. Data also showed that the mass of the particle, if any, should be very small.

Following the discovery of the neutron [3, 4] by Chadwick in the early 30's, nuclear models with neutrons and protons bound together were proposed by Heisenberg and others [5, 6]. In 1934, Enrico Fermi developed a new theory to explain the beta decays [7], nicknaming the new particle escaping the nucleus as the small neutron or *neutrino*.

Because they only feel the weak force, it was not until the '50s that they were directly detected by Cowan and Reines [8, 9] through the inverse-beta reaction:

$$\overline{\nu}_e + p \rightarrow e^+ + n,$$

measuring the characteristic signal produced by electron-positron annihilation into a pair of photons of 511 keV each followed by a neutron capture few microseconds later. The measured cross-section of the reaction $\sigma = (11 \pm 0.26) \times 10^{-44}$ cm^2 was in agreement with Fermi's calculations. For this discovery, Reines was awarded with the Nobel Prize in 1995. Evidence of the muon and tau neutrinos was found in 1962 and 2001 respectively [10, 11].

1.2 Neutrinos in the Standard Model of Particle Physics

Today we know neutrinos produced in beta decays are *electronic* (anti)neutrinos (ν_e), one of the three flavors present in the Standard Model (SM) of Particle Physics. It is important to note that under the usual formulation of the SM, neutrinos are massless. Although the discovery of neutrino oscillations has demonstrated otherwise, the mechanism originating the neutrino masses is unknown, a question that remains yet to be answered.

The SM of Particle Physics describes the fundamental particles and the three main interactions in absence of gravity: the weak, strong and electromagnetic interactions, as well as the Higgs field, which gives mass to the SM particles. Particles with no strong interactions and spin 1/2, such as electrons and neutrinos, are referred to as leptons, while particles composed of bounded quarks (protons, pions, neutrons...) are called hadrons (see Figure 1.1). Hadrons and leptons interact through the exchange of bosons with spin 1, the force carriers associated with the excitation of each bosonic field.

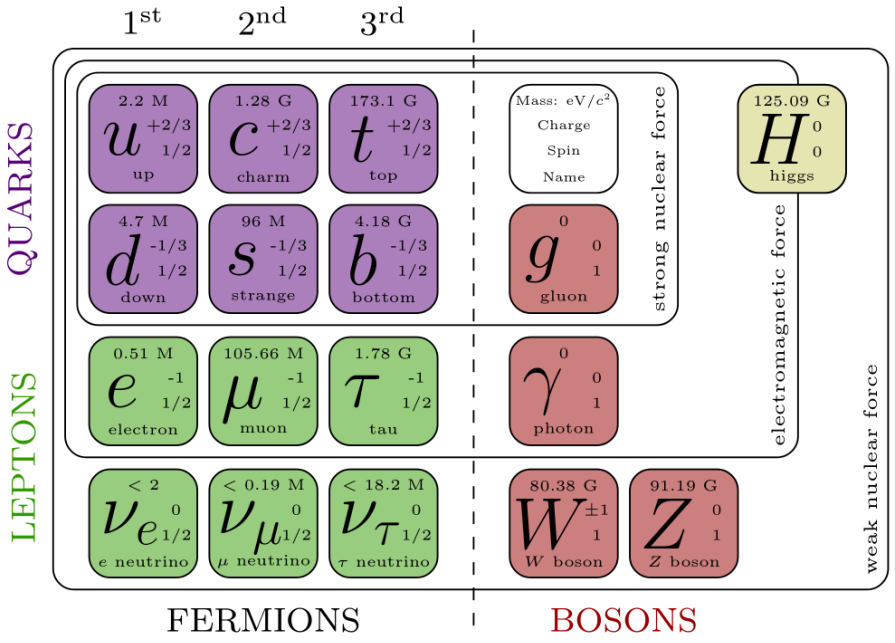

Figure 1.1: Standard Model of elementary particles.

The SM Lagrangian has a local $\mathrm{SU}(3)_C \times \mathrm{SU}(2)_L \times \mathrm{U}(1)_Y$ (for color, weak isospin and hypercharge respectively) gauge symmetry, which under spontaneous symmetry breaking through the Higgs mechanism transforms into $\mathrm{SU}(3)_C \times \mathrm{U}(1)_{EM}$. This phenomenon gives mass to the weak interaction carriers: the Z^0 and $\mathrm{W}^\pm$ bosons. The first can transfer energy, spin and momentum but not electric charge, thus processes mediated by exchange of a Z^0 boson are usually referred to as *neutral currents*. The $\mathrm{W}^\pm$ bosons can also transfer electric charge, producing *charged current* interactions . In the SM neutrinos are massless particles with three flavors, each of them forming a weak isospin doublet with its respective charged lepton:

$$\begin{pmatrix} \nu_e \\ e \end{pmatrix} \begin{pmatrix} \nu_\mu \\ \mu \end{pmatrix} \begin{pmatrix} \nu_\tau \\ \tau \end{pmatrix}. \tag{1.1}$$

Neutrinos interact with other particles through the neutral and charged currents:

$$\begin{aligned} -\mathcal{L}_{NC} &= \frac{g}{2\cos\theta_W} \sum_l \bar{\nu}_{Ll} \gamma^\mu \nu_{Ll} Z^0_\mu \\ -\mathcal{L}_{CC} &= \frac{g}{\sqrt{2}} \sum_{Ll} \bar{\nu}_l \gamma^\mu l^-_L W^+_\mu + \text{h.c.}\,, \end{aligned} \tag{1.2}$$

where $l = e, \mu, \tau$ is the lepton flavor, g is the SU(2) weak coupling constant and θ_W the Weinberg angle [12]. The left component of the fermion fields (ν_L, l_L) is given by the projection operator $P_L = (1 - \gamma^5)/2$, and is the only one coupled to the weak boson fields $(W^\pm, Z^0)$. This is depicted in Fig 1.2, where a neutrino interacts with a nucleon.

Charged currents produce an outgoing lepton with the same flavor which allows us to determine the nature of the incident neutrino.

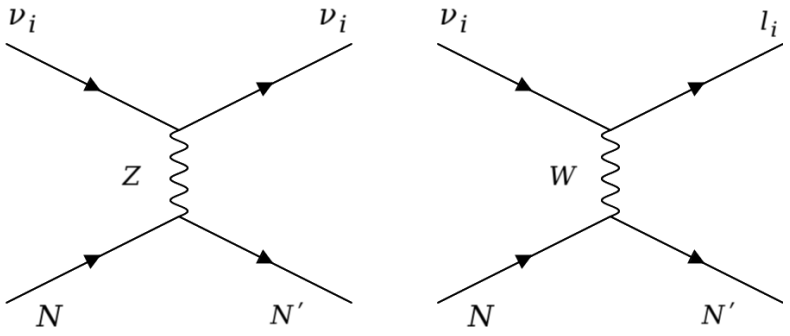

Figure 1.2: Left (Right): Feynman diagrams for the interaction between an incoming neutrino, ν_i with $i = e, \mu, \tau$, and a nucleon, N, for the neutral (charged) case. l_i is the outgoing lepton.

In the SM neutrinos (antineutrinos) are only left (right) handed. A right-handed neutrino component, not coupled to the weak carriers, could form Dirac mass terms through the Yukawa couplings:

$$\mathcal{L}_{\text{Yuk}} = m_D(\bar{\nu_L}\nu_R + \bar{\nu}_R\nu_L) \tag{1.3}$$

if neutrinos are Dirac particles, where $\nu_{L,R}$ represents a generic neutrino flavor field projected in the usual chiral (left-right) components. The neutrino mass (m_D) originates after the Higgs field acquires a vacuum expectation value (v):

$$m_D = c\frac{v}{\sqrt{2}}. \tag{1.4}$$

with c the (Yukawa) coupling to the Higgs field.

Neutrinos could also be Majorana particles with a mass term of the form:

$$\mathcal{L}_M = \frac{1}{2}m_M\bar{\psi}\psi^c + h.c. \tag{1.5}$$

In this case, the neutrino would be its own antiparticle, thus violating the total lepton number conservation.

Although the nature of the neutrino fields is still unknown, the experimental evidence indicates that there are three light neutrinos that interact weakly. The Z^0 boson can decay to a quark-antiquark, a charged lepton-antilepton or a neutrino-antineutrino pair. By measuring the total decay width of the Z^0 resonance, a constraint on the number (N_ν) of light neutrino flavors ($m_\nu < m_Z/2$) coupled to the weak force [13] can be

obtained. These are usually referred as active neutrinos. The LEP (Large Electron-Positron Collider) experiments at CERN combined results [14] for the number of weakly-coupled neutrinos

$$N_\nu = 2.9840 \pm 0.0082$$

are compatible with the three flavor paradigm. Any new neutrino must be right-handed (not coupled to the weak force). They are usually referred as *sterile* neutrinos. The detection of a sterile neutrino poses a technical challenge: a neutral particle not coupled to any of the three forces in the SM.

1.3 Beyond the Standard Model: the neutrino mass problem

As of today, the value of the neutrino mass is unknown. The current upper limits on the neutrino masses come from three different sources:

1. The standard cosmological model (ΛCDM) indirectly constrains the total neutrino mass ($\sum m_\nu$) using "cold" or relic neutrinos. These neutrinos come from the early universe, and thus were relativistic in origin. They became non-relativistic after the universe cooled down, transitioning to matter-like behavior and affecting the formation of galaxies, global structures, etc. The current limit combining DESI and CMB data yields an upper limit $\sum m_\nu < 0.072$ eV [15].

2. Direct end-point searches led by the KATRIN experiment, which measures with high precision the end point of the electron energy spectrum produced in tritium beta decays. Their current best value is $m_\nu < 0.45$ eV [16]. This method is purely based on the kinematics of the interaction and does not assume their Majorana or Dirac nature.

3. Neutrino-less double beta decay ($0\nu\beta\beta$) searches [17]:

$$(A, Z) \rightarrow (A, Z+2) + 2\,e^- + 2\cancel{\bar{\nu}_e} + Q_{\beta\beta}, \tag{1.6}$$

   where the 'annihilation' of the antineutrino pair leaves a clear signal with only 2 electrons produced at the same time and matching the remaining energy $Q_{\beta\beta}$. The discovery of this reaction would imply that SM neutrinos are Majorana particles and the total lepton number is violated, while no observation constrains the allowed phase space for Majorana neutrinos. The leading upper limits on the effective

Majorana mass ($m_{\beta\beta}$) is given by the KamLAND experiment $m_{\beta\beta}$ <28–122 MeV [18].

However, neutrinos were considered to be massless particles for a long time. Even today, many calculations assume the neutrino masses are negligible since they are below the eV scale [19]. In most cases, we can treat neutrinos as ultra-relativistic particles traveling at (almost) the speed of light. The natural question arises: how do we know their mass is not exactly zero?

The first experiment to observe a deficit of neutrino events with respect to the expected flux was the Homestake experiment led by Ray Davis [20]. Placed 1.47 km underground in the homonymous mine in South Dakota, it measured the neutrino flux from the Sun. The location mitigated the background from cosmic rays in the detector. The chosen target for ν interactions was perchloroethylene (C_2Cl_4), rich in chlorine which would react with neutrinos from the Sun producing ^{37}Ar:

$$\nu_e + {}^{37}\mathrm{Cl} \quad \longrightarrow \quad {}^{37}\mathrm{Ar} + e^-,$$

which decays into ^{37}Cl, producing Auger electrons detected with a proportional counter. The flux measured by Ray Davis was significantly smaller than expected, almost one third of the neutrino capture rate that John N. Bahcall calculations predicted [20]. By the 90's, a deficit in the solar neutrino flux was also confirmed by the other chlorine, water Cherenkov and gallium experiments [20–23].

Around the same time, different experiments measured the neutrinos produced by the interactions of cosmic rays with the upper atmosphere of the Earth [24–28]. The subsequent decay of pions and kaons constitutes a source of *atmospheric* neutrinos. At first order, a two-to-one ratio between muon and electron neutrinos was expected. While some experiments reported a deficit of muon neutrinos, the results were not conclusive.

The answer came from two independent experiments. First, the Super-Kamiokande collaboration measured with high precision the atmospheric flux as a function of the zenith angle. In 1998, they reported a deficit in the muon neutrinos coming from the antipodes with a simple explanation assuming a 2-oscillation model of muon and tau neutrinos [29]. Secondly, the SNO experiment measured both the neutral and charged currents from the solar neutrino flux [30]. While the charged current distributions showed a deficit similar to other experiments, events from neutral current were consistent with the prediction from the solar models: electron neutrinos were oscillating into muon and tau neutrinos.

Subsequent experiments have confirmed theses results and measured neutrino oscillations both in appearance and disappearance channels [31–34]. The nature of the oscillations requires neutrinos to have mass, although the oscillation phenomena is only sensible to the squared mass differences. A description of the oscillation formalism is given in the following section.

1.4 Neutrino oscillations

The idea of lepton flavor violation was already proposed by Bruno Pontecorvo. In 1957–58, he discussed the possibility of more neutrino states [35]. In particular, he noticed that [36]:

> “ *... one cannot exclude the possibility that the apparent contradiction... is partially due to the possibility that ... the stream of neutral particles changes its composition on the way from reactor to detector.* ”

Four years later, Maki, Nakagawa and Sakata [37] developed a simple two-neutrino flavor oscillation model. After the discovery of the τ [38] in 1975, the addition of ν_τ and subsequent extension to the current three flavor paradigm was straight forward.

In analogy with the quark sector and the CKM (Cabibbo-Kobayashi-Maskawa) matrix [39, 40], neutrino oscillations require neutrinos to have a mass term such as the one in Equation 1.3 and/or 1.5. For both Dirac and Majorana cases, the neutrino propagation states are the mass eigenstates (ν_1, ν_2, ν_3), and relate to the standard flavor states $(\nu_e, \nu_\mu, \nu_\tau)$ through the PMNS (Pontecorvo–Maki–Nakagawa–Sakata) matrix:

$$\begin{pmatrix} \nu_e \\ \nu_\mu \\ \nu_\tau \end{pmatrix} = \begin{pmatrix} U_{e1} & U_{e2} & U_{e3} \\ U_{\mu 1} & U_{\mu 2} & U_{\mu 3} \\ U_{\tau 1} & U_{\tau 2} & U_{\tau 3} \end{pmatrix} \begin{pmatrix} \nu_1 \\ \nu_2 \\ \nu_3 \end{pmatrix} \tag{1.7}$$

This matrix is unitary and has N^2 degrees of freedom. $N(N-1)/2$ can be identified with Euler rotations in Euclidean space. Re-defining the neutrino fields multiplying by a phase:

$$|\nu_j\rangle \rightarrow e^{i\phi_j} |\nu_j\rangle \tag{1.8}$$

allows us to remove unphysical degrees of freedom. The number of phases that can be absorbed this way depends on the Majorana or Dirac nature of the fields. For Dirac

(Majorana) fields and $N \geq 3$, $2N-5$ $(3N-6)$ can be interpreted as physical phases that may cause CP symmetry breaking [12]. For $N=3$ flavors and assuming a Dirac nature, there are three Euler angles and one complex phase (usually referred to as the CP phase or δ_{CP}). A common parametrization of the PMNS matrix is given by:

$$U_{\text{PMNS}} = \begin{pmatrix} c_{12}c_{13} & s_{12}c_{13} & s_{13}e^{-i\delta_{CP}} \\ -s_{12}c_{23} - c_{12}s_{23}s_{13}e^{i\delta_{CP}} & c_{12}c_{23} - s_{12}s_{23}s_{13}e^{i\delta_{CP}} & s_{23}c_{13} \\ s_{12}s_{23} - c_{12}s_{23}s_{13}e^{i\delta_{CP}} & -c_{12}s_{23} - s_{12}c_{23}s_{13}e^{i\delta_{CP}} & c_{23}c_{13} \end{pmatrix} \tag{1.9}$$

where s, c stand for the sine and cosine functions and the subscript labels the Euler angles: $\theta_{12}, \theta_{13}, \theta_{23}$. As in the hadron sector, CP violation requires $\delta_{CP} \neq 0, 180°$. In the Majorana case, two extra complex phases (α, β) are added:

$$U = U_{\text{PMNS}} \times \text{diag}(1, e^{i\alpha}, e^{i\beta}). \tag{1.10}$$

Because all SM neutrinos are light and their mass differences are below the eV scale, neutrino mass eigenstates $|\nu_i\rangle$ can interact coherently as they propagate in vacuum:

$$|\nu_i(x,t)\rangle \equiv \mathrm{e}^{-\mathrm{i}E_i t}\,|\nu_i(x,0)\rangle \tag{1.11}$$

The starting neutrino $(t=0)$ corresponds to a fixed flavor eigenstate and thus, a linear superposition of mass eigenstates. Each mass eigenstate has a different mass $(m_1 \neq m_2 \neq m_3)$, and so does their time evolution following Eq 1.11. As a result, there is a non-negligible probability of flavor change. The oscillation probability in vacuum depends on the energy of the neutrinos, the squared mass differences between mass eigenstates $(\Delta m^2_{ij} = m^2_j - m^2_i)$ and the total distance (L) traveled by the neutrino [13]:

$$\begin{aligned} P(\nu_\alpha \to \nu_\beta) =& \delta_{\alpha\beta} - 4\sum_{i>j=1}^{3} \text{Re}(K_{\alpha\beta,ij}) \sin^2\left(\frac{\Delta m^2_{ij} L}{4E}\right) \\ &+ 4\sum_{i>j=1}^{3} \text{Im}(K_{\alpha\beta,ij}) \sin\left(\frac{\Delta m^2_{ij} L}{4E}\right) \cos\left(\frac{\Delta m^2_{ij} L}{4E}\right) \end{aligned} \tag{1.12}$$

with:

$$K_{\alpha\beta,ij} = U_{\alpha i} U^*_{\beta i} U^*_{\alpha j} U_{\beta j} \tag{1.13}$$

For antineutrinos, the second term has the opposing sign and thus is sensible to the violation of the CP symmetry. This is the cause of the deficit observed in atmospheric neutrinos. The ones produced in the antipodes propagate through the Earth over longer distances (L) than the ones produced on top of the detectors, and therefore oscillate to other flavors.

Solar neutrinos suffer a similar effect but they have to travel through a dense plasma medium rich in free electrons. Because of this, the neutrinos also suffer from matter effects as they propagate through the Sun which modifies the oscillation probability in equation 1.12. For example, for the ^{8}B neutrinos it is estimated that more than 90% leave the star in the ν_2 mass eigenstate [41]. Indeed, that is what SNO experiment confirmed by measuring the total neutral and charged currents and their relative ratio [42].

It is important to note that equation 1.12 depends on the squared mass differences and thus is not sensitive to the absolute value of the neutrino masses. Due to the nature of the oscillations, it can also be shown that the possible Majorana phases associated with neutrinos would cancel out and thus are not measurable through oscillation analyses.

Last, note that the right-hand side from equation 1.12 vanishes if neutrinos were to be massless ($\Delta m^2_{ij} = 0$), but also if the PMNS angles $\theta_{\alpha\beta}$ were equal to 0. Complementary, for SM neutrinos to oscillate at least two of the three masses must be different from zero. The order of the mass eigenstates ($m_1 < m_2 < m_3$ called normal, $m_3 < m_1 < m_2$ called inverted) is still unknown.

The most recent values of the oscillation parameters from a global fit to the available data are given in Table 1.1 .

1.4.1 Open problems in neutrino physics

To date, the following questions remain open:

- The octant of θ_{23}, with preferred values between 40° and 52°. The current experimental data favors the second octant ($\theta_{23} \sim 49°$).
- The neutrino hierarchy as normal or inverted (depicted in Figure 1.3).
- The amount of CP violation in the lepton sector (determining the value of δ_{CP}).
- The absolute value of the neutrinos masses m_i.

	Normal Ordering (best fit)		Inverted Ordering ($\Delta\chi^2 = 2.3$)	
	bfp $\pm 1\sigma$	3σ range	bfp $\pm 1\sigma$	3σ range
$\sin^2\theta_{12}$	$0.307^{+0.012}_{-0.011}$	$0.275 \to 0.344$	$0.307^{+0.012}_{-0.011}$	$0.275 \to 0.344$
$\theta_{12}/^\circ$	$33.66^{+0.73}_{-0.70}$	$31.60 \to 35.94$	$33.67^{+0.73}_{-0.71}$	$31.61 \to 35.94$
$\sin^2\theta_{23}$	$0.572^{+0.018}_{-0.023}$	$0.407 \to 0.620$	$0.578^{+0.016}_{-0.021}$	$0.412 \to 0.623$
$\theta_{23}/^\circ$	$49.1^{+1.0}_{-1.3}$	$39.6 \to 51.9$	$49.5^{+0.9}_{-1.2}$	$39.9 \to 52.1$
$\sin^2\theta_{13}$	$0.02203^{+0.00056}_{-0.00058}$	$0.02029 \to 0.02391$	$0.02219^{+0.00059}_{-0.00057}$	$0.02047 \to 0.02396$
$\theta_{13}/^\circ$	$8.54^{+0.11}_{-0.11}$	$8.19 \to 8.89$	$8.57^{+0.11}_{-0.11}$	$8.23 \to 8.90$
$\delta_{\rm CP}/^\circ$	197^{+41}_{-25}	$108 \to 404$	286^{+27}_{-32}	$192 \to 360$
$\frac{\Delta m^2_{21}}{10^{-5}\ \text{eV}^2}$	$7.41^{+0.21}_{-0.20}$	$6.81 \to 8.03$	$7.41^{+0.21}_{-0.20}$	$6.81 \to 8.03$
$\frac{\Delta m^2_{3\ell}}{10^{-3}\ \text{eV}^2}$	$+2.511^{+0.027}_{-0.027}$	$+2.428 \to +2.597$	$-2.498^{+0.032}_{-0.024}$	$-2.581 \to -2.409$

Table 1.1: Neutrino oscillation parameters: best values and confidence intervals from the global fit to the available experimental data. All values taken from [43].

- The mechanism originating the neutrino mass term, and the neutrino nature as a Majorana or Dirac particle, implying the violation or conservation of the total lepton number.

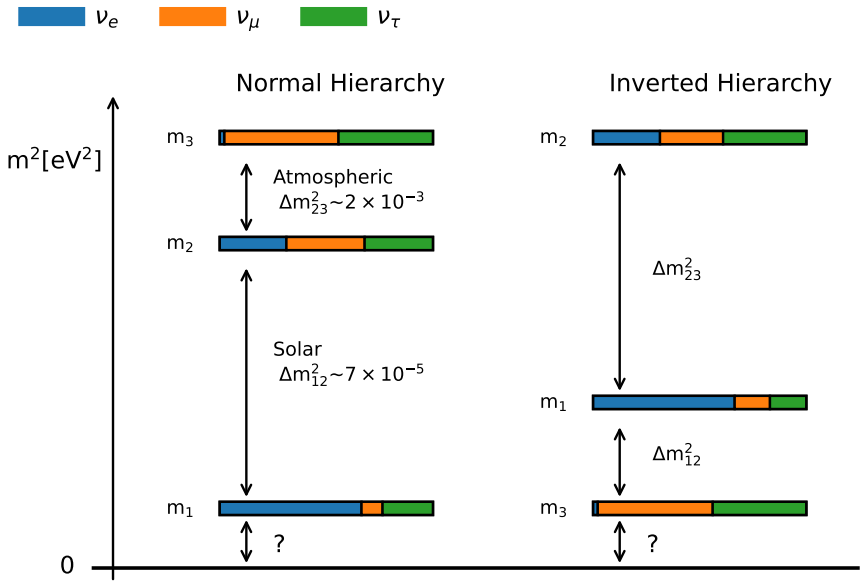

Figure 1.3: Normal and inverted hierarchy current status. Values taken from [43].

The first three questions will be addressed by next-generation long baseline oscillation experiments, particularly the DUNE and Hyper-Kamiokande collaborations [44, 45].

The foruth and fifth ones are the target of β decay and $0\nu\beta\beta$ searches respectively (see section 1.3).

1.5 Sterile neutrinos

So far, we have discussed the three-flavor paradigm, where *active* SM neutrinos interact through the weak force with other SM particles. There are, however, experimental anomalies suggesting more *non-active* or *sterile* neutrino mass states may exist [46].

1.5.1 Experimental hints

The LSND experiment observed in 2001 an excess of electron anti-neutrinos in a $\bar{\nu}_\mu$ beam at a 3.8σ confidence level (Figure 1.4-Left) [47]. The MiniBooNE collaboration reported a 4.7σ low-energy excess of electron-like events in neutrino mode (Figure 1.4-Right) and a total 4.8σ excess combining neutrino and antineutrino datasets [48, 49]. Being a Cherenkov detector, MiniBooNE was not capable of distinguishing between photon and electron induced signals. Thus, the nature of the anomaly remains unknown as charged ν_e current and neutral current (π^0 for example) events could cause the excess.

For this reason, other experiments like MicroBooNE (a liquid argon TPC located next to MiniBooNE) have searched for similar signals, but their results were not conclusive with those of MiniBooNE. Although MicroBooNE did not find excess of electron or photon events [50], a simple explanation to these anomalies would be the addition of a fourth light sterile neutrino. The global constraints to a 3+1 framework from short baseline experiments oscillation fits are shown in Figure 1.5. The Short-Baseline-Neutrino program (SBN) at Fermilab [51, 52] will look for these eV-scale sterile neutrinos in the upcoming years.

More hints come from the so-called *Gallium anomaly* [53], reported by the GALLEX, SAGE, and BEST detectors observing a deficit in charged-current ν_e events. For more than ten years, there has also been a *reactor anomaly* [54] showing a deficit of measured $\bar{\nu}_e$ from various nuclear reactor experiments. However, some models in newer flux calculations appear to relax tensions between the expected $\bar{\nu}_e$ reactor flux and data [55]. Additionally, cosmological models can constrain the effective number (N_{eff}) of light sterile neutrinos as they contribute to the energy density of the universe [46]. The latest measurements from Plank data estimate $N_{eff} = 2.99 \pm 0.17$ in agreement with the SM prediction ($N_{eff} = 3.046$) [56].

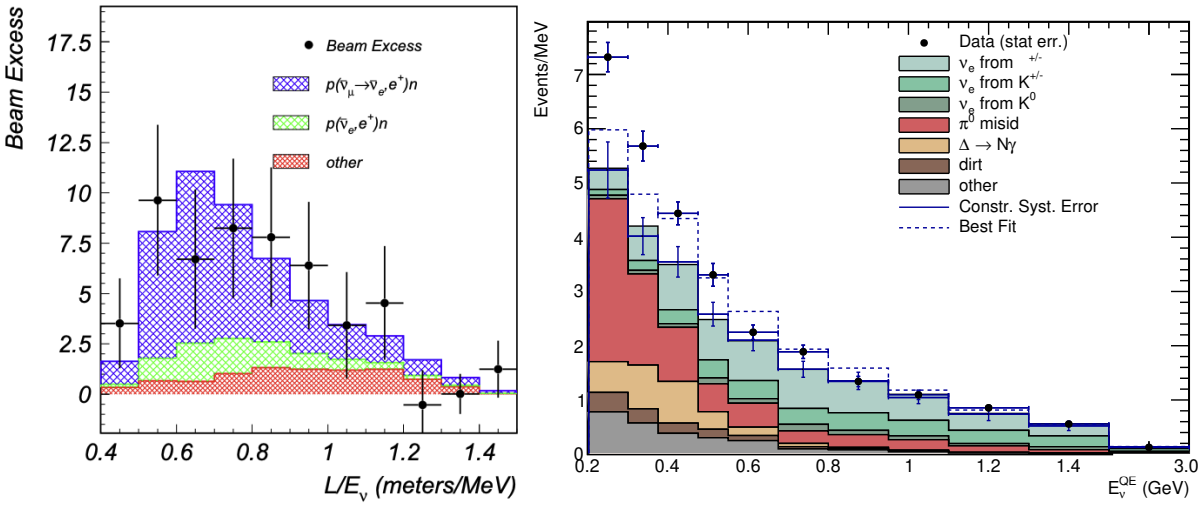

Figure 1.4: Left: LSND reported excess of $\bar{\nu}_e$ over background events as a function of the L/E_ν ratio [47]. Right: excess of electron-like events observed by MiniBooNE in neutrino mode [49]. The LSND and MiniBooNE excesses can be interpreted as an oscillating light neutrino of ~ 1 eV, incompatible with the current data available of the three active neutrinos.

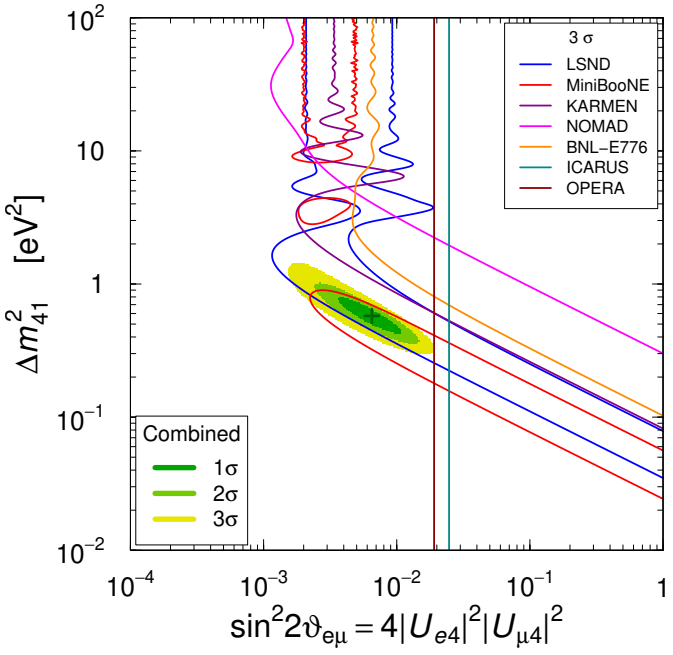

Figure 1.5: Global constraints to a 3+1 oscillation model from short-baseline experiments. MiniBooNE and LSND lines are allowed regions at 3σ while the rest exclude the region to the right at 3σ. The allowed regions from a combined fit are shown with filled color. Graph taken from [46].

It is worth mentioning that some data exhibit contradictory tendencies, for example, in the global 3+1 fits between the $\nu_\mu \to \nu_e$ appearance and the $\nu_\mu \to \nu_\mu$ disappearance data [46]. There is also tension between the reactor and gallium experiments, particularly in the $\nu_e \to \nu_e$ disappearance channel [57–59].

1.6 Heavy neutral leptons

The fundamental idea of Heavy Neutral Lepton (HNL) models is the addition of one or more heavy sterile neutrinos (m_N), making the lighter neutrino masses (m_ν) inversely proportional to the heavier states [60]. One can introduce more neutrino mass states by expanding the usual PMNS matrix to a $(3+n, 3+n)$ matrix with n the extra mass states:

$$\begin{pmatrix} \nu_e \\ \nu_\mu \\ \nu_\tau \\ \vdots \\ \nu_{s_n} \end{pmatrix} = \begin{pmatrix} U_{e1} & U_{e2} & U_{e3} & \cdots & U_{en} \\ U_{\mu 1} & U_{\mu 2} & U_{\mu 3} & \cdots & U_{\mu n} \\ U_{\tau 1} & U_{\tau 2} & U_{\tau 3} & \cdots & U_{\tau n} \\ \vdots & \vdots & \vdots & \ddots & \vdots \\ U_{s_n 1} & U_{s_n 2} & U_{s_n 3} & \cdots & U_{s_n n} \end{pmatrix} \begin{pmatrix} \nu_1 \\ \nu_2 \\ \nu_3 \\ \vdots \\ \nu_n \end{pmatrix} \tag{1.14}$$

The 3+1 model in the eV-scale proposed to explain the anomalies observed by experiments has one key feature: the new sterile neutrino oscillates with the rest of the SM neutrinos. In general, this will happen if the new neutrino is light enough for its wave packet to propagate coherently with the SM neutrinos [61, 62]. HNLs, on the other hand, are heavier and decohere from the active neutrinos, not participating in neutrino oscillations.

Figure 1.6 illustrates the propagation of the neutrino wave packets. The decoherence from the SM packets occurs if the new sterile neutrino travels slow enough with respect to the distance between the production point and the detector. We define Δd_ν as the difference:

$$\Delta d_\nu = \frac{pL}{c}\left(\frac{1}{m_{\text{active}}} - \frac{1}{m_{\text{sterile}}}\right) \tag{1.15}$$

with p the neutrino momentum and L the distance traveled. Noting the size of the wave packet in the propagation direction as σ_z, we then can distinguish light sterile neutrinos if $\Delta d_\nu \ll \sigma_z$ and heavy when $\Delta d_\nu \sim \sigma_z$. For the distances and energies available at SBN ($L < 1$ km and $E_\nu \sim 700$ MeV), sterile neutrinos with $m \geq 1$ MeV lose the coherence with SM neutrinos.

Different see-saw types have been developed depending on the mediator(s) involved and the associated operators added to the SM Lagrangian. In the common Type I see-saw, the HNL is a right-handed singlet, whereas Types II and III introduce scalar and fermion triplets, respectively. An extensive review is given in [60]. The range of HNL masses spans from few keV to TeV and even energies at the grand unified theory scale.

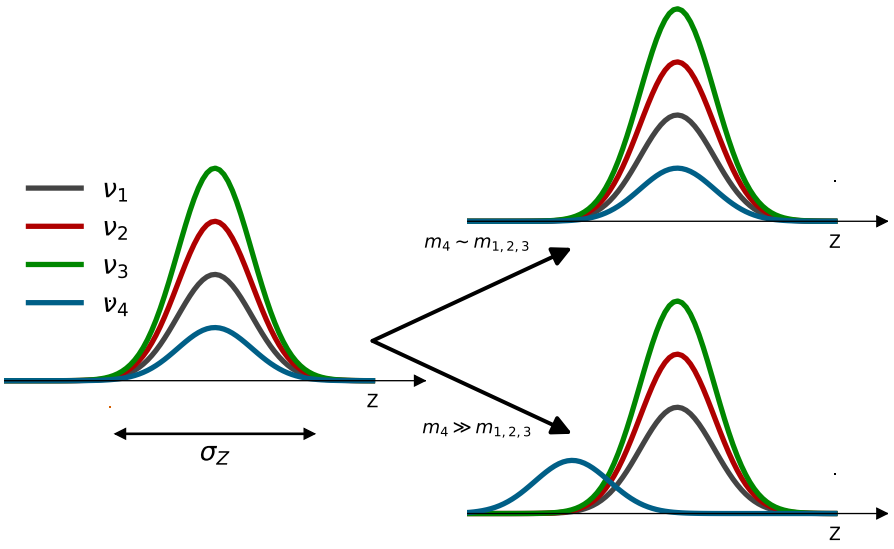

Figure 1.6: Cartoon depicting propagation of the neutrino wave packets. Left: wave packet at the creation instant. Right: the light (top-right) and heavy (bottom-right) sterile neutrino cases are shown. The decoherence occurs if the delay is comparable or bigger than the scales of the distances between production and decay of the neutrino mass states.

HNL searches can also be divided by the light active neutrino the HNL is coupled to $(\nu_e, \nu_\mu, \nu_\tau)$. Figure 1.7 shows the current experimental limits from beam experiment searches for the case where one of the three couplings dominates and the other two can be neglected.

Electron-coupled HNLs ($|U_{e4}|^2 \neq 0$) can be produced with masses up to ∼130 (490) MeV from pion (kaon) decays. The current limits in electron-coupled HNLs in the [30–490] MeV range come from the PIONEER, NA62 and PIENU experiments [60].

HNLs coupled to muon neutrinos ($|U_{\mu4}|^2 \neq 0$) have allowed mass regions up to (30) 388 MeV from pion (kaon) decays. The SBN program [52] is competitive in this mass range [30-380] MeV with world leading results coming from the MicroBooNE, T2K, PS191 PIENU and E949 experiments [63–69].

Tau-coupled HNLs ($|U_{\tau4}|^2 \neq 0$) are kinematically forbidden for the BNB energies. The leading results in these searches come from CHARM, Belle, and DELPHI collaborations [60].

In all three cases, a lower limit of the HNL coupling to Standard Model neutrinos can be derived using Big Bang nucleosynthesis (BBN) data. In particular, the decays of HNLs in the early plasma would affect the abundance of light elements [70].

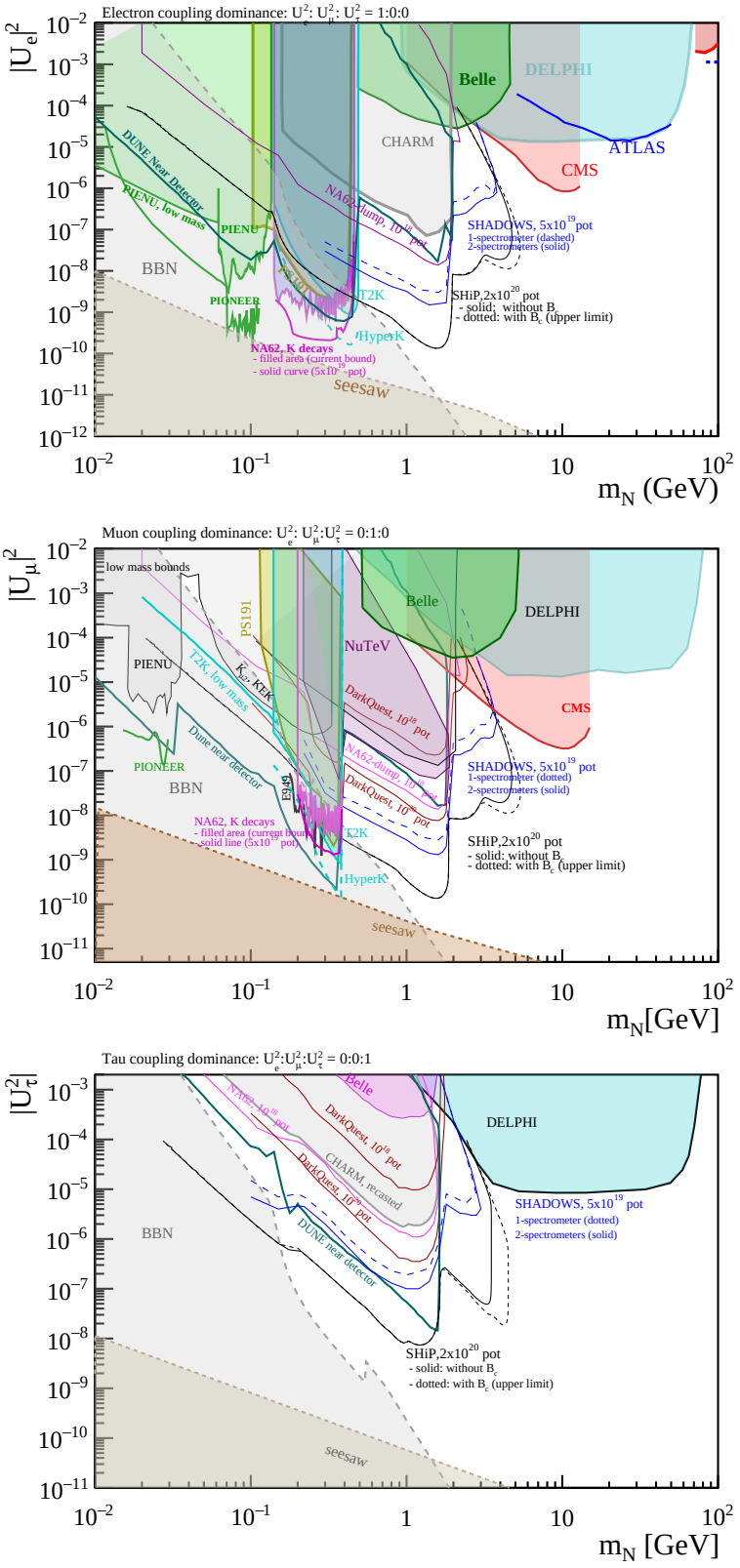

Figure 1.7: Current experimental limits (solid regions) and projected limits (solid lines) on electron, muon and tau coupled HNL searches (top, center and bottom respectively) from beam experiments and prospects for DUNE and HyperK. The lower limits from BBN data and seesaw models (shaded regions) are also shown. Figures taken from [60].

Chapter 2

SBND in the SBN program

Neutrinos are particles only coupled to the weak force. With a small cross section, their detection and characterization is a challenging task. In this chapter, a review of the SBND detector and the SBN program is given. First, a general overview is outlined in Section 2.1. The neutrino beam employed in the SBN program at Fermilab is described in Section 2.2, while Section 2.3 reviews the technology chosen for the three detectors of the SBN program: the Liquid Argon Time Projection chamber. The details of the SBND experiment are given in Section 2.4.

2.1 The Short-Baseline Neutrino program

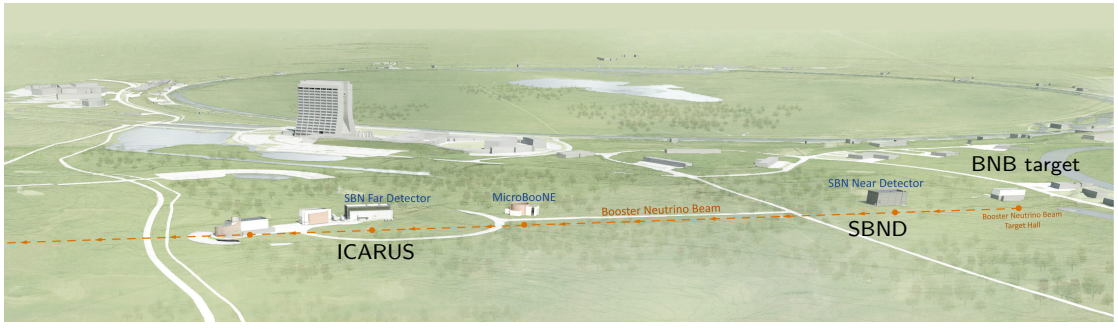

Figure 2.1: Map of the SBN program at Fermilab. The three SBN detectors (in blue): SBND, MicroBooNE and ICARUS, have baselines of 110 m, 470 m and 600 m respectively. The Booster Neutrino Beam (in red) delivers a 99.5% ν_μ flux with $\langle E_{\nu_\mu} \rangle = 0.7$ GeV.

The Short-Baseline Neutrino (SBN) program at Fermilab [51, 52] consists of three Liquid Argon Time Projection chamber (LArTPC) experiments at different baselines from the Booster Neutrino Beam (BNB): SBND, MicroBooNE and ICARUS (see Figure 2.1).

The SBN program will look for light sterile neutrinos in the eV mass scale and test the excess seen by both LSND and MiniBooNE detectors [47, 48]. To constrain the systematic uncertainties, the three detectors employ the same technology: the liquid argon time projection chamber [71].

MicroBooNE, with an active volume of 89 tons and located 470 meters from the BNB target, operated from 2015 to 2021 [72]. MicroBooNE recorded data equivalent to 13.2 $\times 10^{20}$ POT from the BNB. The detector was placed close to the MiniBooNE detector vault to directly test its anomaly, as LArTPCs are capable to separate electron from photon-induced signals [73, 74].

ICARUS took neutrino beam data from 2010 to 2013 at Gran Sasso (Italy)[75, 76]. After major upgrades to the charge and light readout systems [77], the four TPCs of ICARUS were moved in 2017 to Fermilab. With an active volume of 476 tons, ICARUS was placed at 600 meters from the BNB target to be the far detector of the SBN program. The experiment started operations at its new location on 2021 [78], searching for oscillations. ICARUS will take data equivalent to 6.6×10^{20} Protons on Target (POT) from the BNB. The difference in the active volumes of ICARUS and MicroBooNE, makes ICARUS dataset larger.

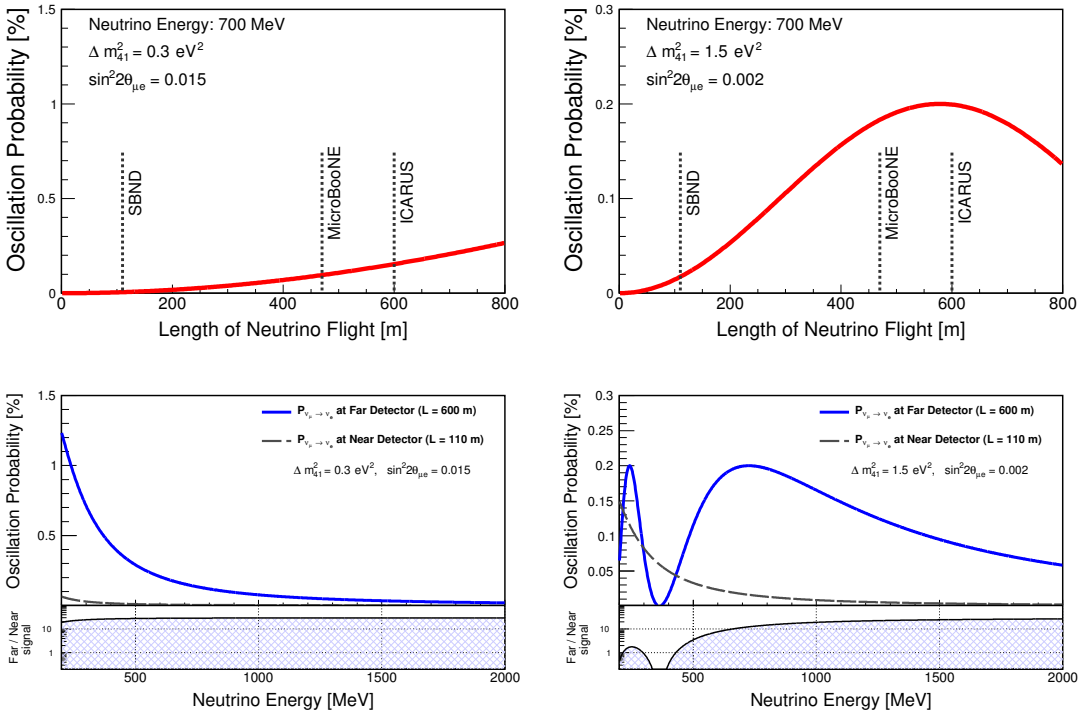

Figure 2.2: Top: $\nu_\mu \rightarrow \nu_e$ oscillation probabilities for a 700 MeV neutrino for different oscillation parameters assuming a 3+1 model. Bottom: oscillation probabilities at the near and far detectors as a function of the neutrino energy. Graphs taken from [52].

SBND, the near detector, is placed at 110 m from the BNB target and has an active volume of 112 ton. Due to its proximity to the beam target, SBND observes the largest flux from the BNB. This represents millions of neutrino events for a total 3-year exposure (10^21 POT). The filling of the detector was completed in March 2024 and physics data taking started in fall 2024. The main characteristics of the three detectors are summarized in Table 2.1.

The specific location of the far detector was chosen to be close to the oscillation maximum assuming a 3+1 neutrino model with a fourth light sterile neutrino in the eV range (see Figure 2.2-Top). The BNB peaks at $\sim$ 700 MeV, close to the second oscillation peak assuming a $\Delta m^2_{41} = 1.5$ eV^2 (Figure 2.2-Bottom). Flux uncertainties as well as the systematic uncertainties associated with nucleon interactions are critical for oscillation searches. Flux uncertainties are constrained by the near detector, while cross-section and interaction uncertainties are reduced by using the same target medium, and detector effects by sharing the same technology, the LArTPC. The exclusion limits for the SBN program combining the three detectors to a 3+1 scenario are shown in Figure 2.3 Left (Right) for the $\nu_e(\nu_\mu)$ appearance (disappearance) channel. The allowed regions (filled brown) show the sensitivity of the SBN Program assuming a sterile neutrino signal with a mass of $\sim$1 eV.

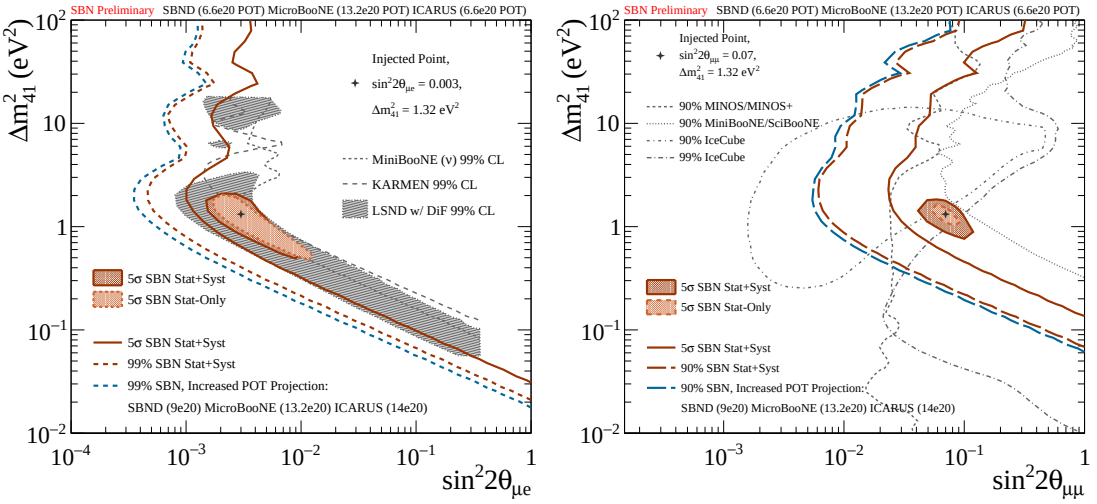

Figure 2.3: Left (Right): SBN exclusion and allowed-region sensitivities to $\nu_e(\nu_\mu)$ appearance (disappearance) under the (3+1) sterile neutrino hypothesis. The exclusion limits are shown with solid and dashed brown lines for the 5σ and 99% confidence levels. The blue dashed line includes the expected increase in exposure for SBND and ICARUS. The filled areas show the SBN sensitivity to a sterile signal with a squared mass difference of $\Delta m^2_{41} = 1.3$ eV^2. The contours produced with data from other experiments are shown with gray lines.

The SBN program will collect millions of neutrino-argon interactions. The proximity of the detectors to the beam target also allows for other beyond Standard Model (BSM)

searches such as dark photons, heavy neutral leptons (HNLs), light dark matter... Massive long-lived particles (LLP) can leave imprints similar to SM neutrinos but delayed with respect to the beam due to the slower propagation [79], while some models leave characteristic topologies with little or none SM equivalents, for example, HNLs decaying into a electron-positron pair and a neutrino, with a clear common vertex (see Chapters 5 and 6).

Detector	Active volume [tons]	L_{BNB} [m]	Exposure [10^{20} POT]	BNB spills/ν	Total ν ($\times 10^6$)
SBND	112	110	10	20	10
MicroBooNE	87	470	13.2	600	0.44
ICARUS	476	600	15	180	1.65

Table 2.1: Summary of the three detectors of the SBN program. For ICARUS and SBND, the expected exposure is shown. The 5th column represents the number of spills from the beam required on average to produce a neutrino interaction at each detector. The total number of events assumes a rate of $5{\times}10^{12}$ POT per BNB spill. A detailed description of the beam characteristics is given in section 2.2.

2.2 The Booster Neutrino Beam

The neutrino beam is produced from the collisions of a 8 GeV proton beam with the beryllium target, as shown in Figure 2.4. First, protons are pumped from the 750 keV injector into the LINAC facility (purple) where they reach 400 MeV and then are injected into the Booster. The Booster (blue) is a 474-meter-circumference synchrotron with a firing frequency of 15 Hz [81]. The Booster has a harmonic number of 84, of which 81 buckets of protons are filled and accelerated up to 8 GeV of kinetic energy. The beam is extracted from the Booster using a fast-rising kicker magnet that extracts all the protons in a single cycle or *spill*. Each spill contains $\sim 5 \times 10^{12}$ protons that hit the beryllium target, usually referred as *protons on target* (POT). Each spill has a total duration of $\sim 1.6\,\mu$s. The structure of the spill contains the 81 bunches separated approximately 19 ns from each other with a 1.3 ns width each [82, 83], as depicted in Figure 2.5. In SBND, one neutrino interaction is expected each 20 beam spills or 4 seconds, since the BNB horn rate is up to 5 Hz.

Before the target, the proton beam intensity, width and position are monitored. The vacuum in the beam pipe extends up to 1.5 m before the target, minimizing the proton interactions. At the target (green dot in Figure 2.4), the accelerated protons hit the seven beryllium cylindrical slugs with a total 71.1 cm length and 0.51 cm in radius. The pions and kaons produced are focused with a magnetic horn. The horn is a pulsed toroidal electromagnet that produces a magnetic field of up to 1.5 Tesla. Because the

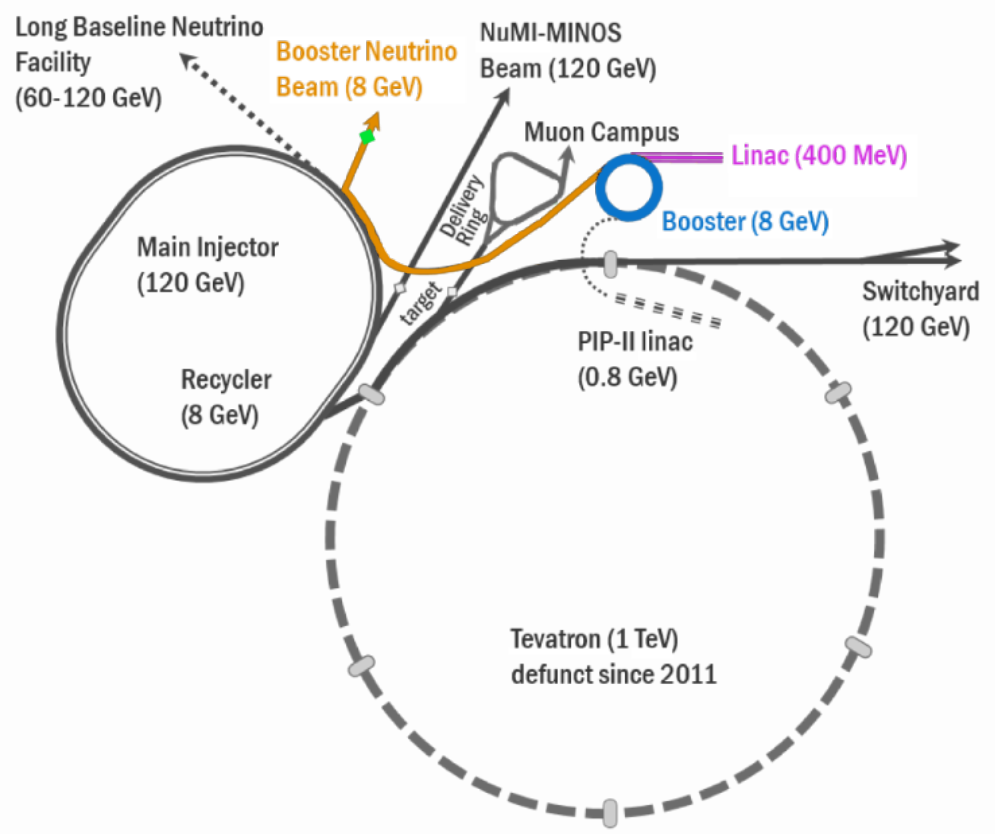

Figure 2.4: Scheme of the Booster facilities at Fermilab in colors [80]. The protons enter the linear accelerator (purple) and are injected in the Booster ring (blue) where they reach up to 8 GeV. Then they are conducted (orange) to the beryllium target (green dot), producing the BNB flux.

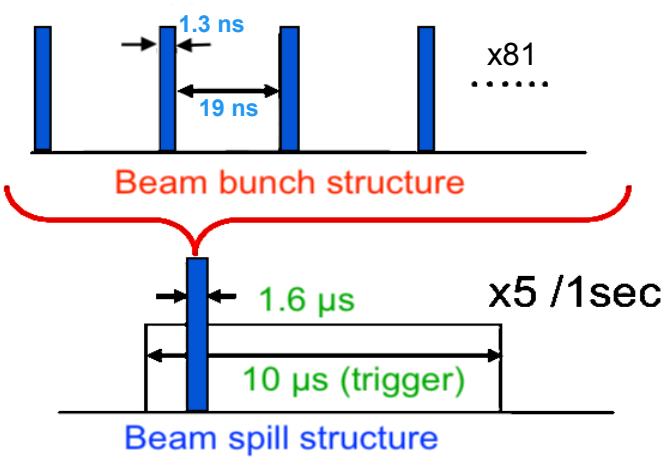

Figure 2.5: Time structure of the BNB spills. At nominal conditions, five spills are delivered per second with a duration of 1.6 μs each. The spill has an inner structure of 81 bunches, separated 19 ns from each other.

polarity of the magnet selects either positive or negative charged mesons, the beam can run in neutrino or antineutrino mode. In the following 50 meters, the decay of the

mesons produces a flux composed mainly of ν_μ, as depicted in Figure 2.6. The neutrino spectra depends on both the neutrino energy (Figure 2.7) and the angle with respect to the beam-line. The produced neutrino beam inherits the bunch structure from the proton beam, convolved with the flight and decay times of the produced mesons.

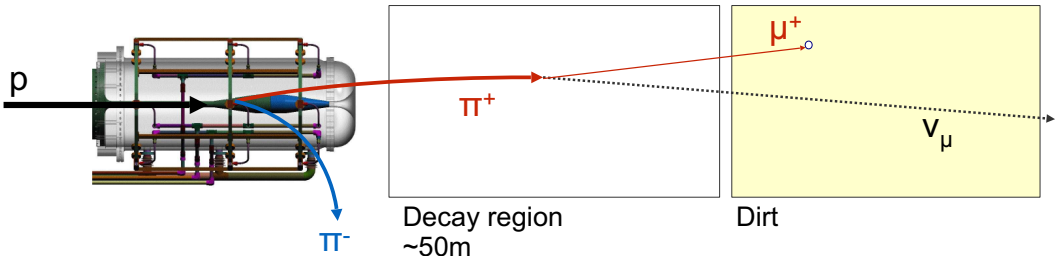

Figure 2.6: Scheme of the BNB target and magnetic horn [84]. The incident protons produce forward-going mesons, which are focused selecting positive (neutrino mode) or negative (antineutrino mode) particles. The main contribution to the neutrino flux comes from pion and kaon decays.

A dedicated Geant4 [85] simulation is used to estimate the arriving neutrino flux at each SBN experiment. The Monte Carlo simulation includes the location and composition of the relevant components of the BNB. The p-Be interaction modeling includes elastic and quasi-elastic scattering with models constrained using external data [81]. The tuning of the $\pi^{\pm}$ production incorporates the HARP dataset using the Sanford-Wang parametrization [81]. The kaon production is constrained by SciBooNE's K^+ production cross-section measurement using high energy neutrinos from the BNB [86]. Produced particles can undergo energy loss and hadronic processes. The magnetic field effect in their trajectories is also included. The simulation keeps any decay chain that contains a neutrino in the final state, saving the parents energies, momenta and initial and final positions.

The resulting neutrino flux at the SBND front face is shown in Figure 2.7-Top. Notice that the neutrino flux in Figure 2.7 also has a small contamination of $\bar{\nu}_\mu$ (while running in neutrino mode) from very forward negative mesons and some ν_e and $\bar{\nu}_e$. Most of the neutrinos are produced by pion decays with a small contribution from kaons and muons as shown in Figure 2.7-Center and Right for the ν_μ and $\bar{\nu}_\mu$ components.

2.3 The LArTPC Technology

The liquid argon time-projection chamber (LArTPC) was first proposed by Carlo Rubbia [71] in the late 1970s with the idea in mind of a scalable, multi-ton neutrino detector that also had precise information of the event topology. At the time, neutrino experiments were divided into two main categories: the high definition but small-sized targets led by

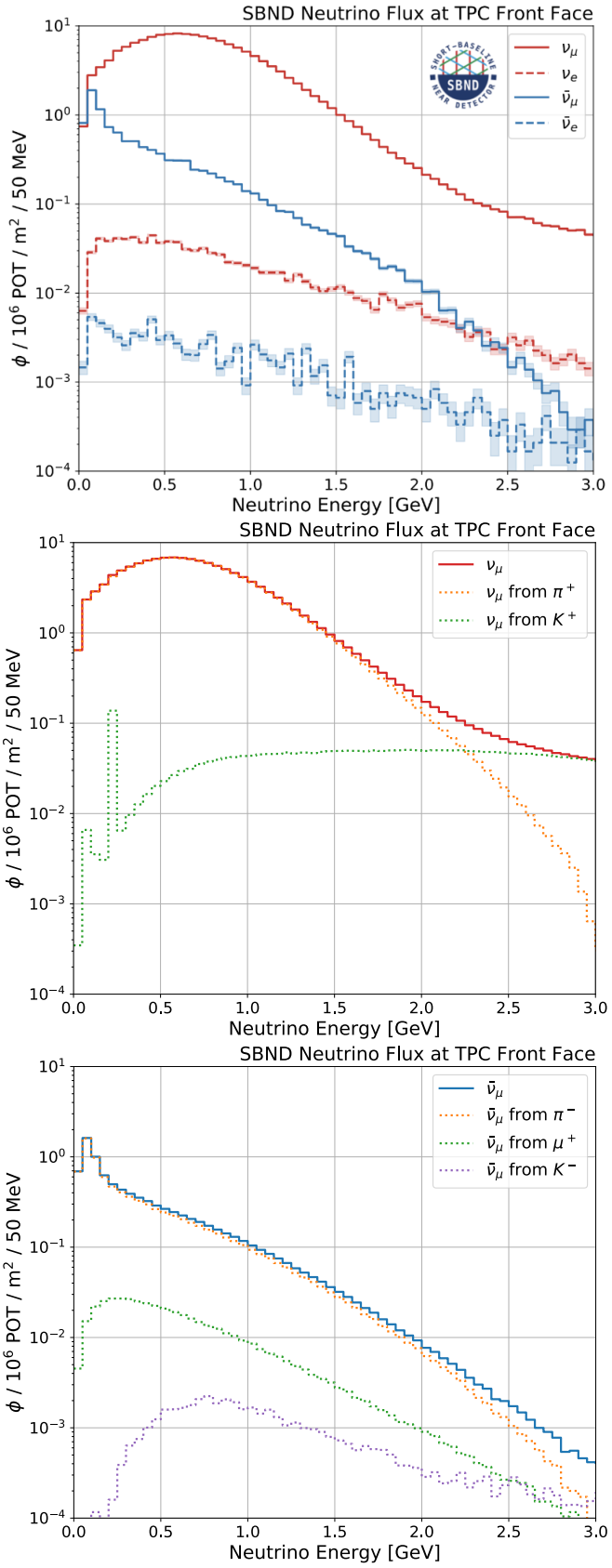

Figure 2.7: Top: BNB flux at the SBND front face by neutrino type [84]. Center and bottom: flux composition by parent meson for the ν_μ and $\bar{\nu}_\mu$ components respectively.

bubble chambers, and targets with bigger masses such as water-Cherenkov approaches where only some of the global features of particle interactions (angle, total deposited energy...) could be estimated.

In a LArTPC, ionization electrons and scintillation photons are produced by the interaction of the charged particles crossing the detector with the argon. The work function values are 23.6 eV and 19.5 eV for electrons and photons respectively [87]. The electrons are then drifted towards the anode readout planes through an applied electric field, typically in the 500 V/cm scale. The readout of the charge in the anode planes allows to create 2D pictures of the interactions. The combination of multiple readout planes gives a 3D reconstruction of the event (Figure 2.8). Because the photons propagate in the ns scale, light signals enable precise determination of the interaction time t_0.

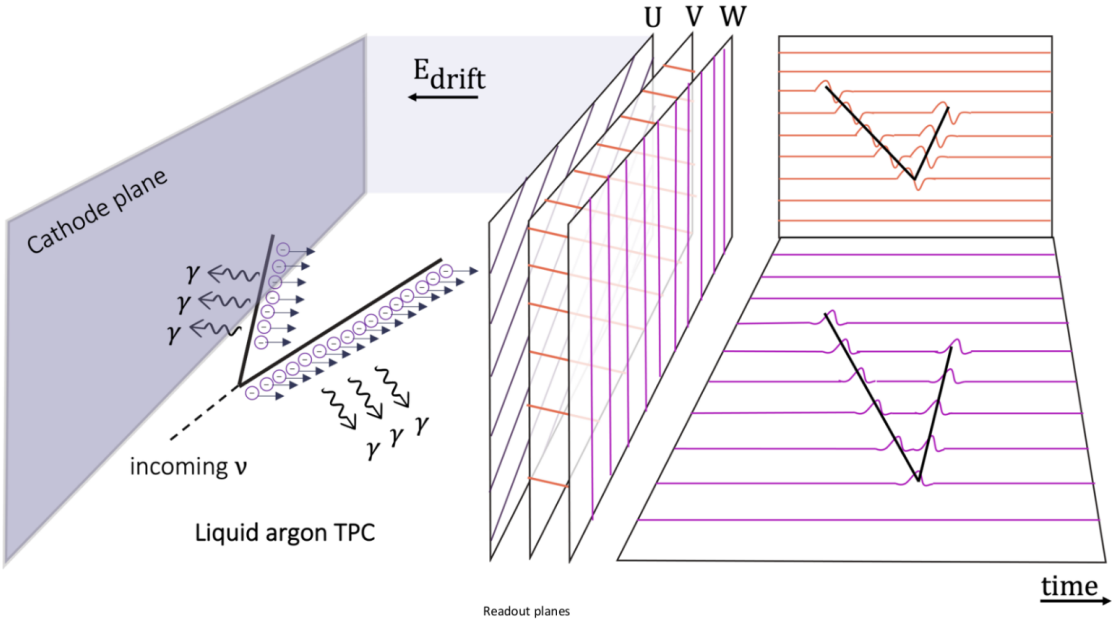

Figure 2.8: Working principle of a LArTPC [88]: charged particles inside the detector deposit energy in the medium ionizing electrons and producing scintillation photons. The electrons are drifted towards the anode planes applying an electric field. From the readout of the electric signals on induction (U,V) and collection (W) planes, a complete 3D picture of the event is produced.

The topological resolution is limited by the wire pitch, the distance between two consecutive wires, with current LArTPCs in the few mm-scale. The area of the wire intensity signal is proportional to the amount of electrons arriving to the wires, with energy thresholds of hundreds of keVs deposited in argon.

The scintillation photons (light information) are produced in the VUV range and travel the TPC at 13.4 cm/ns [89] providing triggering, timing and complementary calorimetry to the ionization electrons (usually refereed as charge or TPC) information. Combining

the light and charge information is essential to reduce backgrounds such as muons from cosmic rays [90].

Maintaining the purity of the LAr is key as free electrons and scintillation photons can be captured by other elements before reaching the readout systems. Another challenge of these detectors is the cryogenic setup required to cool and maintain the argon in optimal conditions given the low boiling point (-186 °C / 87 K at 1 atm) of LAr, as well as operating the TPC and light readout systems immersed in the argon. There are, however, significant advantages that outweigh the complexity of using this element as a target medium [71]:

- A high atomic mass number means more nucleons for the neutrinos to interact with. The liquid argon also has a high density (1.39 g/cm^3).
- Argon is transparent to its own scintillation light, meaning that photons produced by argon dimers are not absorbed again.
- TPC-crossing electrons can be measured at the anode planes without being re-captured by argon atoms, given sufficient purity of the argon ($<$ 1 ppb of O_2) is achieved [91]. Drift distances up to 6 meters have been tested and operated [92, 93], to prepare for the upcoming kilo-ton scale that DUNE far detectors will employ.
- The high electron mobility ($\mu : v = \mu \times E$, with E the applied electric field) allows the readout of detectors with drift distances of few meters in the milliseconds scale [94].
- Argon is the most abundant noble element in the atmosphere (0.94%). It is easy to extract and purify and a relatively cheap material.

The main relevant physical parameters of liquid argon are summarized in Table 2.2. Progressively larger LArTPCs have been developed over the past decades [51, 72, 75, 93, 95] increasing the number of recorded neutrino events and pushing the knowledge of the field.

2.3.1 Charge production and transport in a LArTPC

Different charged particles will leave different signatures in a LArTPC. For the neutrino energies available at the BNB (hundreds of MeVs to few GeVs), the products of the interaction with argon nuclei can be split into two categories by the topology in the detector:

Property	**Value**	**Unit**
Boiling point	87.30	K
Density at 87K	1.397	g cm^{-3}
When held in a 500 V cm^{-1} electric field and at 87 K		
Electron mobility	329.7	cm^2 V^{-1} s^{-1}
Electron drift velocity	0.1648×10^6	cm s^{-1}
Longitudinal diffusion coefficient	6.823	cm^2 s^{-1}
Transverse diffusion coefficient	13.16	cm^2 s^{-1}
Critical energy, $e^{\pm}$	32.8	MeV
Critical energy, $\mu^{\pm}$	485	GeV
Molière radius	9.04	cm
Radiation length	14.0	cm
Nuclear interaction length	85.7	cm
Minimum specific energy loss	2.12	MeV cm^{-1}

Table 2.2: Relevant physical properties of liquid argon. Values taken from [12, 96].

- Protons, muons and pions deposit energy mainly by collisions [97], leaving in most cases a clear straight line of ionized electrons usually called a track (see Figure 2.9). Muons tend to leave longer tracks, some of them escaping the active volume of the detectors. Some notable exceptions are low energy protons with track lengths in the few centimeters. MeV-scale electrons (below 100 MeVs) also leave track-like signals.

- GeV-scale electrons deposit their energy by radiative photon production through bremsstrahlung. Photons of few MeVs produce electron-positron pairs. Secondary pairs can radiate photons producing extra e^+e^- pairs, as shown in Figure 2.10. The cascade of particles is usually called an electromagnetic shower. Photons present a gap between the creation vertex and the start of the shower when the e^+e^- pair is produced. Their radiation length in LAr is 14 cm. Electrons, on the other hand, start the shower at the interaction vertex.

A LArTPC does not distinguish the sign of the charge of an ionizing particle without applying a magnetic field. However, the mean rate of energy loss per unit distance (dE/dx) described by the Bethe-Bloch equation [12] can be used to separate different massive charged particles in the detector:

$$-\left\langle \frac{dE}{dx} \right\rangle = Kz^2 \frac{Z}{A} \frac{1}{\beta^2} \left[\frac{1}{2} \ln \frac{2m_e c^2 \beta^2 \gamma^2 T_{\max}}{I^2} - \beta^2 - \frac{\delta(\beta\gamma)}{2} \right], \tag{2.1}$$

where K is a constant factor, z the charge of the particle crossing the material, Z, A the atomic and mass numbers of the medium, I the mean ionization energy, $\delta(\beta\gamma)$ a

Figure 2.9: Neutrino event candidate with showers (white) and tracks (orange).

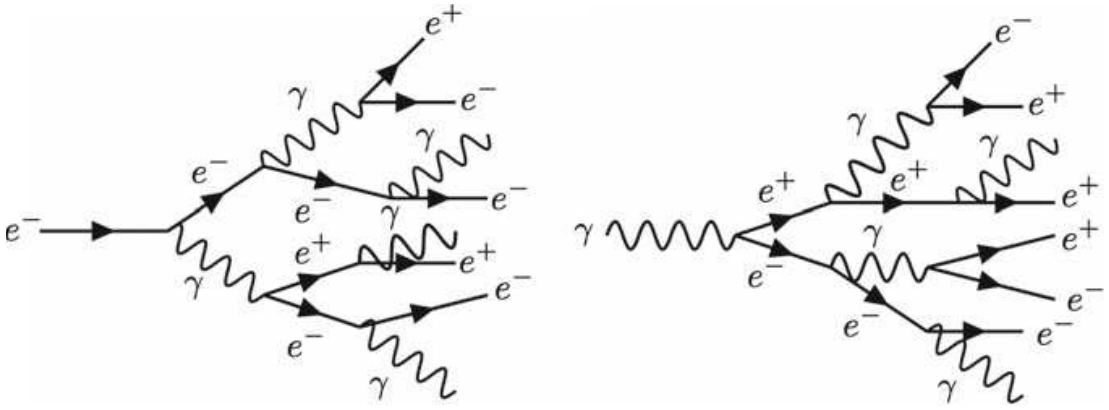

Figure 2.10: Scheme of different shower types if the starting particle is an electron (Left) or a photon (Right). Picture taken from [98].

density correction term, and β, γ the usual relativistic factors: $\beta = v/c$, $\gamma = \sqrt{1-\beta^2}$. For reference, a minimum ionizing particle (MIP) leaves ~ 2 MeV/cm. The maximum energy transferred through scattering, $T_{\max}$ depends on the mass M of the charged particle:

$$T_{\max} = \frac{2m_e\beta^2\gamma^2}{1 + (2\gamma m_e)/M + (m_e/M)^2}. \tag{2.2}$$

This allows for the identification of protons from muons and pions, as shown in Figure 2.11. Muons and pions themselves are harder to separate due to their similar masses.

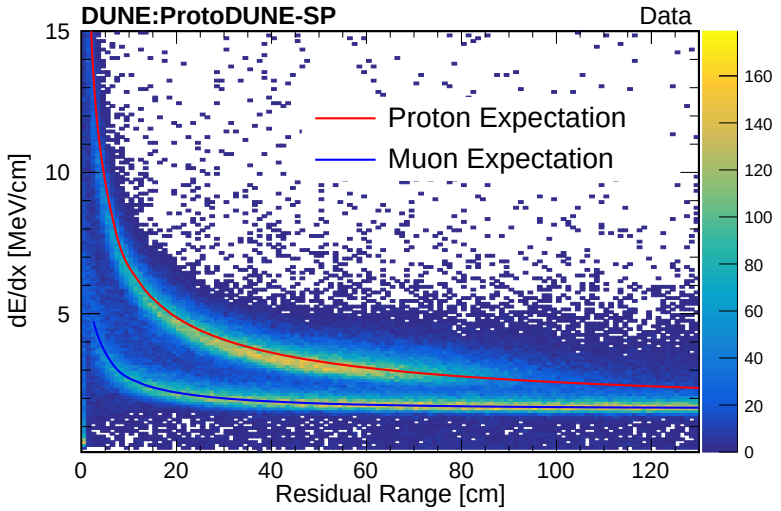

Figure 2.11: dE/dx versus residual range for stopping protons (upper band) and muons (lower band), picture taken from [93].

Recent studies, however, suggest that looking at the small energy depositions (*blips*) at track endpoints may help to distinguish them [99].

For showers, the dE/dx along the first centimeters of the shower can be used to separate electron and photon induced cascades, as shown by ArgoNeuT (see Figure 2.12) and MicroBooNE experiments [100, 101].

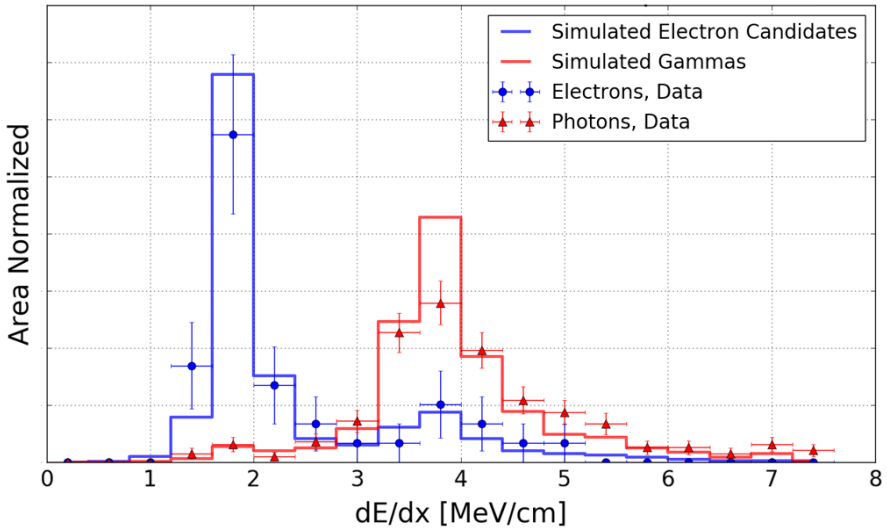

Figure 2.12: dE/dx distribution for electrons (blue) and gammas (red) for simulated (solid) and data (points) events from ArgoNeuT [100].

In a uniform electric field, the original position of an ionized electron is given by:

$$d = v \times (t - t_0). \tag{2.3}$$

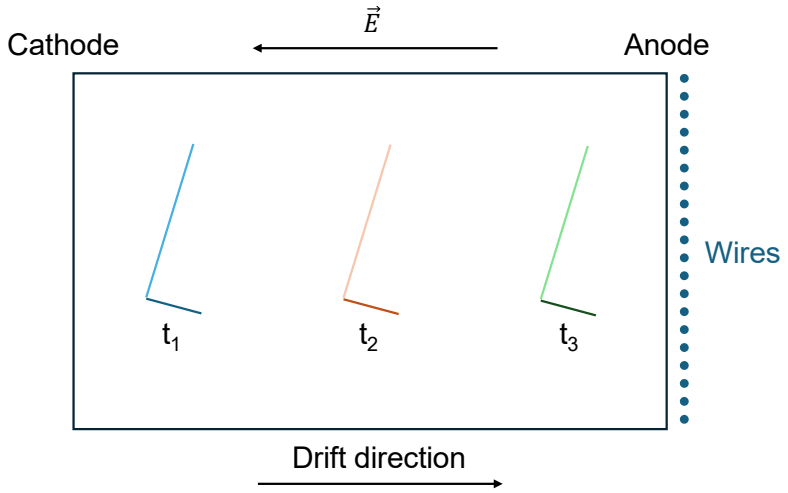

Figure 2.13: Cartoon showing the ambiguity in the t_0 determination. The same signal could be produced at different times ($t_3 > t_2 > t_1$) along the drift direction.

where v is the electron velocity in liquid argon, and t_0 the time when the electrons were freed from the atom nuclei. There is, however, ambiguity when estimating the t_0 of the interaction (see Figure 2.13). Because the ionizing electrons take milliseconds to reach the wires, the interaction can happen at different times $t_{1,2,3}$ and drift lengths. However, the amount of photons collected by the photon sensors strongly depends on the drift distance. The photons also reach the sensors a few nanoseconds after the interaction. Therefore, a matching between light and charge signals is made to fix the t_0 offset [90]. This is crucial for surface detectors, as muons from cosmic rays can mimic beam signals.

Electron lifetimes (the mean time spent by a free electron in the LAr before being captured) of tens of milliseconds are required to minimize the charge loss. Drift distances up to 6 meters have been tested [92, 93], achieving electron lifetimes of up to 30 ms [102]. The path of the ionized electrons is affected by non-uniformities in the electric field [103]. These *space-charge* effects (SCE) are specially concerning for LArTPCs at the surface (up to 10%), as muons from cosmic rays are a continuous source of slow-moving positive argon ions (Ar^+) inside the detector. The argon ion drift velocity is around 4 mm/s [104], 5 orders of magnitude slower than the freed electrons. Spatial offsets up to 15 cm in the reconstructed trajectories of muon tracks have been observed by MicroBooNE [103].

Another transportation effect inside the TPC is the diffusion of the electrons in both the transverse and longitudinal directions. This means the further the electrons are produced from the wire planes, the more the resulting signals will be smeared out. Diffused electrons can also be detected by neighbor wires, faking their original position. These effects need to be accounted for both in the simulations and the reconstruction with data as they can shift the dE/dx calculation by up to 4% [105].

Both SCE and diffusion processes can affect the calculation of the deposited energy per distance as its estimation depends on the electric field $\vec{E}$, the collected charge (Q) in the wires, and the distance (x).

2.3.2 Light production and propagation in a LArTPC

Liquid argon is a prolific scintillator with a light yield up to 40,000 photons/MeV in absence of an electric field [87, 97], and ~24,000 photons/MeV when an electric field of 500 V/cm is applied. The light spectrum produced by argon dimers, Ar_2^*, peaks in the vacuum ultra-violet range at 127 nm [106] or 9.7 eV. Impurities such as nitrogen and oxygen reduce the total light yield by quenching whereas doping the argon with elements such as xenon can compensate these effects [107].

The argon dimers (Ar_2^*) are produced by two mechanisms: the direct excitation of argon atoms $Ar^*+Ar \rightarrow Ar_2^*$, or the ionization and posterior electron capture (recombination),

$$\begin{aligned} Ar^+ + Ar &\rightarrow Ar_2^+ \\ Ar_2^+ + e^- &\rightarrow Ar_2^* \end{aligned} \tag{2.4}$$

as shown in Figure 2.14.

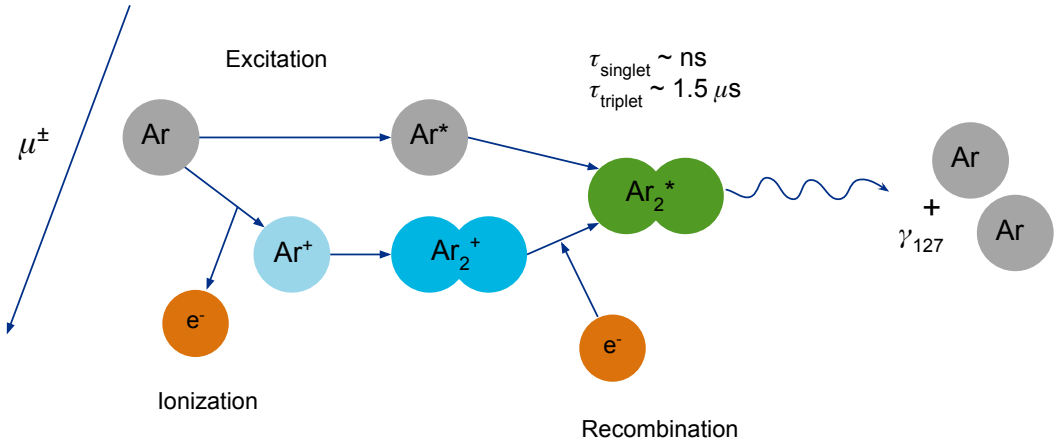

Figure 2.14: Diagram of the scintillation photon production in liquid argon. A charged muon crosses the detector, depositing energy. LAr dimers Ar_2^* are formed after either direct excitation or ionization and recombination.

In both cases, argon dimers are produced in two energy states: singlet and triplet $^{1,3}\Sigma_u^+$ [108]. The characteristic decay times are in the nano-second scale for the singlet (τ_{fast}) and the microsecond scale for the triplet (τ_{slow}), whose transition to the ground state is forbidden in the Russell-Saunders approximation ($\Delta S = 0$) [108]. Because of the

difference in their decay times, they are usually labeled as fast and slow components. The total photon production over time can be described with the following relation:

$$f(t) = \frac{A_{\text{fast}}}{\tau_{\text{fast}}} e^{-t/\tau_{\text{fast}}} + \frac{A_{\text{slow}}}{\tau_{\text{slow}}} e^{-t/\tau_{\text{slow}}}, \tag{2.5}$$

with $A_{\text{fast}}(A_{\text{slow}})$, the relative number of photons produced by decays of the single (triplet) states. From the relative ratios of the fast and slow components particle identification between neutrons and nuclear recoils, and electrons and muons can be performed [109].

Although LAr is transparent to its own scintillation scintillation light, VUV photons are still affected by Rayleigh scattering. This produces a diffusion of the produced light, but not a decrease of the light yield. Rayleigh scattering lengths in LAr have estimated values between ∼60 cm [110] and 1 meter [89].

The total light (L) and charge (Q) produced in a LArTPC depend on the amount of deposited energy, as well as the electric field applied to the medium, as it affects the recombination mechanism [111]. The LArIAT experiment showed how combining both pieces of information enhances the energy resolution for low energy showers [112].

The measured light yield decreases with the distance of the photon sensors to the emission point, as the solid angle subtended by the sensor surface decreases. An alternative to the xenon doping is the use of reflectors covered with wavelength-shifters away from the photon sensors. In this fashion, part of the light is converted to longer wavelengths, less affected by absorption and scattering effects. This is the approach followed by the SBND experiment, described in the next section.

2.4 SBND: the Short-Baseline Near Detector

The Short-Baseline Near Detector (SBND) is the near detector of the SBN program [51, 52]. Located only 110 meters away from the BNB target, it has an active volume of $4 \times 4 \times 5$ m3 or 112 tons of liquid argon. The detector was filled in February–March 2024 and is currently being commissioned. Data taking at the nominal electric field started in July. Physics quality started in fall 2024 as the BNB resumed operations after the summer shutdown.

The SBND physics program includes:

- The search for eV-scale sterile neutrinos, as a part of the SBN program. Measuring the un-oscillated neutrino flux, SBND will play a key role to understand the excesses of electron-like events observed by the MiniBooNE and LSND experiments [47, 48].
- Measuring with world-leading statistics many neutrino-nucleon cross sections in argon. Constraining the statistical uncertainties below the percent level for many channels, SBND data will pave the way for next-generation LArTPC experiments such as DUNE, as the cross section is one of the main systematic uncertainties.
- A broad BSM program that also includes searches for long lived particles: heavy neutral leptons, QCD axions, dark photons... with the intense beam and the location of SBND.
- Research and development of new light detection technologies such as X-ARAPUCA sensors [113, 114] and TPB-coated reflective foils. This is of special relevance for the DUNE experiment, whose light detection system in the far detector is fully-composed of X-ARAPUCAs.

SBND has 3 subsystems (Figure 2.15): the charge readout system at the anode planes (the cathode plane in the middle divides the volume in two TPCs), the photon detection system, located behind the wire planes and an external cosmic-ray tagger system, located outside surrounding the cryostat. The three of them are described in detail in the following subsections.

2.4.1 Charge readout system

The SBND active volume is split in two TPCs by the cathode plane in the middle. The anode planes are 200 cm away each from the cathode (Figure 2.15). Each anode plane has three wire planes (wires are made of copper-beryllium): two induction (U, V) and one collection (W) plane, for a total of 11264 wires. The wires of the collection plane have a vertical orientation while the two induction planes are angled $\pm 60^{\circ}$ with respect to the collection planes (see Figure 2.16). The wire-pitch is 3 mm with wires themselves having a diameter of 150 μm [115].

The cathode is set at a voltage of -100 kV and the APAs at ground for a nominal field of 500 V/cm. An electron in the TPC takes 1.25 milliseconds to cross the complete drift distance (200 cm), given a drift velocity ~ 1.6 cm/μs [94]. As continuously reading the TPCs would be impractical, only readout windows of 1.3 ms are recorded plus an additional 0.2 ms before and after each readout window per issued trigger. In this way, we record anything that could interact in the detector when the trigger was issued.

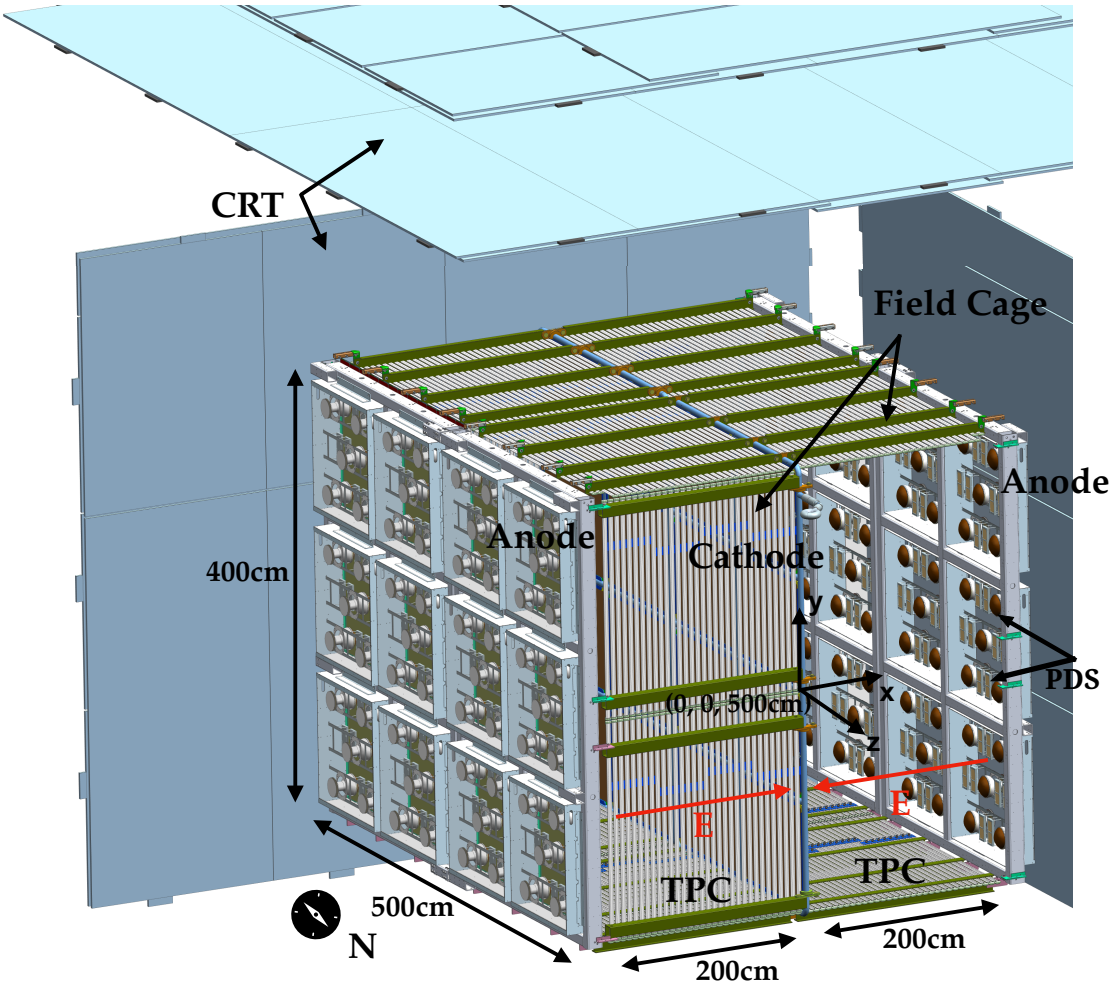

Figure 2.15: Scheme of the SBND detector. The CRT walls (blue) cover the detector outside of the cryostat, not shown in the picture. The detector is divided in two TPCs with the cathode plane in the direction of the BNB (South to North). The charge readout (anode planes) are 200 cm away each from the cathode plane. The photon detection system is located behind the wire planes.

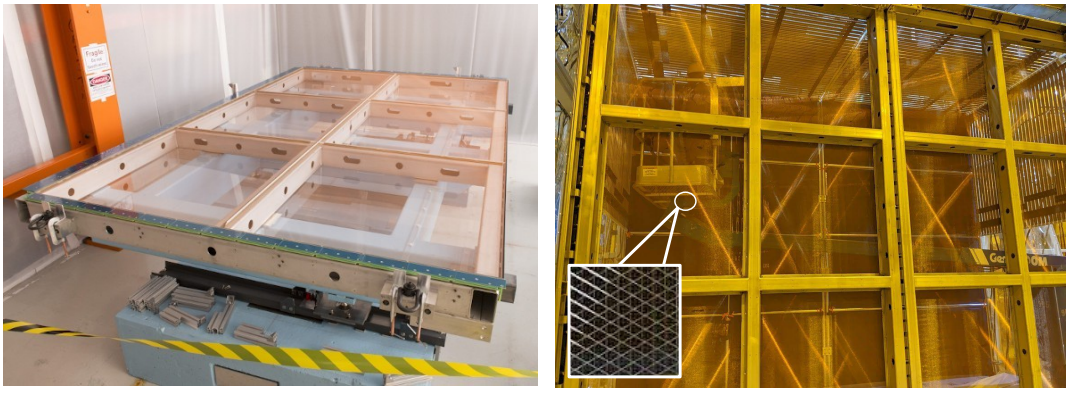

Figure 2.16: Left: one Anode Plane Assembly (APA) built in UK and moved to Fermilab for the installation in the detector. Right: APAs assembled at D0 assembly building (DAB) at Fermilab and close-up of the wire planes.

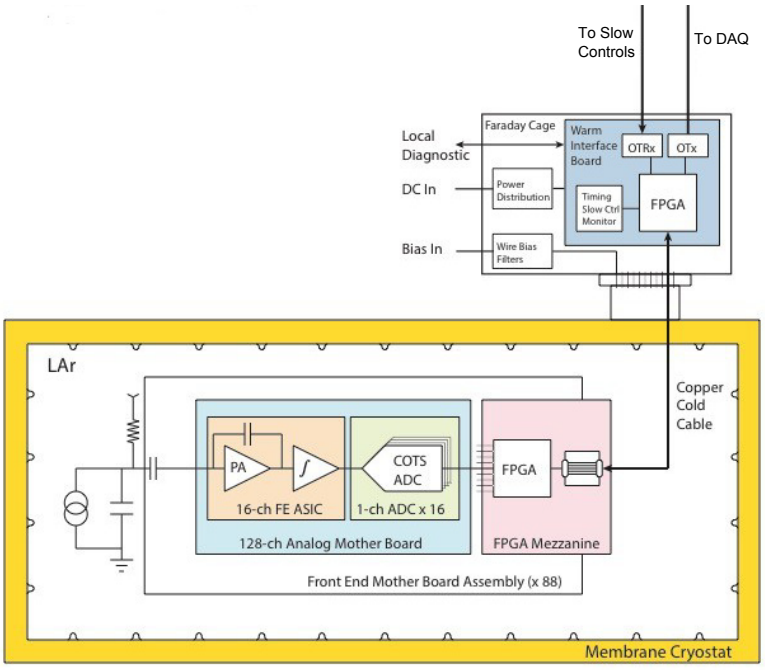

Figure 2.17: Scheme of SBND TPC readout electronics. The TPC channels are read out by the FEMBs. Each FEMB consists of an analog motherboard (AM) and an FPGA Mezzanine (FM). Digitized signals are sent to warm interface electronics and then to the DAQ and slow control systems. Picture from [116].

The TPCs are readout with 88 Front-End Motherboards (FEMBs) installed in the four APAs. Each FEMB has 128 readout channels, an analog motherboard and an FPGA mezzanine [116, 117]. The chosen ADC (12-bit AD7274) has an estimated lifetime of 6.1×10^6 years at its nominal 2.5 V operation voltage [118] and a sampling frequency of 2 MHz [119]. To achieve the best signal-to-noise ratio (SNR) the signals are amplified in the FEMBs with typical gains of 7.8 or 14 mV/fC, minimizing the cable from the signal electrodes to the pre-amplifier. The requirements ensure that a minimum ionizing Particle (mip) with a 3 mm path length produced in the cathode can be resolved. The warm interface electronics, placed on top of the flanges outside the detector cryostat, are connected to the cold electronics through 8 m cold copper cables (see Figure 2.17). Six Warm Interface Boards (WIBs) per crate read and send the TPC digitized signals to the DAQ system through ten 2 GB/s fiber optical links. The warm electronic boards are surrounded by a Faraday cage to mitigate external noise. The TPC cold electronics installation finished in 2019. Noise measurements during commissioning in 2024 have shown an average RMS of 2 ADC in the induction and collection planes, meeting the design requirements. An example of a recorded event in the collection view from early July data is shown in Figure 2.18. A charged current ν_μ candidate can be seen in the zoomed region.

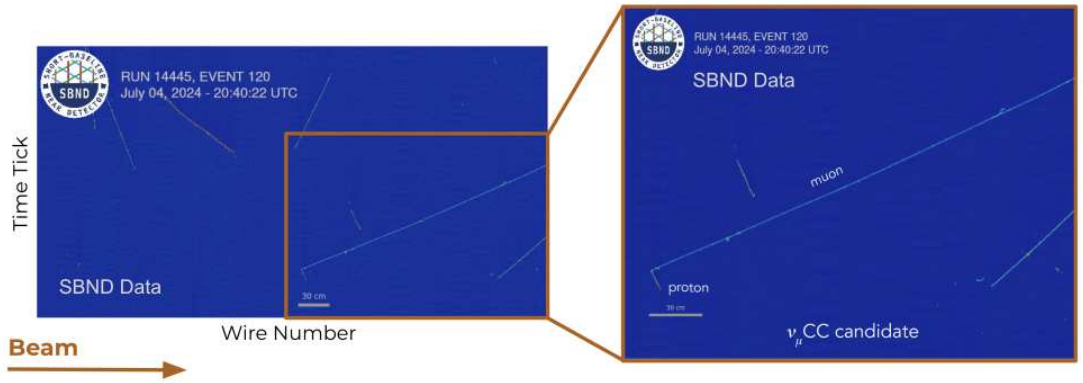

Figure 2.18: Example of a recorded event in the collection view and zoom (Right) to the muon neutrino charged current interaction candidate.

2.4.2 Cosmic Ray Tagger system

Thousands of muons from cosmic rays will cross SBND per second. For reference, MicroBooNE measured a muon flux rate of $\sim$ 110 ev/m^2/s [120]. Cosmic muons are a continuous source of positive ions in the TPC. They can also mimic neutrino beam-events and produce triggers in the expected BNB window. For this reason, many analysis techniques have been developed to reduce the cosmic background that affects all neutrino experiments at surface level [83, 121]. Cosmic muons can cross the detector in a variety of directions, and their time distribution is expected to be flat for the millisecond time scales of the TPC readout [122]. To veto cosmic muons or select calibration samples with well-known topologies [103], SBND is equipped with a Cosmic Ray Tagger (CRT) system similar to MicroBooNE and ICARUS designs [123].

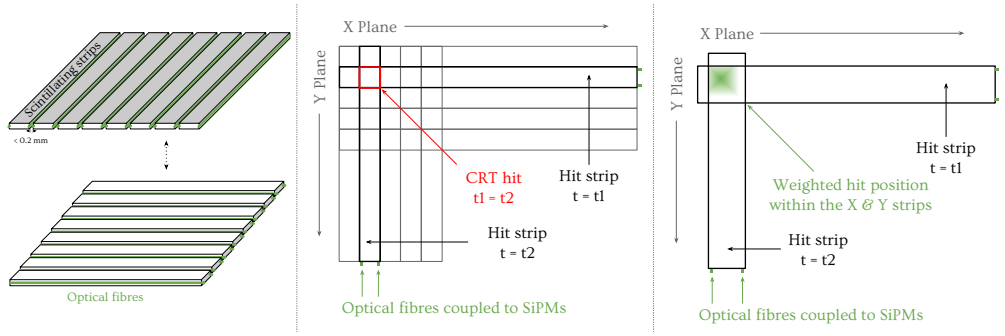

Figure 2.19: Working principle of the CRT system: each plane module has 16 scintillator strips (Left). Each strip has two optical fibers coupled to SiPMs on the strip end (center). Using the information of orthogonal modules, 2D location of the CRT hit is performed (Right).

The idea is to surround the outside of the cryostat with panels made of strips with plastic scintillator. When the muons cross the panels, the CRT strips produce photons, measured at the strips end with SiPMs. The propagation time of the light is in the

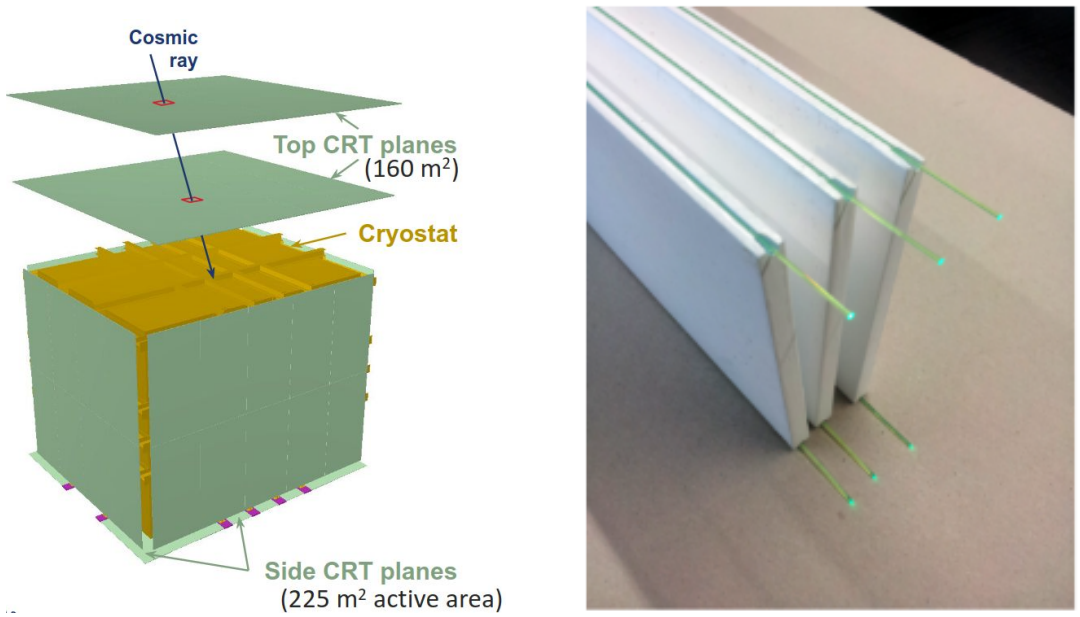

Figure 2.20: Left: CRT walls surrounding the SBND cryostat. A crossing muon leaves hits on the top-walls. Right: example of a scintillator strip with the two optical fibers one on each side.

nano-second scale. Each CRT wall has 2 layers with 10.8 cm wide strips in orthogonal directions to locate the point where the muon crossed the wall with centimeter precision as shown in Figure 2.19. Points in different walls correlated in time are very likely to correspond to the same muon crossing the cryostat volume (Fig 2.20-Left). Then, we can look for candidate tracks in the TPC signals. Since the triggers from the BNB are expected in a narrow window, CRT signals outside the trigger window are good indicators of non-beam events.

The use of multiple layers also reduces the amount of fake CRT signals as SiPM coincidence over a threshold in different layers is required to form a CRT hit.

SBND has 7 CRT walls, one for each side of the detector and an extra wall above the top tagger. CRT walls are made out of modules, each module consists of 16 strips. The plastic scintillator is a mixture of polystyrene with a small fraction of p-Terphenyl (pTP) and 1,4-bis[2-(phenyloxazolyl)]-benzene (POPOP). The SiPMs (Hamamatsu S12825-050P) match the light guide emission spectrum [51]. A Front-End Board (FEB) biases the SiPMs and reads the SiPM signals of each CRT module, storing the peak of each pulse above threshold. The FEB has a nanosecond-timing resolution combining a coarse 250 MHz counter and a delay-chain interpolator. The bottom wall does not fully cover the bottom side since the cryostat supports are located below the detector.

The installation of the CRT walls started in 2019 with the bottom CRT planes. Operations resumed after the detector filling in February 2024 (Figure 2.21-Left) and finished

with the top walls installation in September 2024. Beam data has been recorded with the expected excess of neutrino events during the 1.6 μs duration of the BNB trigger window. Figure 2.21-Right shows this distribution for the CRT upstream wall. The CRT upstream wall is located before the TPC in the beam direction. The excess of events in this wall comes mainly from *dirt* neutrino interactions with the concrete of the building before reaching the detector.

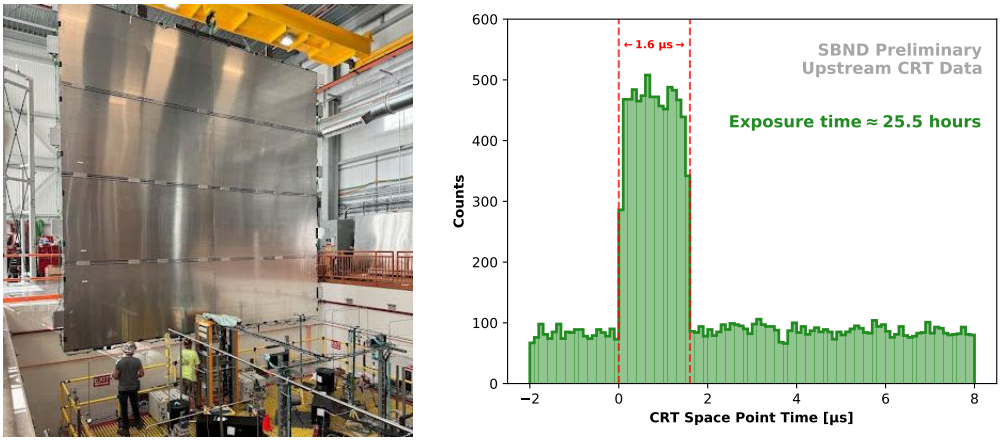

Figure 2.21: Left: installation of the south (upstream) CRT wall in April 2024. Right: Time distribution of clustered CRT signals (space points) at the SBND upstream wall. The excess from beam-events during the BNB window (1.6 μs wide) is clearly visible over the constant cosmic background.

2.4.3 Photon Detection System

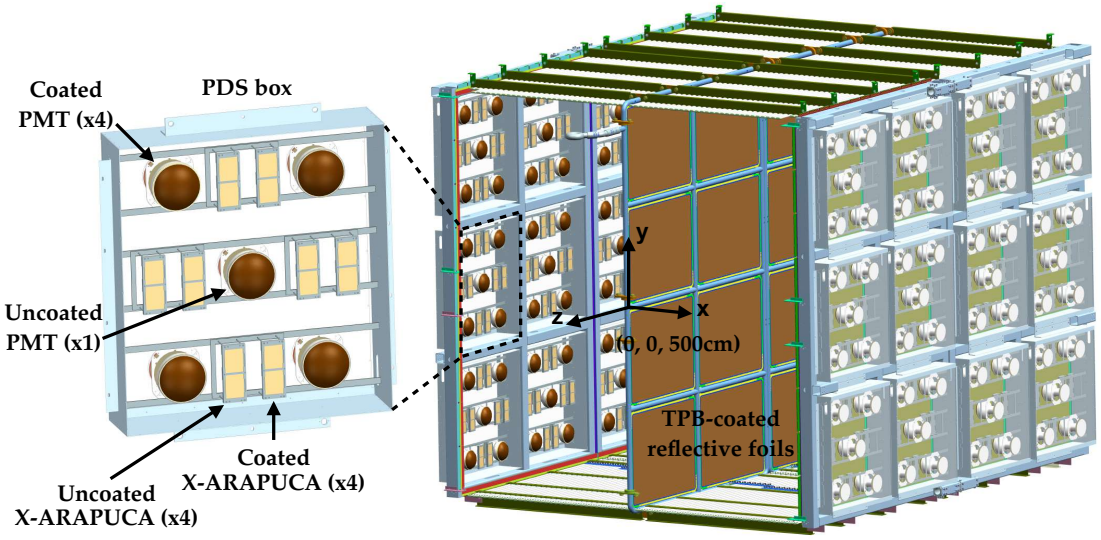

Figure 2.22: View of the SBND PDS with the coated TPB foils in the center of the detector and the PDS boxes behind the wire planes. Each PDS plane contains 12 PDS boxes while each PDS box (Left) holds 5 PMTs and 8 X-ARAPUCA sensors: 4 coated PMTs, 1 uncoated PMT, 4 coated X-ARAPUCAs and 4 uncoated X-ARAPUCAs.

SBND has a high coverage Photon Detection System (PDS), with 156 light sensors located behind the wire planes and a grounding mesh to shield wires from PDS signals on each side of the TPC (see Figure 2.22). The SBND PDS is composed of 120 photo-multiplier tubes (PMTs) Hamamatsu R5912-MOD model [124], and 196 X-ARAPUCA sensors, a new scalable technology that will also be used by the DUNE experiment [114, 125] described in more detail in the next chapter. The cathode plane in the center of the detector is equipped with reflective foils coated with Tetraphenyl Butadiene (TPB). TPB captures the VUV scintillation photons and re-emits them in visible wavelengths [126], peaking at 420 nm.

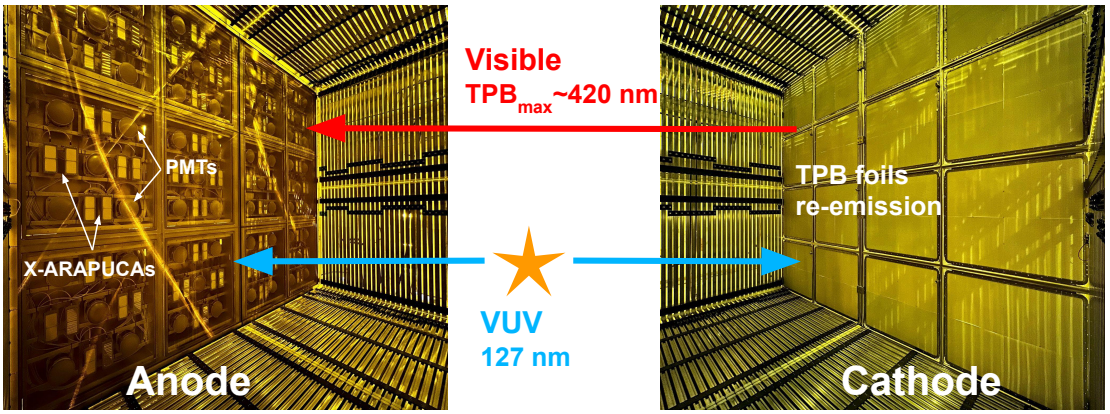

Figure 2.23: Left: photo of the PDS sensors located behind the TPC wire planes. Right: image of the cathode plane and the TPB-coated reflective foils. PDS sensors collect direct VUV light (blue) and re-emitted photons by the TPB in the visible range (red).

Figure 2.23 illustrates he different light production mechanisms in SBND. Thanks to the TPB-coated foils in the middle, we recover part of the VUV light yield as we move away from the PDS sensors. The VUV and visible light are usually referred as direct and reflected components. Thereby, we can also classify the PDS sensors by the light they are sensitive to:

- **Coated units:** they have wavelength shifter materials deposited on the sensor surface. The shifter (TPB for PMTs and pTP for X-ARAPUCAs) absorbs and re-emits the direct VUV light in longer wavelengths. Coated units are also sensitive to the reflected light component.
- **Uncoated units:** They are only sensitive to the reflected light produced in the middle of the detector by the TPB foils re-emission.

The combination of units sensitive to light produced in different locations of the detector allows SBND to reconstruct the drift distance of the events (X in Figure 2.22) using only light information [127]. The collection area of the PMT (X-ARAPUCA) system

is 1.92 (1.42) m^2 on each PDS plane which represents a 16.7% coverage (PMTs + X-ARAPUCAs) of the total plane surface. For comparison, ICARUS and MicroBooNE have a coverage of 5% and 4.2% respectively.

The 8-inch PMTs are the primary PDS sub-system, used for triggering. The PMTs are read out using eight CAEN VX1730SB digitizer modules with a 500 MHz sampling (2 ns per time-tick). Typical gains are in the range of 10^7 at voltages of $\sim$ 1200 V.

The 192 X-ARAPUCA units are equally split in coated and uncoated modules. X-ARAPUCAs are read out using an amplifier similar to the DUNE model [128] located outside the cryostat. Their signals are digitized using 62.5 MHz sampling CAEN V1740B modules.

The readouts for both systems are located in the mezzanine floor, with the DAQ servers for the different systems. The delay introduced by the 30 m of cables connecting the PMTs and the readouts (outside the cryostat) introduce a delay of $\sim$ 135 ns. The effect of the cables on the X-ARAPUCAs signal shape and delay is quantified in Chapter 4.

The PDS system boxes were installed and wired behind the APA frames between March and September 2022. Multiple quality assurance/control tests were performed before and after closing the cryostat to ensure the good conditions of the PDS sensors. PMT sensors were powered on after the detector filling and took beam data before the BNB summer shutdown (see Figure 2.24). The commissioning of the PDS is taking place. Early PMT gain equalization was performed using late light pulses from scintillation light signals in spring 2024. The installation of the X-ARAPUCA warm electronics is ongoing.

SBND has an ambitious R&D program that incorporates passive (TPB-coated reflective foils) and active (X-ARAPUCA sensors) features into their PDS. Chapter 3 describes the characterization of the X-ARAPUCA subsystem properties and the measurements performed at the CIEMAT lab, including the estimation of the photon detection efficiency (PDE) of X-ARAPUCA coated units. The MC simulations and reconstruction algorithms developed to evaluate the X-ARAPUCA expected performance [127] are discussed in detail in Chapter 4.

2.4.4 Trigger and DAQ system

SBND physics goals require a trigger system capable of selecting efficiently neutrino events over a high rate of cosmic backgrounds. Additionally, calibration data and background characterization samples are taken while simultaneously collecting beam data.

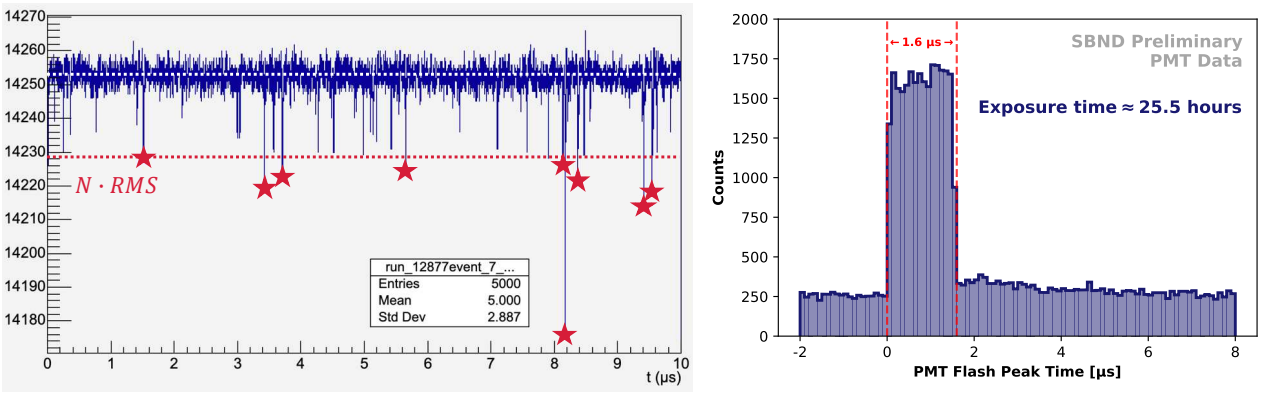

Figure 2.24: Left: example of a PMT waveform used in gain calibrations: the selected peaks (red stars) surpass a baseline RMS threshold (dashed red line). Right: time distribution of clustered PMT signals (flashes) from early June 2024 data. As in the CRT case (Figure 2.21-Right), the excess from beam events is visible during the BNB window.

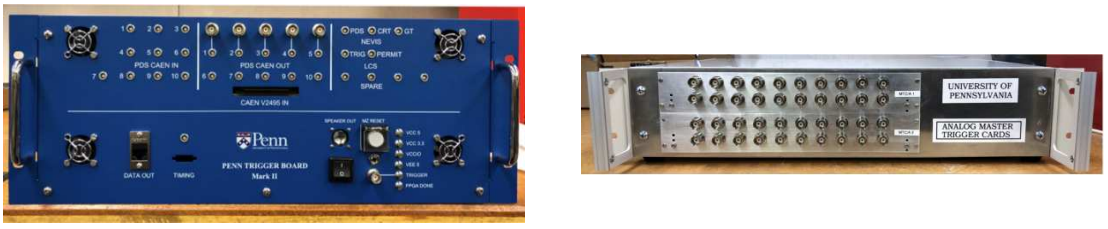

Figure 2.25: SBND hardware trigger components: MTC/A (Left) and PTB (Right).

Information from the PDS, the CRT and the accelerator signals is used to make a decision. The hardware trigger has two main components:

- **The Master Trigger Card Analog**: the MTC/A takes as input a signal proportional to the number of PMT pairs that surpass a threshold for each CAEN V1730 board. Then, the card compares the analog sum of the signals to three configured thresholds and sends a logic signal when each threshold is crossed.
- **Penn/Photon Trigger Board:** the PTB combines the MTC/A, beam early warning and CRT signals and issues the trigger to the TPC/Nevis Trigger Board and the different SBND systems to prompt data acquisition.

In the PTB, each system has configurable low-level triggers that are combined forming high level triggers including inputs from the different systems. The primary trigger uses the prompt scintillation light produced in LAr and measured by the PMTs.

The SBND data acquisition system (DAQ), sbndaq, is based on the **artdaq** framework and shared with the ICARUS collaboration [129]. For each trigger issued by the PTB, the Nevis Trigger Board creates an art event, pulling data (usually called *fragments*)

from all the systems into the same event. A precise synchronization between all the systems is required to ensure the correct fragments are put together.

After the TPC ramp-up to nominal voltage in early July, data has been taken with two trigger configurations for commissioning. The first trigger fires on all the BNB beam spills, and recorded the data shown in Figures 2.24, 2.21 and 2.9. The second trigger records crossing muons leaving signals in opposing CRT walls.

Chapter 3

Characterization of SBND X-ARAPUCA photodetectors

In this chapter, a detailed description of the SBND X-ARAPUCA system is given. Their main features are outlined in Section 3.1. Sections 3.2 and 3.3 describe the setup developed at CIEMAT and the calibration measurements performed to characterize SBND X-ARAPUCA sensors. The measurements of their photon detection efficiency to the VUV and visible light are discussed in Sections 3.4 and 3.5.

3.1 Introduction

With the increment in the scale of LArTPC detectors, cost-effective and scalable alternatives to the standard photo-multiplier tubes have been developed in the past decade to detect argon scintillation light. The technology of choice for DUNE far detectors is the X-ARAPUCA sensor [125]. This device traps the incoming photons in a highly reflective box where light sensors, placed in the inner sides of the X-ARAPUCA, collect them. In the words of one of its creators:

> *“Arapuca is a Brazilian word, it’s an indigenous Guarani word that means ‘a trap to catch birds.’”*

The typical X-ARAPUCA device has the following components, shown in Figure 3.1:

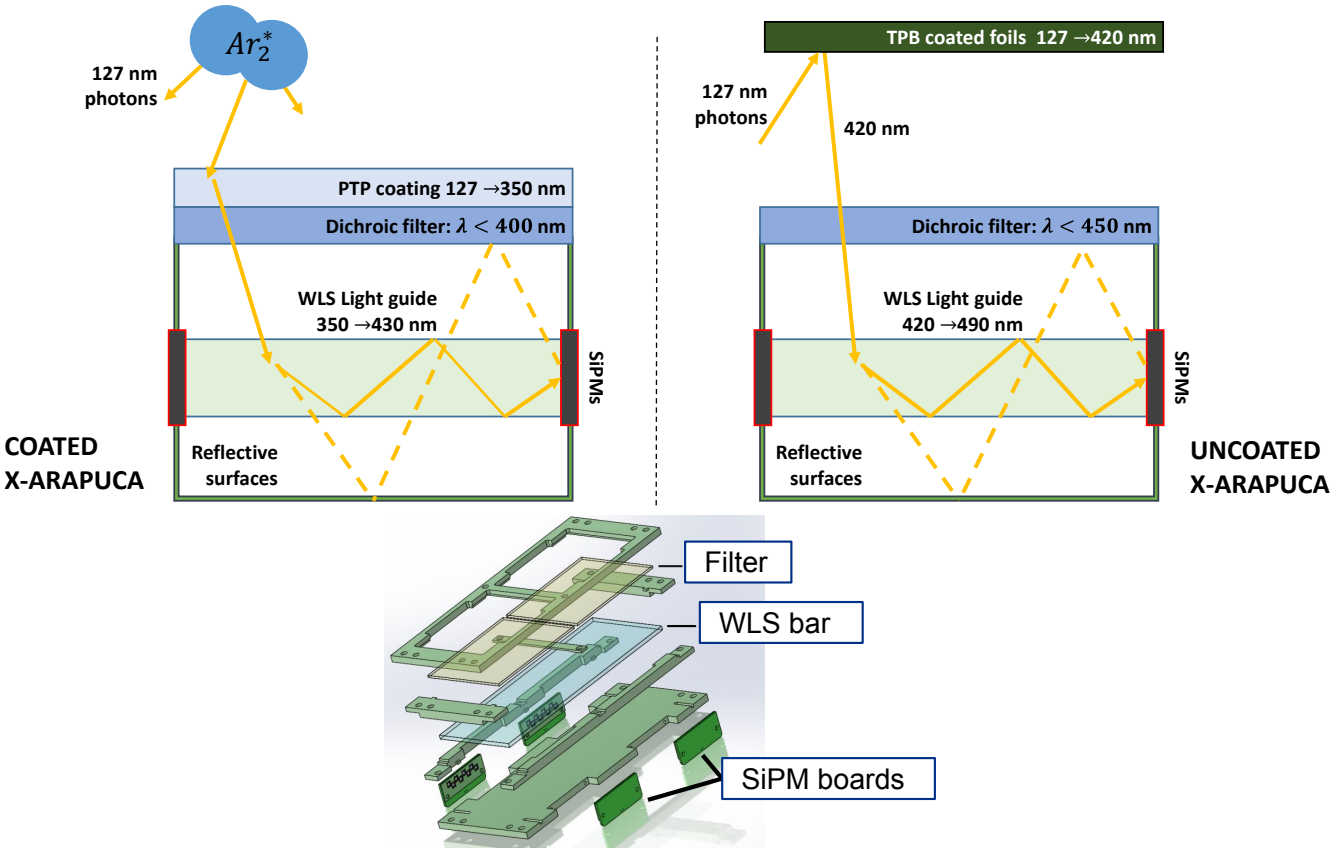

Figure 3.1: Top-Left(Right): working principle of the X-ARAPUCA sensor for coated (uncoated) SBND X-ARAPUCAs. In the uncoated units, the conversion from VUV to visible wavelengths occurs at the TPB-coated foils in the middle of the detector. Bottom: 3D scheme of SBND X-ARAPUCAs: each module has 4 SiPM boards.

- First, a wavelength shifter (WLS) material is placed on top of the collection windows. Half of SBND X-ARAPUCAs are coated with paraterphenyl (pTP) [130], and are sensitive to the direct VUV light produced by excited argon dimers Ar_2^* (Figure 3.1, Top-Left). The pTP reemits VUV photons in the 300–400 nm range, peaking at $\sim$ 350 nm.

- Then, a dichroic filter selects the photons that enter the X-ARAPUCA box and reflects the other wavelengths. The coated units filter allows photons in the 300–400 nm to pass. The cutoff, however, is highly dependent on the angle of incidence of the incoming photons. For this reason, a small fraction of the visible photons produced by the TPB-coated foils (TPB peak is $\sim$ 420 nm) is detected by the coated X-ARAPUCAs (see Figure 3.2). The visible X-ARAPUCA filter (400–450 nm) only transmits visible photons, absorbing the direct VUV scintillation light.

- Inside the X-ARAPUCA, a WLS light guide converts the photons to longer wavelengths where the dichroic filter is highly reflective. The photons can either reach

the light sensors by multiple reflections or total reflection in the guide. The conversion also increases the detection probability, as SiPMs are more efficient in the visible light range. X-ARAPUCA models with Glass-To-Power bars have shown superior performance compared to the Eljen models in similar prototypes developed for DUNE far detectors [131]. The absorption and emission spectra of both Eljen bars are shown in Figure 3.3.

- On two lateral sides, at the end of the light guide, silicon photo-multipliers (SiPMs) collect the trapped photons. While SBND X-ARAPUCAs use up to three different SiPM models, more than 90 % of the 192 X-ARAPUCA units are equipped with the Onsemi MICROFC-30050-SMT SiPMs. The other 16 (placed in the middle of SBND's APA planes) use two different Hamamatsu models. Onsemi (Hamamatsu) X-ARAPUCAs have 8 (4) SiPMs per board (see Figure 3.1 Bottom), for a total 32 (16) SiPMs per X-ARAPUCA.

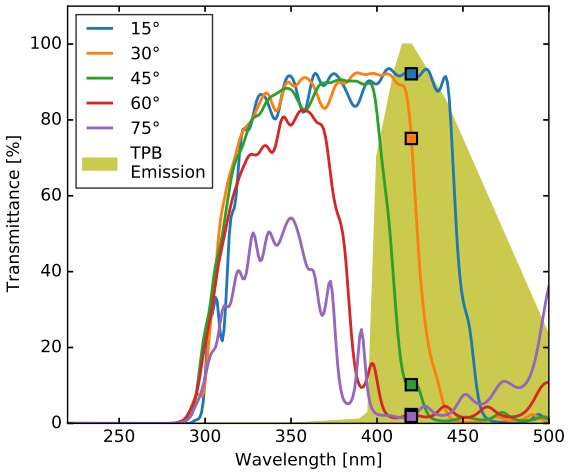

Figure 3.2: Transmittance curves of the pTP-coated 400-nm dichroic filter for different angles of incidence (AOI) light as a function of the wavelength. The TPB emission spectrum is shown in solid green. The values of the transmittance at 420 nm (TPB peak) are highlighted with squares. Note that AOIs $\leq 45°$ let part of the visible photons pass.

The SiPMs are a multi-pixel array of single-photon avalanche diodes (SPADs) in Geiger mode. When incoming photons trapped in the X-ARPAUCA hit the SiPM surface, a characteristic di-exponential shape signal is produced per triggered cell. The SiPMs provide single-photon detection at cryogenic temperatures while requiring much smaller operation voltages ($\sim$ 40 V) than the standard PMTs ($\sim 10^3$ V). They are relatively small, $\sim$3–6 mm side. The X-ARAPUCA effectively increases the total collection window, making the final sensor cost-effective, scalable, and ideal for large areas with tight space constraints.

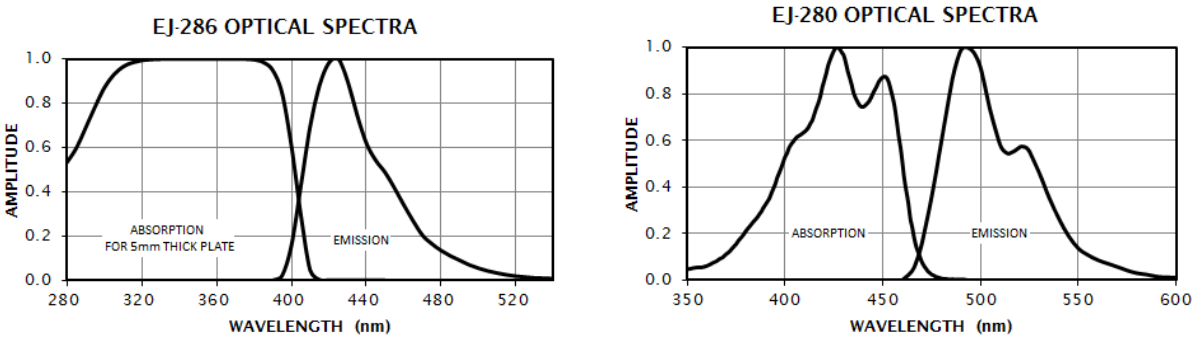

Figure 3.3: Left (Right): absorption and emission spectra of the 286 (280) Eljen WLS bars, used in Onsemi coated (uncoated) units.

SBND counts with six different configurations of X-ARAPUCAs. An overview of the different hardware components for each can be found in Table 3.1, while the main features of the different SiPM models at room temperature provided by the manufacturers are summarized in Table 3.2.

Manufacturer	SiPM Model	Dichroic filter cutoff	WSL bar	Units
Onsemi	MICROFC-30050-SMT [133]	pTP-coated 400-nm	Eljen EJ-286 [132]	88
		450-nm	Eljen EJ-280 [132]	88
Hamamatsu	Hamamatsu S13360-6050-VE [134]	pTP-coated 400-nm	Glass-To-Power Blue [113]	6
		450-nm	Glass-To-Power Green	6
	Hamamatsu S13360-6050-HS [135]	pTP-coated 400-nm	Glass-To-Power Blue	2
		450-nm	Glass-To-Power Green	2

Table 3.1: Different X-ARAPUCA units in SBND by technical components. Note that the values of the dichroic filter cutoff are given for an incident angle of 45°. In blue, the measured units characterized at the CIEMAT lab are highlighted.

SiPM model	Operation Overvoltage [V]	PDE at 420 nm [%]	Crosstalk [%]	Dark count rate [MHz]	Gain [10^6]
Onsemi MICROFC-30050-SMT	4.5	40	10	0.4	4
Hamamatsu S13360-6050-VE	3	40	4	0.5	1.7
Hamamatsu S13360-6050-HS	3	50	10	0.6	2.5

Table 3.2: Relevant properties of the different SiPM models in the SBND X-ARAPUCAs at room temperature provided by the manufacturers. All quantities taken from [133–135].

Various measurements of the efficiency of different SiPMs at cryogenic temperatures [136, 137] suggest photon detection efficiencies (PDEs) in the range of 10–20% depending on the wavelength, SiPM model, etc. The complete X-ARAPUCA unit has an

expected PDE to VUV light in the 1.5–3% range from measurements with similar configurations [131, 138]. The configurations installed at SBND, however, have never been measured before. Thus, the complete SBND X-ARAPUCA unit performance has to be characterized with all the components assembled. The next sections describe the dedicated cryogenic setup developed to test 2 out of the 6 different X-ARAPUCA configurations in SBND. They are highlighted in blue in Table 3.1 and are referred from now on as coated Onsemi and Hamamatsu X-ARAPUCAs unless stated otherwise. For each configuration, gain determinations, crosstalk estimations and non-linearities studies were performed. The last sections explain in detail the event selection and data filtering used to compute the PDE of both coated configurations to the VUV and visible light.

3.2 Experimental setup at CIEMAT

To measure the X-ARAPUCA PDE, the X-ARAPUCA response to VUV and visible light sources was compared with four reference SiPMs of known PDEs characterized at CIEMAT [136]. Thanks to the reference sensors, the PDE measurement is independent of the purity of the argon (assuming no attenuation in the propagation is produced).

The coated Onsemi and Hamamatsu X-ARAPUCAs were tested in two separated runs. The group at UNICAMP provided the dichroic filters, WLS, X-ARAPUCA structure and Hamamatsu SiPM boards. The group at University of Michigan supplied the Onsemi boards.

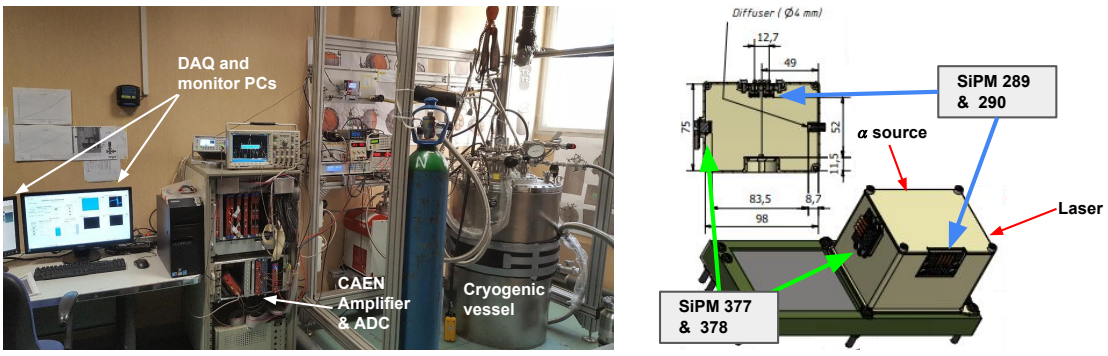

Figure 3.4: Left: picture of the complete setup at CIEMAT. Right: 3D scheme of the black box that holds the components, and zenithal view. The reference SiPMs 289 and 290 are in front of the alpha source, while the 377 and 378 are in front of the laser.

The light sources employed in the setup reproduce the conditions that will be present at SBND. The visible wavelength light source is a 420±10 nm laser (PicoQuant – PDL828+LDH-P-C-420 [139]) which corresponds to the TPB emission peak. The laser includes a diffuser that distributes the visible light following a cosine law. The VUV scintillation light is produced by the interaction of alpha particles emitted by an ^{241}Am

radioactive source with argon. The α particles have energies of 5.485 MeV (84.45%) and 5.443 MeV (13.23%) , emitting approximatly 200k scintillation photons in liquid argon per event. The α source has an activity of (54.53 $\pm$ 0.82) Bq [140].

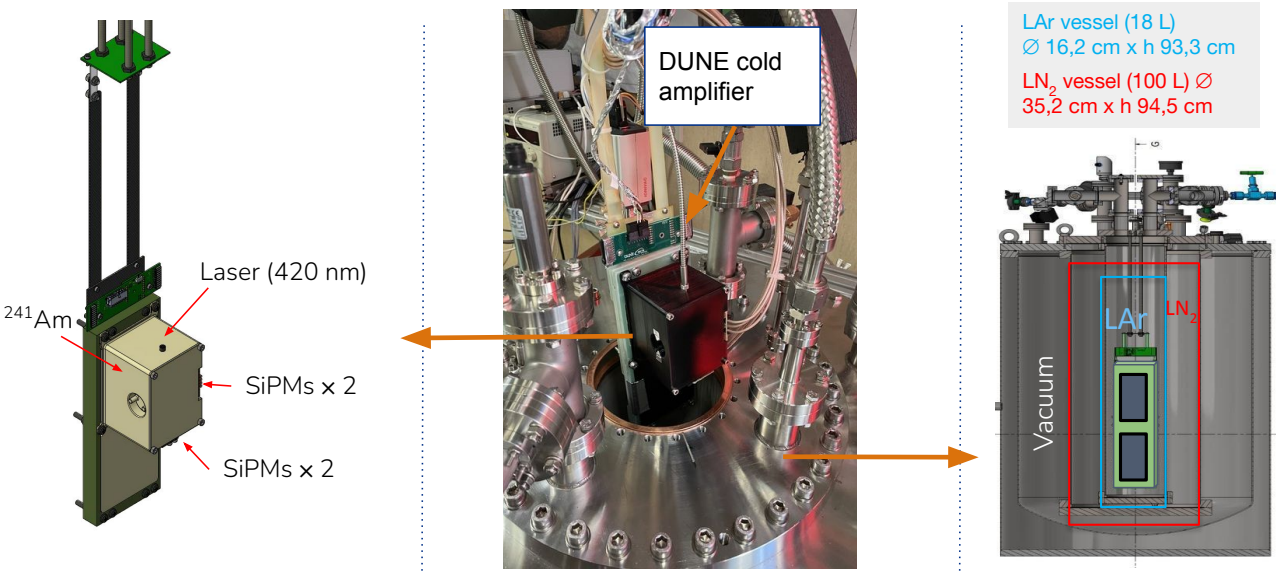

Figure 3.5: Left and Right: schemes for the structure used to support the light sources, X-ARAPUCA module, and the system of stainless steel vessels used to contain them. Center: Photo of the installation of all the elements in the inner vessel.

To calibrate the amount of light produced by the light sources, four reference Hamamatsu-VUV4 SiPMs, characterized at CIEMAT to VUV and visible light sources, are used [136], placing a pair in front of each light source. The reference SiPMs 289 and 290 are in front of the alpha source, while the 377 and 378 are in front of the laser, as depicted in Figure 3.4. The components are held by an opaque black box that also suppresses light contamination from other sources such as cosmic muons crossing the vessel, as shown in Fig 3.5 Left and Center. One of the two windows of the X-ARAPUCA was illuminated. The other X-ARAPUCA window was kept covered to avoid light contamination. The distance and position of the light sources and the reference SiPMs was optimized performing Monte Carlo simulations using the Geant4 (G4 from now on) software package [85]. In particular, there is a pair of reference SiPMs in front of each light source to minimize angular effects on the reference SiPMs. The two SiPM in front of the alpha source were also used in coincidence for triggering.

The reference sensors, the light sources, the X-ARAPUCA module and a cold amplification electronics (based on a DUNE model [141]) are introduced in an inner vessel of stainless steel. Gaseous argon is pumped into the vessel and liquefied using the liquid nitrogen in an intermediate vessel to cool it down (Fig 3.5-Right). To prevent the system from warming up, a vacuum is induced in the outer vessel.

Reference SiPM signals are amplified with a CAEN N979 amplifier [142] in warm. The amplification factors were set to a factor of 5 for the reference SiPMs and 31.2 for the X-ARAPUCA. To read the sensors, a 14 bit, 500 MHz ADC (model CAEN DT5725S [142]) is used. A pulse generator which can trigger the ADC was connected to the laser to perform calibrations. The pulse generator can trigger the laser with a sharp signal (∼ns wide), which approximates a delta function pulse. An scheme of the DAQ system at CIEMAT is shown in Figure 3.6.

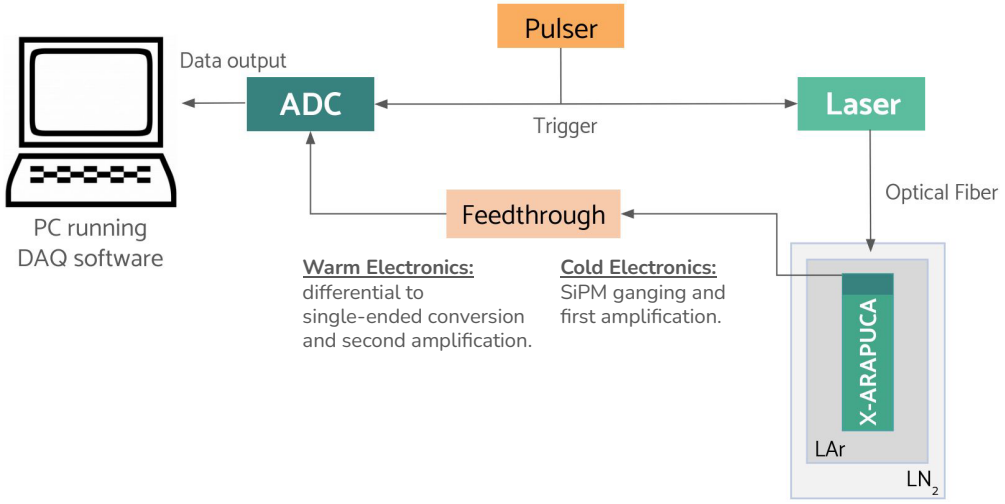

Figure 3.6: Scheme of the data acquisition system at the CIEMAT setup [114].

Each data taking lasted for 3 days per X-ARAPUCA configuration. For each configuration, different measurements (from now on runs) were performed:

- Calibration runs: they use the pulse generator as a trigger source, with the laser at low intensity. The value was tuned to match the range of few photo-electrons (PEs). From the integrated charge spectra (usually called finger plots), gain values for different over-voltages (OVs) on each sensor are computed.
- High intensity runs: they employ the same trigger as calibration runs, but with a higher laser intensity. These runs characterize the sensor response shape, and are used for the determination of the PDE of the X-ARAPUCA to the visible light.
- Noise runs: runs taken using the same trigger as calibration runs, but with the laser switched off. Their purpose is to characterize possible correlated noises with the pulse generator and the baseline.
- Alpha runs: where data recording was triggered by reference SiPMs exceeding an amplitude threshold value. Configurations triggering in a single SiPM, coincidences of the 2 SiPM in front of the alpha source, and coincidence of the 4 reference SiPMs

were tested. The aim of these runs is to trigger only on events produced by the α source, used to determine the PDE to the VUV light.

- Muon runs: events with coincidence of the 4 SiPMs, with higher values for the amplitude thresholds than the alpha runs were recorded. These runs have a low event rate (∼1 Hz), and were collected during the nights.

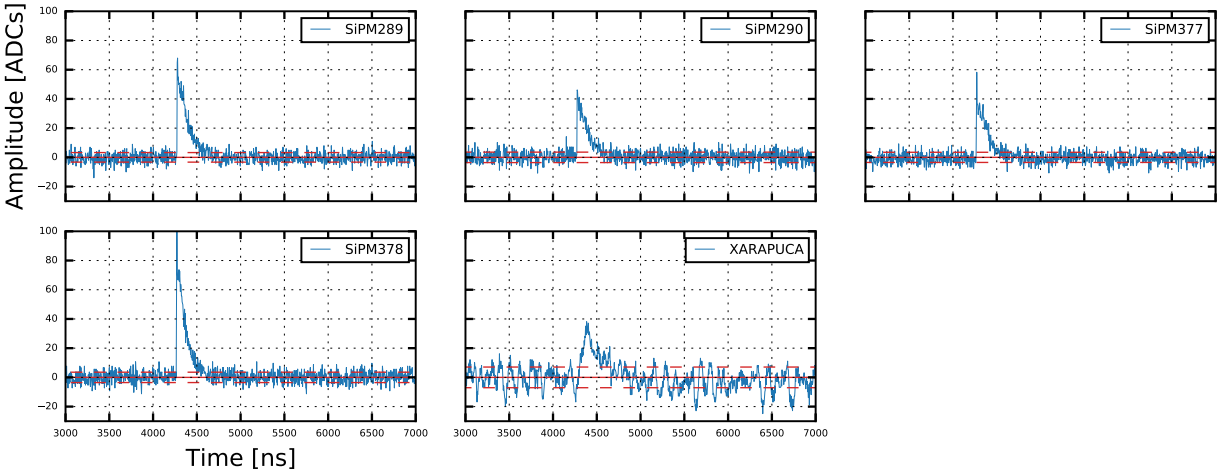

Figure 3.7: Zoomed signals ($4\mu s$) of a recorded event from a calibration run for the coated X-ARAPUCA with Onsemi SiPMs. The average baseline and 1σ region are showed in solid and dashed red lines respectively. The baseline has been estimated and subtracted.

For each issued trigger, a 20 μs window is recorded with 4 μs (20%) of pre-trigger to compute the baseline. The pedestal is determined with a sliding window algorithm. The first 3.2 μs are split into 8 windows of equal length (400 ns). The mean of the segment with lowest standard deviation is taken as the pedestal value and subtracted from the waveform for each channel. Negative polarities are also inverted. This is depicted in Fig 3.7 for all the optical channels. Notice the larger amplitude noise in the X-ARAPUCA channel, driven by the higher amplification of the original signal (more than 5 times the reference SiPMs amplification). The average STD of the baseline for the reference SiPM (X-ARAPUCAs) channels was found to be 3.6 (7) ADC counts. The single photo-electron of both the reference SiPMs and the X-ARAPUCA had a typical amplitude of 20 ADC.

The first step towards the estimation of the PDE is the calibration of the reference sensors and the X-ARAPUCA units, discussed in the next section.

3.3 Calibration

3.3.1 Gain measurement

The first step of the calibration is the gain factor determination, that is, how much charge is produced in the sensor per photo-electron. For all the sensors, we need to know the number of detected PEs per light pulse. The gain is defined as:

$$\text{Gain} = \frac{Q}{e} \tag{3.1}$$

where e is the electron charge and Q the charge associated with the signal of a single PE. In a SiPM, the gain corresponds to the amplification of electrons on each cell–pixel since the avalanche is started after a photon hits the SiPM surface and frees an electron until the torrent of electrons reaches the discharge region, producing a signal. To measure the total charge of the signal we have to take into account the amplification factors of cold an warm electronics, as well as the conversion between ADC counts and voltage. In this case, 2^{14} corresponds to 2 Volts. The impedance of the ADC (R_{ADC}) is 50 Ohms and the period or time between two consecutive ADC samples is 4 ns (250 MHz).

As the total charge of the pulse is proportional to the area of each light pulse, a criteria is needed to determine the integral of each pulse. The chosen criteria is to select a fixed integration time range where the average waveform is contained. Since the pulse generator triggers the data acquisition for calibration runs, the signals are already aligned and no extra correction is needed. After computing the average pulse, the integration limits are chosen left and right from the signal peak (Amp_{max}) as the first bins that satisfy $\text{Amp} < 1\%\,\text{Amp}_{\text{max}}$ (see Fig 3.8). These limits are computed per run and channel. The method prevents pedestal fluctuations from biasing the charge, as uncorrelated noise is averaged out. In the X-ARAPUCA signals, an undershoot of $\sim 10\%$ is observed.

After computing the charge for every signal, the charge histogram is fitted to a sum of Gaussian functions:

$$f(x, A_i, \mu_i, \sigma_i) = \sum_i A_i \exp\left(-\frac{(x-\mu_i)^2}{2\sigma_i^2}\right) \tag{3.2}$$

A first processing of the histogram profile finds peaks over a fixed threshold. Figure 3.9-Center shows this procedure for a calibration run of the coated Onsemi X-ARAPUCA. Notice the peak centered at 0 charge corresponds to events with no signal.

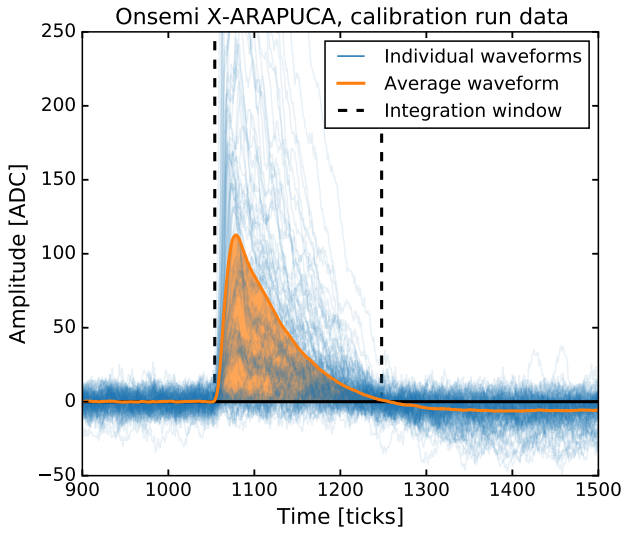

Figure 3.8: Example of charge estimation: individual pulses from calibration data in blue, and average waveform shape in orange for a calibration run of the coated Onsemi X-ARAPUCA. The integration limits satisfying Amp $< 1\%$ Amp$_{\text{max}}$ are shown with black dashed lines. The undershoot caused by the AC couplings produces dipolar signals that cross the baseline, in solid black.

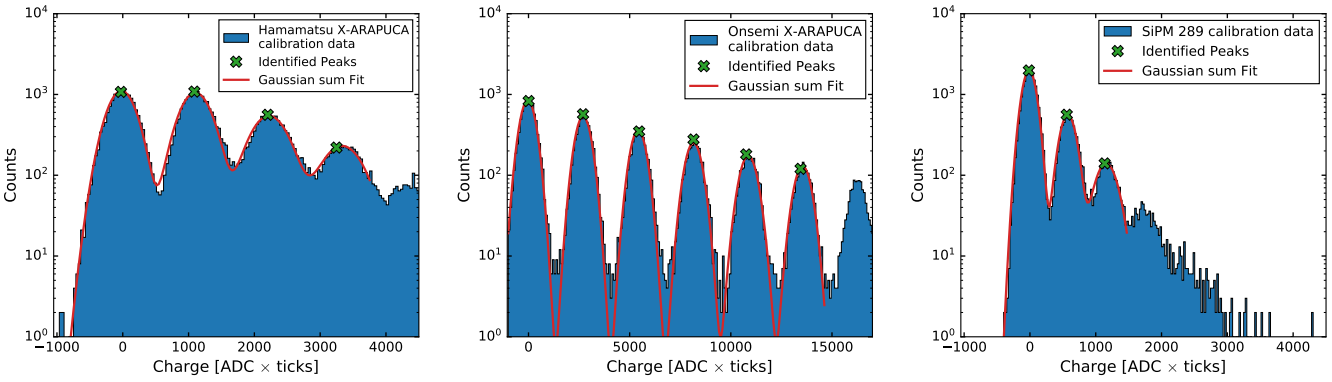

Figure 3.9: Charge histograms from calibration data of the Hamamatsu (Left) and Onsemi (Center) X-ARAPUCA and the reference SiPM 289 (Right) in blue. The peaks found in pre-processing stage and the combined Gaussian sum fit are shown in green markers and red lines respectively.

Finally, one can compute the gain using the difference in means of Eq 3.2 for consecutive peaks:

$$G_i = \frac{\mu_{i+1} - \mu_i}{e} \times C \tag{3.3}$$

where μ_i has units of electric charge and C is the constant that converts from ADC×ticks units to coulombs. For the computation of the gain value $\langle G \rangle$, the first 4 peaks are used as for bigger number of PEs it is observed a small decrease ($\sim 2\%$) in the G_i value.

The over-voltages (voltage of the sensor over the breakdown voltage: OV $= \text{V}_{\text{Operation}} - \text{V}_{\text{Br}}$) chosen for each coated X-ARAPUCA (see Table 3.3) are close to the expected

operation voltage at SBND. These OVs correspond to similar PDEs at room temperature for the individual SiPMs according to the manufacturers (see Table 3.2), with a PDE of 40% for an OV of 4.5 (3) V for the Onsemi (Hamamatsu) SiPMs.

The results are in agreement with the specs given by the manufacturers. The X-ARAPUCA SiPMs have smaller gains (Fig 3.10) in the [2–4] $\times 10^6$ range, while the reference SiPMs are in the [5–9]$\times 10^6$ range. Both X-ARAPUCA configurations exhibit a similar gain for the same over-voltage.

X-ARAPUCA type	V_{Br} **[V]**	**OV [V]**	**Gain** [$\times 10^6$]
Hamamatsu	41.4	2	1.49 ± 0.01
		2.5	1.87 ± 0.01
		3	2.25 ± 0.01
Onsemi	42.15	3.25	2.52 ± 0.01
		4.25	3.31 ± 0.01
		5.75	4.46 ± 0.01

Table 3.3: Summary of the obtained gains for both X-ARAPUCA units tested.

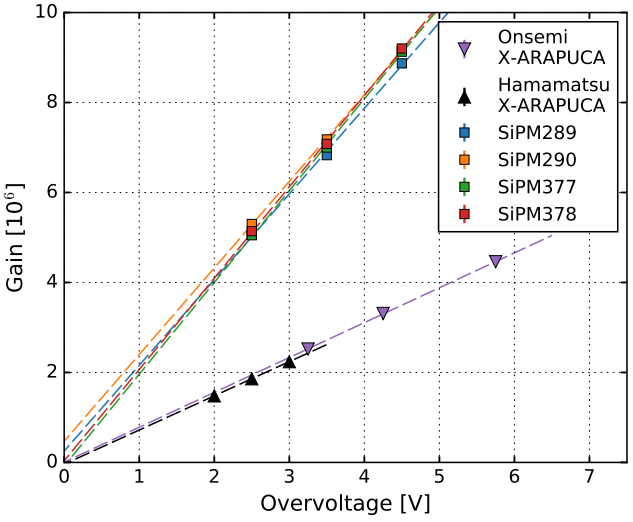

Figure 3.10: Calibration curves for both coated X-ARAPUCA configurations tested at CIEMAT with Onsemi and Hamamatsu SiPMs, and the reference Hamamatsu-VUV4 SiPMs.

Reference SiPM	**Gain at OV 2.5** [10^6]	**Gain at OV 3.5** [10^6]	**Gain at OV 4.5** [10^6]
SiPM 289	4.95±0.01	6.75±0.01	8.65±0.02
SiPM 290	5.12±0.01	6.98±0.01	8.96±0.02
SiPM 377	4.99±0.01	6.90±0.01	8.96±0.02
SiPM 378	5.06±0.01	6.97±0.01	9.06±0.02

Table 3.4: Summary of the obtained gains for all four reference SiPMs for a typical calibration run.

Although the sensors were stable during data takings, small variations ($< 5\%$) in the reference SiPMs were observed. To reduce the uncertainty in the charge estimation the calibration of each day was used to estimate the charge of the other runs taken during that day. The uncertainties on the fit parameters are the leading factor but in all cases are below the 1% level.

3.3.2 Crosstalk measurement

To correctly estimate the charge detected by both reference SiPMs and the X-ARAPUCA one has to take into account the probability of a fired SiPM cell to induce an avalanche in neighbor pixels, usually refereed as crosstalk or crosstalk probability. Following the Vinogradov approximation [143], crosstalk can be modeled at first order by a compound Poisson distribution where each fired cell has a probability CT to fire an adjacent cell. Secondary cells can also induce avalanches on their neighbors, with a geometric progression that imposes the condition CT < 1 as CT=1 means all cells would be fired eventually.

For a constant light source that follows a Poisson distribution, with $\langle\mu\rangle$ the mean number of primary fired cells, the fired cell distribution can be computed as:

$$f(n;\mu,CT) = \frac{e^{-\mu}}{n!}\sum_{i=0}^{n} B_{i,n}[\mu\cdot(1-\mathrm{CT})]^i\cdot \mathrm{CT}^{n-i}, \tag{3.4}$$

where the factor $B_{i,n}$ is defined as:

$$B_{i,n} = \begin{cases} 1 & \text{when } i=0 \text{ and } n=0 \\ 0 & \text{when } i=0 \text{ and } n>0 \\ i!(i-1)!(n-i)! & \text{otherwise.} \end{cases} \tag{3.5}$$

This is illustrated in Figure 3.11, where the distributions for a fixed μ and different crosstalk values are shown. We can also define the duplication factor $\mathrm{K_{dup}} = \frac{\mathrm{CT}}{1-\mathrm{CT}}$ which represents the fraction of increased charge with respect to the no crosstalk case. The initial and measured fired cells $\mu_{\mathrm{in}}, \mu_{\mathrm{meas}}$ then follow the simple relation:

$$\mu_{\mathrm{meas}} = \frac{\mu_{\mathrm{in}}}{1-\mathrm{CT}} = \mu_{\mathrm{in}}(1+\mathrm{K_{dup}}) \tag{3.6}$$

Because Equation 3.4 depends on 2 parameters, only calibration runs with at least 5 good consecutive peaks (including the 0-PE or pedestal peak) were used in the crosstalk

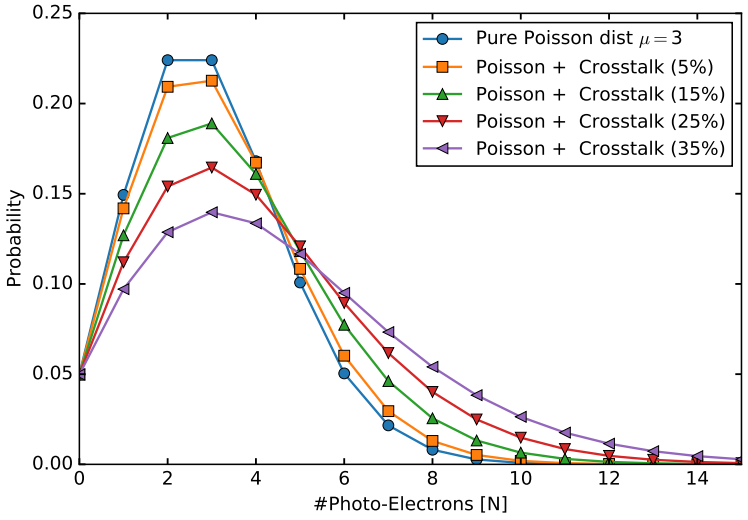

Figure 3.11: Probability distribution following Equation 3.4 for the same mean primary number of PE $\mu = 3$ and different crosstalk values. Notice how the shape of the distribution is shifted towards higher number of N(PEs) for bigger crosstalk values.

calculations. The procedure is shown in Figure 3.12 for a calibration run of the Onsemi X-ARAPUCA at an over-voltage of 4.25 V.

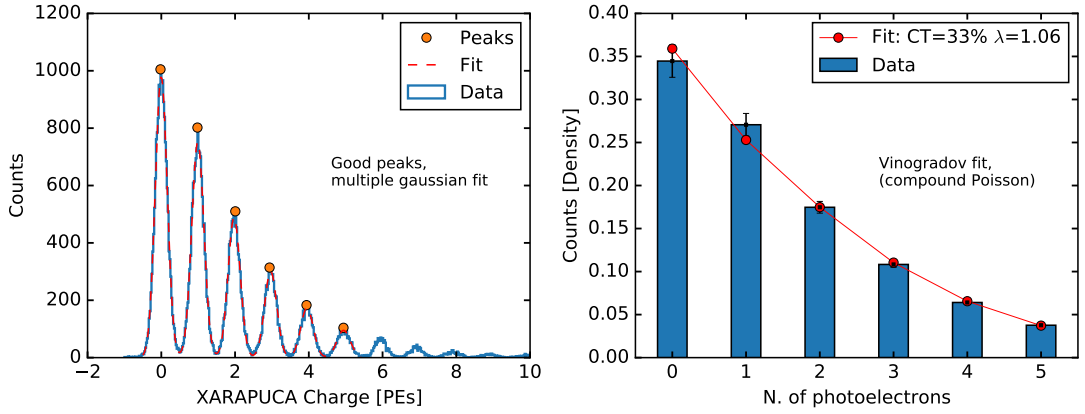

Figure 3.12: Crosstalk determination procedure: the identified good peaks (orange circles) are fitted to a sum of Gaussian functions (Left) for an Onsemi X-ARAPUCA calibration run. The number of events is determined by the area of each Gaussian, and the density distribution fitted to Equation 3.4. The error bars display $\times 2$ the Poisson uncertainty in each bin $\sim \sqrt{N}/N$.

In opposition to the gain values, the crosstalk is consistently lower for Hamamatsu SiPMs than for the Onsemi model. The X-ARAPUCA equipped with Hamamatsu SiPMs also presents crosstalk values at the same OV similar to the reference Hamamatsu VUV4 SiPMs, around 10 % at an OV of 3 V. For the Onsemi case, values up to 40 % are found at the highest OV tested (5.75 V).

This result has been incorporated in the official MC simulation of SBND. The crosstalk value chosen is 42.4%, as most of the X-ARAPUCAs (176 of 192) are equipped with Onsemi SiPMs and 5.75 V is the OV closer to the expected operation voltage. The simulation and reconstruction workflow described in Chapter 4 includes the result.

Sensor type	**OV [V]**	**Crosstalk [%]**
Hamamatsu X-ARAPUCA	2	6.2 ± 0.4
	2.5	7.1 ± 0.8
	3	10 ± 2
Onsemi X-ARAPUCA	3.25	20.5± 0.3
	4.25	29.5± 0.5
	5.75	42.4± 0.5
Reference SiPMs	3	10.02± 0.08
	4	14.9± 0.3
	5	24± 1

Table 3.5: Summary of the obtained crosstalk values for both X-ARAPUCA units and the reference Hamamatsu VUV4 SiPMs in liquid argon.

The uncertainty in the crosstalk value from individual fits was at the few percent level. To reduce the errors, a crosstalk mean weighted with the inverse of the errors was taken using the best fits from different calibrations at the same over-voltage.

3.3.3 Linearity study

For the linearity studies, measurements in very similar conditions to the ones in LAr were taken (same electronics, reference SiPMs, ...) but cooling the Onsemi X-ARAPUCA in liquid nitrogen. Calibration runs were taken and then a scan in the laser intensity range was performed. There are two main effects to be addressed when discussing the non-linear regime of SBND light sensors:

- Charge saturation: an effect that causes a loss of observed vs expected charge. This has been observed for both PMTs and SiPMs sensors [144].
- Pulse shape variations: it has been reported previously for PMTs [145, Chapter 3] that the amount of collected light might affect the sensor response. Although no shape variations are expected for SiPM sensors, a direct confirmation using the whole X-ARAPUCA unit is useful.

To study the first effect we look at the total collected charge by each sensor. In SBND, the single PE X-ARAPUCA signal is expected to have an amplitude of 8 ADC counts or 4 mV for the CAEN V1740. The 12 bit ADC (4096 counts) then will saturate at 512 PEs (arriving simultaneously). Thus, it is enough to ensure that the X-ARAPUCA

does not deviate from the linear regime in the [0–500] PEs range as higher intensities will saturate the ADC.

The SiPM charge saturation modeled in [144] is at first order the probability that a photon hits an already fired cell. This effect is more likely to happen the more activated pixels (total charge) the SiPM has at a given moment. For this reason, the behavior of the SiPMs (and the X-ARAPUCA) will be linear if the number of fired cells N_{fired} is negligible with respect to the total number of pixels N_{total} ($N_{fired} \ll N_{total}$). Labeling the expected number of fired cells as N_{exp} (the cells fired in absence of saturation effects) the following relation holds:

$$N_{fired} = N_{total} \times \left[1 - \exp\left(-\frac{N_{exp}}{N_{total}}\right)\right] \tag{3.7}$$

and in the low-charge regime this reduces to the non-saturated behavior $N_{fired} \sim N_{exp}$. For reference, Hamamatsu-VUV4 SiPMs have $N_{total} = 6400$ cells, while each On-semi (Hamamatsu) SiPM has 2668 (4336) cells. Equation 3.7 predicts a 5% deficit in N_{fired}/N_{exp} for $N_{exp} = 10\%N_{total}$. Light yields below that threshold can be considered in the linear regime.

For the charge saturation effects, no significant deviation from the linear behavior was found when comparing the total charge of the pulse from X-ARAPUCA signals vs the reference sensors charge (Figure 3.13). The four reference SiPMs are sensitive to different light yields due to their geometric position in the setup. The ratio between the charge collected by each of them and the others was found to be constant for all laser intensities, indicating that all of them were indeed in the linear regime. Since the maximum charge observed by the reference SiPM 289 is ∼200 PEs, following Eq: 3.7, the saturation effects of the X-ARAPUCA are below 2% up to 850 PEs.

To study the second effect, average waveforms and charge vs amplitude plots were computed for each sensor at different laser intensities. They are shown in Figure 3.14 with darker blue tones for the higher laser intensities. The mean charge for each laser intensity (125 to 850 PEs) is included in the legend of the Figure. After normalizing each waveform dividing by its maximum amplitude (Figure 3.14-Bottom), no significant deviation in the pulse peak shape or the undershoot was found for the different laser intensities up to 850 PEs.

3.4 VUV photon detection efficiency

The photon detection efficiency of a light sensor is simply the ratio of measured PEs to the total number of incident photons:

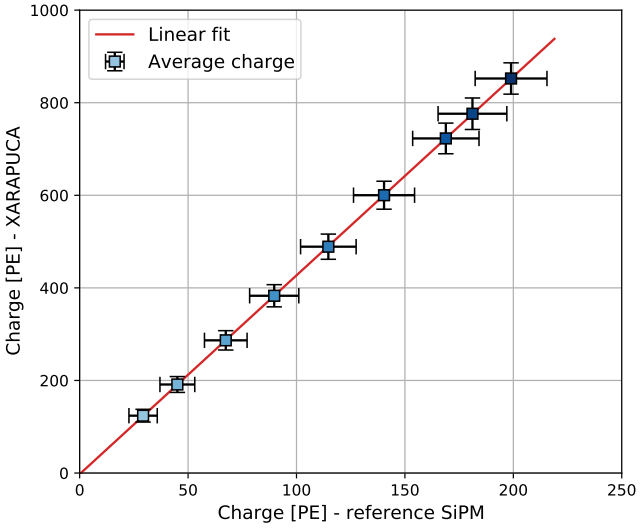

Figure 3.13: Average charge and dispersion (STD) for the different intensities as seen by the reference SiPM 289 and the Onsemi X-ARAPUCA.

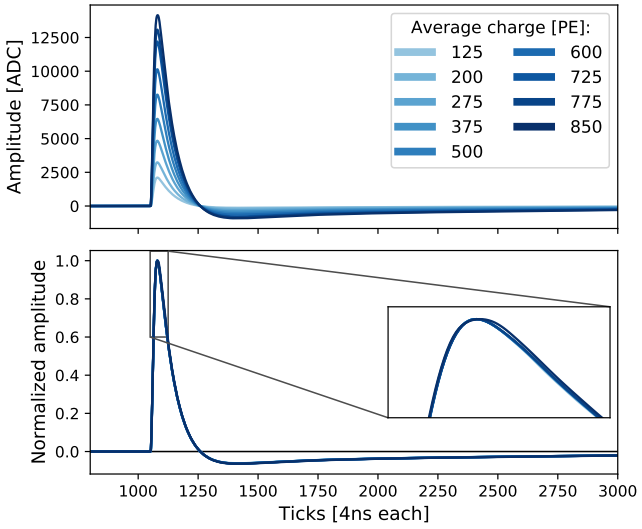

Figure 3.14: X-ARAPUCA average waveforms for the different laser intensities tested in absolute (Top) and normalized amplitude (Bottom) with a closer zoom to the peak.

$$\text{PDE} = \frac{\#\text{Detected Photo-electrons}}{\#\text{Incident Photons}}. \tag{3.8}$$

Following formula 3.8, we are interested in the X-ARAPUCA photon detection efficiency (PDE_{XA}). The number of arriving photons at each sensor only depends on the setup geometry as the deposited energy of the alpha source is fixed. Using the reference SiPMs, we can estimate the alpha source flux and thus the number of arriving photons at the X-ARAPUCA surface, making the measurement independent of impurities that affect the total light production. It is easy to show that:

$$\mathrm{PDE_{XA}} = \frac{\mathrm{PE_{XA}}}{\mathrm{PE_{SiPM}}} \times \frac{\mathrm{Photons_{SiPM}}}{\mathrm{Photons_{XA}}} \times \mathrm{PDE_{SiPM}} \tag{3.9}$$

where $\mathrm{PE_{XA}}$($\mathrm{PE_{SiPM}}$) is the number of photo-electrons in the X-ARAPUCA (reference SiPM) and $\mathrm{Photons_{XA}}$($\mathrm{Photons_{SiPM}}$) the number of arriving photons at the X-ARAPUCA (reference SiPM). Defining the geometrical factor $\mathrm{F_{Geo}} = \mathrm{Photons_{XA}}/\mathrm{Photons_{SiPM}}$ and correcting the effect of the crosstalk (Equation 3.6), the X-ARAPUCA PDE can be expressed as:

$$\mathrm{PDE_{XA}} = \frac{\mathrm{PE_{XA}^{meas}}}{\mathrm{PE_{SiPM}^{meas}}} \times \frac{1-\mathrm{CT_{XA}}}{1-\mathrm{CT_{SiPM}}} \times \frac{\mathrm{PDE_{SiPM}}}{\mathrm{F_{Geo}}} \tag{3.10}$$

with $\mathrm{PE_{XA}^{meas}}$($\mathrm{PE_{SiPM}^{meas}}$) the measured charges with the crosstalk effect included. The reference SiPMs efficiency ($\mathrm{PDE_{SiPM}}$) was measured at the CIEMAT lab using the absolute light yield of the alpha source [136]:

$$\mathrm{PDE_{SiPM}^{3.5OV}} = 12.3 \pm 1\,\%$$

The uncertainties arising from the angular dependence of the PDE with the incident light [146] were reduced by only using the SiPMs in front of the α source (289 and 290) in the VUV PDE estimation.

To estimate $\mathrm{F_{Geo}}$, Monte Carlo simulations using G4 were performed (see Fig 3.15). A simple analytical toy-model, detailed in Appendix A, was developed to understand the charge distribution observed in the X-ARAPUCA, caused by geometrical effects, and to serve as a crosscheck to G4 estimations.

The dedicated G4 simulations also included the absorption and Rayleigh scattering effects. Per each G4 event, 192k photons are emitted isotropically from a random point in the α source surface. Both the analytical and G4 estimations of the geometrical factor:

$$\mathrm{F_{Geo\,VUV}} \quad = \quad 42.35 \pm 1.36$$

agree up to 0.8% (see Appendix A and Table A.1 for details). Uncertainties in the final position of the sensors were taken into account. We performed G4 simulations with the reference SiPMs and X-ARAPUCA windows displaced ±1 mm from their original positions. The reference SiPMs were also rotated ±5°. The variation in the solid angle estimated was found to be 2% for the X-ARAPUCA and 2.5% for the reference SiPMs 289 and 290. These values were considered as uncertainties.

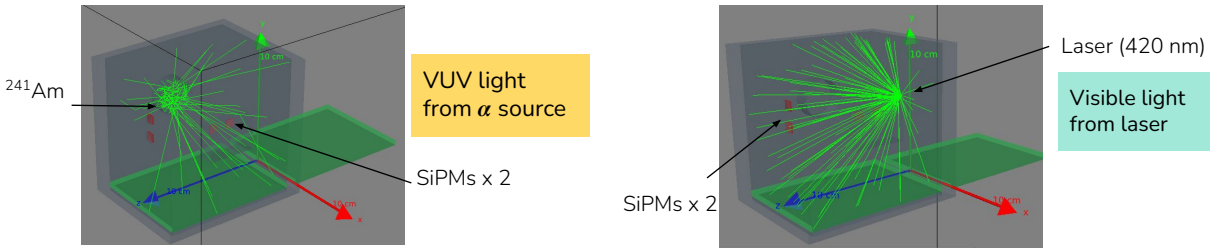

Figure 3.15: Examples of the G4 simulations carried out to estimate the number of photons arriving at each sensor for VUV (Left) and visible (Right) light. Notice that the alpha source has a non-negligible extension while the visible light can be approximated by a point-like source.

The last ingredient required by Equation 3.10 is the SiPM and X-ARAPUCA measured charges. Since the X-ARAPUCA signals are bipolar, the scintillation tail of liquid argon is hidden in the signal undershoot. To remove the sensor effect, a deconvolution and Gauss filtering of the raw signals (see Chapter 4) was performed using the template of the single photo-electron mean waveform. The procedure is shown in Figure 3.16. The raw signal has visible late light pulses in the undershoot around 1500 ns. After the processing, the late light is clearly visible in the scintillation tail before recovering the baseline level. The charge was then estimated from the de-convolved waveforms, showing a ∼10% increase of the total measured charge, as expected. The reference SiPM signals are unipolar and thus needed no further processing.

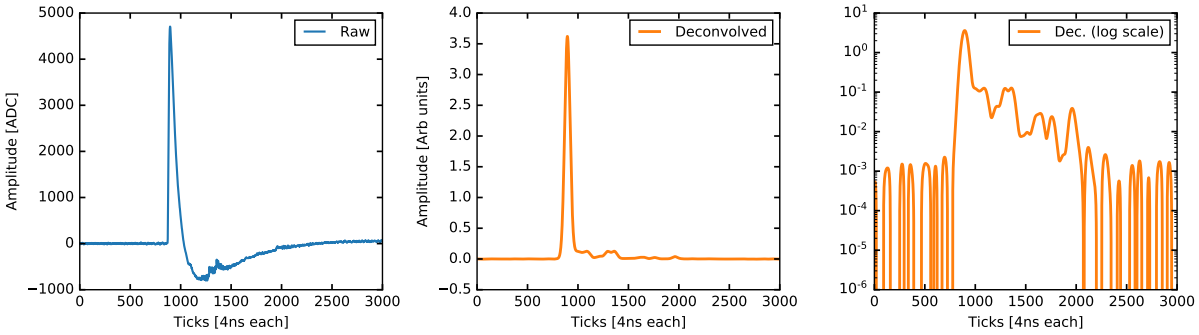

Figure 3.16: X-ARAPUCA signal processing with a VUV scintillation pulse. Small secondary pulses from the slow component are visible. The raw signal (Left) is deconvolved removing the sensor response and noise filtered (middle). After the processing, the scintillation tail is clearly visible in logarithmic scale (Right).

An event selection is applied to ensure only events triggered by the alpha source are used for the PDE determination. To do so, we take advantage of the different scintillation profiles that depend on the charge and mass of the charged particle. Specifically, we compare the fast or prompt charge to the total charge of the signal. This is illustrated in Figure 3.17-Left, where the F90 (fraction of charge in the first 90 ns) is displayed vs the total charge; the α source events are clearly isolated. The band centered at F90=0.5

is driven by cosmic muon events and electron recoils. The wide shape of the events triggered by the α source (Figure 3.17-Right) is caused by geometrical effects: the alpha source has a wide area (22 mm radius), and the geometrical aperture (solid angle) of the X-ARAPUCA depends on where each alpha particle was produced in the disk.

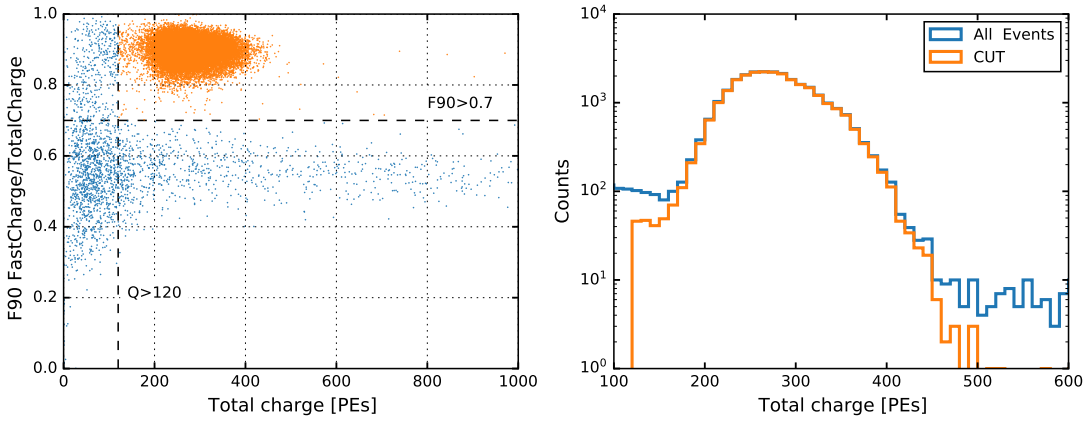

Figure 3.17: Left: event distribution detected by the coated Onsemi X-ARAPUCA in fast vs total ratio (F90) and total charge for an alpha source run with the applied cuts. Right: total charge distribution before and after cuts, 90 % of the events pass the cuts.

Figure 3.18 shows the average light waveforms from different sources. The SiPM response from a calibration laser run, and the average waveforms from muon and alpha runs are displayed. The scintillation tails are clearly visible over the sensor response.

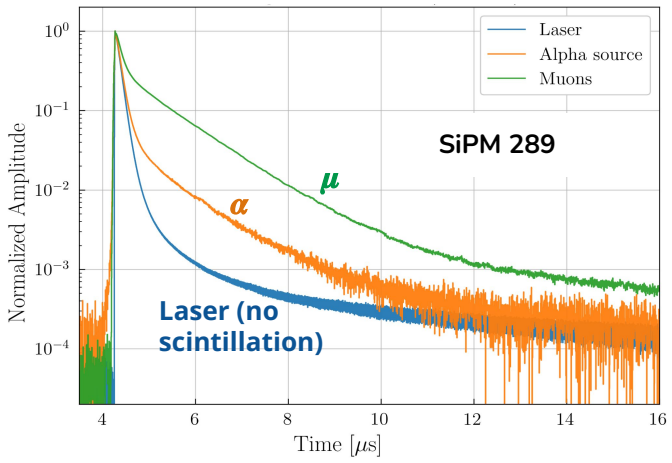

Figure 3.18: Average waveforms for a calibration run with the laser (blue), an alpha run (orange) and a muon run (green).

The firsts α runs of each data taking were used to compute the PDE as increasing impurities in the liquid argon reduced the amount of total PEs collected from the alpha source each day. The ratio of measured charge between sensors, however, was constant.

This indicates that the impurities do not impact significantly the propagation of photons for this small setup ($L \sim 10$ cm) but only the total light produced. The average charges from alpha runs for the X-ARAPUCAs and the sum of the reference SiPMs 289 and 290 are summarized in Table 3.6. The measured charge of the reference SiPMs is compatible within errors between measurements which indicates the setup was stable between different data takings.

Sensor	**OV [V]**	$\langle Q \rangle$ **[PEs]**
Reference SiPM 289 & 290	3.5	35.40 ± 0.4
Onsemi X-ARAPUCA	3.25	163 ± 1
	4.25	218 ± 2
	5.75	340 ± 3
Reference SiPM 289 & 290	3.5	36.0 ± 0.3
Hamamatsu X-ARAPUCA	2	212 ± 2
	2.5	251 ± 2
	3	272 ± 2

Table 3.6: Mean charge measured from the α source events for the two X-ARAPUCA configurations tested and the reference SiPM 289 and 290 in front of the α source that calibrate the light flux.

For the final PDE numbers, crosstalk from both X-ARAPUCAs and the reference SiPMs has been corrected at each over-voltage. Following Eq 3.10, the results are shown in Table 3.7. PDE Values at the expected nominal OVs are in the 2% range, compatible with similar measurements ([114, 131] and references therein). The Hamamatsu unit is equipped with more efficient WLS bars and the SiPM model has a higher PDE at the same over-voltage, resulting in greater PDE values than the Onsemi X-ARAPUCA. Measurements of an X-ARAPUCA prototype for DUNE far detector with a comparable size found values of 1.8 and 2.9 % with Eljen and Glass-To-Power bars, respectively [131].

Sensor type	**OV [V]**	**PDE at 127 nm [%]**
Hamamatsu X-ARAPUCA	2	1.99 ± 0.20
	2.5	2.17 ± 0.24
	3	2.29 ± 0.23
Onsemi X-ARAPUCA	3.25	1.27± 0.11
	4.25	1.57± 0.14
	5.75	2.20± 0.22
DUNE prototype - Eljen bar [131]	2.7	1.8± 0.1
DUNE prototype - G2P bar [131]	2.7	2.9± 0.1

Table 3.7: Summary of the obtained PDE values at 127 nm for both X-ARAPUCA units in liquid argon. For comparison, an X-ARAPUCA prototype for DUNE far detectors with different SiPMs but similar size is included.

The uncertainty of the measurement is dominated by the reference SiPM PDE ($\sim 8\%$). For the Hamamatsu unit, the second biggest uncertainty is the crosstalk determination

($\sim [5-7]\%$), as their calibration charge spectra have less resolution (individual PE peak separation from each other) compared to the Onsemi X-ARAPUCA (see Figure 3.9 Left and Center). The geometrical uncertainty in the solid angles, and therefore in the F_{Geo} factor is $\sim 3\%$.

3.5 Visible photon detection efficiency

As in the VUV PDE measurement, we use the reference SiPMs to predict the photon flux arriving at the X-ARAPUCA. The reference sensors used (SiPMs 378 and 379) were placed in front of the light source, the diffuser in this case. No deviation from Gaussian-shaped distributions in the charge of the X-ARAPUCA or the SiPMs was observed. This is expected: the laser-diffuser combination is a point-like source in our setup. The diffuser emission is not isotropic but follows a curve close to a cosine law provided by the manufacturer [147] (see Figure 3.19). The precise intensity histogram was fed to G4 as input to estimate the number of arriving photons at each sensor. The geometrical factor for the visible case is:

$$F_{Geo\,Vis} = 38.3 \pm 1.1$$

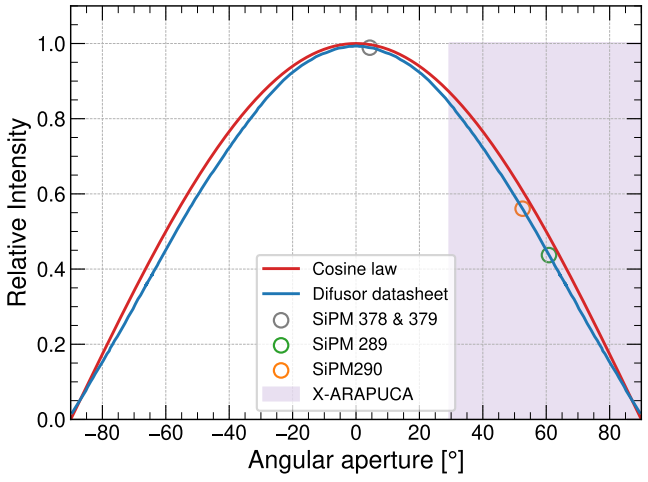

Figure 3.19: CCSA1 cosine corrector normalized intensity (blue) with respect to the angular aperture. The red line indicates a pure cosine law. The expected relative intensity at each reference SiPM is indicated with circular markers. The angular region seen by the X-ARAPUCA is shown in purple.

The PDE of the reference SiPMs to the visible (420 nm) light is:

$$PDE_{SiPM}^{420\ nm} = 21.02 \pm 0.44\,\%$$

The measured charges for the reference SiPMs 378 and 379 and the two X-ARAPUCA configurations are summarized in Table 3.8.

Sensor	**OV [V]**	$\langle Q \rangle$ **[PEs]**
Reference SiPM 289 & 290	3.5	193 ± 2
Onsemi X-ARAPUCA	3.25	63.0 ± 0.5
	4.25	81 ± 1
	5.75	124 ± 1
Reference SiPM 289 & 290	3.5	363 ± 3
Hamamatsu X-ARAPUCA	2	121 ± 1
	2.5	139 ± 1
	3	155 ± 2

Table 3.8: Mean charge measured from the laser high intensity runs for the two X-ARAPUCA configurations tested and the reference SiPM 378 and 379 in front of the diffuser that calibrate the light flux.

3.5.1 Angular dependence

For coated units, the VUV light is converted to visible photons isotropically in the X-ARAPUCA surface through the pTP coating, making the PDE independent of the angle of incidence (AOI) of the incoming photons. The visible case is different, as no conversion is involved. The cutoff wavelength of the dichroic filters depends on the AOI of the incoming photons. This is shown in Figure 3.2 where the AOI dependence in the filters transmittance is superposed to the TPB emission spectrum. To model this dependence, the angular distributions of photons arriving to the X-ARAPUCAs at the CIEMAT setup and the expected at SBND (from the TPB WLS foils) were estimated through G4 simulations.

First, the transmittance values at 420 nm for different AOIs (Figure 3.2) were fitted to a sigmoid function to extract the angular dependence of the transmittance T(AOI) (Figure 3.20). Then, from the CIEMAT lab measurements, the PDE as a function of the AOI was estimated assuming that the PDE is proportional to the transmittance: PDE $\propto$ T(AOI) at the 420 nm peak. Since the filter's transmittance was measured in air, Snell's law was used taking into account the difference in refraction indexes ($^{\mathrm{LAr}}_{420\mathrm{nm}}$=1.23) [148, 149] to extrapolate the curve from air to LAr.

Finally, using the angular distribution expected at SBND from the dedicated simulation (Figure 3.21), a mean value of the visible PDE for the coated units in SBND can be derived. The SBND simulation incorporates the reflectivity of the stainless steel of the field cage, as well as the shadowing caused by the TPC wire planes. 20 million visible photons following the TPB emission spectrum were produced in the middle of the SBND

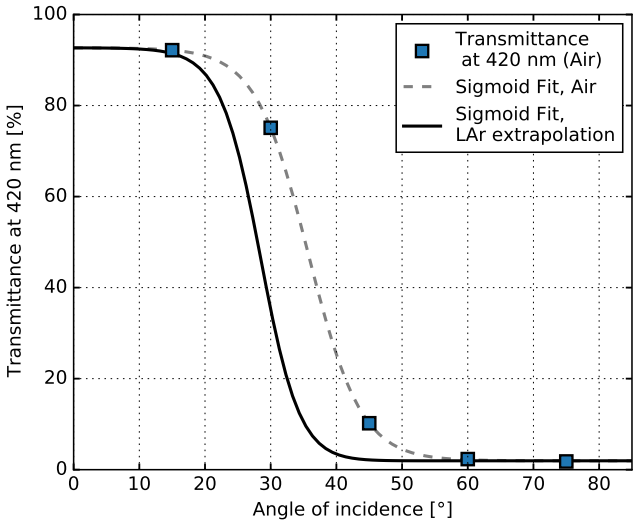

Figure 3.20: Sigmoid fit to the 420 nm points modeling the transmittance as a function of the AOI. Notice that for AOIs> 45° the filter is opaque to most of the TPB re-emitted light. The fit to the measured points in Air is shown with dashed lines, and the extrapolation to LAr with solid black line.

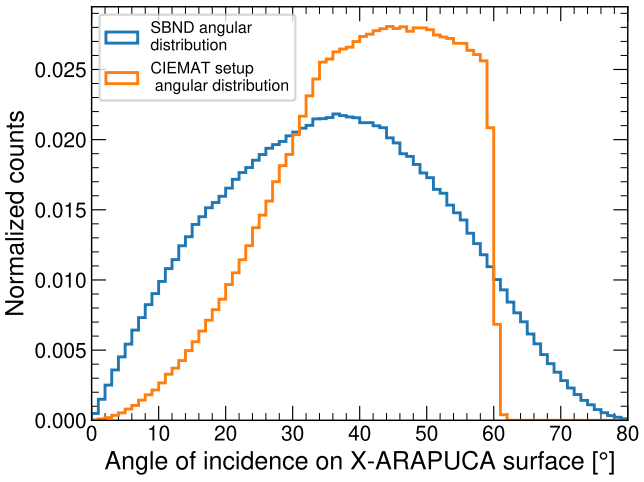

Figure 3.21: Angular distribution of visible photons arriving at the X-ARAPUCA window at SBND (blue) and CIEMAT setup (orange). The estimation of the SBND distribution includes the effects of the shadowing from the wire planes and the mesh grid between them and the PDS sensors.

detector, where the TPB foils are located. For any photon hitting an X-ARAPUCA surface, the AOI was recorded.

The measured PDE values at CIEMAT setup are shown in Figure 3.22 and Table 3.9. The results are in agreement with the trend for the VUV PDE: Onsemi SiPMs have comparable values at the higher OVs. Both Onsemi and Hamamatsu X-ARAPUCAs have low values as these units are not intended for visible light detection, unlike the uncoated units. The extrapolated PDE as a function of the angle of incidence reaches a

plateau around 1.2 % for AOIs close to 0. The mean value expected at SBND is bigger ($\sim 0.4\%$) than the value at the CIEMAT setup, as the expected mean angle of incidence is smaller than the one at CIEMAT setup.

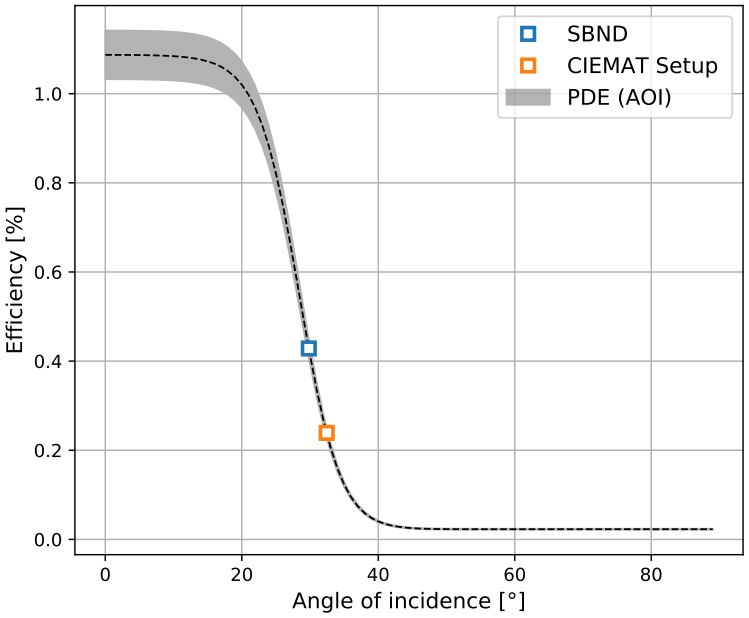

Figure 3.22: PDE at the CIEMAT setup (orange square) for the coated Onsemi X-ARAPUCA at an over-voltage of 5.75 V, extrapolation as a function of the angle of incidence (black) and expected mean value at SBND (blue square). The error band is extrapolated from the values obtained at CIEMAT setup.

Sensor type	**OV [V]**	**PDE at 420 nm [%], CIEMAT setup**	**PDE at 420 nm [%], extrapolated to the AOI at SBND**
Hamamatsu X-ARAPUCA	2	0.20 ± 0.01	0.36 ± 0.02
	2.5	0.23 ± 0.02	0.41 ± 0.03
	3	0.25 ± 0.02	0.45 ± 0.03
Onsemi X-ARAPUCA	3.25	0.17 ± 0.01	0.30 ± 0.01
	4.25	0.19 ± 0.01	0.34 ± 0.01
	5.75	0.24 ± 0.01	0.43 ± 0.02

Table 3.9: Summary of the obtained PDE values at 420 nm for both X-ARAPUCA units in liquid argon.

Ongoing measurements, beyond the scope of this thesis, are being performed to characterize the uncoated units with the same setup geometry.

Chapter 4

Light simulation and reconstruction in SBND

The photon detection system is essential for achieving a good performance in a LArTPC detector. From event triggering to complementary calorimetry and background rejection capabilities, a proper understanding and modeling of the light generation, propagation and readout is vital for any modern LArTPC detector. In this chapter, the main ingredients of the SBND simulation framework are discussed, focusing on the production of the LAr scintillation light and its detection with the X-ARAPUCA sensors.

4.1 Light simulation

In SBND, all the simulations are carried out within the LArSoft package [150, 151]. LArSoft is built upon the *art* framework developed for event-processing at Fermilab [129]. LArSoft allows for both data analysis and Monte Carlo simulations to be processed using the same tools and algorithms with a common framework. The initial particles are produced by *particle generators*. The generators compute their positions and momenta at a given time. Each generator specializes in a different particle source:

- SM neutrino interactions are simulated using the GENIE software [152]. The GENIE tuning used is the `AR23_20i`, a baseline model for SBN and DUNE oscillation analysis (see [153] for more details).
- The cosmic muons are modeled with CORSIKA [154]. This tool reproduces the interactions of cosmic rays with the atmosphere and the showers of particles produced afterwards. The average rate, $\sim$ 130 evts/s/m^2, was calibrated using MicroBooNE data [120].

- For Beyond Standard Model searches, the SBN program has developed its unique event generator, MeVPrtl. A more detailed description is given in chapter 5.

Once the particles are placed in the detector geometry, their propagation and subsequent interactions are modeled with Geant4 [85] (Geant4.10.6.p01). For example, they can collide elastically with atom nuclei, ionize atoms, decay into different particles... The energy depositions of primary and daughter particles are computed along their trajectories. The full physics list (the processes that the simulated particles can experience) is based on Geant4's QGSP_BERT list. This chapter focuses on the production, detection and reconstruction of light signals. A complete review of the TPC and CRT event simulation and reconstruction is given in Chapter 6.

4.1.1 Light production and propagation

The number of ionized electrons (Q) and scintillation photons (L) produced by a particle in a LArTPC are proportional to the deposited energy. The electric field affects the recombination process decreasing the total amount of emitted photons and increasing the amount of detected ionization charge, as depicted in Figure 4.1. This phenomenon is usually referred as anti-correlation [111]. In SBND, $\sim$ 20k photons per MeV of deposited energy are produced at the nominal drift field (500 V/cm). The specific light yield depends on the charged particle (see Table 4.1). The relevant parameters of VUV photons from direct scintillation light are given in Table 4.1. The produced electrons undergo diffusion and space charge effects described in Chapter 2.

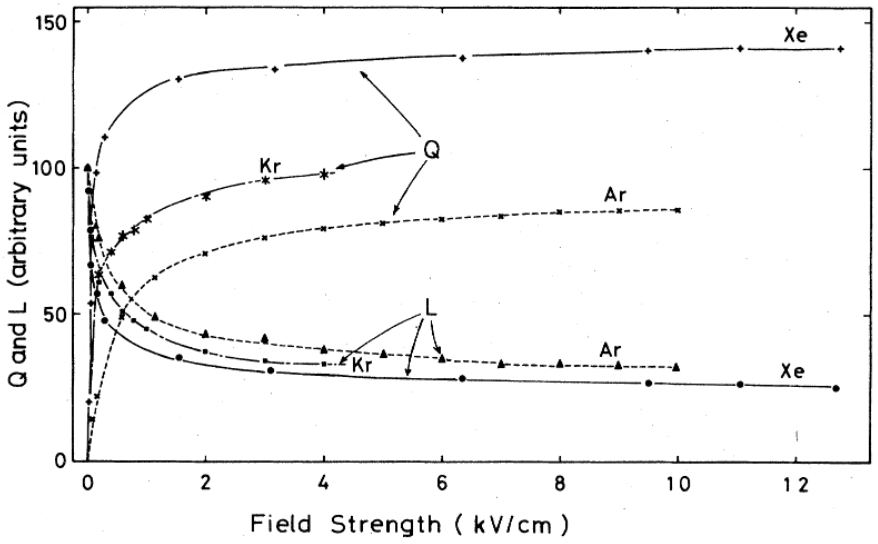

Figure 4.1: Luminescence intensity (L) and collected charge (Q) as a function of the applied electric field for liquid xenon, argon and krypton. Picture taken from [111].

Properties of LAr scintillation light	
Fast decay time [ns] (τ_{fast})	6
Slow decay time [ns] (τ_{slow})	1300
Mean group velocity [cm/ns]	13.5
Rayleigh scattering length [cm]	99.9

Particle	τ_{fast} ratio	Light yield [photons/MeV]
Pions	0.23	24000
Muons	0.23	24000
Electrons	0.27	20000
Kaons	0.23	24000
Protons	0.29	19200
Alpha particles	0.56	16800

Table 4.1: Scintillation (VUV) light parameters used in SBND simulations taken from [87, 89, 108, 155]. τ_{fast} ratio is defined following equation 2.5 as the fraction of total light emitted in the fast component: τ_{fast} ratio $= A_{\text{fast}}/(A_{\text{fast}} + A_{\text{slow}})$

A complete tracking (full simulation) of each photon would be too CPU intensive given that reflection, absorption and scattering effects are included. Previous LArTPC experiments such as MicroBooNE, developed the use of *optical libraries* [156]. These lookup tables are produced dividing the detector in small voxels (typically $5 \times 5 \times 5$ cm^3) and running a complete tracking simulation for each voxel. A high number of photons ($\sim 5 \times 10^5$) is thrown per voxel. From the number of photons arriving at each sensor we compute the visibility (fraction of detected photons). Once the library is produced, fast simulations simply look up the visibility tables to determine the amount of detected light generated by the particle along its trajectory.

Photon libraries scale with the detector volume and depend on the voxel size. Their high memory use O(GB) and lack of time transport effects are a concern for next generation LArTPCs such as DUNE. To address these issues, an alternative *semi-analytic* model was developed [157]. This approach takes advantage of the isotropic emission of scintillation light. At first order the number of detected photons (N_D) is proportional to the solid angle that the aperture of the photodetector subtends. After comparing the number of photons obtained from a full G4 simulation (N_{Geant4}) and the analytical estimation using the solid angle (N_Ω), corrections to the analytical model can be applied using Gaisser-Hillas (GH) functions [158] of the form:

$$GH(d, \theta_i) = N_{\max} \left(\frac{d - d_0}{d_{\max} - d_0} \right)^{\frac{d_{\max} - d_0}{\lambda}} e^{\frac{d_{\max} - d}{\lambda}} \tag{4.1}$$

with d_0, λ free parameters describing the width of the distribution and $N_{\max}$ the maximum of the function located at $d_{\max}$ (in our case $d_{\max} \sim 100$ cm). Figure 4.2 shows the ratio between the number of photons derived from a pure geometric assumption and the Geant4 estimations with a full simulation including scattering effects, reflections, etc for a SBND-like geometry [157]. For each bin in the offset angle θ_i (see Figure 4.2-Left) a fit to equation 4.1 is performed, estimating the free parameters. Then, the total number of photons can be estimated simply by correcting the prediction from the analytical method (N_Ω) by:

$$N_D \;=\; N_\Omega \;\times\; GH(d, \theta_i)/\cos(\theta). \tag{4.2}$$

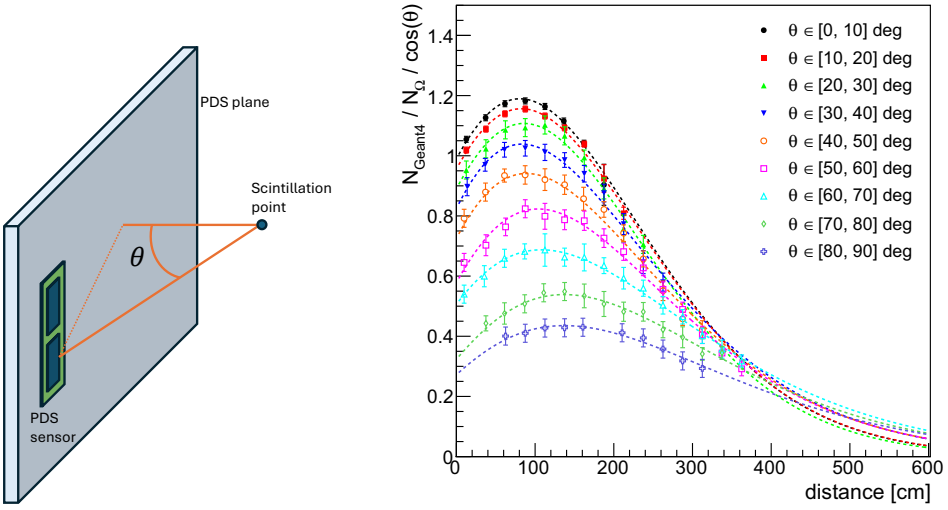

Figure 4.2: Left: cartoon exemplifying the offset angle θ from the normal of the scintillation point to the PDS plane. Right: Relation between the number of Geant4 simulated photons on the PDS and a pure geometrical estimation of the photons based on the solid angle subtended by each PD sensor for different offset angles. Figure taken from [157].

Time transport effects are modeled with a composite *Landau + Exponential* function for direct (VUV) light (t_t):

$$t_t(x) = \underbrace{N_1 \frac{1}{\xi}\frac{1}{2\pi i}\int_{c-i\infty}^{c+i\infty} e^{\rho s + s\,log\,s}\,ds}_{\text{Landau}} \;+\; \underbrace{N_2\, e^{\kappa\, x}}_{\text{Exponential}}\;, \tag{4.3}$$

where $\rho = (x-\mu)/\xi$, μ and ξ are the most probable value and width of the Landau function, κ is the (negative) slope of the exponential and $N_{1,2}$ are normalization constants. The value of these parameters is obtained by fitting the function to the time distribution obtained with a full Geant4 simulation. For the reflected visible light (t_s),

an empirical formula approximates the distribution:

$$t_s = t + (t - t_f)[\exp(-\tau \ln(x)) - 1]. \tag{4.4}$$

with t_s the smeared arrival time, τ a smearing factor, x a random number between 0.5 and 1 and t_f the fastest possible arrival time (calculated geometrically). The τ factor is fixed fitting the distribution in Equation 4.4 to the obtained with the one generated with a full Geant4 simulation.

The *semi-analytic* model can only be used for light produced inside the TPC active volume (X = [-196.5, 196.5] cm, Y = [-200, 200] cm, Z = [0, 500] cm) due to its geometric approach, but contributions from outside the active volume may also be relevant. For example, cosmic muons crossing behind the PDS can lead to fake triggers and affect the trigger efficiency studies. Thus, a *hybrid* model is implemented in SBND simulations with a scaled-down optical library for the light emitted outside the active volume and the *semi-analytic* approach inside the active volume. The voxels for the scaled-down library are $8 \times 10 \times 10$ cm^3.

For the case of visible (reflected) light, we need to account not only for the transport effects but also for the emission spectrum of the TPB. Following reference [155], a four-exponential shape is assumed with the decay times and abundances shown in table 4.2.

Component	Decay time [ns]	Abundance [%]
τ_1	6	60
τ_2	49	30
τ_3	3550	8
τ_4	309	2

Table 4.2: Characteristic TPB decay times. Values taken from [155].

4.1.2 Photon detector simulation

After simulating the propagation inside the TPC, an histogram with 1 ns binning is filled with the number of arriving photons at the active surface of each optical sensor. The VUV and visible components are stored in separated histograms as the sensor behavior depends on the wavelength of the incoming photons. The sensor simulation then follows the same steps for each PDS channel:

1. First, we estimate the number of photo-electrons per arriving photons at each sensor using the sensor efficiency and random number generators from the CLHEP library [159]. The efficiencies of the different light sensors to the VUV and the visible components are summarized in Table 4.3. An additional factor is included

in the efficiency values to correct for the mesh transparency between the wire planes and the PDS sensors (80%) which is not considered in the simulation. In addition, the visible component includes a factor (79%) representing the effective area of the TPB-coated foils over the total CPA plane.

Sensor type & light component	**PMT PDE [%]**	**X-ARAPUCA PDE** [%]
Coated sensor VUV	12% [160]	2.19 % [1]
Coated sensor visible	17%	0.43% [1]
Uncoated sensor VUV	0%	0%
Uncoated sensor visible	25% [124]	2% [161]

Table 4.3: Photon detection efficiencies for the different optical sensors used in SBND simulations.

2. Then, correlated noise effects are included for X-ARAPUCAs. The main effect to consider is the SiPMs crosstalk, quantified in previous chapter.

3. For each PE, a waveform representing the single electron response (SER) is created. Variations in the SER amplitude are also included. For the PMTs, they are based on fluctuations at the first PMT dynode and follow a Poisson distribution (see Figure 4.3). For the X-ARAPUCAs they are characterized from the analysis of cryogenic test data available described in the next pages. To minimize the cables and allow high-voltage application, SBND PDS sensors are AC coupled. This means that the SER signals are bipolar and integrate to zero. This can be seen in Figure 4.3 for the PMT (Left) and X-ARAPUCA SER (Right).

4. Signals due to dark current (uncorrelated noise) are added. Dark current noise is modeled following a uniform distribution.

5. White Gaussian noise caused by the ADC with an RMS of 0.65 (2.6) ADCs is summed to the X-ARAPUCA (PMT) waveforms. The values are extracted from the ADC manufacturer especifications [142].

6. ADC dynamic range is simulated. For X-ARAPUCAs readout (CAEN V1740), that means the ADC values must be between 0 and 4096 (12 bit digitizer), while the PMTs ADC (CAEN V1730) range (14 bits) goes from 0 to 16384.

The relevant parameters of the PMT and X-ARAPUCA sensor simulations are summarized in Table 4.4. For simplicity, all X-ARAPUCA units are simulated as Onsemi X-ARAPUCAs (176 out of the total 192 units). The next pages describe in detail the key components of the X-ARAPUCA sensor simulation.

[1] Values for the (Onsemi) X-ARAPUCA coated units PDEs are estimated in Chapter 3.

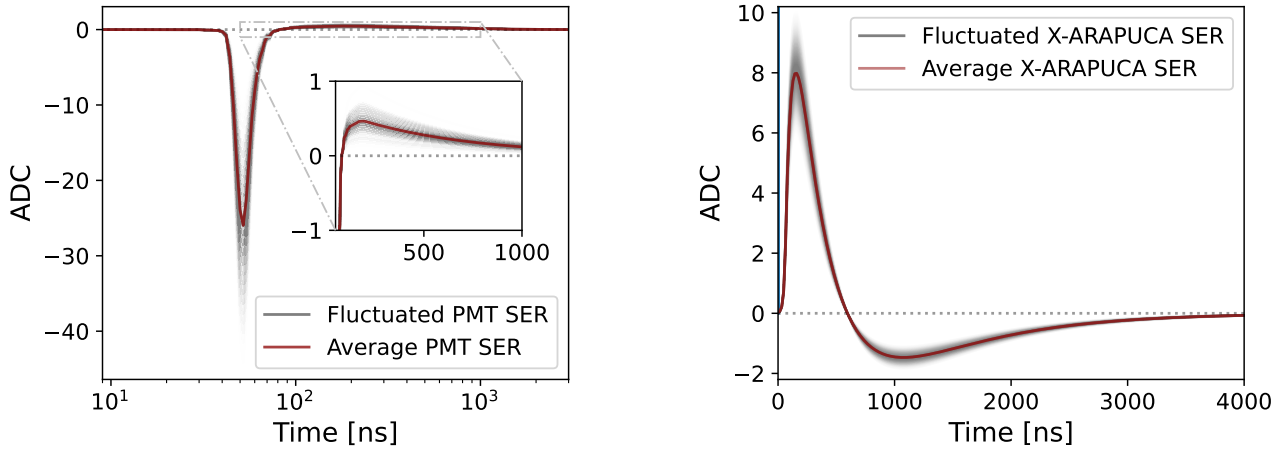

Figure 4.3: Left (Right): measured PMT (X-ARAPUCA) single electron response (SER). The amplitude fluctuations 22% (10%) are also shown in gray.

Parameter	**PMTs**	**X-ARAPUCAs (Onsemi)**
Crosstalk [%]	-	42.4
Dark current [Hz]	1000	10
ADC noise RMS [ADC]	2.6	0.65
ADC sampling [MHz]	500	62.5
ADC resolution [bits]	14	12
SER amplitude [ADC]	26	8
SER undershoot/Overshoot [%]	1.8	18.4
ADC saturation [PEs]	630	512
Amplitude fluctuations [%]	22	10

Table 4.4: Parameters for the simulation of PMT and X-ARAPUCA sensors. Values taken from the official SBND MC simulation [162], sbndcode v09_88_00_02.

Time response effects

A spread of the PMT transit times (from the PMT photocathode to the anode) of 2.4 ns width following a Gaussian distribution is also simulated.

The time response of the coated X-ARAPUCA units to VUV light is modeled with dedicated Geant4 simulations that include the pTP emission time $\tau_{\text{pTP}} = 1.14\,\text{ns}$, and the inner WLS bar decay time ($\tau_{\text{EJ-286}} = 1.2\,\text{ns}$) [132, 161, 163]. For the visible component, no bar response is simulated as the EJ-286 bar is transparent to the 420 nm light.

For uncoated X-ARAPUCAs, a single exponential decay to account for the EJ-280 bar ($\tau_{\text{EJ-280}} = 8.5\,\text{ns}$ [132]) is used. The absorption and emission spectra of the Eljen bars are shown in previous chapter in Figure 3.3. Their specifications can be found in [132].

Time transport effects inside the SBND X-ARAPUCAs are below 1 ns given the relatively small dimensions of the units (20 cm long).

Single electron response characterization

The template for the X-ARAPUCA SER and the estimations for the SER amplitude variation are extracted from the analysis of cryogenic tests performed at Fermilab [164]. The setup included one of the 4 SiPM boards of an X-ARAPUCA equipped with 8 Onsemi SiPMs. The board within a cryocooler was illuminated with a blue LED (see Figure 4.4).

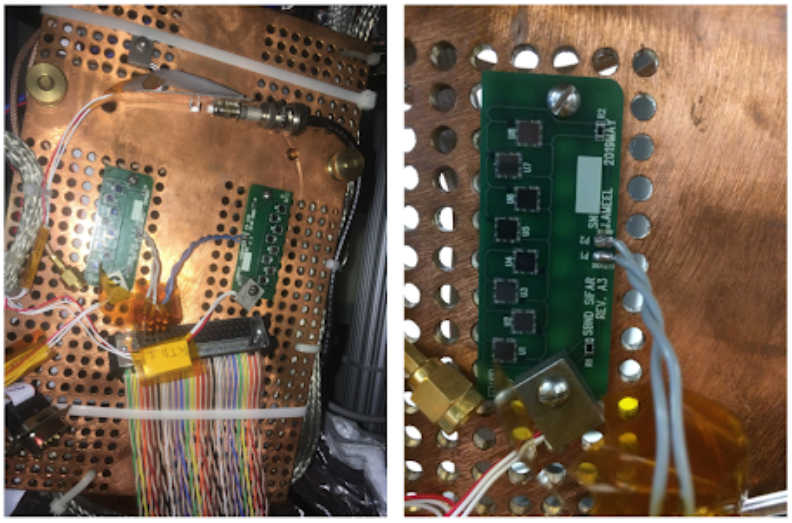

Figure 4.4: Left: cold test setup with two SiPM boards at Fermilab. In the final setup, one SiPM board was connected, and the LED (top of the frame) was re-positioned to point directly to the board. Right: Zoom-in of board-copper connection.

From the charge histograms of calibration data the first few photo-electrons were identified and their average waveforms computed (Figure 4.5-Right). The variation (σ) in the amplitude of the SER (μ) was found to be 10% assuming a Gaussian distribution (Figure 4.5-Left).

The normalized SER shape from cold data shown in Figure 4.5-Right was fitted to the 3 exponential formula:

$$y(t) = \begin{cases} e^{(t-t_{\text{peak}})/\tau_1} & t \leq t_{\text{peak}} \\ \frac{1}{1-A} e^{-(t-t_{\text{peak}})/\tau_2} - \frac{A}{1-A} e^{-(t-t_{\text{peak}})/\tau_3} & t > t_{\text{peak}} \end{cases} \tag{4.5}$$

to have a continuous parametrization. The original data was taken with a prototype based on the Mu2e electronics (80 MHz digitizer) [165] and was resampled to meet the

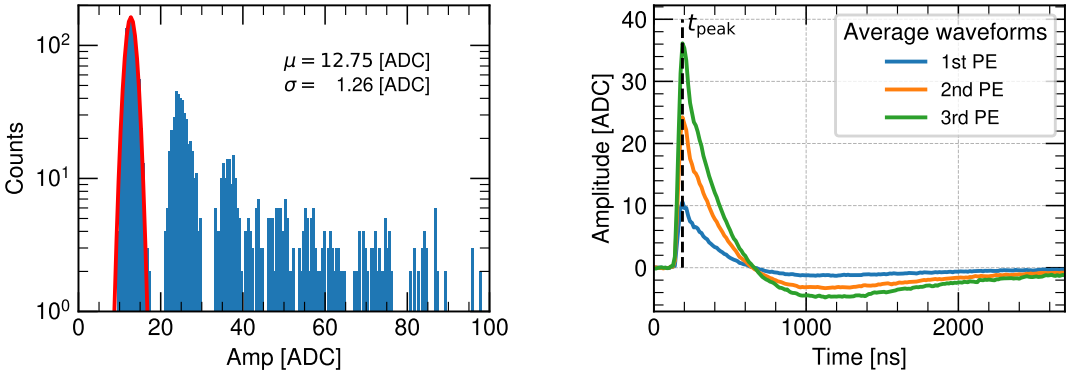

Figure 4.5: Left: Amplitude spectrum of calibration data from Fermilab test-stand and Gaussian fit to the first photo-electron. The variation in amplitude is found to be 10% of the total amplitude of the SER. Right: average waveforms from consecutive peaks. The amplitude of the undershoot was found to be approximately 18% of the total signal amplitude.

62.5 MHz of the CAEN V1740. The constant A is fixed by the bipolar condition (the total charge of the pulse must be equal to zero):

$$A = \frac{\tau_1 + \tau_2}{\tau_1 + \tau_3}. \tag{4.6}$$

Finally, the effect of 12.2 meters of CAT6 cable is included. The cable has a capacitance of 46 pF/m and an impedance of 100 Ω. Thus, a single exponential with a decay constant of $\tau = \mathrm{R} \times \mathrm{C} = 56$ ns was convolved with the best fit from Eq 4.5.

The resulting SER shape is used in SBND simulations and shown in Figure 4.3-Right. The undershooting of the signal is around 18% of the maximum amplitude with a deep trough 1 μs after the pulse start. The undershooting poses a technical difficulty to estimate the charge and arrival time. Figure 4.6 shows how PEs in the scintillation tail are 'hidden' under the main undershoot caused by the prompt light. The reconstruction workflow developed to recover the original time profile from PDS waveforms in SBND is discussed in detail in the next section.

4.2 Light reconstruction

The original photon distribution that arrives at each sensor is distorted by the PDS response and induced effects: noise, saturation... Before putting together the information from different PDS channels it is desirable to process the raw signals, recovering as much as possible the original distribution. After the processing, we identify light depositions

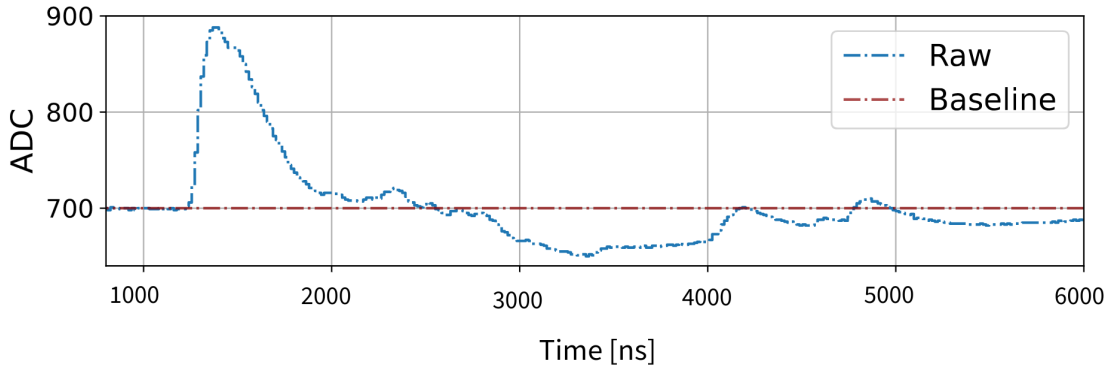

Figure 4.6: Raw simulated X-ARAPUCA waveform of scintillation light in liquid argon (corresponding to $\sim$ 35 PEs) produced by a neutrino interaction in SBND (blue) and baseline (red). The time $t = 0$ corresponds to the moment when the first proton bunch of the BNB reaches the beryllium target.

(*optical hits*) in each optical channel and cluster them forming *optical flashes* which represent an event detected by the PDS. This workflow is illustrated in Figure 4.7.

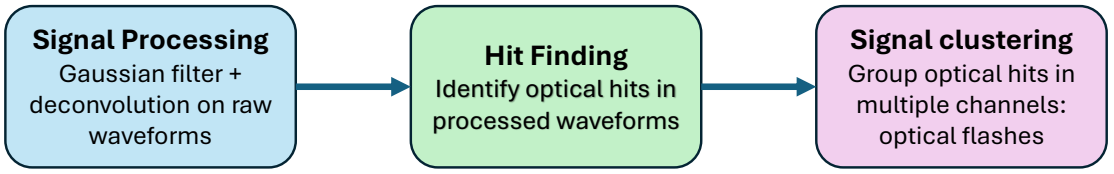

Figure 4.7: Scheme of the different stages in the light reconstruction chain, starting from the measured raw waveforms and finishing with the optical hits and optical flashes (clusters).

4.2.1 Signal processing

LArTPC experiments have long been employing signal processing techniques. Deconvolution methods for TPC signals were pioneered by ArgoNeuT and MicroBooNE collaborations [166] to estimate the underlying charge distribution from wire signals. Notably, TPC induction wire planes face similar challenges as their signals are also bipolar.

If we assume a linear response of the light sensor $r(t)$ to the original signal distribution $s(t)$, the final raw waveform is the convolution of both:

$$f(t) \equiv s(t) * r(t) \equiv \int_{-\infty}^{\infty} s(t) r(t-\tau) d\tau \tag{4.7}$$

which can be expressed in the frequency domain as:

$$f(t) = s(t) \star r(t) \xrightarrow{\mathcal{F}} F(\omega) = S(\omega) R(\omega) \tag{4.8}$$

where $\mathcal{F}$ denotes the Fourier transform. In addition, real data include background and electronics noises $n(t)$. The measured signal is then distorted: $f(t) \equiv s(t) * r(t) + n(t)$. In these cases, a filter $g(t)$ is usually applied. Following the convolution theorem, we can express the original signal distribution as:

$$s(t) = \mathcal{F}^{-1}\left\{G(\omega)\frac{F(\omega)}{R(\omega)}\right\}, \tag{4.9}$$

with $\mathcal{F}^{-1}$ the inverse Fourier transform. In numerical applications, the Fast Fourier Transform algorithm is implemented [167] to speed up computations. The choice of the filter depends on the differences between the expected signal and noise distributions. One common choice is the Wiener filter [168]:

$$G_{\text{Wiener}}(\omega) = \frac{|S(\omega)|^2|R(\omega)|^2}{|S(\omega)|^2|R(\omega)|^2 + |N(\omega)|^2} \tag{4.10}$$

which has a simple interpretation in the frequency domain: it suppresses the regions where the noise, $|N(\omega)|$, is comparable or bigger than the signal ($G(\omega) \to 0$) and do nothing otherwise $G(\omega) \to 1$. The Wiener filter minimizes the mean square error [169]. Another option is the Gaussian filter:

$$G_{\text{Gaussian}}(\omega) = \begin{cases} e^{-\frac{1}{2}\cdot\left(\frac{\omega}{\omega_c}\right)^2}, & \omega_c > 0 \\ 0, & \omega_c = 0, \end{cases} \tag{4.11}$$

effectively, a low-pass filter with a cut-off frequency ω_c. The Gaussian filter is simple and straightforward to apply once the cut-off frequency has been fixed. The Wiener filter has better signal to noise ratio but may introduce artifacts in the signal tails (see Figure 4.8-Right).

In the SBND approach, the Wiener filter for a single photo-electron waveform is first constructed, and then a Gaussian function is fitted to it (Eq 4.11). From the fit, the selected cut-off frequency ω_c is set. The result is shown in Figure 4.8-Left for the X-ARAPUCA system. The Wiener filter requires a hypothesis of the noise spectrum $N(\omega)$. In the SBND case, we assume a white Gaussian noise with an RMS of 2.6 and 0.65 ADC counts for V1730 (PMTs) and V1740 (X-ARAPUCAs) models respectively.

After the filtering, we deconvolve, subtracting the detector response from the waveforms. The process is illustrated in Figure 4.9: first, using the scintillation photon distribution arriving at each light sensor raw signals are simulated. After filtering and deconvolving

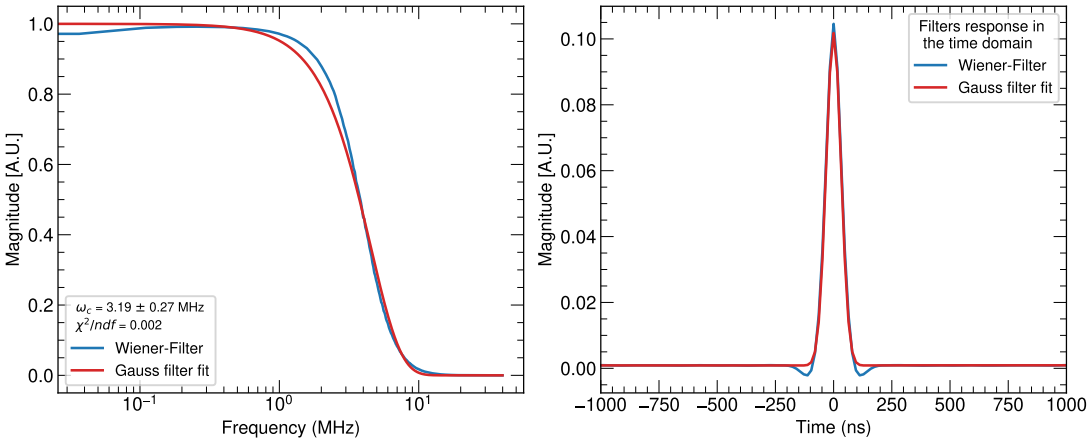

Figure 4.8: Left: Wiener filter and fitted Gaussian filter for the simulated noise distribution in SBND X-ARAPUCA channels in the frequency domain. Right: Filters response function in the time domain. The wiggles for the Wiener filter are visible in the tails.

the detector response, hit-finder algorithms described in next section are applied to identify the main peaks.

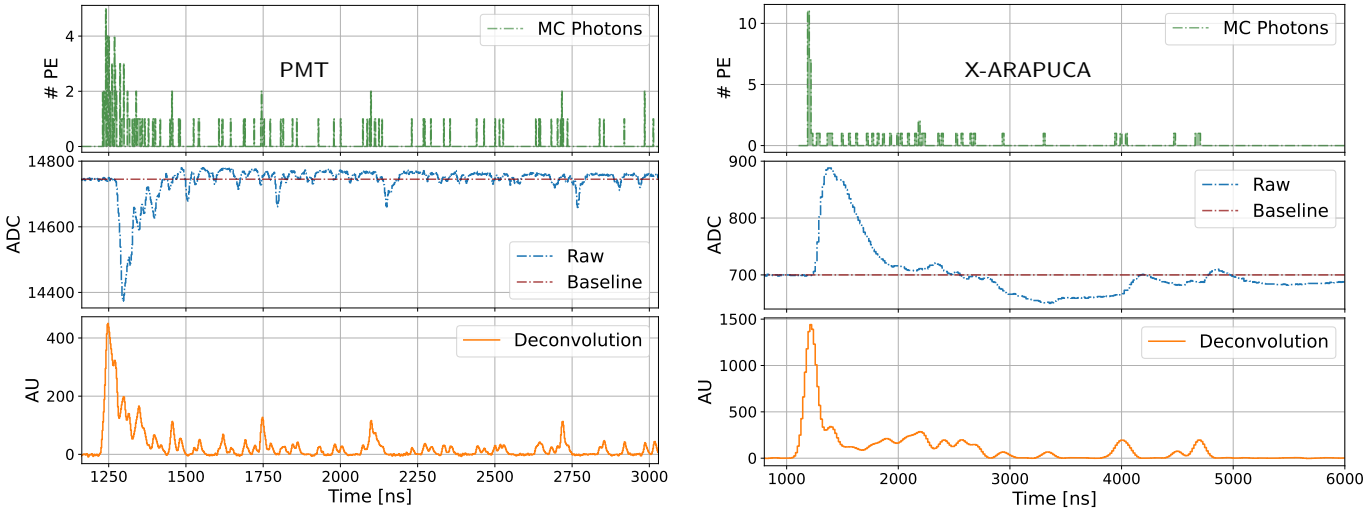

Figure 4.9: Left (Right): True simulated photon distribution at a PMT (X-ARAPUCA) channel (green). Raw PMT (X-ARAPUCA) simulated waveform (blue) and deconvolved signal (orange) with the sensor response subtracted. Notice how the signal processing removes the overshooting (undershooting) in the scintillation tail. The time $t = 0$ corresponds to the moment when the first proton bunch of the BNB reaches the beryllium target.

4.2.1.1 Hit finding

From the scintillation light signals (see Figure 4.9) single energy depositions or *optical hits* can be identified. An optical hit is described by its total charge, PDS channel and the times associated to the rise and maximum amplitude of the pulse. The baseline is first

subtracted using the initial 400 ns or 200 (25) initial ticks in the PMT (X-ARAPUCA) signal window. Then, a sliding window algorithm searches for regions above 1/4 of the total SER amplitude and 3 times the standard deviation of the baseline. The baseline must be recovered before starting a new hit. For this reason, part of the slow component is usually merged in a single optical hit. The results of the hit finding stage are shown in Figure 4.10 for a simulated X-ARAPUCA scintillation signal.

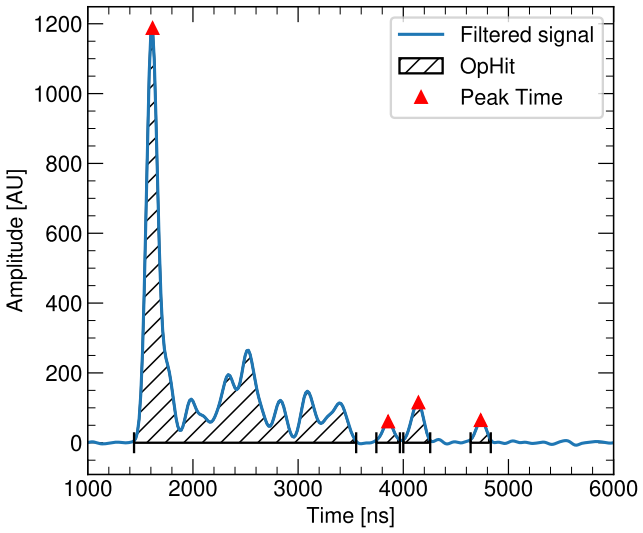

Figure 4.10: Performance of the optical hit finder algorithm on a simulated and deconvolved X-ARAPUCA waveform. Four optical hits are identified. The fast and part of the slow component are merged in the first hit.

Optical hit time

For the PMTs, the rise time of the optical hit is taken as the first bin that surpasses a 15% of the maximum amplitude in that hit. In the X-ARAPUCA case, a finer tuning is needed since the peak spreads is dozens of nanoseconds and the ADC sampling frequency is slower. Following the example of MicroBooNE [83], we can achieve timing resolutions below the sampling frequency using the information from multiple bins of the waveform with the proper fit function. For deconvolved X-ARAPUCA signals, different approaches were tested: linear, exponential and Gaussian fits to the deconvolved pulse shape and its derivative. A Gaussian fit to the first pulse peak was found to be the best method.

The difference between the photon arrival time at the PDS sensor and the reconstructed optical hit times are shown in Figure 4.11 with a global 5.9 ns time resolution. For the PMT system, using the rise time of the waveform, the overall optical hit time resolution is found to be 1.6 ns [127]. A delay bias of approximately 10 ns between the optical hit time and the true time of the first photon is also observed.

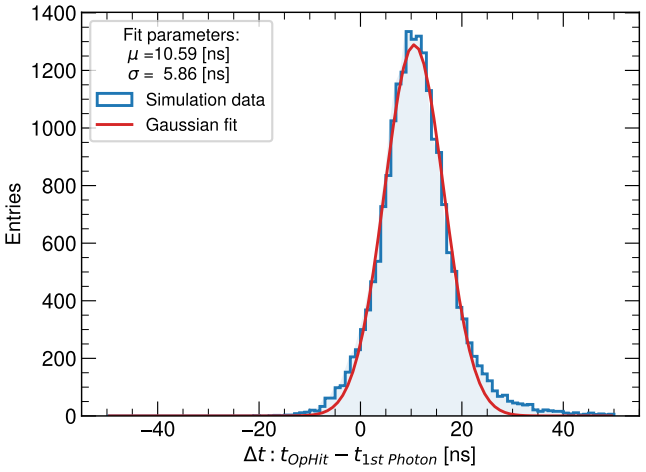

Figure 4.11: Time difference between the optical hit time and the first arriving photon in that X-ARAPUCA channel.

Better timing resolutions could be achieved through the analysis of raw waveforms as deconvolution spreads the signal to neighbor bins. However, the deconvolution approach is key to make precise calorimetry estimations, and therefore, achieving a good matching when comparing with TPC signals.

4.2.2 Signal clustering

In SBND, interactions depositing more than 30 (5) MeV are expected to leave light signals on multiple X-ARAPUCA (PMT) channels. Because light propagates in the nano-second scale, a simple approach that clusters optical hits from different channels in time coincidence is chosen. Optical flashes can be formed by hits from PDS channels in the same TPC if they surpass a fixed charge threshold. The relevant parameters are summarized in Table 4.5. To start a flash candidate, a minimum of 6 PEs by at least 4 optical channels channels is required in a short time window: 10 and 30 ns for PMTs and X-ARAPUCAs respectively. This algorithm is illustrated in Figure 4.12. The top histogram shows the time of the hits in each channel, with the color palette representing the number of PEs. A histogram with the binning equal to the time interval for coincidence (10ns) shows the accumulated number of PEs in all channels. Bins colored in blue also satisfy the multiplicity condition (more than 3 channels with hits in the time interval for coincidence). If at least a total of 20 PEs are deposited in the following 8 μs, a flash is claimed. During a flash window, no other flash in the same TPC can start (veto-window). The 8 μs window captures the late light from the scintillation tail, and prevents missing late signals of Michel electrons from muon decays.

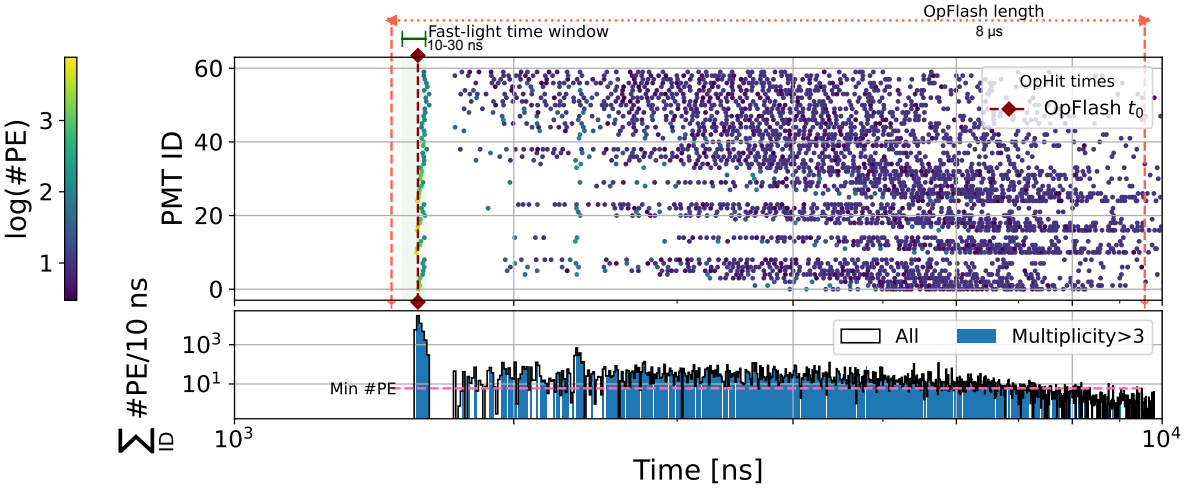

Figure 4.12: Scheme of the OpFlash finder algorithm [127]. The dotted orange (solid green) horizontal line represents the OpFlash length (fast emission) window. In solid, the histogram in blue (OpFlash X-axis projection) represents the time intervals that satisfy the multiplicity condition. The minimum number of PEs per optical channel to claim a flash is shown in pink.

Once the flash is formed, a total charge and a time is assigned to it. The charge of the flash is the sum of the charges of the hits contained in it. Extra information can be obtained by considering the charge spatial distribution in the different PDS sensors.

The time of an optical flash t_{flash} is an estimation of the interaction time t_{int}. For the PMT subsystem, a "hot spot" algorithm is used. First, a 30 ns window is opened around the interval with the largest number of PEs in the flash. Then, the flash time (t_{flash}) is taken as the average of the optical hits with the highest number of PEs that collectively contribute 50% of the total light in that interval (t_{HS}). For X-ARAPUCAs, with a lower light yield, an extra bias that depends on the drift distance was observed applying this method. For this reason, the average of the 10 first optical hits (t_{FH}) is computed. Because t_{FH} only depends on the initial hits in a flash, it usually outperforms t_{HS}. However, in some cases the scintillation tails from other particles and dark-current signals can bias the first optical hits in flashes from neutrino (approximately 1% of the total flashes). To overcome this issue, the t_{flash} is taken as t_{FH} if both estimations are sufficiently close and t_{HS} (less precise but more robust) otherwise:

$$t_{\text{XA-flash}} = \begin{cases} t_{FH}, & \text{if } |t_{FH} - t_{\text{HS}}| < 16 \text{ ns} \\ t_{\text{HS}}, & \text{else.} \end{cases} \tag{4.12}$$

In the next section the charge, spatial and timing reconstruction performance of the reconstructed flashes are evaluated using simulated BNB interactions with cosmic ray backgrounds.

Parameter	Value
Flash candidate minimum number of PEs	6 PE
Minimum number of optical channels in coincidence	4 ch
Time interval for coincidence (PMT / X-ARAPUCA)	10 ns / 30 ns
Flash total PEs threshold	20 PE
OpFlash length	8 µs
Time window for t_0	30 ns
Veto-window	8 µs

Table 4.5: List of OpFlash parameters used in the SBND reconstruction workflow. All the parameters but one, the time interval of the starting flash window, are shared by PMTs and X-ARAPUCAs.

4.3 Light reconstruction efficiency

To evaluate the performance of the workflow described in the previous section a sample of 30,000 simulated BNB neutrino events with cosmic rays overlaid in SBND was produced. For each neutrino event, an average of 10–15 cosmic muons cross the TPC leaving light signals during one SBND drift window (1.3 ms). Only events with ≥5 MeV of deposited energy in the detector are considered. On average, less than 1 (2) X-ARAPUCA (PMT) waveform is saturated per event (see Figure 4.13-Left). The saturated signals are removed from the analysis as it affects the pulse shape and hence the deconvolution result (Figure 4.13-Right).

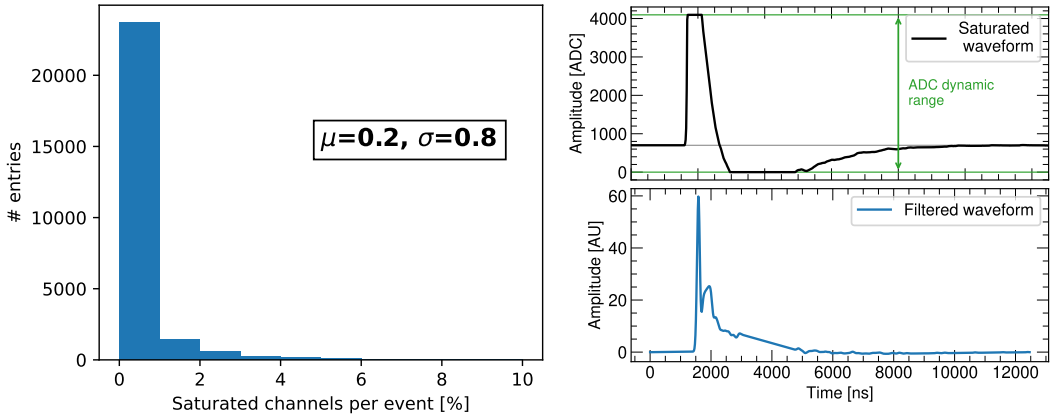

Figure 4.13: Left: Saturated X-ARAPUCA channel distribution for the simulated BNB and cosmic sample. Right: saturated waveform before (black) and after (blue) signal processing. The shape of the filtered waveform is visibly distorted.

An interaction that occurred at t_{int} is said to be *reconstructed* if there is a nearby flash that satisfies: $|t_{\text{int}} - t_{\text{flash}}| < 100$ ns. Events with few MeVs or energy depositions away from PDS sensors might not trigger enough channels to produce a flash. Figure 4.14 shows this energy (Left) and drift (Right) dependence of the flash reconstruction efficiency. An overall reconstruction efficiency of 92.2% and 95.8% for the X-ARAPUCA

and PMT system respectively is achieved. The truth drift variable $\langle d_{drift} \rangle^{MC}$ represents the average distance of the energy depositions along the X drift coordinate. For example, depositions at the center of the detector ($X = 0$) correspond to a distance $\langle d_{drift} \rangle^{MC} =$ 200 cm.

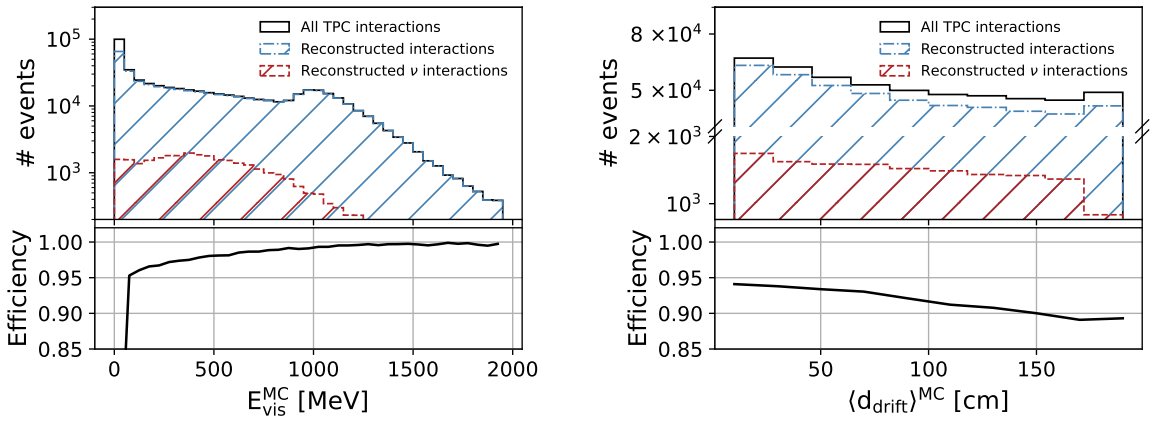

Figure 4.14: Reconstruction efficiency of X-ARAPUCA optical flashes for the sample of BNB neutrino interactions with cosmic rays overlaid as a function of the deposited energy (Left) and averaged drift distance (Right). The distribution is a convolution of the neutrino (red histogram) and cosmic spectra with the detector acceptance. The bump around 1000 MeV is due to crossing-muons in the detector volume.

4.3.1 Calorimetry resolution

For the matched flashes, the number of reconstructed photo-electrons from the clustered optical hits, PE^{reco}, and the total number of arriving photons at each sensor multiplied by the sensor PDE, PE^{MC}, are compared. For the X-ARAPUCA case, the crosstalk effect is also corrected. A bias below 1% and a resolution better than 6% are achieved for X-ARAPUCA channels with more than 250 PEs, as shown in Figure 4.15-Right. In the PMTs case, with higher collection efficiencies, saturation and non-linearity effects appear in channels with more than 3000 PEs. A deficit of up to 10% in the collected charged is observed for PMT channels with more than 8000 collected PEs (Figure 4.15-Left).

For neutrino events, each flash deposits an average of 36 PEs in X-ARAPUCA channels with light signals (see Figure 4.16). However, the PE^{reco} distribution peaks around 5–6 PEs with a long tail and a few channels with more than 1000 PE. Less than 1% of the X-ARAPUCA channels have more than 340 PEs per optical flash. This further confirms that the contribution from saturated signals is negligible since at least 500 simultaneous PEs are required to fill the dynamic range of the ADC.

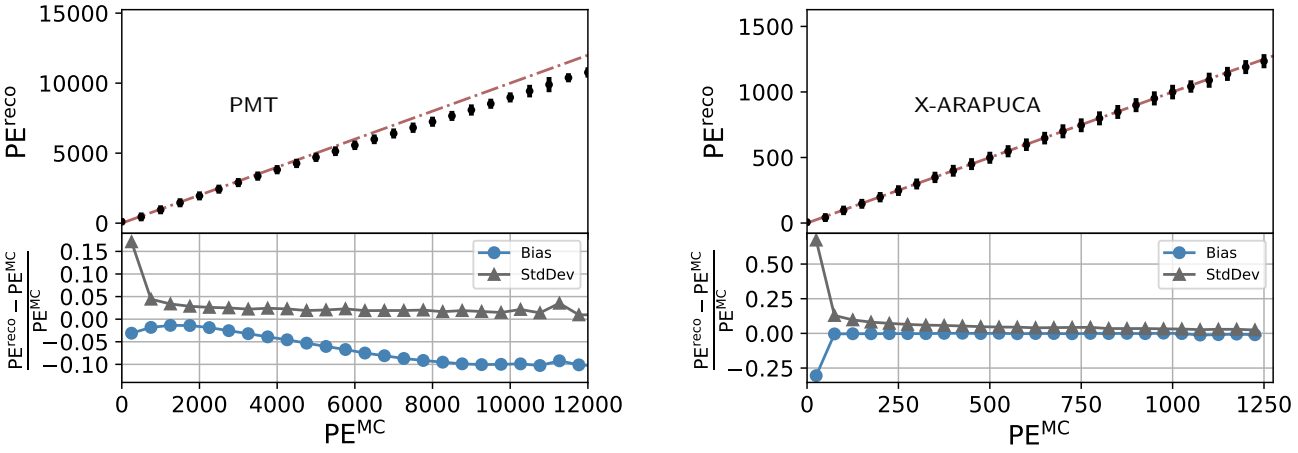

Figure 4.15: Left (Right): Reconstructed number of PEs from all OpHits within an OpFlash, and fractional bias and resolution (≡ StdDev), as a function of the total number of simulated PEs within one PMT (X-ARAPUCA) channel.

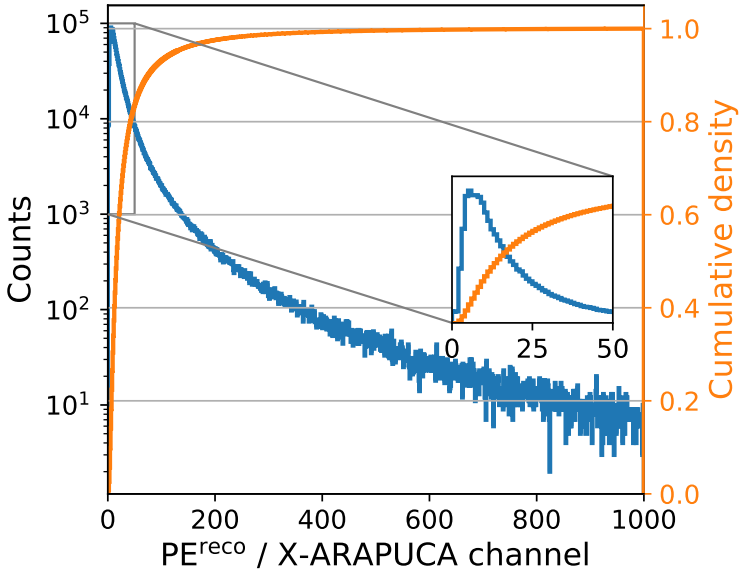

Figure 4.16: Distribution of the number of PEs per X-ARAPUCA channel within a neutrino flash and zoom to the low PEs region: a mean of 36 PEs per channel and flash is expected. The distribution has a long tail, the most probable value (mode) is 6 PEs per channel. Some events deposit up to 1,000 PEs in a single channel.

4.3.2 Detected light yield

Each neutrino flash contains a total average of 3500 PEs in all X-ARAPUCA channels. The total light yield in the X-ARAPUCA system is expected to be 7.7 PE/MeV. However, the amount of collected light strongly depends on the location of the energy depositions. This is shown in Figure 4.17: the number of detected PEs decreases in regions

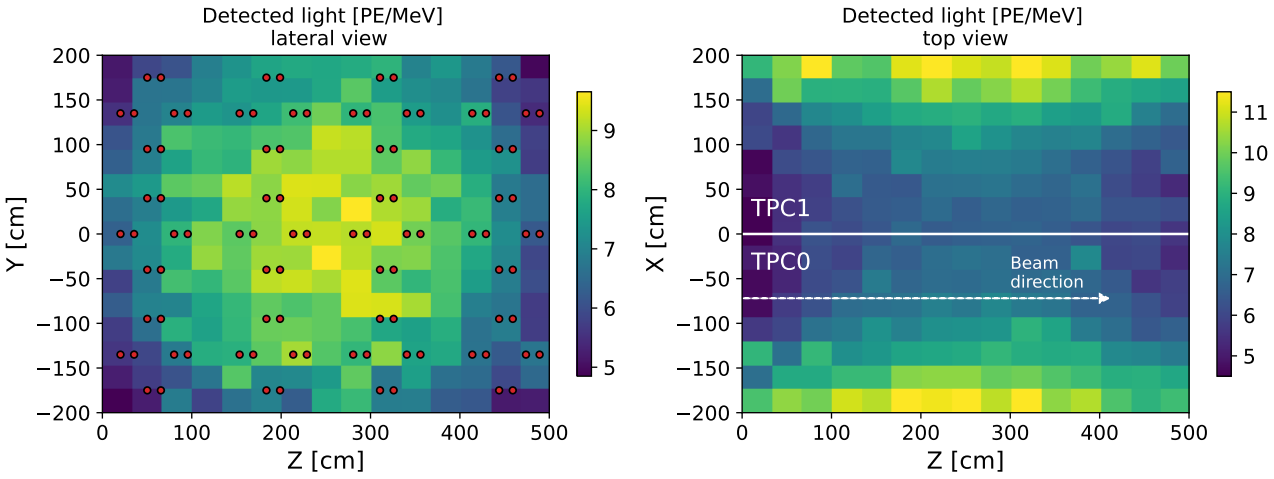

Figure 4.17: X-ARAPUCA system detected light yield maps for the lateral–PDS plane (Left) and top (Right) views of the detector. The location of the X-ARAPUCA sensors is shown with red dots (Left). The beam direction is shown with a dashed white line (Right), the PDS planes are located behind the wire planes ($X = \pm 200$ cm).

close to the borders and corners of the active volume (Figure 4.17, Left), and also as we move away from the PDS sensors in the drift direction, X (Figure 4.17, Right). The TPB coated foils convert VUV photons to visible wavelengths, increasing by more than a factor of two the light yield in the middle of the detector (X=0). Figure 4.18 shows the light yield in the drift direction (X) for the coated and uncoated X-ARAPUCA units. The contribution of the uncoated devices represents more than 20% of the total collected light for drift distances bigger than 75 cm, and is the main component in the 175–200 cm range.

In the PMT case the contribution from the visible light is more significant, as all coated and uncoated units are sensible to the visible photons. The detected light yield for the PMT system varies from 170 PEs/MeV near the anode planes to 100 PEs/MeV at the center of the detector, where more than 70% of the detected light comes from the visible component [127].

4.3.3 Position resolution

Z and Y coordinates

Thanks to the high density of light sensors, the beam (Z) and vertical (Y) directions can also be estimated with light information. To reduce border effects, only the most illuminated channels are used. The Z or Y coordinate is taken as the weighted mean of

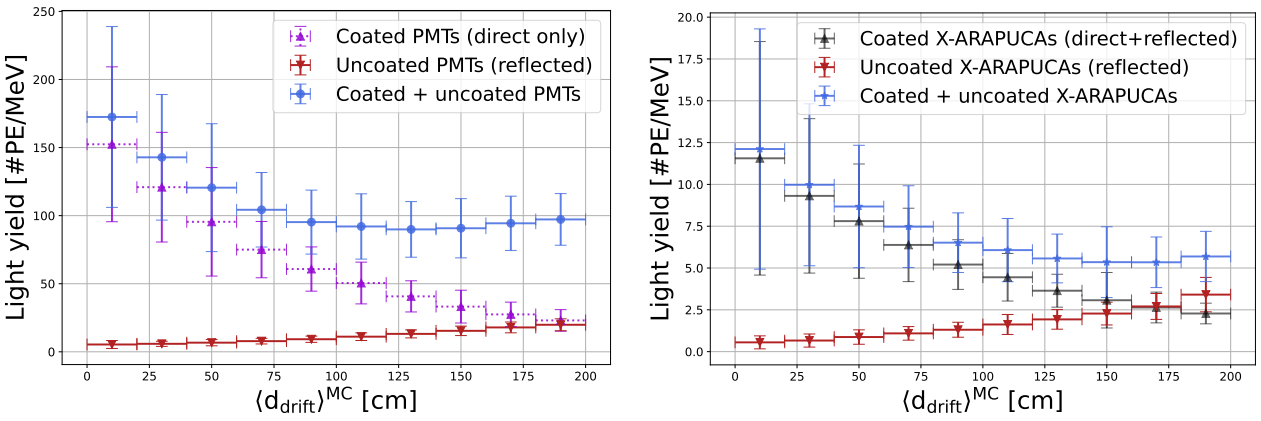

Figure 4.18: Left (Right): Total PMT (X-ARAPUCA) light yield as a function of the averaged drift distance in blue. The contribution from uncoated units is shown in red.

the 15 channels with the highest number of PEs, each channel weighted with the number of measured PEs. The results of this procedure are shown in Figure 4.19 for the Z (Left) and Y (Right) coordinates. An almost flat resolution is achieved. In both coordinates, the bias grows for energy depositions closer to the detector sides.

The PMT system uses a similar algorithm, only keeping sensors with at least 80% of the channel with the highest number of PEs for each row or column. The observed bias shows a similar trend with deviations from zero appearing for distances closer than 100 cm to the detector border [127].

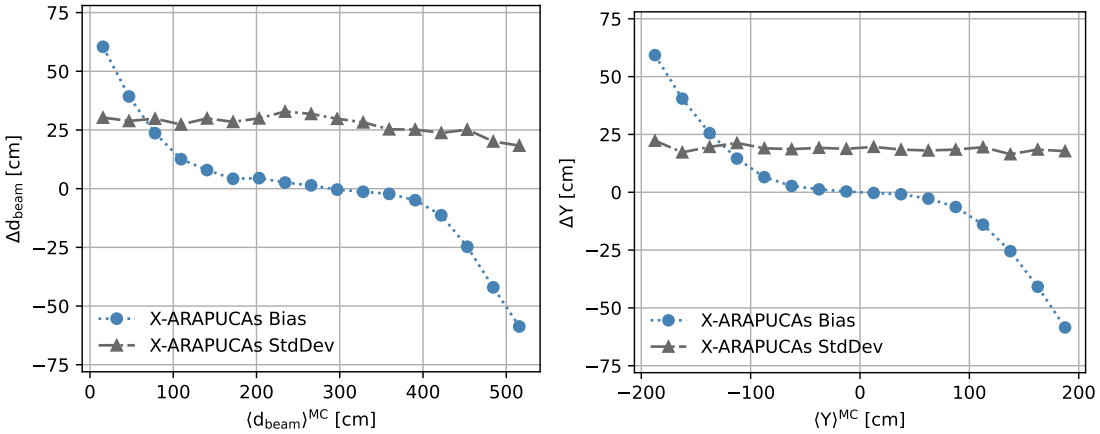

Figure 4.19: Resolution (gray triangles) and bias (blue circles) of the X-ARAPUCA system in the Z (Left) and Y (Right) directions for simulated BNB neutrino interactions.

Drift coordinate

The decrease and increase of the VUV and visible components, respectively, with the drift distance allows us to estimate the drift coordinate using only light information. The $\eta_{\text{X-ARAPUCA}}$ ratio is defined as the fraction of visible light to total light collected:

$$\eta_{\text{X-ARAPUCA}} \equiv \frac{\sum \text{PE}_{\text{uncoated}}}{\sum \text{PE}_{\text{coated}} + \sum \text{PE}_{\text{uncoated}}}. \tag{4.13}$$

The visible contribution varies from 5% close to the wire planes (drift equal to 0) to more than 60% of the total light yield at the middle of the detector. The calibration curve for the $\eta_{\text{X-ARAPUCA}}$ parameter was obtained from a simulated sample of cosmic muon tracks contained in narrow (10 cm) slices along the drift (see Figure 4.20). These muon tracks in SBND data can be selected using the CRT system, which can trigger on these topologies with a resolution under 2 cm.

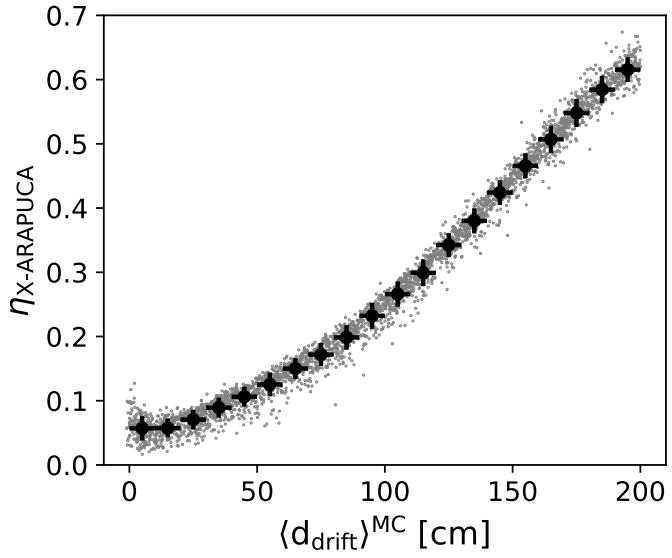

Figure 4.20: Calibration curve (black markers) for the $\eta_{\text{X-ARAPUCA}}$ parameter. The vertical lines represent the dispersion in the vertical axis. A custom sample of cosmic muons parallel to the beam direction was used to produce the curve (grey points).

The drift coordinate is then computed as it follows:

$$\text{d}_{\text{drift}}\,(\text{cm}) = \begin{cases} 10, & \eta < 0.05 \\ \text{d}_{\text{drift}}(\eta), & 0.05 \leq \eta \leq 0.61 \\ 190, & \eta > 0.61 \end{cases} \tag{4.14}$$

where $\text{d}_{\text{drift}}(\eta)$ is the linear interpolated value obtained from the curve of Figure 4.20. Following formula 4.14, the drift coordinate was estimated for the complete BNB neutrino dataset (Figure 4.21). An overall resolution of 20.4 cm with a -4.6 cm bias was obtained. The resolution is mainly limited by the light yield, improving up to 16 cm for events with more than 500 MeVs of deposited energy. The bias however is highly dependent on border effects, for example, when the mean deposited energy is close to the light sensors (drift $<$ 50 cm) or far away from them (drift $>$ 150 cm). The PMT

system achieves resolutions in the drift distance in the 10–15 cm range, and a slightly smaller bias [127].

The overall resolutions and biases for the three spatial directions are summarized in Table 4.6 for the X-ARAPUCA flashes while similar numbers were obtained for the PMT optical flashes [127]. For all three coordinates, resolutions below 30 cm were obtained. The bias is affected by border effects while the resolution in the drift direction is mainly limited by the total light yield of the event.

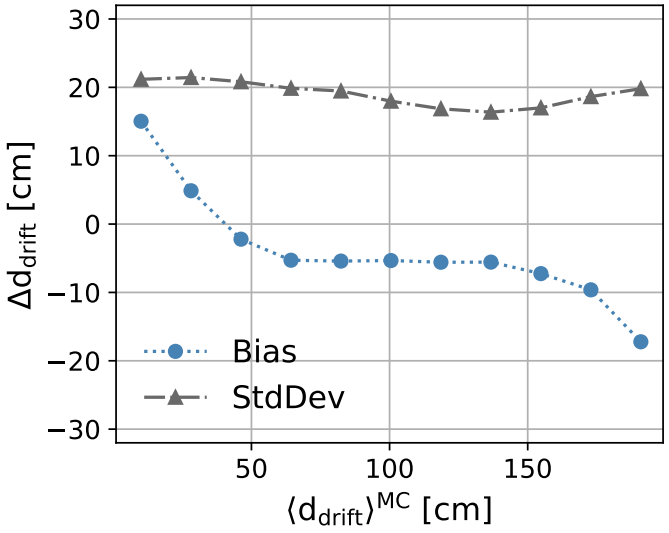

Figure 4.21: Bias (blue circles) and resolution (gray triangles) of the drift distance estimation using the $\eta_{\text{X-ARAPUCA}}$ parameter.

Coordinate	Bias [cm]	Resolution [cm]
X (drift)	-4.6	20.4
Z (beam)	17.7	27.3
Y (vertical)	18.7	18.9

Table 4.6: Overall geometric resolution for the three space coordinates using X-ARAPUCA light flashes.

4.3.4 Timing resolution

The flash time is computed following Equation 4.12. The difference between the truth and reconstructed interaction times ($\Delta_{t_0} = t_{\text{flash}} - t_{\text{int}}$) is shown in Figure 4.22 as a function of the drift distance. Three different regions can be identified:

a) The VUV dominated region: where direct scintillation light arrives first at PDS sensors. The time delay increases approximately linearly with the drift distance.

b) The intermediate region: near the turning point. In this region the direct VUV and the reflected visible light components arrive at the PDS at similar times.

c) The visible dominated region: where first arriving photons come from the visible component. In this region the delay decreases as the distance of VUV photons to the TPB-coated reflective foils in the cathode shortens.

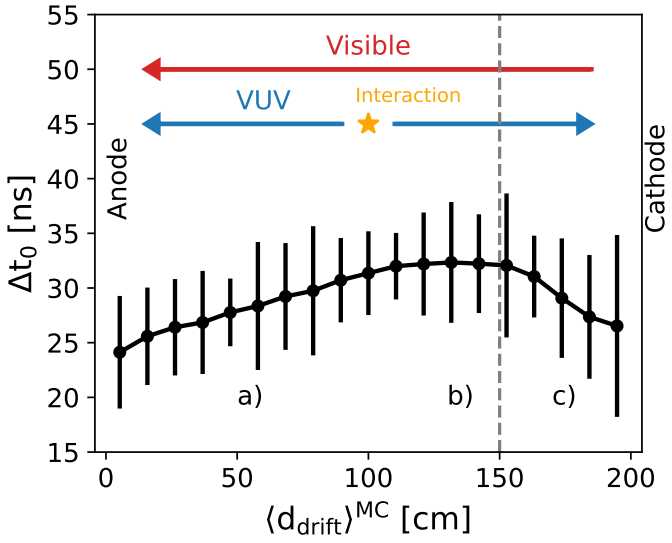

Figure 4.22: Time difference between the reconstructed optical flash time and the true interaction time, as a function of the drift distance. The error bars represent the standard deviation in each drift bin. The scheme on top represents the two light sources in SBND: the VUV light (blue) produced by an interaction (orange star) is either collected at the PDS (behind the anode planes) or re-emitted in the cathode to visible wavelengths (red). The gray line marks the turning point where visible light starts arriving prior to direct VUV light.

The produced optical hits and subsequent flashes are affected by different timing delays. First, to reconstruct the original interaction time, the time of flight of the photons from the emission point to the PDS sensors (ToF_γ) must be subtracted (see Figure 4.23). The first photons arriving at SBND photosensors will travel almost perpendicularly to the PDS plane. The SBND coordinate system (see Figure 2.22) has the origin in the cathode plane ($X = 0$). The PDS sensors are at a drift distance $X_{\mathrm{PDS}} = 213$ cm from the cathode plane. Defining the turning point as:

$$\mathrm{X_T} \equiv \frac{\mathrm{X_{PDS}}}{2}\left(1 - \frac{\mathrm{V^{VUV}_{group}}}{\mathrm{V^{Vis}_{group}}}\right), \tag{4.15}$$

with $\mathrm{V^{VUV}_{group}} = 13.5$ nm/s ,$\mathrm{V^{Vis}_{group}} = 23.9$ nm/s. We can then estimate the corrected optical flash subtracting the photons time of flight (ToF_γ) time as:

$$\mathrm{T_{OpFlash}} \rightarrow \begin{cases} \mathrm{T_{OpFlash}} - \dfrac{\mathrm{X_{PDS}} - \langle \mathrm{X_{reco}} \rangle}{\mathrm{V^{VUV}_{group}}} & \text{if } \langle \mathrm{X_{reco}} \rangle > \mathrm{X_T}, \\ \mathrm{T_{OpFlash}} - \left(\dfrac{\langle \mathrm{X_{reco}} \rangle}{\mathrm{V^{VUV}_{group}}} + \dfrac{\mathrm{X_{PDS}}}{\mathrm{V^{Vis}_{group}}} \right) & \text{if } \langle \mathrm{X_{reco}} \rangle < \mathrm{X_T}. \end{cases} \tag{4.16}$$

This formula requires an estimation of the drift (X_{reco}) coordinate, obtained using the ratio of VUV and visible light procedure described in detail in the previous section.

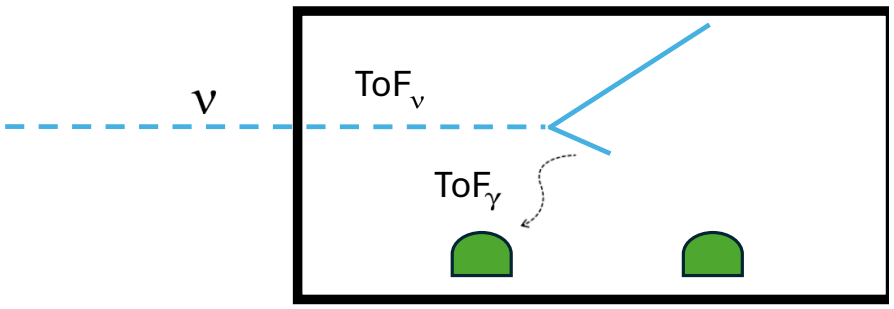

Figure 4.23: Cartoon depicting the time of flight of an interacting neutrino (dashed blue), and the produced photons (dashed black) to the PDS sensors (green).

By subtracting the photon time of flight from the initial flash time, a global bias shift of 25 ns is obtained (Figure 4.24-Left). The resolution increases with the energy, achieving an overall resolution of 6.04 ns including all events with more than 5 MeV of deposited energy (solid lines in Figure 4.24). After selecting events with at least 200 MeV of deposited energy and a single flash during the BNB trigger window, the overall resolution is 4.29 ns (dashed lines in Figure 4.24).

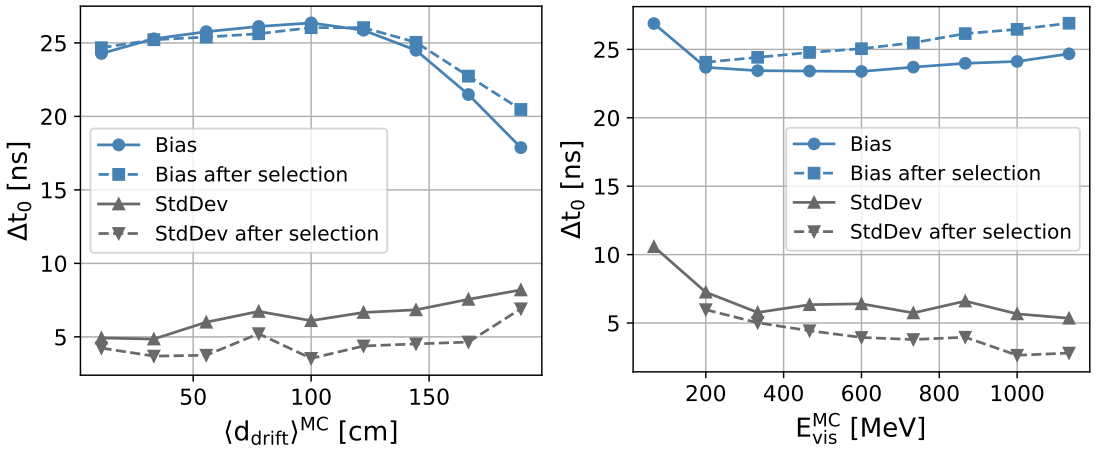

Figure 4.24: Time bias (blue) and resolution (gray) of the X-ARAPUCA system as a function of the drift distance (Left) and deposited energy (Right) after correcting for the photon time of flight. The dashed lines correspond to the selection used to resolve the BNB bucket structure: only events with more than 200 MeVs of deposited energy and a single flash during the BNB window are selected.

Resolving the BNB bunch structure

Precise reconstruction of interactions times is a powerful tool to mitigate the backgrounds from cosmic rays and to look for decays from massive BSM particles arriving later than Standard Model neutrinos [83]. To recover the original bunch structure of the BNB (detailed in chapter 2), the propagation of the neutrinos inside the detector

must be accounted for. This is because 5 meters in the beam Z direction represent a 17 ns difference between neutrinos interacting at upstream (Z=0) and downstream (Z=500 cm) walls. The space between BNB bunches (∼19 ns) is comparable. This is depicted in Figure 4.25 where the time of flight of the first five neutrino bunches is represented as a function of the beam distance (Z).

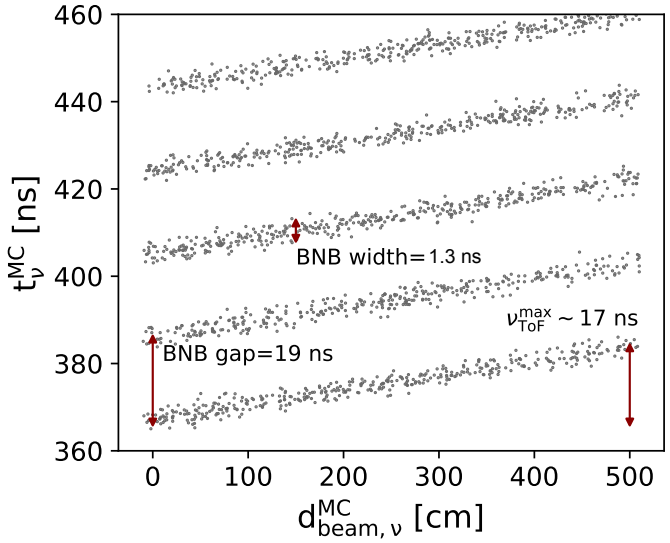

Figure 4.25: BNB neutrinos time of flight from the creation to the interaction inside SBND as a function of the beam (Z) direction for the first five bunches.

The width of the bunches is smeared by the decay time of the parent meson. The effect depends on the energy of the neutrino and is below 2 ns. Neutrinos take a minimum time of 367 ns to travel from the BNB beryllium target to the SBND upstream wall. Because of the energy dependence of the time resolution, only neutrino events with more than 200 MeV of deposited energy and a single flash during the BNB window have been considered.

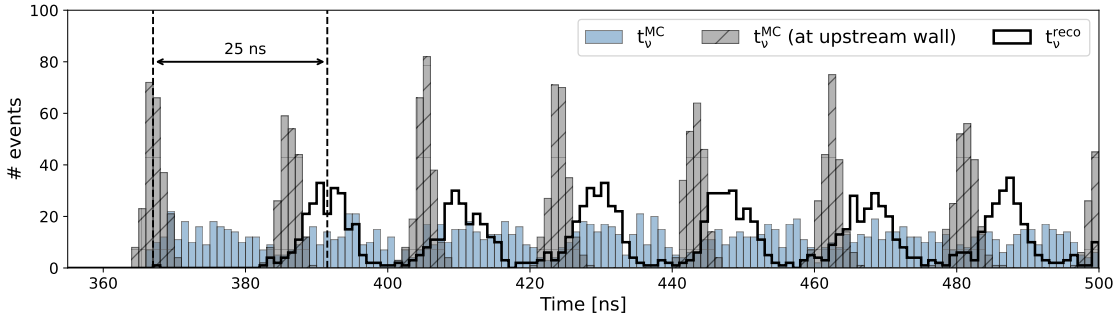

Figure 4.26: True neutrino arrival time at SBND upstream wall (gray) and interaction time in the detector volume (blue) using X-ARAPUCA optical flashes. The reconstructed distribution after correcting for the neutrino and photon time of flight is shown in black. There is an overall delay shift of approximately 25 ns in the reconstructed time estimation.

The reconstructed structure after correcting for the propagation of the neutrino (using only light information) inside the detector is shown in Figure 4.26. The truth neutrino times at the upstream wall conserve the bunch structure while the interaction times inside the detector (blue) are smeared by the time of flight of each neutrino inside the detector volume. An overall shift to the right is observed in the reconstructed distribution (black), which corresponds to the 25 ns delay from Figure 4.24.

An overall resolution can be estimated by subtracting the bunch time ($t^{MC}_{BNB\ Bunch}$) to the reconstructed time t^{reco}_{ν} (the flash time after subtracting the neutrino and photon ToF), and merging the 81 bunches into a single peak. A Gaussian fit is then applied to the resulting distribution (Figure 4.27) finding an average 24.48 ns bias and a 3.05 ns resolution. Subtracting the intrinsic width of the BNB proton bunches $\langle\sigma_{BNB}\rangle = 1.31$ ns [82], an intrinsic 2.76 $\pm$ 0.04 ns resolution is found in this analysis.

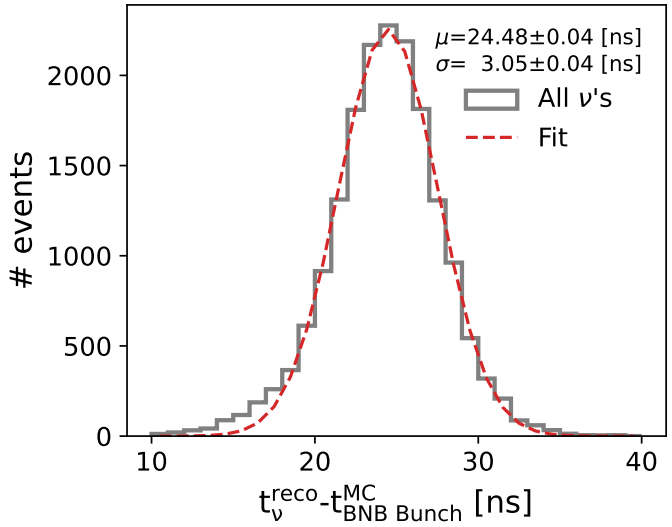

Figure 4.27: Neutrino interaction times of the BNB bunches merged into a single peak after correcting for both the photon propagation and the time of flight of the neutrinos inside the detector.

These results demonstrate the capability of the X-ARAPUCA system to resolve the BNB bucket structure. While the algorithms presented here are simple and robust, more refined methods can enhance the final performance. A simple 1D convolutional neural network model trained with the 20 nearest time samples to the first waveform peak showed a preliminary improvement on the optical hit timing resolution up to 4 ns. The flash time determination can be enhanced by using the PDS sensors position explicitly.

Applying the same corrections to the photon propagation time (drift direction) and the propagation of the neutrino inside SBND (beam direction) to reconstructed PMT flashes yields an overall resolution of 2.34 $\pm$ 0.03 ns and an intrinsic resolution of 2 ns after subtracting the width of the BNB proton bunches [127].

In the following sections the timing of the PMT flashes will be used to discriminate the delayed heavy neutral leptons from the SM neutrino bunches. Future work will look into including the X-ARAPUCAs into the selection given the performance achieved.

Chapter 5

Heavy neutral lepton signal and background simulation

Thanks to the proximity of the SBND detector to the BNB origin, many BSM models coupled to SM neutrinos or mesons can be probed at SBND. In particular, long-lived massive particles produced by the beam could appear at the detector slightly delayed with respect to neutrino beam events. In this chapter, the production and decay of heavy neutral leptons (HNLs) at SBND is discussed, as well as the background simulation from the SM neutrinos. Sections 5.1 and 5.2 review the signal and background simulation. In the following chapters (6 and 7), a sensitivity study of muon-coupled HNLs in the decay channel $N \to e^+e^-\nu$ and the low mass region [30–150] MeV is performed using Monte Carlo simulated data and SBND standard reconstruction tools [1]. A description of the MC samples generated for this analysis described in the following chapters is given in Appendix B.

5.1 Signal simulation

Figure 5.1: Feynman diagram of the SM ν_μ (Left) and HNL (Right) production from positive kaon decay.

[1]The SBNDcode version used for generating and analyzing all the events for this search was $v09\_82\_02\_01$. This version can be found in the SBN Software GitHub organization, inside the SBNDcode repository [170].

In SBND, HNLs can be produced from the decay of pions, kaons and muons (see Figure 5.1) from the BNB. The main features of the BNB G4 simulation were described in Section 2.2.

To simulate BSM signals, the MeVPrtl tool has been developed. This dedicated generator provides both ICARUS and SBND an interface to produce samples of various BSM models: Higgs portal scalars, axion-like particles... The following pages are focused on the implementation of HNLs generated from the BNB. The generator follows the steps sketched in Figure 5.2:

1. First the BNB flux files are read. For the HNL production in SBND, only kaons producing neutrinos are considered as they are the leading contribution for most of the available phase space. For muon-coupled HNLs, the production from pion 2-body decays becomes only relevant for HNL masses below 30 MeV.

2. Then, the mesons decay into the particular BSM particle of choice. Only meson two-body decays are simulated. A weight associated with the particular width of the decay is computed per event.

3. The BSM particles are propagated and the ones that reach the detector surface are kept. This process is usually referred as ray-tracing. An associated weight (w_{Ray}) that estimates the probability of that direction in the parent meson rest frame is computed:

$$w_{Ray} = \frac{1}{4\pi} \oiint_{\text{Detector}} d\Omega \,, \tag{5.1}$$

   with Ω the solid angle spanned by the detector in the rest frame of the parent.

4. Finally, the decay inside the detector volume is simulated given the branching ratios of each BSM model. A list of truth particles with the positions and momenta of the daughters from the BSM particle decay is computed and saved into the art file.

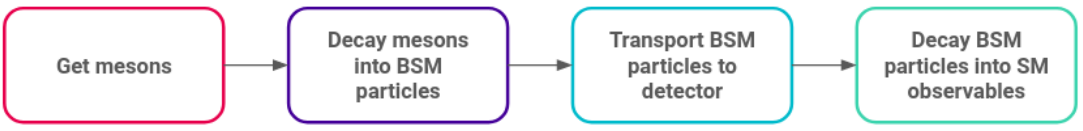

Figure 5.2: Workflow diagram of the MeVPrtl generator.

After the MeVPrtl stage, the daughter particles from the BSM decay follow the standard simulation and reconstruction chain described in the previous chapter: G4 simulations

compute the energy depositions and subsequent interactions of the initial particles, estimating the number of ionization electrons and scintillation photons produced. After the propagation inside the detector, the sensor readout is simulated, and the output signals are analyzed following the same reconstruction chain as SM neutrino interactions.

5.1.1 HNL production

The branching ratio of the parent meson decaying into an HNL can be expressed in terms of the corresponding SM neutrino branching ratio [171]:

$$Br(m^+ \to l_\alpha^+ N) = Br(m^+ \to l_\alpha^+ \nu_\alpha) \left(\frac{|U_{\alpha 4}|^2}{1 - |U_{\alpha 4}|^2} \right) \rho_N \left(\frac{m_{l_\alpha}^2}{m_{m^+}^2}, \frac{m_N^2}{m_{m^+}^2} \right), \tag{5.2}$$

with $Br(m^+ \to l_\alpha^+ \nu_\alpha)$ the branching ratio of the charged meson m^+ that decays into a lepton l_α^+ and an SM neutrino ν_α, m_{m^+} is the mass of the charged meson, m_{l_α} is the mass of the lepton and m_N is the mass of the HNL. The branching ratios and lifetimes of the parent mesons considered in the BNB simulation are summarized in Table 5.1.

Particle	Lifetime (ns)	Decay mode	Branching ratio (%)
π^+	26.03	$\mu^+ + \nu_\mu$	99.9877
		$e^+ + \nu_e$	0.0123
K^+	12.385	$\mu^+ + \nu_\mu$	63.44
		$\pi^0 + e^+ + \nu_e$	4.98
		$\pi^0 + \mu^+ + \nu_\mu$	3.32
K_L^0	51.6	$\pi^- + e^+ + \nu_e$	20.333
		$\pi^+ + e^- + \bar{\nu}_e$	20.197
		$\pi^- + \mu^+ + \nu_\mu$	13.551
		$\pi^+ + \mu^- + \bar{\nu}_\mu$	13.469
μ^+	2197.03	$e^+ + \nu_e + \bar{\nu}_\mu$	100.0

Table 5.1: Particle lifetimes and branching ratios of neutrino-producing decays in the BNB simulation [81].

The kinematic factor $\rho(x, y)$ takes into account the available phase space:

$$\rho_N(x, y) = \frac{(x + y - (x - y)^2)\sqrt{1 + x^2 + y^2 - 2(x + y + xy)}}{x(1 - x)^2}, \tag{5.3}$$

where x, y correspond to $m_{l_\alpha}^2/m_{m^+}^2$ and $m_N^2/m_{m^+}^2$ respectively in Equation 5.2. Figure 5.3-Left shows the kinematic factor for the production channels available at SBND: $\pi^+ \to Ne^+$, $\pi^+ \to N\mu^+$, $K^+ \to Ne^+$ and $K^+ \to N\mu^+$.

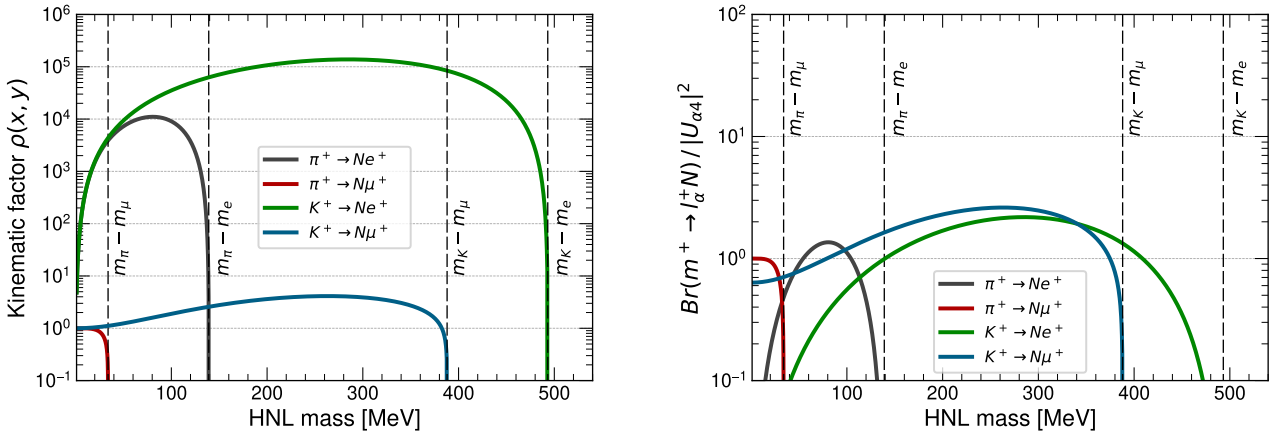

Figure 5.3: Left: kinematic ρ factor as a function of the HNL mass for the relevant production channels from meson decays available at SBND. Right: branching ratios (divided by the squared of the HNL coupling) of the HNL production as a function of HNL mass for the relevant production channels. The black dashed lines represent the kinematic limits for each channel.

The kinematic factor is bigger for electrons than muons neutrinos because their mass is two orders of magnitude smaller than the muon and pion masses. The positive kaon and pion two-body decays into a positron suffer from helicity suppression as they are lighter than the muons. For this reason it is harder to produce a left handed positron that matches the helicity of the neutrino (the original kaon/pion has a total spin of 0) [12]:

$$\begin{aligned} Br(K^+ \to e^+ + \nu_e) &= 1.58 \times 10^{-5} \\ Br(\pi^+ \to e^+ + \nu_e) &= 1.23 \times 10^{-4}. \end{aligned} \tag{5.4}$$

Because HNLs are heavier than electrons, their production from meson two-body decays experiences a helicity unsuppression. This is shown in Figure 5.3-Right where the kinematic factors are multiplied by the neutrino branching ratios. This corresponds to the HNL production branching ratio divided by the coupling $|U_{\alpha 4}|^2$ (see Equation 5.2).

HNLs from kaon decays have a larger mass range (up to 490 MeV) as more energy is available. In the following studies, it is assumed that the HNL is coupled only to the muon neutrino from the SM ($|U_{e4}|^2 = |U_{\tau 4}|^2 = 0$, $|U_{\mu 4}|^2 \neq 0$).

5.1.2 HNL propagation

The BNB target is 110 meters away from the upstream wall of SBND. HNLs arriving at SBND travel from the parent meson decay point to the SBND upstream wall. The beam is very collimated and the acceptance angle is $\sim 2^\circ$ with respect to the beam direction.

Because of the heavier mass, HNLs will appear slightly delayed with respect to the SM neutrinos. The delay increases with the HNL mass as less kinematic energy is available. The arrival time distribution is the combination of the various effects taking place. First, the 81 proton bunches of each BNB spill have an intrinsic width of 1.3 ns each. Then, kaons propagate and decay in the decay region after the beryllium target. Lastly, the neutrinos and HNLs propagate to the detector location. A neutrino produced in the BNB target takes ~ 367 ns to reach the SBND upstream wall.

MicroBooNE, further away from the BNB target ($L = 470$ m), has exploited this delay implementing a specific trigger window after the beam window [79] to select HNLs candidates in a *background free* region. SBND, however, is closer to the BNB target. Because of this, the delay of HNL is typically a shift of a few nanoseconds with respect to the SM neutrinos. On the other hand, this shift is enough to perform searches between the BNB bunches in the beam trigger window if timing resolutions below 3 ns are achieved, which SBND is capable of (see Chapter 4). The velocity decreases for heavier HNL masses, increasing the delay. This is represented in Figure 5.4 for different HNL masses, and the SM neutrinos from the BNB at SBND.

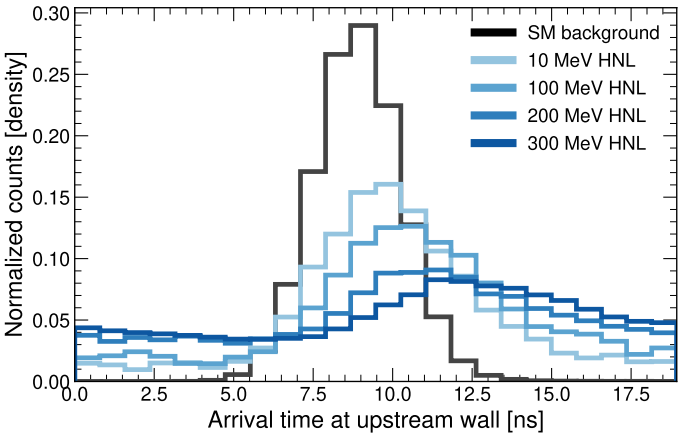

Figure 5.4: Arrival time distributions at the SBND upstream wall of the SM neutrinos (black) and HNL with different masses (blue tones). All the 81 BNB bunches have been merged.

Figure 5.5 shows the timing distribution of the SM neutrinos and an HNL of 300 MeV at the SBND upstream wall. There are background free regions, between the BNB beam bunches and after the beam window, highlighted with colored areas. The regions between bunches were taken 3σ ($\sigma_{BNB} = 1.3$ ns) away from the center of each bunch. Counting the total number of HNL events, the fraction of HNLs in background free regions can be estimated.

The results are shown in Figure 5.6 for the region between bunches, the HNLs that arrive after the beam window and the sum of both. The main fraction of HNLs arrives

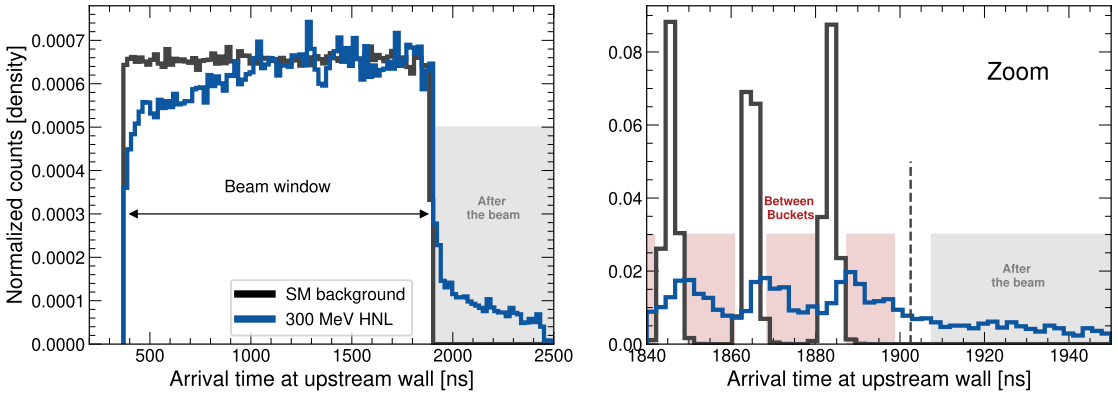

Figure 5.5: Truth time distributions of the SM neutrino background and a 300 MeV HNL at the SBND upstream wall (Left) and close up to the beam end (Right). The background free regions are shaded in red between the BNB bunches and gray after the beam window.

in coincidence with the beam. Nevertheless, up to a 10% of the total HNL events for the higher masses arrive after the beam trigger window. For searches in the low mass region, most of the HNL events are *in time* with the SM neutrinos and thus require precise timing analysis and reconstruction to separate them from the SM backgrounds.

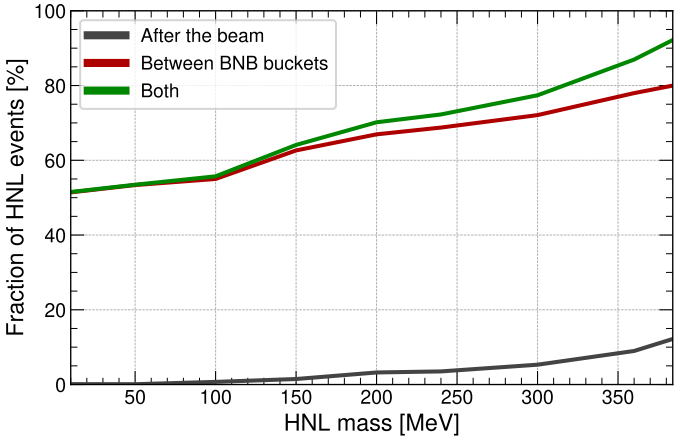

Figure 5.6: Fraction of HNL events in background free regions for different HNL mass: between the standard BNB bunches (red) and after the beam trigger window (gray). The sum of both contributions is shown in green.

5.1.3 HNL decay

The simulated channels used to compute the total HNL decay width for the mass ranges of HNLs available at SBND are shown in Figure 5.7. Three main channels are of particular relevance due to its dominance in their respective mass ranges:

- The channel $N \to e^+e^-\nu$ allows us to probe HNLs in the low mass range < 140 MeV. It is the dominant channel, apart from the non-detectable three-ν decay, before the HNL has sufficient energy to produce a π^0.
- The channel $N \to \nu\pi^0$ probes the intermediate mass range between 140 and 260 MeV, where the muon and pion production becomes relevant.
- The channel $N \to \mu\pi$ enables the probing of HNL masses as high as 388 MeV, limited by the maximum available mass for the HNL which is the kaon mass minus the mass of the outgoing muon.

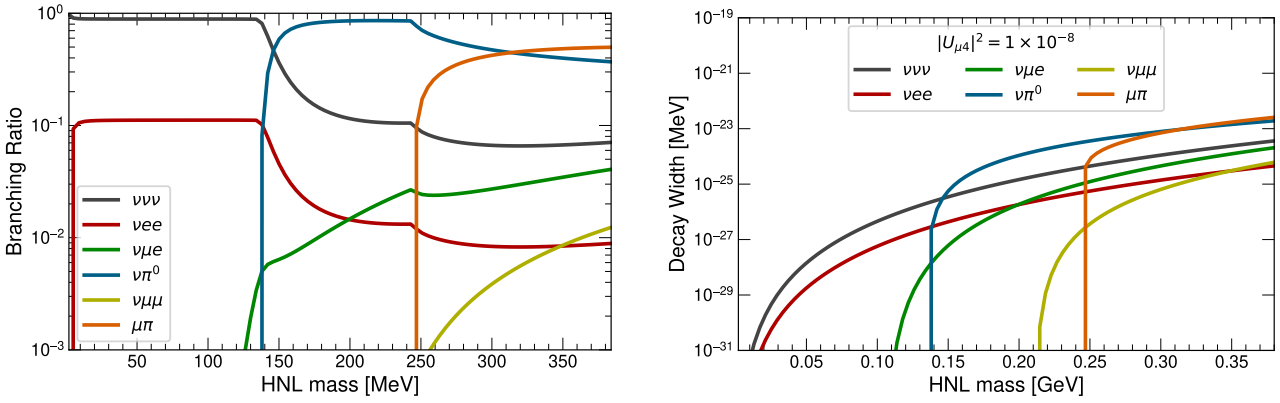

Figure 5.7: HNL Branching ratios (Left) and decay widths (Right) of the channels simulated in the MeVPrtl generator assuming a ν_μ only coupling ($|U_{e4}|^2$=$|U_{\tau 4}|^2$= 0, $|U_{\mu 4}|^2 \neq 0$).

The decay widths of these channels are given by [172, 173]:

(a) $N \to e^+e^-\nu$:

$$\Gamma\left(N \to \nu_\alpha e^+ e^-\right) = \frac{G_F^2 m_N^5}{96\pi^3} |U_{\alpha 4}|^2 \left[\left(g_L g_R + \delta_{\alpha e} g_R\right) I_1\left(0, \frac{m_e}{m_N}, \frac{m_e}{m_N}\right) + \left(g_L^2 + g_R^2 + \delta_{\alpha e}(1 + 2g_L)\right) I_2\left(0, \frac{m_e}{m_N}, \frac{m_e}{m_N}\right) \right], \tag{5.5}$$

with $\alpha = e, \mu, \tau$, G_F the Fermi constant [12], $g_L = -1/2 + \sin^2\theta_W$, $g_R = \sin^2\theta_W$, and $I_{1,2}$:

$$\begin{aligned} I_1(x,y,z) &= 12 \int_{(x+y)^2}^{(1-z)^2} \frac{ds}{s} \left(s - x^2 - y^2\right)\left(1 + z^2 - s\right) \sqrt{\lambda\left(s, x^2, y^2\right)} \sqrt{\lambda\left(1, s, z^2\right)}, \\ I_2(x,y,z) &= 24yz \int_{(y+z)^2}^{(1-x)^2} \frac{ds}{s} \left(1 + x^2 - s\right) \sqrt{\lambda\left(s, y^2, z^2\right)} \sqrt{\lambda\left(s, y^2, z^2\right)}, \\ \lambda(a,b,c) &= a^2 + b^2 + c^2 - 2ab - 2bc - 2ca. \end{aligned} \tag{5.6}$$

(b) $N \to \nu\pi_0$:

$$\Gamma\left(N \to \nu_\alpha \pi^0\right) = \frac{G_F^2 f_\pi^2 m_N^3 \left|U_{\alpha 4}\right|^2}{32\pi}\left[1 - \left(\frac{m_{\pi^0}}{m_N}\right)\right]^2 \tag{5.7}$$

The expression here for $N \to \nu\pi^0$ contains an additional factor of 2 suggested by Ref. [174] compared to Ref. [172, 173].

(c) $N \to \mu\pi$:

$$\Gamma\left(N \to \mu^\pm \pi^\mp\right) = \left|U_{\mu 4}\right|^2 \frac{G_F^2 f_\pi^2 \left|V_{ud}\right|^2 m_N^3}{16\pi} I\left(\frac{m_\mu^2}{m_N^2}, \frac{m_\pi^2}{m_N^2}\right), \tag{5.8}$$

with $f_\pi = 130$ MeV the pion decay constant, $|V_{ud}|^2$ the element from the CKM matrix [12], and I:

$$I(x,y) = \left[(1 + x - y)(1 + x) - 4x\right]\sqrt{\lambda(1,x,y)}. \tag{5.9}$$

All these widths are valid for Dirac HNLs. For Majorana HNLs the equations are multiplied by a factor of two, to account for the new possible charged conjugated final states. The corresponding branching ratios are not affected by the Majorana nature of the HNL.

The SM neutrinos come mainly from the decays of pions, whereas the only contribution of HNLs with a mass above 30 MeV is the decays of kaons. Because pions are lighter than kaons, neutrinos produced by pion decays are more forward focused. This is depicted in Figure 5.8: the density of neutrinos from kaon decays is uniform in the detector surface as opposed to neutrinos from the decays of pions which are concentrated around the beam direction.

Because HNLs are mostly produced by kaons, they are also uniformly distributed across the detector surface, as opposed to most of the SM neutrinos (see Figure 5.9).

Figure 5.10 shows the energy spectrum of HNLs decaying into an electron-positron pair and a neutrino with darker blue tones for the higher HNL masses and a fixed coupling ($|U_{\mu 4}|^2 = 10^{-5}$) and exposure (10^{21} POT). The decay widths and total number of HNL events increase with the power of the HNL mass. Heavier masses predict a higher number of HNLs in the detector for the same coupling value. The shape of the spectra in Figure 5.10 presents a sharp peak at lower masses which comes from the fraction of kaons that decay at rest (KDAR) in the SBND rest frame.

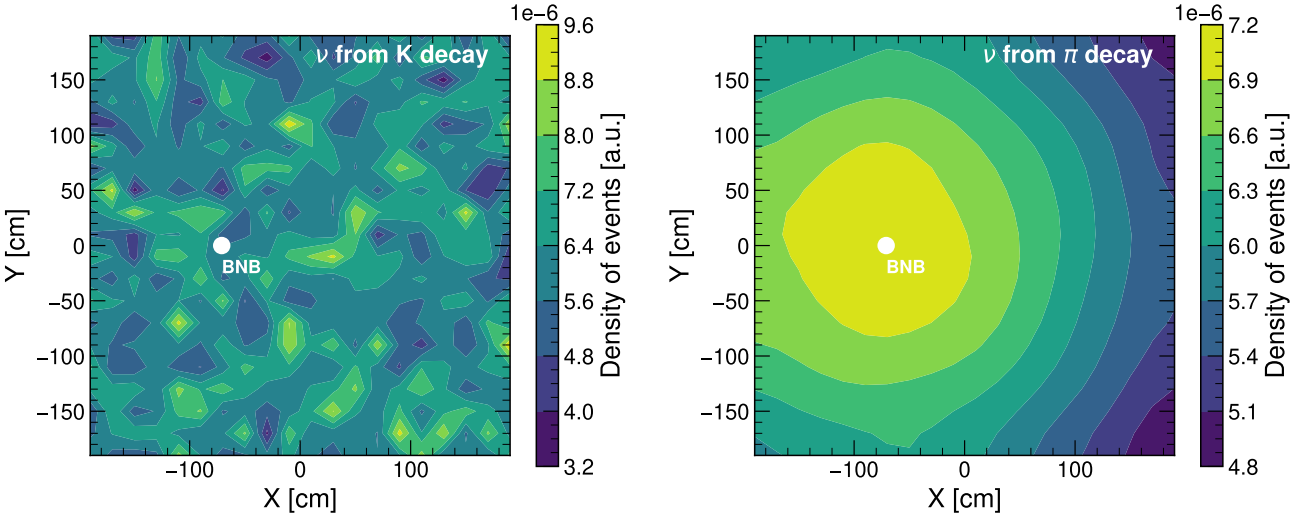

Figure 5.8: Density of the events at the SBND upstream wall in the perpendicular plane (XY) for SM neutrinos produced from the decays of kaons (Left) and pions (Right). The beam line crosses SBND at (x,y)=[-73.78,0] cm in the detector coordinate system (white dot).

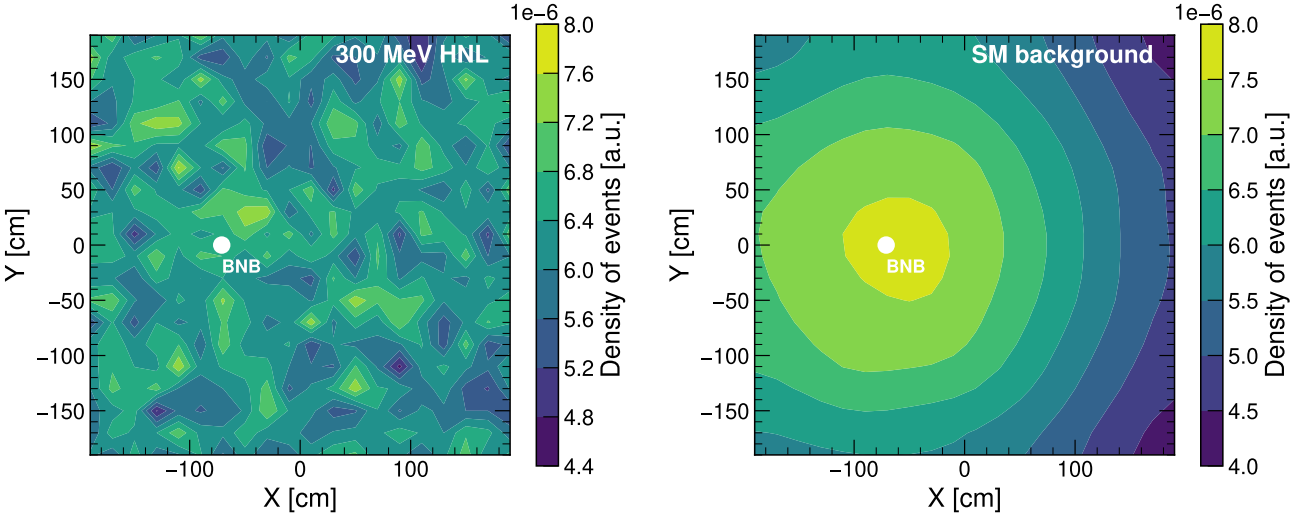

Figure 5.9: Density of the events at the SBND upstream wall in the perpendicular plane (XY) for an HNL signal of 300 MeV (Left) and the SM backgrounds (Right). The beam line crosses SBND at (x,y)=[-73.78,0] cm in the detector coordinate system (white dot).

5.1.4 HNL decay product kinematics

Henceforth, only HNL decays into an electron-positron pair and a neutrino are considered, focusing in the lower mass range [10–150 MeV]. An example of such a decay ($N \to e^+e^-\nu$) with an overlaid cosmic muon is shown in Figure 5.11. One of the reconstruction challenges discussed in detail in the next chapter is the small angle between

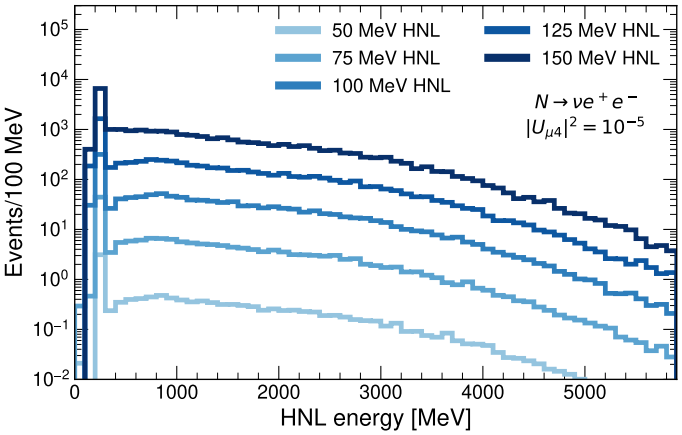

Figure 5.10: Energy spectrum of HNL events decaying into an electron-positron pair and a neutrino at SBND for different masses and a expected exposure of 10^{21} POT.

the lepton showers. The products are more forward-focused for lower masses making difficult to correctly separate both electromagnetic showers.

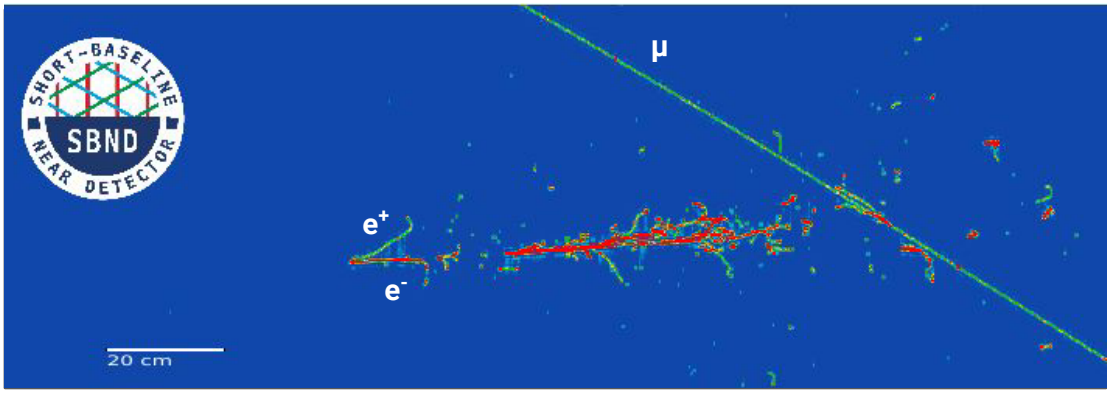

Figure 5.11: Example of a simulated HNL event inside the SBND TPC. An overlaid crossing muon can be seen on the right side.

Anisotropies in the distribution of energy among daughter particles and the direction of the decay are taken into account to produce a precise simulation of the HNL final state kinematics.

In the three-body scenario $N \to l_\beta^+ l_\beta^- \nu$ both the anisotropies induced by the polarization of the HNL (relevant for Dirac HNL) and the electroweak contribution to the vertex are considered.

To simulate the final states, the differential decay width given by [175, 176]:

$$\frac{\Gamma\left(N \to l_\beta^+ l_\beta^- \nu\right)}{\mathrm{d}m_{ll}^2 \mathrm{d}\cos\theta_{ll} \mathrm{d}m_{\nu m}^2 \mathrm{d}\gamma_{ll} \mathrm{d}\phi} = \frac{1}{(2\pi)^5} \frac{1}{64 m_N^3} \sum_{j=1}^{13} C_j K_j \tag{5.10}$$

is sampled. The nonzero C_j coefficients are given in Table 5.2 in the case of the HNL only interacting with the SM by mixing with the light neutrinos. The rest of them vanish for the case of two outgoing leptons of the same flavor. With $g_{L,\alpha\beta} = |U_{\alpha 4}|^2 \left[\delta_{\alpha\beta} - \frac{1}{2}\left(1 - 2\sin^2\theta_W\right)\right]$ and $g_R = |U_{\alpha 4}|^2 \sin^2\theta_W$. The Lorentz-invariant quantities K_j are defined as:

$C_{j\alpha\beta}$	Dirac N	Dirac $\bar{N}$	Majorana N
C_1	$64 g_{L,\alpha\beta} g_R$	$64 g_{L,\alpha\beta} g_R$	$128 g_{L,\alpha\beta} g_R$
C_4	$64 g^2_{L,\alpha\beta}$	$64 g^2_R$	$64(g^2_{L,\alpha\beta} + 64 g^2_R)$
C_5	$64 g^2_R$	$64 g^2_{L,\alpha\beta}$	$64(g^2_{L,\alpha\beta} + 64 g^2_R)$
C_8	$-64 g_{L,\alpha\beta} g_R$	$64 g_{L,\alpha\beta} g_R$	0
C_9	$-64 g^2_{L,\alpha\beta}$	$64 g^2_R$	$64(g^2_R - g^2_{L,\alpha\beta})$
C_{10}	$-64 g^2_R$	$64 g^2_R$	$64(g^2_R - g^2_{L,\alpha\beta})$

Table 5.2: Coefficients determining the angular anisotropy in HNL decays.

$$
\begin{aligned}
K_1 &= \frac{1}{2} m_m m_p \left(m_N^2 - m_{ll}^2\right) \\
K_4 &= \frac{1}{4}\left(m_{\nu m}^2 - m_m^2\right)\left(m_N^2 + m_m^2 - m_{\nu m}^2\right) \\
K_5 &= \frac{1}{4}\left(m_{\nu m}^2 + m_{ll}^2 - m_p^2\right)\left(m_N^2 + m_m^2 - m_{ll}^2 - m_{\nu m}^2\right) \\
K_8 &= \frac{P}{2} m_m m_p \left(m_N^2 - m_{ll}^2\right)\cos\theta_{ll} \\
K_9 &= \frac{P m_N}{2}\left(m_{\nu m}^2 - m_m^2\right)\left(|p_m|(\cos\gamma_{ll}\sin\theta_{ll}\sin\theta_{\nu m} - \cos\theta_{ll}\cos\theta_{\nu m}) - \frac{m_N^2 - m_{ll}^2}{2m_N}\cos\theta_{ll}\right) \\
K_{10} &= -\frac{P m_N}{2}\left(m_N^2 + m_m^2 - m_{\nu m}^2 - m_{ll}^2\right)|p_m|\left(\cos\gamma_{ll}\sin\theta_{ll}\sin\theta_{\nu m} - \cos\theta_{ll}\cos\theta_{\nu m}\right)
\end{aligned}
\tag{5.11}
$$

Where P is the polarization of the HNL, m_m and m_p the masses of the negatively and positively charged leptons respectively, m_{ll} the invariant mass of the charged lepton pair, $m_{\nu m}$ the invariant mass of the neutrino-negatively charged lepton system, p_{ll} the momenta of the charged lepton system, cosθ_{ll} the angle between the HNL spin direction and p_{ll}, γ_{ll} the angle of rotation of the charged lepton subsystem around the direction of p_{ll}, and $\theta_{\nu m}$ the opening angle between the outgoing negatively charged lepton and the neutrino. As a validation the kinematic distributions obtained were compared to those in reference [176] finding good agreement between them.

Figure 5.12 shows the energy of the leading shower in an HNL decay into an electron-positron pair and a neutrino. On average, the leading electron or positron carries ~ 640 MeV of energy, mostly focused in the beam direction.

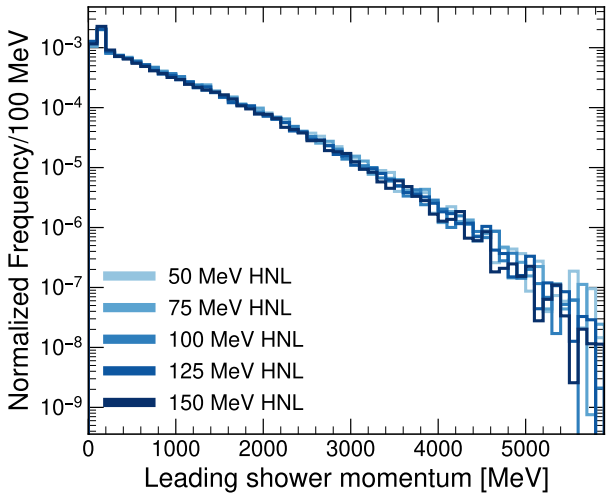

Figure 5.12: Energy distribution of the leading electron or positron for the $N \rightarrow e^+e^-\nu$ decay channel for different HNL parent masses.

The distributions of the opening angle between the two showers θ_{ee} is shown in Figure 5.13 in absolute frequency (Left) and accumulated density (Right). The correct reconstruction of both showers for the lower masses (< 50 MeV) is challenging, as more than 60% of the lepton pairs have 10° or less between them.

HNL events are very beam-focused in this mass range. Figure 5.14 displays the angle of the leading shower with the beam direction θ_{lead}. The forward boosting causes 90 (65)% of the events to be collimated with an opening angle between the leading shower and the beam direction below 10° for decays of HNLs with a mass of 50 (150) MeV. For all masses, in less than 1% of the events the leading shower is pointing *backwards* ($\theta_{lead} > 90°$). The outgoing neutrino carries on average 430 MeV of energy for this mass range.

5.2 Background simulation

As in chapter 4, the SM neutrinos are simulated with the GENIE software [152] and the cosmic backgrounds with CORSIKA [154]. The events simulated for the HNL studies included the *dirt* interactions with the materials before the detector. Any interaction produced by GENIE in the buffer volume (5 m surrounding the detector) or the *Rockbox* volume, 15 meters long before the buffer volume (see Figure 5.15) is saved, as their products could deposit energy in the detector.

For HNLs decaying into an electro-positron pair and a neutrino the signal consist in two outgoing electromagnetic showers that share a common vertex. The main backgrounds

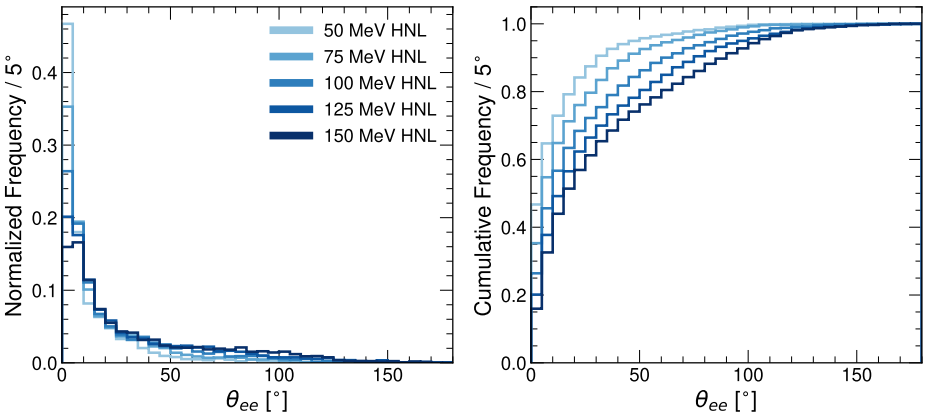

Figure 5.13: Left: distribution of the angle between the electron and positron pair for the $N \to e^+e^-\nu$ decay channel for different HNL parent masses. The cumulative distribution is shown on the Right.

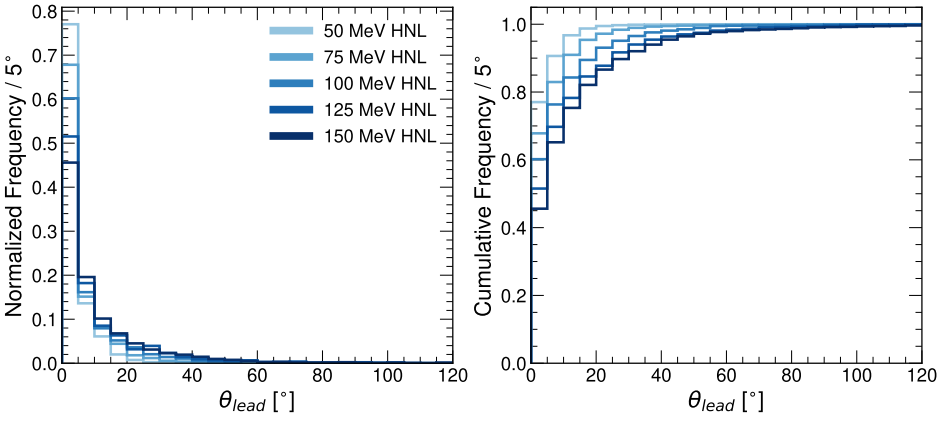

Figure 5.14: Left: distribution of the angle of the leading electron/positron with the beam direction for the $N \to e^+e^-\nu$ decay channel for different HNL parent masses. The cumulative distribution is shown on the Right.

are caused by the miss-reconstruction of NCπ^0 and CCν_e events. For this reason, enriched simulated samples for both were produced in addition to the inclusive BNB sample containing all the expected interactions from the neutrino beam with the argon in the detector.

Neutral pions produce two outgoing photons which result in a di-shower signature each shower separated by a $\sim$ 10 cm gap from the decay point of the π^0 (Figure 5.16-Left) [177]. This is caused by the short conversion length ($\sim$18 cm) of photons in LAr [178]. The ν_e charged-current interactions produce a single shower (electron) as shown in Figure 5.16-Right.

Because the products of the HNL decay are very forward-focused, it is common for both showers to overlap if there is an angle $< 10°$ between them. In this case, the signal

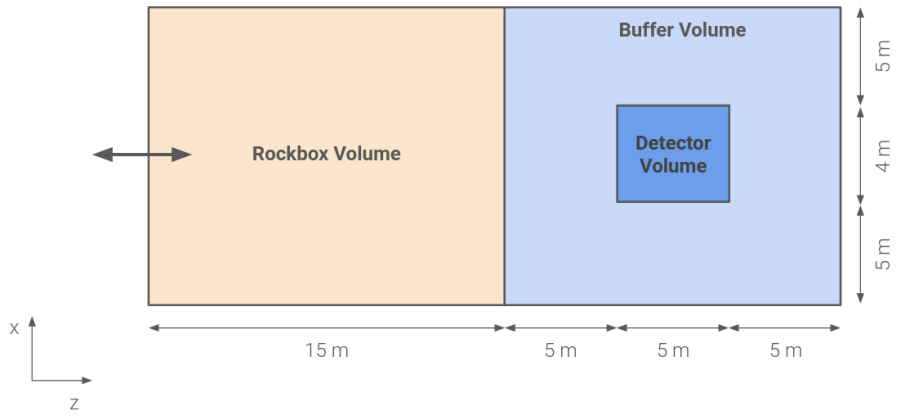

Figure 5.15: Boundaries of the GENIE generator in SBND. In addition to the detector surroundings (buffer volume), interactions produced up to 20 meters before the detector (Rockbox volume) are saved.

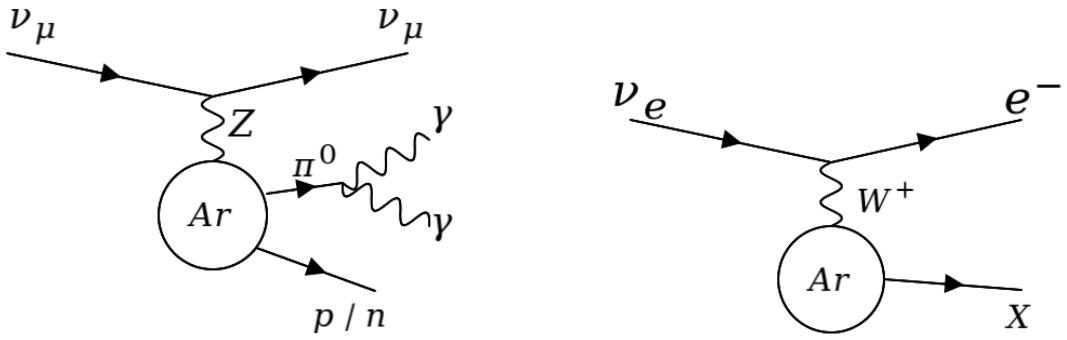

Figure 5.16: NCπ^0 (Left) and CCν_e (Right) interactions with an argon nucleus.

may be reconstructed as a single shower, as depicted in Figure 5.17. Therefore, the cause for tagging NCπ^0 and CCν_e backgrounds as signal events depends on the number of reconstructed showers. The main reconstruction problems for both NCπ^0 and CCν_e events are outlined in Table 5.3.

Background	1 reconstructed shower	2 reconstructed showers
NCπ^0	- 2 showers are reconstructed as 1. - 1 shower is out of the detector or not reconstructed.	- 2 showers appear as coming from the same vertex. - 1 shower split into 2 reconstructed showers.
CCν_e	- The dE/dx determination fails. 1 single CCν_e shower mimics 2 overlapping signal showers.	- 1 shower split into 2 reconstructed showers.

Table 5.3: Most common problems that cause the NCπ^0 and CCν_e backgrounds to be miss-reconstructed as an HNL signal.

A description of the signal and background samples produced for the analysis can be found in Appendix B. The next chapter reviews the reconstruction tools used to perform the selection of HNL events decaying into an electron-positron pair and a neutrino.

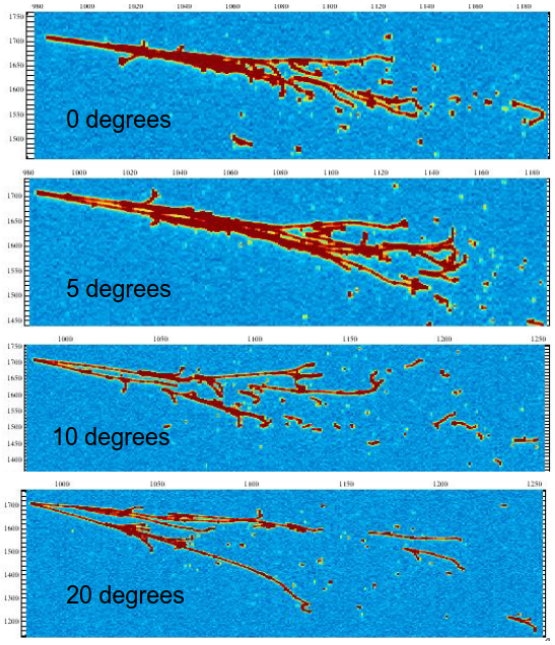

Figure 5.17: TPC image of simulated e^+e^- pairs for different angles between them.

Chapter 6

Detector simulation, reconstruction and selection of HNL candidates

In this chapter, the detector simulation and reconstruction of events in SBND is discussed with particular emphasis in the TPC and CRT systems. The light signal simulation and reconstruction are extensively described in Chapter 4. High-level reconstruction tools used to suppress cosmic backgrounds and perform particle identification are discussed. Finally, a selection of HNL events in the low mass range, [10–150] MeV, is performed on the samples described in Chapter 5. These results are employed in Chapter 7 to estimate the expected exclusion limits in case of no observation of SBND to an HNL decaying into an electron-positron pair and a neutrino.

6.1 General overview

The SBND event simulation has four main stages represented in Figure 6.1: the event generation, the particle propagation and interaction with detector materials, the simulation of the sensor's response (TPC, PDS and CRT systems), and the signal processing and reconstruction from the raw signals of each system to complex objects such as tracks, showers and optical flashes. High-level reconstruction tools such as the flash (TPC-PDS) and TPC-CRT matching combine information from multiple systems.

The SM interactions are modeled using GENIE for beam neutrinos and CORSIKA for the cosmic rays crossing the detector; more details are given in Section 4.1. HNL

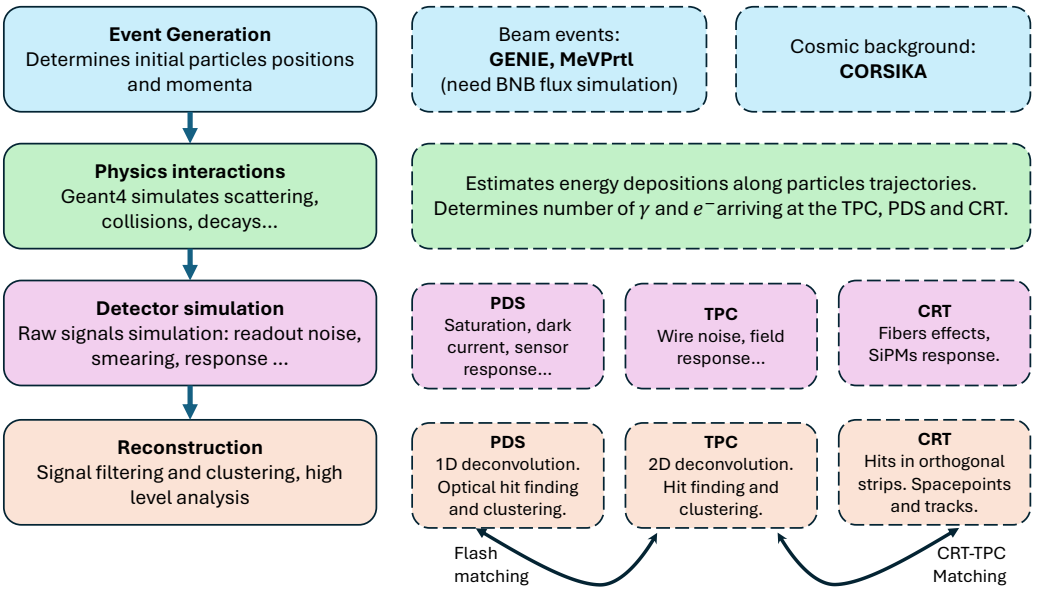

Figure 6.1: Workflow of SBND simulation.

generation with MeVPrtl, the BSM generator used in SBND and ICARUS, was discussed in Section 5.1.

The Geant4 stage predicts the energy depositions and interactions of the particles along their trajectories inside the detector. After the detector physics is simulated, the response of each system to different signals (ionization electrons and scintillation photons) is incorporated. The workflow of this stage for the TPC and CRT case is outlined in sections 6.2 and 6.4.

CRT, TPC and PDS raw signals are filtered and processed at the beginning of the reconstruction stage. Different algorithms identify energy depositions and cluster them in spatial and time coincidence. The tools developed to analyze the TPC and CRT signals are described in sections 6.3 and 6.5.

From these building blocks, higher analyses are performed using the clusters and combining the information from the three different systems; they are reviewed in section 6.6. The HNL selection performed to study SBND's sensitivity to HNLs in the low mass range [10–150] MeV is presented in section 6.7.

6.2 TPC simulation

As discussed in Chapter 2, ionization electrons are affected by different processes inside a LArTPC:

- First, electrons can be captured by positive ions (recombination). The recombination factor (R) varies with the energy loss over distance (dE/dx) [179, 180]. The value of R is computed using ArgoNeuT's Modified Box model, tuned with experimental data [180]. The parameters used were $\alpha = 0.93; \beta = 0.212$ which correspond to an electric field of of 0.481 kV/cm.

- The propagation of the electrons is affected by both diffusion and absorption by impurities in the argon, and the non-uniformity of the electric field. This non-uniform electric field affects the recombination process and modifies the spatial information, affecting the track/shower direction. The current simulation obtains the modified electric field analytically using Fourier series in a 3D grid and interpolating values between the points in the grid. These effects can be calibrated using laser systems which can be pulsed in known directions [181].

- Ionization electrons passing the induction planes towards the collection plane induce a current on nearby wires following Shockley-Ramo's theorem [182].

- The bias voltage applied to each wire forces the electrons away from regions close to the induction wires. The bias is chosen so that the first two induction planes are transparent and all the charge reaches the collection plane [183]. This behavior is illustrated in Figure 6.2.

- Finally, the noise and the readout electronics response is convolved with the current from the wires, creating the raw signals that are recorded and processed.

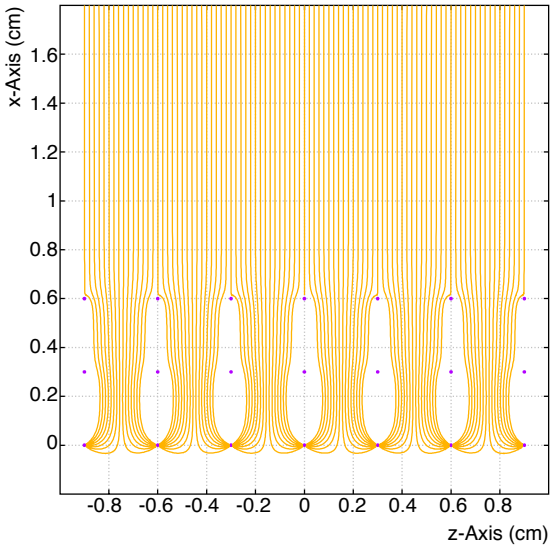

Figure 6.2: Example of electron drift paths with two induction planes and a collection plane at x=0. Picture taken from [184].

In SBND, transport effects are simulated using the Wire-cell toolkit [184, 185]. The package also estimates the shape of the raw waveforms convolving the field response and

the electronics response. The electronics response includes the gain (14 mV/fC) and the shaping (2 μs) introduced by the pre-amplifier circuits. An example of the raw simulated waveforms can be seen in Figure 6.3 with and without the effect of neighboring wires.

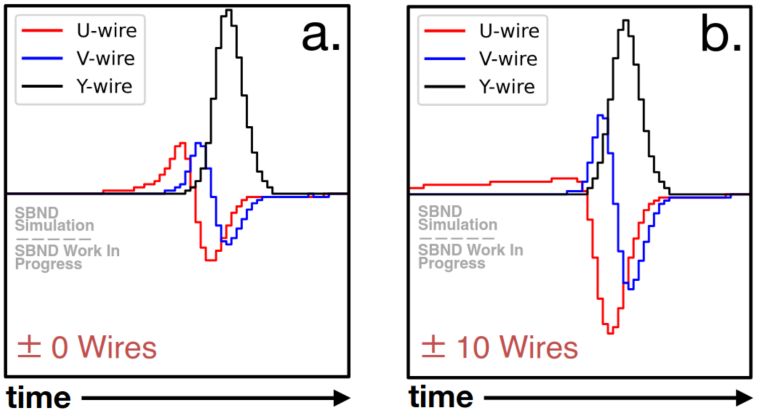

Figure 6.3: Wire response function for a single electron in the two induction planes (red and blue) and the collection plane (black) including (a) no neighboring wires or (b) [-10,+10] neighboring wires.

6.3 TPC reconstruction

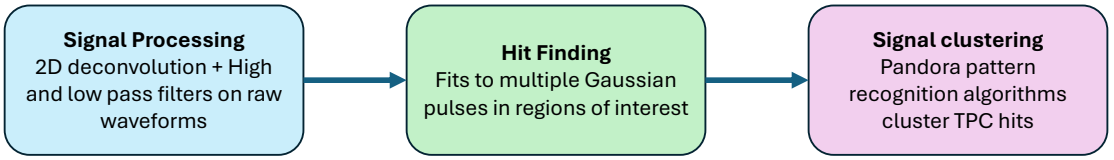

Figure 6.4: Scheme of the different stages in the TPC reconstruction chain, starting from the raw waveforms and finishing with the TPC hits and Pandora clustering algorithms.

In analogy with the PDS reconstruction workflow, TPC signals are processed before identifying the hits of deposited energy (see Figure 6.4). Following MicroBooNE's TPC processing workflow, since induction effects in neighboring wires are relevant raw TPC signals first undergo a 2D-deconvolution (wire number and time) to remove the electronics response [184]. High-frequency filters are then applied to the induction and collection planes to reduce the noise. A low-frequency filter is applied to the induction planes only to smooth the baseline [186]. The result of this proccess is shown in Figure 6.5 for a 1.23 GeV electron crossing the TPC. For showers, a decrease of the collected charge from deconvolved waveforms up to 50% in the induction planes is observed. The effect is mainly driven by the cancellation of consecutive bipolar signals in the same wire in the raw waveforms.

A 'GausHitFinder' algorithm is applied to deconvolved waveforms [187]. It attempts to fit a series of Gaussian pulses to the waveform. The number of peaks to fit is taken as the

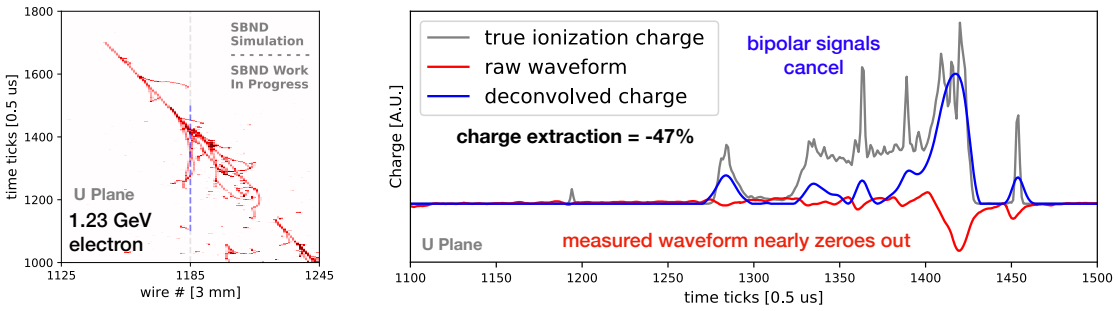

Figure 6.5: Left: TPC image of a shower induced by a 1.23 GeV electron in the first induction plane. Right: simulated raw waveform as seen in a particular wire of the induction plane. The induced current (gray) is convolved with the electronic response and the noise producing raw signals (red). The output after deconvolving and filtering the raw signals is shown in blue. In the induction planes, because the raw signals are dipolar, wide charge distributions cancel out and the recorded signal suffers from charge loss.

number of maxima in the differentiated waveform. Figure 6.6 shows this procedure for an electron interaction. After the fitting, the individual Gaussian pulses are identified as hits. The center of the Gaussian is taken as the peak time of the hit while the height and width are used to compute the deposited charge in that hit.

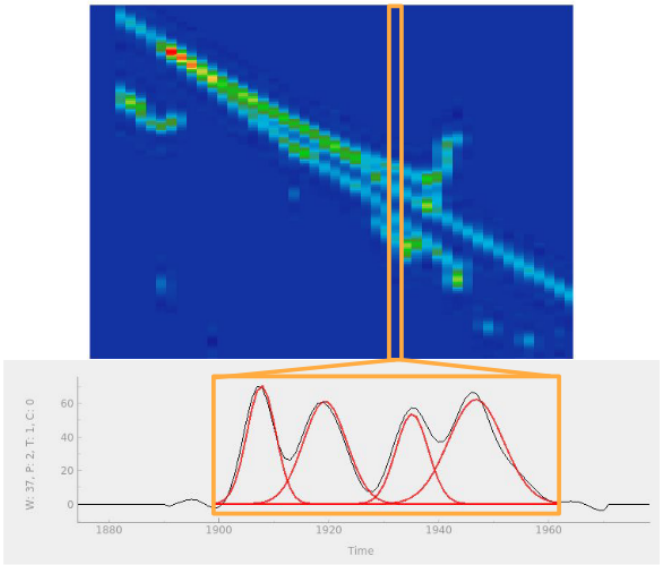

Figure 6.6: GausHitFinder algorithm applied to deconvolved TPC waveforms (black) from an electron event [188]. The top view shows the produced shower with color representing the collected charge on the wires (horizontal axis) and the vertical axis representing the time. The multiple Gaussian fit (red) for a given wire is shown in the bottom view.

6.3.1 Pandora pattern recognition

Identified hits on each TPC plane are given as an input to the Pandora toolkit [189, 190]. Pandora is a multi-algorithm approach to pattern recognition. It uses more than 100

algorithms to gradually cluster and reconstruct the interactions. The software is detector agnostic and is used by multiple LArTPC experiments [190, 191].

The two pathways in Pandora reconstruction, PandoraCosmic and PandoraNu, are depicted in Figure 6.7. The first removes hits that form obvious cosmic-rays. The remaining hits are the input of the PandoraNu reconstruction.

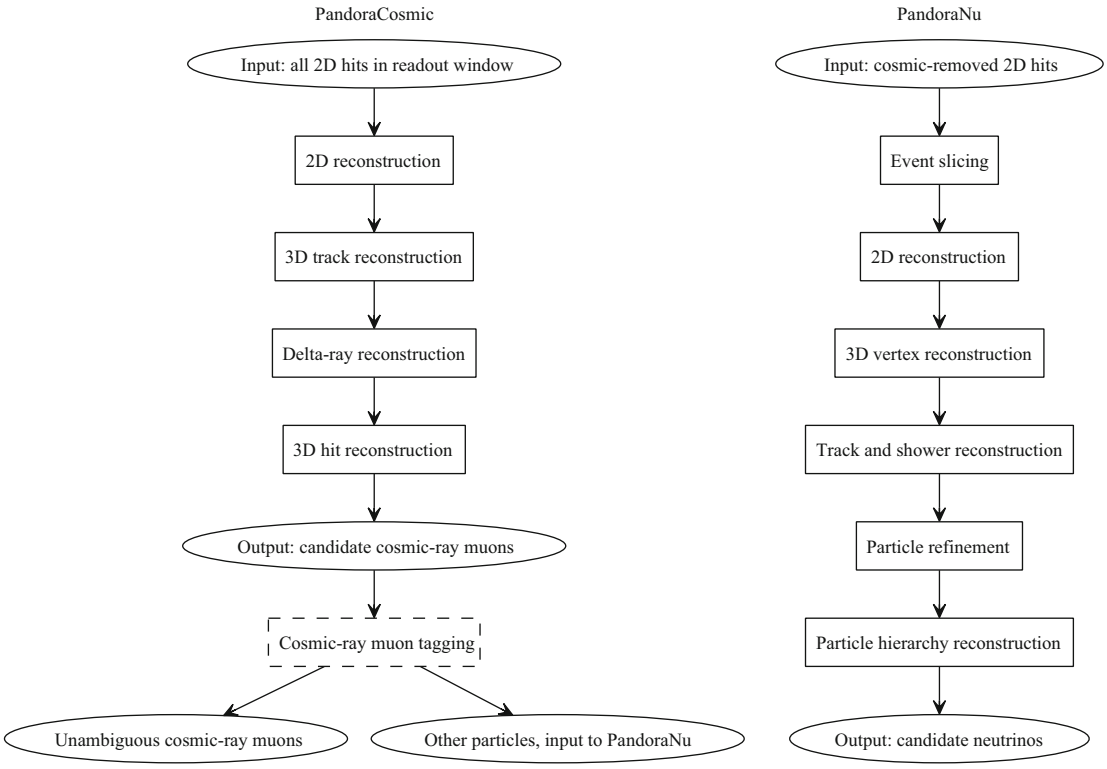

Figure 6.7: Representation of the two Pandora reconstruction paths. Hits associated with unambiguous cosmic-rays are removed. The remaining hits then follow the PandoraNu reconstruction. Figure from [190].

The PandoraCosmic reconstruction starts with the clustering of the hits in each TPC plane (2D reconstruction), looking for track-like objects. Initial clusters are then merged taking into account gaps in the detector and other ambiguities such as crossing particles. Then, 3D clusters are created by overlapping clusters from different planes with similar spans in the drift direction. The best candidates in 2 planes are projected into the third one where a χ^2 test estimates the consistency between planes. Clusters with good matches in the three TPC planes are combined into a Particle Flow Object (PFO). Subsequent stages that merge and split the clusters are run aiming to improve the arrangement. Once the 3D object is formed, each hit receives a 3D position or *space point*.

Clusters tagged as unambiguous cosmic-rays are excluded and the rest of the clusters (and their hits) are input into the PandoraNu reconstruction. The cosmic-ray tagging

criteria looks for vertical and straight tracks that are out of the drift window at the trigger time and close to the detector walls [188].

In the PandoraNu stage, the events are first divided into sections referred as *slices*. Ideally, each slice contains all the hits originated by the same interaction. Clusters are grouped into slices taking into account their proximity and direction. Once slices are formed, the 2D clustering is repeated assuming clusters can be either track-like or shower-like. After the re-clustering, Pandora assigns a vertex to the interaction for each slice and a hierarchy to the clusters that form the slice. The vertex is chosen comparing candidates with a multivariate analysis that uses information from both the complete slice and the surroundings of the vertex [188]. The hierarchy identifies primary daughter clusters from the interaction vertex and their subsequent daughters.

Each PFO is reconstructed under both track-like and shower-like assumptions. A final track score is assigned with scores < 0.5 (≥ 0.5) indicating a shower (track)-like behavior. The score is calculated by a dedicated boosted decision tree (BDT) [192] using several features of the cluster such as the cluster principal direction, its width and length, or the fraction of hits outside the Molière radius (10 cm in LAr) [188, 193, 194].

An example of a reconstructed slice is shown in Figure 6.8 for a simulated CCν_μ interaction with resonant pion production. Two tracks corresponding to a muon and a proton, and the two showers produced by the decay of a π^0 are identified from the primary interaction vertex.

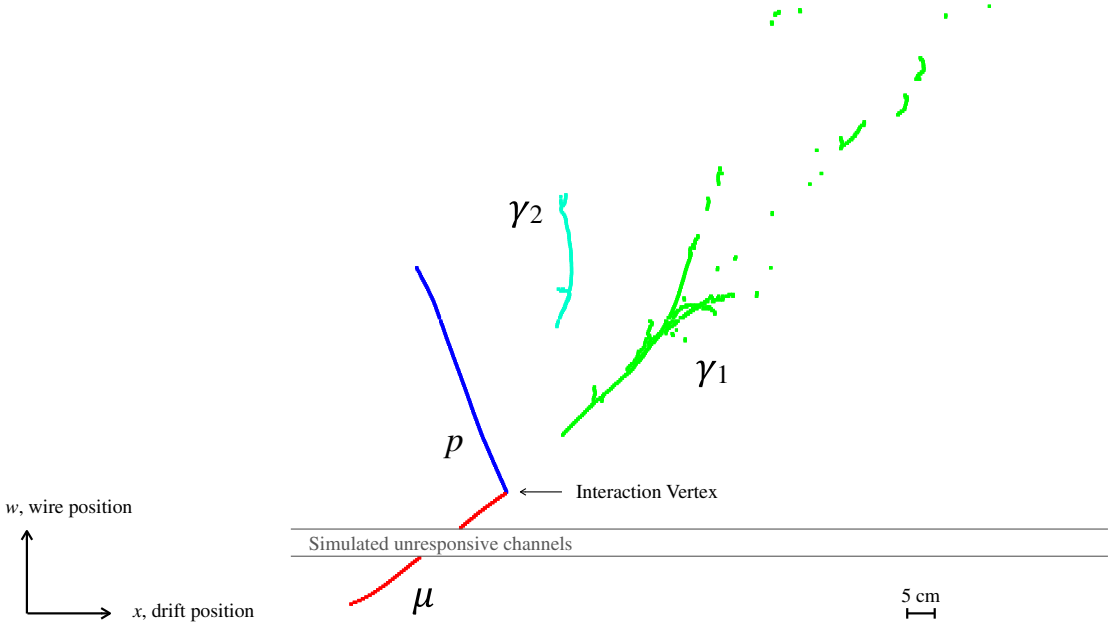

Figure 6.8: Example of a CCν_μ interaction with an outgoing muon (red), a proton (blue) and the two showers (blue and green) produced by the decay of a π^0. Image taken from [190].

Clustered hits can then be used to estimate physical quantities such as the shower or track length, energy, dE/dx and direction. To calculate the cluster energy, first ADC units (area of the TPC signals) are converted to charge (Q) multiplying by a calibration constant, one for each plane (U,V,Y): $(C_U, C_V, C_Y) = (49.8, 49.8, 49.7)$ $e^-/(\text{ADC} \times \text{ticks})$. Once the charge loss ($dQ/dx$) has been estimated, the conversion to energy for track objects is done using ArgoNeuT's Modified Box model [180]:

$$\frac{dE}{dx} = \frac{1}{\beta}\left[\exp\left(\beta W_{\text{ion}}\frac{dQ}{dx}\right) - \alpha\right] \tag{6.1}$$

were $W_i = 23.6$ eV is the work function of ionization electrons in liquid argon and α, β are the constants used to determine the recombination factor in Section 6.2.

For showers, the calibration constant $\gamma : \frac{dE}{dx} = \gamma \times \frac{dQ}{dx}$ is assumed to be independent of the electric field (the simulated value is $\gamma = 36.9$ eV$/e^-$) and can be measured using the reconstructed invariant mass of π^0 events as a standard candle.

The estimation of the energy loss per unit of distance in the shower case is performed using only the starting hits of the showers [188], as photons produce an electron-positron pair and their dE/dx should be twice the one produced by an electron-induced shower (see section 2.3.1). This variable is of great importance to the HNL searches in the $N \to e^+e^-\nu$ channel as it allows to separate SM backgrounds as CCν_e interactions from signal events.

Lastly, the angle of the shower cone is computed as $\theta_{\text{cone}} = \tan^{-1}(\text{shower width} \,/\, \text{shower length})$ with the width and length of the shower taken as the 90% percentile where all the shower hits lie from the center of the shower in each direction [188].

6.4 CRT simulation

Each CRT module FEB is connected to a total of 32 SiPMs (two SiPMs per strip and sixteen strips per module). Unlike the other systems, the PDS and TPC, the complete CRT signals are not saved. Instead, the amplitude of the signal measured by the 32 SiPMs in a module is recorded 75 ns after any self trigger is issued (the signal peak is delayed with a shaper in the FEB). Self triggers can be produced when a pair of SiPMs in a strip surpass a fixed amplitude threshold or by the coincidence of orthogonal strips in different CRT modules.

The simulation starts with the energy depositions located inside any CRT strip. The number of photons arriving at each SiPM is assumed to increase linearly with the deposited energy and decrease quadratically with the distance. Differences in the number of photo-electrons recorded by the SiPM in each fiber of a strip are modeled with a exponential absorption model. The empirical corrections applied are tuned with recorded muon data.

In the simulation all SiPMs are assumed to have the same gain. The equalization of the gains in different channels and modules is ongoing as part of the commissioning of the detector. To compute the ADC value of the CRT signal a waveform measured from real data is interpolated (see Figure 6.9).

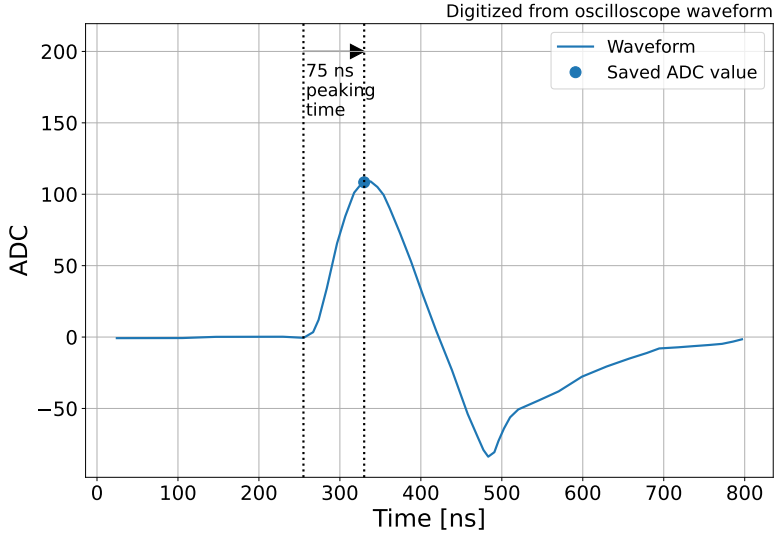

Figure 6.9: Measured SiPM waveform from real data. The simulated ADC value saved is interpolated 75 ns after the pulse surpassed the amplitude threshold, where the peak of the signal is expected. The threshold is set at an amplitude ~ 0.5 PE.

The output of the simulation at the sensor stage is a vector of 32 elements per CRT module, each one corresponding to the ADC value at a different SiPM.

6.5 CRT Reconstruction

First, an amplitude cut identifies the channels above the amplitude thresholds. The number of PEs on each SiPM is estimated assuming a linear dependency with the SiPM amplitude. Then, hits from nearby strips located in orthogonal layers in a 50 ns coincidence window are matched forming 3D space points. The space points contain the number of PEs measured by the SiPMs as well as the position and timing information corrected by the propagation delay from the hit point in the strip to the SiPM. An

example is shown in Figure 6.10 where a crossing muon leaves hits in two different strips of a CRT wall.

Space points in multiple CRT walls are matched in time coincidence to form CRT tracks, which are later compared to the TPC and PDS clusters.

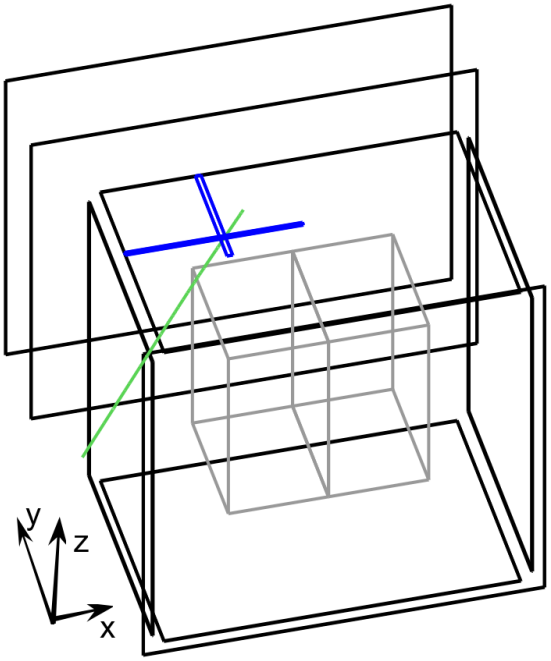

Figure 6.10: Example of a crossing muon (green) leaving hits in two different CRT strips (blue) of the CRT walls (black). The TPC volume is shown in gray.

6.6 High-level reconstruction

6.6.1 Beam flash matching

As detailed in Chapter 2, the slow drift velocity of electrons in LAr introduces an ambiguity when determining the time of the interaction. To overcome this problem a common technique used in LArTPCs is the association of light signals with TPC charge clusters. This method is usually referred as *flash-matching*. These algorithms compare the light pattern observed by the PDS sensors (O_i) and a hypothesis of the predicted light at each PDS channel (H_i).

In SBND, the hypothesis is built using the semi-analytic model described in Chapter 4 and the space points of the PFOs in a given TPC slice. The efficiencies of each PDS sensor to VUV and visible light are also taken into account. Finally, the hypothesis and measured charges are normalized by the total PEs predicted and observed in all PDS channels. A chi-square discriminant is built:

$$\chi^2 = \frac{1}{N_{\text{det}}} \sum_{i=1}^{N_{\text{det}}} \frac{(H_i - O_i)^2}{H_i + (0.1H_i)^2}, \tag{6.2}$$

with the statistical uncertainty ($\sqrt{H}$) and an extra 10 % smearing term. A score = $1/\chi^2$ associated with each flash is saved per matched flash with higher scores indicating better matches. We are interested in the BNB neutrino interactions, thus only flashes contained in the 1.6μs beam window are considered. The current configuration is one-to-many: each optical flash is compared with all the slices recorded during the drift window. Two flashes can be matched to the same slice. This occurs typically in events that cross the middle of the detector and thus have hits in both TPCs. Since each TPC can form its own flashes, only TPC hits in the TPC of each flash are used to compute the hypothesis.

6.6.2 Particle identification

Thanks to its high granularity imaging, a LArTPC can measure the angles, directions and energies of the outgoing particles in an interaction. In order to perform the correct particle identification (PID) of each Pandora cluster, several kinematic and topological variables are computed and compared. For example, a measurement of track-like behavior is the density or number of hits close to the line formed by the cluster start and end. In SBND, once the TPC hits have been clustered by Pandora (see section 6.3.1 for details), these quantities are fed into 3 different Boosted Decision Trees implemented with the ROOT TMVA package [195] that perform the PID.

Razzle (shower PID)

The Razzle PID BDT specializes in shower classification [188]. The input variables to the BDT are: the conversion gap (distance from the shower start to the primary vertex of the slice), the dE/dx, the shower cone angle θ_{cone}, and the hit multiplicity and energy densities.

The output of the Razzle BDT is a triad of scores (electron, photon, or other). The sum of the scores is normalized to 1. The particle can be classified as the label with the higher score; additionally, cuts on the minimum or maximum score can be performed.

Dazzle (track PID)

Similarly, the Dazzle PID BDT specializes in track characterization. Some of its inputs variables are: the track length, a score that identifies Bragg peaks using the energy loss

profile of the last 20 cm of the track, the dE/dx, and the number of daughter particles (Michel electrons for stopping muons or inelastic hadron interactions).

The output of the BDT is a set of four scores (muon, pion, proton and other).

Razzled (shower + track PID)

The third PID BDT combines variables from the Pandora clusters characterized as both showers and tracks. As input variables it takes the Razzle and Dazzle variables plus: the fraction of charge in the last part of the cluster (closer to track-shower end), the standard deviation of charge hits and the ratios of the 2nd and 3rd eigenvalues of a principal component analysis (PCA) to the first eigenvalue.

The output of Razzled is a set of six scores (photon, electron, muon, pion, proton and other). Figure 6.11 shows the confusion matrix selecting the highest score as the PID of the particle. Electrons are mainly misclassified as photons 11% of the times.

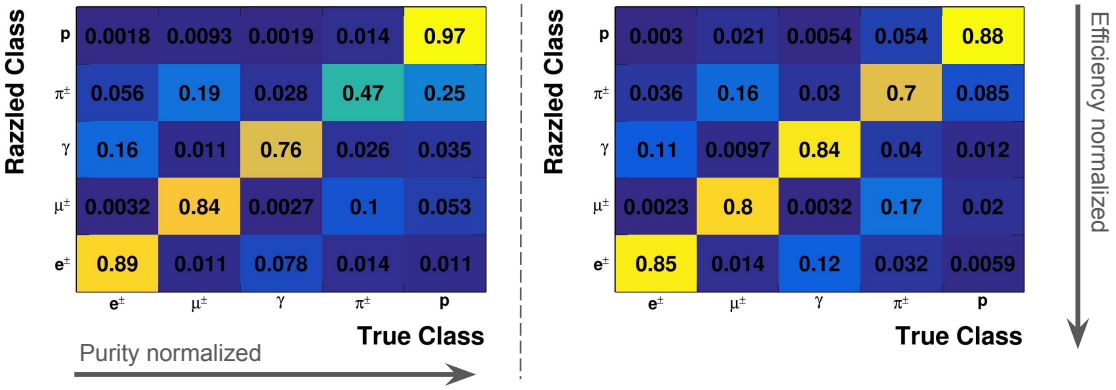

Figure 6.11: Left (Right): Confusion matrices of the Razzled BDT normalized such as the sum of each row (column) equals 1.

6.6.3 CRT-TPC Matching

The matching between TPC clusters and CRT signals is performed by two separated algorithms:

- **CRT Hit - TPC track matching:** trajectories from exiting TPC Pandora tracks are extrapolated to near CRT walls, where they would leave CRT signals. The distance of the closest CRT points to the TPC track is used to evaluate the match.
- **CRT track - TPC track matching:** exiting Pandora tracks are compared with CRT tracks. A score is given to each match using the tracks distance of closest

approach (DCA) and the angle θ between the two tracks (lower score equals better matching): **score** = DCA + 4θ

6.6.4 CRUMBS

To further mitigate the cosmic backgrounds, a tool for cosmic rejection using multi-system BDT score (CRUMBS) has been developed in SBND. CRUMBS employs information from the three systems (CRT, PDS and TPC) to build a score for each TPC slice from -1 to 1. A low (high) CRUMBS score indicates a likely cosmic (neutrino) interaction. To include the CRT and PDS information it is necessary to first match the TPC slice to its corresponding optical flash and CRT track.

CRUMBS input variables from the different systems include:

- **TPC variables:** number of hits in a given slice, number of identified clusters (PFOs) by Pandora in the slice, the number of hits in the vicinity of the slice vertex (10 cm), or the ratio of the first and second eigenvalues of a PCA of spacepoints close to the vertex.
- **PDS variables:** time associated to the matched flash, flash match score and total number of PEs in the flash.
- **CRT variables:** the matched track and hit scores, and their respective times.

Figure 6.12 shows the CRUMBS score in the training and validation samples for the cosmic backgrounds and neutrino signals employed to tune the BDT.

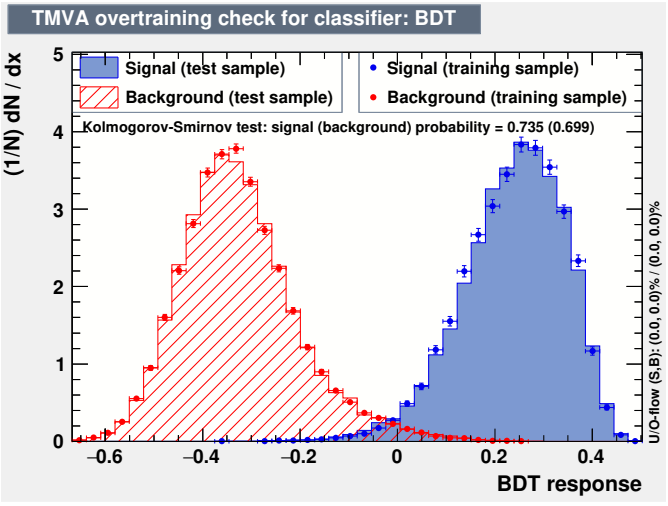

Figure 6.12: CRUMBS score distributions for signal (SM ν, blue) and background slices (cosmic rays, red) in both the training and validation samples.

6.7 HNL event selection

The complete simulation and reconstruction workflow described in previous sections is applied to the simulated samples described in Appendix B. The HNL selection is based on reconstructed Pandora slices. Each Pandora slice is accounted as an interaction. A slice is labeled as a signal event if more than 50% of the TPC hits contained in the slice were produced by the results of an HNL interaction. Similarly, the different background slices (cosmic rays, CCν_e, NCπ^0..) are classified by the leading contribution of hits to each slice.

6.7.1 Preselection

A first preselection is applied to ensure the quality of the slices considered. This stage aims to keep as much signal as possible while rejecting the majority of the cosmic background interactions. The following four cuts are shared with other analyses in SBND:

1. **Pandora unambiguous cosmic removal**

   First, unambiguous cosmic-ray clusters are removed after the PandoraCosmic stage, leaving ∼10% of the muon signals. For a total 3-year data taking (10^{21} POT), approximately 185 million cosmics are reconstructed as slices in SBND's TPC after PandoraNu stage. HNL and BNB events are mostly unaffected by this cut with less than 1% of their interactions discarded.

2. **Flash time within beam spill**

   The next step is to remove slices out of the beam window. Only slices with a matched flash in the BNB time window are considered. The arrival time of the particle at the SBND upstream wall is defined as the time of the matched flash corrected by the propagation time in the beam direction. To estimate the propagation time inside the TPC, the Pandora vertex Z component (V_Z) of the slice is used: $t_{upstream} = t_{flash} - V_Z/c$ (c = 29.97 cm/ns). A slightly wider window is chosen: [0.350–1.984] μs to account for smearing effects introduced in the reconstruction stage. The instant $t = 0$ represents the time when the first BNB proton bunch collides with the BNB target. A good match between the slice and the flash (flash score> 450) is also required.

3. **CRUMBS**

To further reject the cosmic backgrounds, a CRUMBS score of 0 or higher is required for the slice to be considered. This cut rejects 97% of the remaining cosmic slices.

4. **Vertex inside fiducial volume**

   Neutrino dirt interactions (see Section 5.2) and cosmic muons can deposit energy close to the detector borders. To prevent this issue, the slice vertex must lie inside the SBND fiducial volume (FV), which corresponds to 70% of the detector volume, and is defined as follows:

   - x-position: -180 cm $< x < -5$ cm; 5 cm $< x <$ 180 cm,
   - y-position: -180 cm $< y <$ 180 cm,
   - z-position: 10 cm $< z <$ 450 cm.

   The drift (x) cut ensures the interactions are not too close to the PDS sensors or the cathode plane. The vertical (y) cut rejects interactions that might intersect from the top of the detector (cosmic rays) while the bottom boundary rejects non-FV/dirt neutrinos. Lastly, the cuts on the beam (z) direction ensure that entering/exiting particles are removed, while also leaving enough downstream volume for showers to grow.

In addition to these shared cuts, another one has been employed to reject most of track-like topologies. We apply a cut on the number of Pandora showers in the slice:

5. **One or two Pandora showers requirement**

   Additionally, in the $N \to e^+e^-\nu$ selection we ask for a slice in which Pandora identifies either 1 or 2 reconstructed PFP particles as showers (truth studies without cosmic backgrounds showed more than 80% of the signal events fall into this category).

The effects of each cut stage on the cosmic, SM neutrino backgrounds and an HNL simulated signal of 100 MeV are shown in Figure 6.13. The PDS matching with the TPC has the higher rejection rate of cosmic ray interactions, reducing more than two orders of magnitude the cosmic slices while keeping most of the HNL and beam interactions.

For the HNL signal, the most significant loss is the fiducial volume cut (25% of the HNL signals). Notice that although the requirement of one or two showers in the slice reduces the signal by a 17% it also removes 68% of the slices produced by SM neutrinos from the beam.

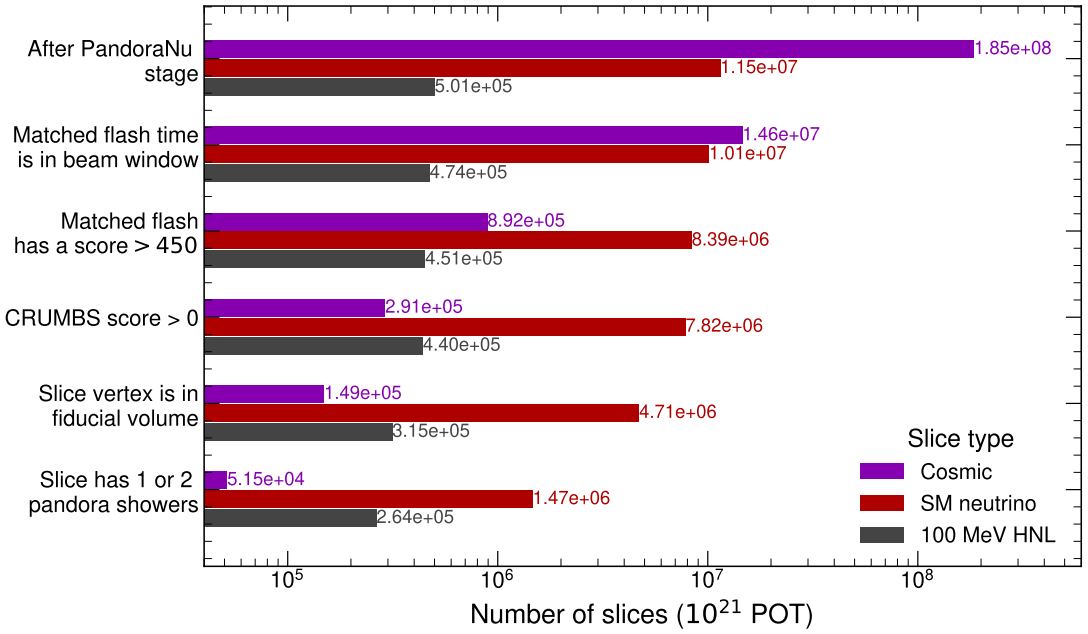

Figure 6.13: Summary of the preselection applied to cosmic, BNB and HNL simulated events for the $N \to e^+e^-\nu$ search. The number of HNL slices corresponds to a coupling of $|U_{\mu 4}|^2 = 2 \times 10^{-4}$.

Cut	Slice type: Cosmic	(%)	SM neutrino	(%)	100 MeV HNL	(%)
After PandoraNu stage	1.85×10^8	100	1.15×10^7	100	5.01×10^3	100
Matched flash in beam window	1.46×10^7	7.89	1.01×10^7	88.4	4.74×10^3	94.7
Matched flash score> 450	8.92×10^5	0.48	8.39×10^6	73.2	4.51×10^3	90.1
CRUMBS score > 0	2.91×10^5	0.16	7.82×10^6	68.3	4.40×10^3	87.9
Slice vertex in fiducial volume	1.49×10^5	0.08	4.71×10^6	41.1	3.15×10^3	62.8
Slice has 1 or 2 showers	5.15×10^4	0.03	1.47×10^6	12.8	2.64×10^3	52.8

Table 6.1: Number and fraction of remaining slices after each cut of the preselection applied to cosmic, BNB and HNL simulated events for the $N \to e^+e^-\nu$. The number of HNL slices corresponds to a coupling of $|U_{\mu 4}|^2 = 2 \times 10^{-4}$.

The remaining timing distribution after the preselection can be seen in Figure 6.14 where the modulus ($t_{upstream}$%18.93 ns) of the arriving time at the SBND upstream wall is shown combining the 81 BNB bunches. The delay of the HNLs with respect to the SM neutrinos is clear, but further suppression of the backgrounds is required. The preselection keeps $\sim 50\%$ of the HNL slices while suppressing by more than three orders of magnitude the number of cosmic slices.

The initial 11 million BNB interactions are reduced to 1.5 million slices after the preselection. The shower requirement reduces the amount of track-like events by more than a factor of 3. Most of other neutral current and CCν_μ events can be removed using the PID tools described in the previous section. As in the signal case, a significant

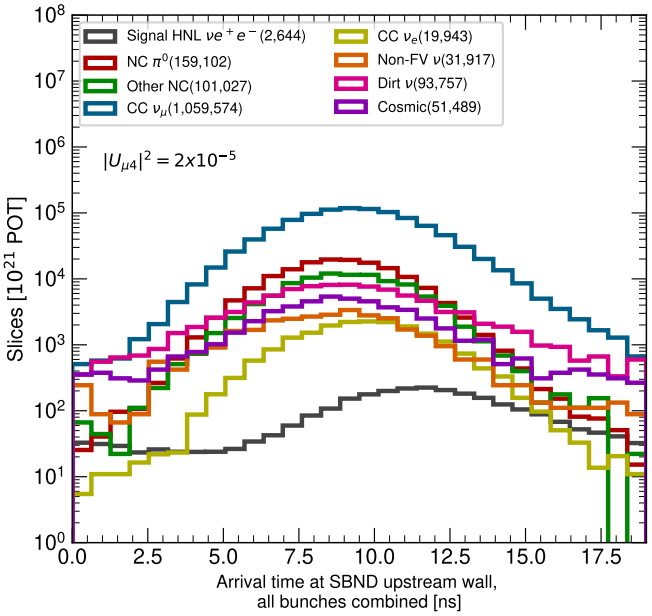

Figure 6.14: Distribution of arrival time for signal and backgrounds for an HNL mass of 100 MeV and total expected exposure of 3 years (10^{21} POT), after the preselection. The delay between the reconstructed arrival times of the signal (gray) and the background (rest) is 2.4 ns on average. A wider spread in the signal arrival times is also observed.

fraction of the NCπ^0 and CCν_e background events passes the preselection. To deal with this backgrounds which can mimic the signal, the particular topology and energy of the events is used. The next section describes the specific tool developed to produce a low-background selection of $N \to e^+e^-\nu$ HNL events.

6.7.2 $N \to e^+e^-\nu$ selection

It has been observed that background-free regions (high background rejection) have more impact in the final sensitivity than high efficiency in signal selection. For this reason, the main objective of this selection is to obtain pure samples of the signal population, even at the cost of reducing the total signal selection efficiency.

A custom BDT was trained to separate the HNL signal and background (cosmic muons and BNB neutrino interactions) populations. The BDT uses key physics variables, including the energy, cone angle, conversion gap, and dE/dx of the leading shower in the slice. Their main features are described below.

BDT input variables

To prevent redundancy, variables with low impact and high correlation with others are removed from the inputs. Some variables were compressed such as the combined PID ratios:

$$\begin{aligned}\text{Razzle-Dazzle Combined} &= \#\text{Primary razzle photons} + \#\text{ Primary razzle electrons} \\ &- \#\text{Primary dazzle protons} - \#\text{Primary dazzle muons} - \#\text{Primary dazzle pions},\end{aligned}$$

$$\begin{aligned}\text{Razzled Combined} &= \#\text{Primary razzled photons} + \#\text{ Primary razzled electrons} \\ &- \#\text{Primary razzled protons} - \#\text{Primary razzled muons} - \#\text{Primary razzled pions},\end{aligned} \tag{6.3}$$

which summarize how *track-like* or *shower-like* is the given slice. For example, a slice with three reconstructed PFPs, two identified as electrons and one as a muon has a combined score of 1. Although both scores are highly correlated (see section 6.6.2), removing either of them resulted in a loss of performance in the BDT and thus both are used as input variables. The normalized distributions of the combined PID ratios for signal and background are shown in Figure 6.15. As expected, the HNLs and the usual shower-only topologies (NCπ^0 and CCν_e) have positive scores indicating a high presence of showers, whereas the other backgrounds tend to lean towards track-dominated slices.

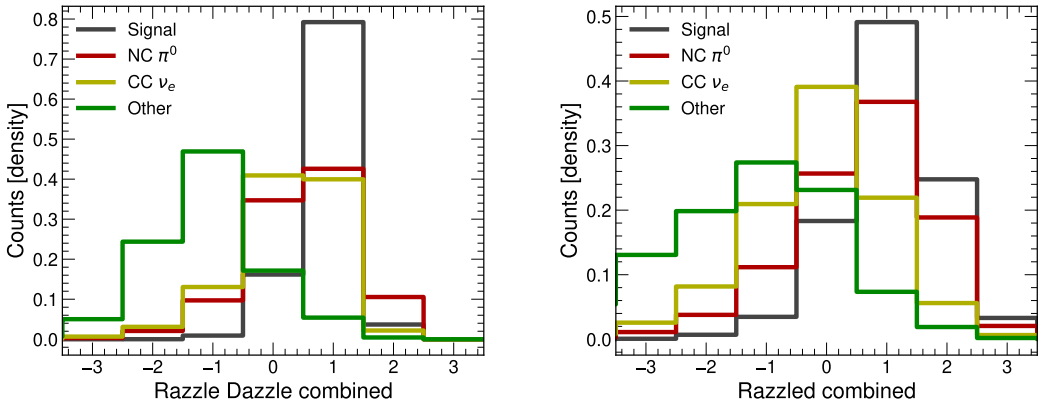

Figure 6.15: Normalized distributions of the razzle-dazzle and razzled combined variables representing the total number of showers minus the total number of tracks in a given slice. As expected, the HNL signal and the NCπ^0 and CCν_e background tend to have scores above 0, whereas the other backgrounds usually contain more tracks than showers in the slice.

The vertex coordinates of the slice, as well as the energy and opening angle of the shower cone of the most energetic shower in the slice are used as inputs to the BDT. Their normalized distributions are displayed in Figures 6.16 and 6.17.

The HNL vertex is uniformly distributed in the volume, as occurs to the neutrinos produced by kaon decays in the BNB. Most of the SM backgrounds (produced from pion decays) have asymmetries in the directions perpendicular to the beam (x and y). The blank space in the center of the X coordinate is where the cathode plane is located. Lastly, a significant excess of backgrounds is close to the start of the active volume in the beam direction (z=0). This effect is caused by beam interactions with the dirt outside the cryostat and deposit energy in the detector.

Differences caused by the parent meson are also noticeable in the distribution of the shower energy. The HNL signal and the CCν_e events have a significant tail as for the higher energies, the ν_e neutrinos are produced mainly by kaon decays. As the angle of the shower with respect to the beam depends on the HNL mass, it has not been included in the BDT. Instead, the angle of the cone (θ_{cone}) was found to be a robust variable for all the HNL masses in the 10–150 MeV range. The angle θ_{cone} is consistently bigger for signal events. This is caused by the proximity of both electron showers and the clustering algorithms, which tend to assign hits from both showers to the bigger shower.

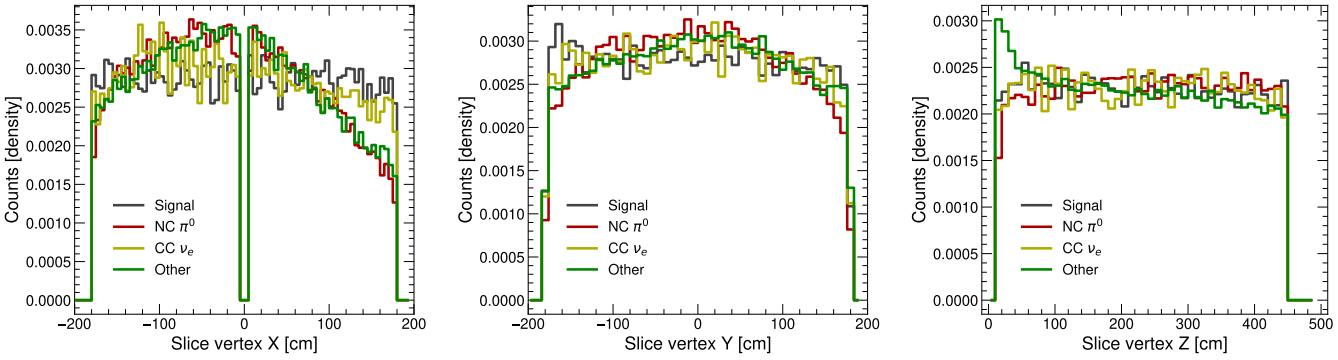

Figure 6.16: Normalized distributions of the x,y and z coordinates of the primary vertex in the slice. The asymmetry in the x (drift) coordinate is expected, as the BNB enters the TPC at x=-74 cm. The peak of background events at low z is caused by SM neutrino interactions with the dirt outside the detector cryostat.

Other relevant variables are the conversion gap (the distance between the shower and the slice vertex), and the dE/dx of the shower. They are displayed in Figure 6.18.

Lastly, PDS-related variables were added into the BDT:

- The flash-match score, as well as the OpT0 fraction defined as:

$$\frac{PE_{\text{Hypothesis}} - PE_{\text{Measured}}}{PE_{\text{Measured}}} \tag{6.4}$$

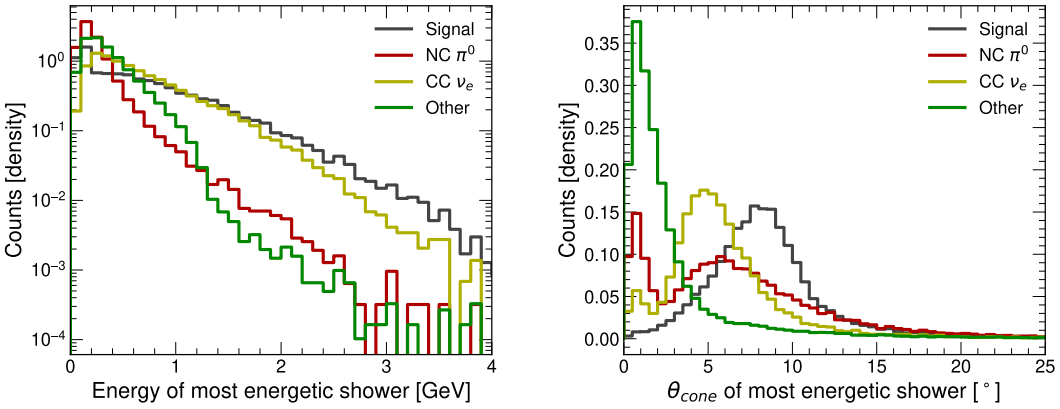

Figure 6.17: Left and Right: Normalized distributions of the energy and opening angle of the shower cone (θ_{cone}) of the most energetic shower in the slice. Because the angle between both electrons in the HNL signal is typically small, hits from the smaller shower tend to be clustered in the leading shower, enlarging the cone width (and thus, the cone angle). Miss-identified tracks (CCν_μ) and other neutral currents have cone angles smaller than 5°.

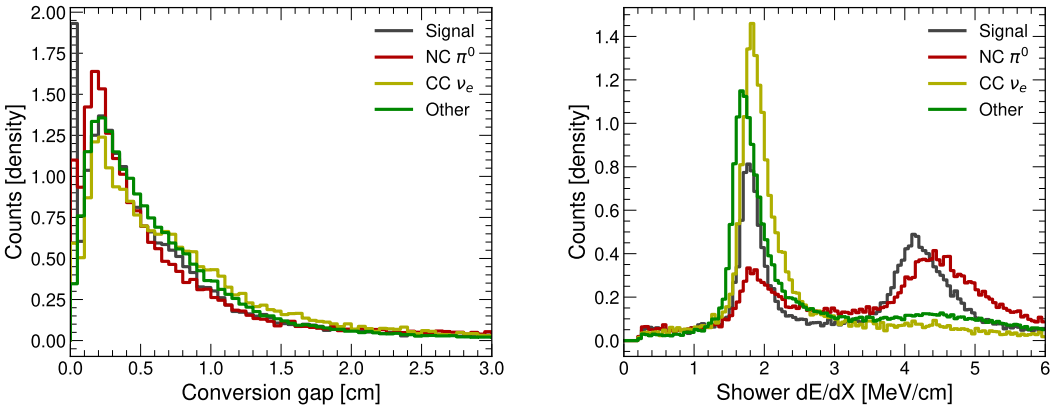

Figure 6.18: Normalized distributions of the conversion gap (Left) and dE/dx (Right) of the most energetic shower in the slice. Each shower of the signal would produce ∼2 MeV/cm. When both electrons are aligned (<5°), the initial hits are grouped together thus mimicking the signal induced by a photon (4 MeV/cm) in a NCπ^0 event.

- The fast amplitude and total amount of charge from the PDS sensors in the first 100 ns of the flash.

The Opt0 fraction describes the agreement between the total light yield measured and the hypothesis. Positive (negative) fractions correspond to an over(under) estimation of the light hypothesis. Using the amplitude of the early pulses accounts for possible effects of optical hit finding algorithms that may also cluster late light into the same hit, as deconvolution introduces smearing in the waveforms. Their distributions are depicted in Figure 6.19. In general, the light hypothesis of energetic showers is overestimated. This drives the difference between the background and signal distributions in Figure 6.19-Left.

The use of the collected light charge serves as a crosscheck to the TPC information as it is not biased by a wrong clustering of the TPC hits.

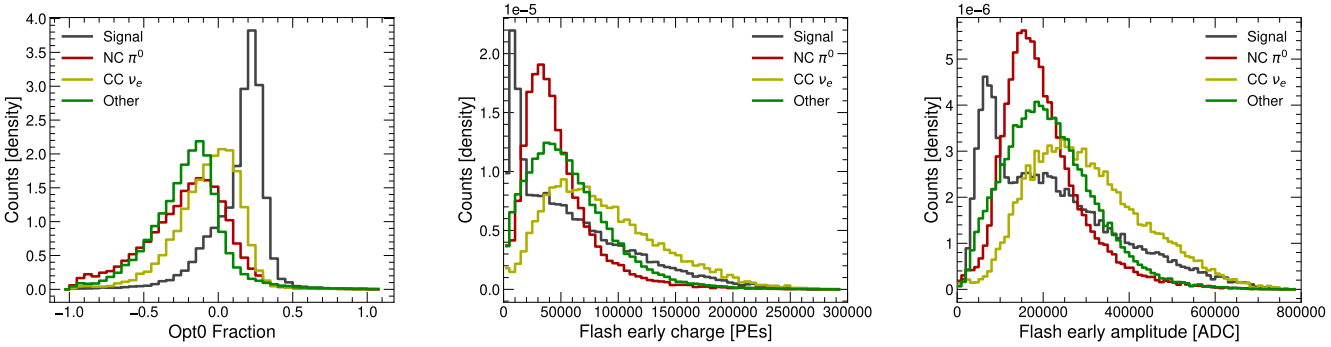

Figure 6.19: Left: distribution of the Opt0 fraction for background and signal slices. Center and right: total charge and amplitude collected in the first 100 ns of the matched flash. The first low energy peak of the signal distributions is caused by the fraction of events produced by KDAR which tend to leave less energy inside the detector.

It is important to note that the BDT has been trained without timing information, as the time of the matched optical flash is transversal to the other variables employed.

BDT properties

The BDT model was constructed using the XGBoost package [196] due to its short training duration and comparable performance to other machine learning approaches such as random forests [197] and support vector machines [198]. The structure of the BDT is described in Appendix C. Both signal and background samples were split to perform the training. The training was performed using the HNL sample corresponding to a mass of 100 MeV. After training, the BDT performance was evaluated across all simulated mass points to ensure that it captures general features independent of the HNL mass.

6.7.3 Results

The results on the training and validation samples are shown in Figure 6.20. Good consistency between both samples is achieved, and no significant over-fitting of the model is observed.

The distributions of the simulated BDT scores corresponding to the total 3-year data-taking of SBND and divided by interaction type are shown in Figure 6.21 in absolute

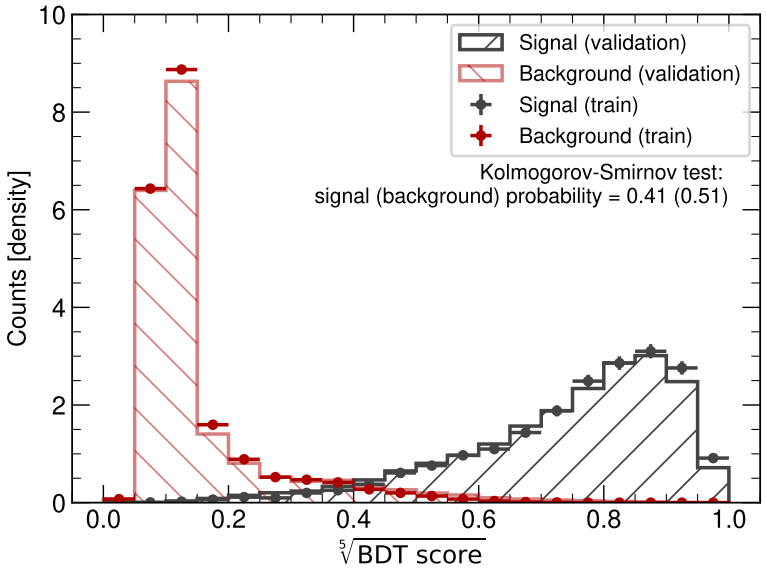

Figure 6.20: Fraction of signal and background events as a function of the BDT score for the train and validation samples. For better visualization, the 5th root of the score is shown.

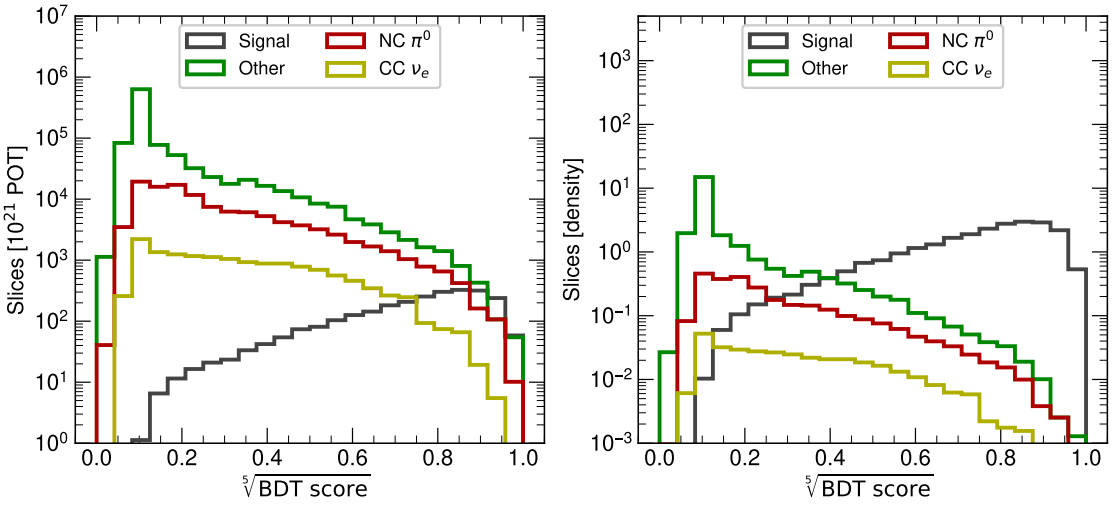

Figure 6.21: Left: distribution of signal and background slices by type as a function of the BDT score for three years of data. The normalized distributions are shown on the right. The backgrounds are normalized to the total number of background events. For better visualization, the 5th root of the score is shown.

numbers for three years of data (Left) and density (Right). The backgrounds are normalized to the total number of background events expected. The training successfully leaves a population of background events comparable to the signal size.

Since most of the sensitivity comes from the tails outside the expected BNB bunches, the BDT score has been selected to allow for a significant fraction of the signal to pass, while maintaining the tails almost background free. This can be seen in Figure 6.22 for

a cut on a 0.5 score, which leaves ∼25% of the signal slices (650) after preselection (see Table 6.2) while reducing the backgrounds by a factor of ×2000, from the starting 1.5 million to only 680 slices.

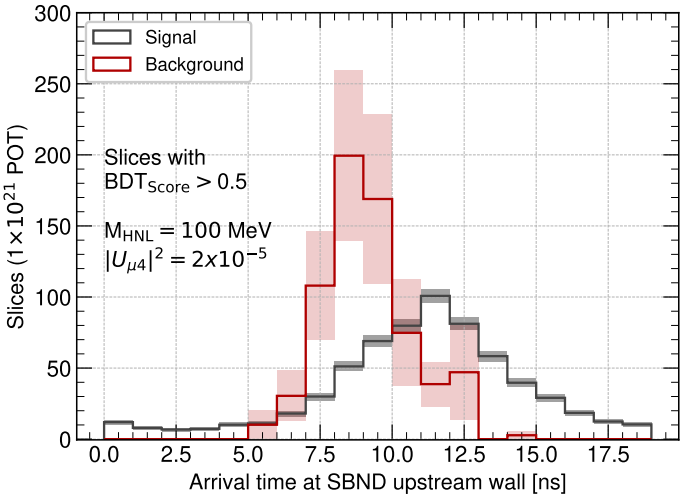

Figure 6.22: Time distribution of signal and background slices (all bunches combined) with a BDT score greater than 0.5. The statistical uncertainty is shown with error bands. The difference in relative errors comes from the difference in the scaling factors of the available samples.

To choose the BDT score (BDT_S) cut value the purity (selected signal slices over the total selected slices) and efficiency (selected signal slices over total signal slices) curves were analyzed for the benchmark mass (100 MeV). The total number of HNL events or Pandora slices at the SBND detector depends on the unknown $|U_{\mu 4}|^2$ coupling. Because of this, the purity numbers are not fixed but rather depend on the particular coupling used to generate the MC samples for the HNL signal. This is illustrated in Figure 6.23 for values of $|U_{\mu 4}|^2 = 1 \times 10^{-5}$and 2×10^{-5}. As expected, lower coupling values correspond to lower numbers of signal events for the same detector exposure, and the fraction of signal over background events decreases. Another feature observed is the fluctuations in the background distribution which appear for $BDT_S > 0.5$. This is caused by the limited size of the BNB inclusive sample. For this reason, no values $BDT_S > 0.5$ have been used for the analysis.

No significant variations on the final results were observed for different BDT score cuts in the range of [0.4, 0.6]. The value $BDT_S = 0.5$ was chosen as an *aggressive cut* (before statistic fluctuations appear in the background). To serve as a crosscheck with more background events a *conservative cut* of $BDT_S = 0.3$ was established. They correspond to a signal selection efficiency (after preselection) of 25% and 50% respectively. Combined with the preselection efficiency (50%), the conservative and aggressive selections retain 25% and 12.5% of HNL events arriving at SBND during the beam window. The

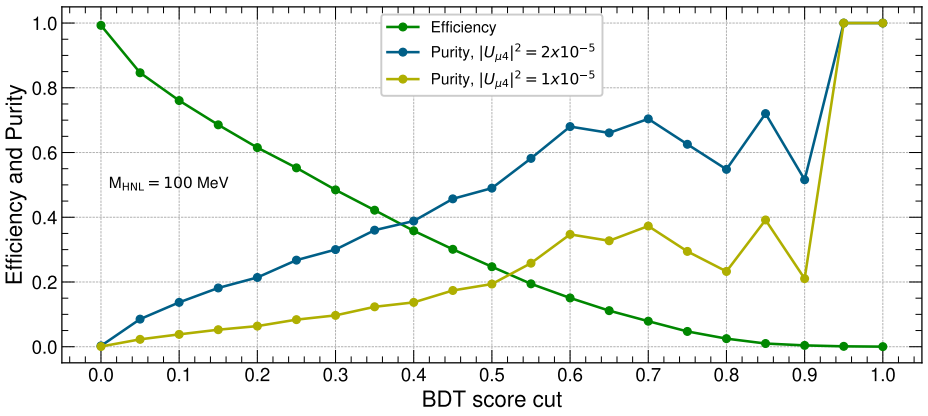

Figure 6.23: Efficiency and purity curves for a HNL mass of 100 MeV and different values of $|U_{\mu 4}|^2$ as a function of the BDT score cut. Preselection cuts are already applied.

main background is, as expected, the NCπ^0 contribution (37% of the background for the aggressive selection) with the rest distributed evenly in mis-reconstructed slices of different types. One of the main limitations of the analysis is the low statistics of the SM BNB inclusive sample (Rockbox sample) due to the large rejection factor.

BDT score Cut	Signal		Background					
	HNL Slices	Eff [%]	Background Slices	Eff [%]	NCπ^0 Slices	Eff [%]	CCν_e Slices	Eff [%]
None	2644	100.00	1528699	100.00	158297	100.00	20015	100.00
0.10	2011	76.06	12665	0.83	4976	3.14	1066	5.32
0.20	1626	61.52	5976	0.39	2335	1.48	376	1.88
0.30	**1281**	**48.46**	**2987**	**0.20**	**1279**	**0.81**	**173**	**0.86**
0.40	946	35.81	1491	0.10	619	0.39	90	0.45
0.50	**653**	**24.71**	**680**	**0.04**	**253**	**0.16**	**27**	**0.14**
0.60	398	15.07	187	0.01	132	0.08	10	0.05
0.70	208	7.89	87	0.01	40	0.03	2	0.01
0.80	66	2.50	54	0.00	10	0.01	0	0.00

Table 6.2: Number of signal and background events left after different cuts in the BDT score for the validation sample with an HNL mass of 100 MeV and a $|U_{\mu 4}|^2$coupling of 2×10^{-5}. The values used for conservative (0.3) and aggressive (0.5) selections are highlighted. The total SBND exposure assumed was 10^{21} POT.

The time distributions for all the mass samples produced are shown in Appendices D and E. In the next section, prospects for the future SBND performance assuming an enhancement on the PDS reconstruction are given using the true timing distributions.

6.7.4 Future prospects: studies with truth variables

To assess the impact of future improvements in the reconstruction chain, a selection using truth information was performed. In particular, two enhancements are proposed.

First, an increase of the intrinsic PDS time resolution, which allows SBND to better resolve the BNB buckets. With better PDS time resolution, less SM neutrinos from the beam are reconstructed in the regions between buckets.

To perform the analysis, the true timing distributions of signal and background at SBND's upstream wall are used, smearing them assuming a fixed PDS resolution that follows a Gaussian distribution. The current resolution of SBND PDS resolving BNB interactions is 2.34 ns [127] or 1.94 ns after subtracting the intrinsic 1.3 ns width of the BNB proton bunches [83]. An overall timing resolution of 1.7 ns corresponding with an intrinsic 1 ns PDS resolution is assumed. This optimistic scenario is motivated by the high frequency readouts of the PMTs (500 MHz) and is compatible with the best results obtained using deconvolved waveforms from the PMT system [127]. To increase the overall timing resolution a fit to the rise profile of the raw PMT waveforms could be performed (each PMT signal contains at least 3 samples in the rising edge). The truth distributions for signal and background before and after the smearing are shown in Figure 6.24 for an HNL of 100 MeV.

Then, an enhancement in the selection is also assumed. A global 30 % reconstruction efficiency of HNL events is taken, while 25 % was obtained for the conservative selection using reconstructed variables. In addition, the background rejection efficiency is set to the aggressive BDT cut level. This represents a factor of two increase in the signal selection efficiency while maintaining the same background suppression, which is feasible given the standard tools are not tuned to reconstruct very-forward shower pairs and thus can be further optimized for this search such as the Wirecell reconstruction and Deep Learning techniques such as 3D convolutional neural networks.

The current reconstruction algorithms identify correctly 20% of the events as two reconstructed showers, another 20% as one track and one shower, 20% as a single shower, and the rest are combinations of multiple shower and track objects in a single slice. More sophisticated analyses can split the selections in different mass ranges and reconstruction cases (single shower, two showers, one shower and one track). Adding the information from the angle between the two showers (when both are reconstructed) and the angle of the leading shower with the beam direction will require a specific BDT training for each mass point as they depend on the HNL mass.

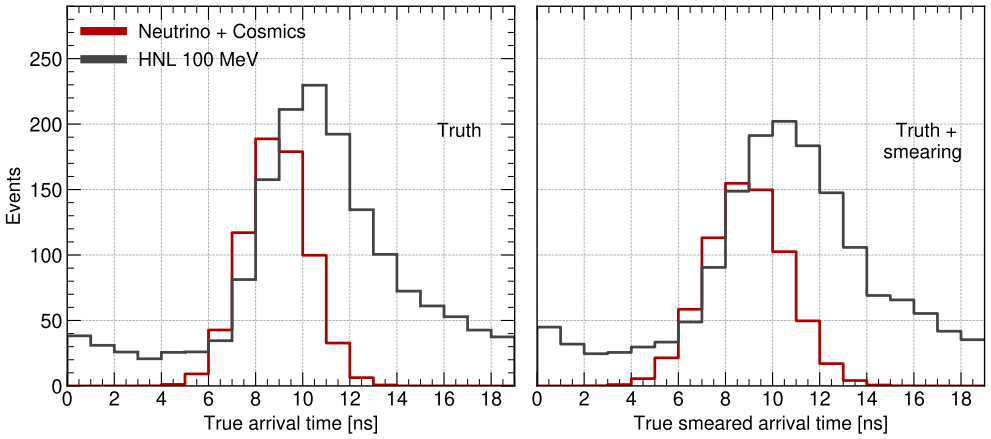

Figure 6.24: Left and right: truth ($\sigma = 1.3$ ns) and smeared truth ($\sigma = 1.7$ ns) arrival distributions at SBND for an HNL signal of 100 MeV and $|U_{\mu 4}|^2 = 2 \times 10^{-5}$ and the SM backgrounds. All bunches are merged taking the modulus ($t_{upstream}$%18.93 ns) of the arrival time at the SBND upstream wall.

The distributions for all the HNL mass points considered are given in Appendix F. In the next Chapter the timing histograms obtained in this selection using both reconstructed and truth variables are used to estimate the SBND sensitivity to HNLs in the low mass range [10–150] MeV.

Chapter 7

SBND sensitivity to HNLs decaying into electron-positron-neutrino

In this chapter the expected sensitivity of SBND to a muon-coupled heavy neutral lepton produced from kaon two body decays and decaying in SBND into an electron-positron pair and a neutrino in the [10–150] MeV range is computed. The uncertainty treatment is detailed in Section 7.1. The procedure followed to compute the exclusion limits is described in Section 7.2. Section 7.3 summarizes the results obtained using the two selections described in Section 6.7 (aggressive and conservative) considering reconstructed variables and the projection estimated with truth information outlined in Section 6.7.

7.1 Uncertainty treatment

This is the first search of HNLs into an electron-positron pair and a neutrino in SBND. The author produced the signal samples employed and participated in the production of the background samples (SM neutrinos from the BNB and cosmic muons). This search requires a high purity sample, and thus, a high background rejection factor. For this reason, the statistical uncertainties in the background samples described in the next pages were found to be the major limitation. Previous cross-section selections in SBND using the same simulation framework estimate an overall 12.5%–13% systematic uncertainty [188, 199] in both track-like and shower-like topologies, below the statistical error of the background in this analysis. For the signal sample, both statistical and systematic uncertainties are comparable (5–10%). In the following, only statistical uncertainties

are considered. They are estimated assuming that each bin in the time distributions obtained in the previous chapter follows a Poisson distribution with variance N, being N the number of counts in that bin. The statistical uncertainty associated to the i bin is:

$$\sigma_i = \sqrt{N_i} \tag{7.1}$$

It is important to note that the statistical uncertainty is estimated at the original generated samples size, that is, without multiplying by their respective scaling factor. For example the errors of bins in Figure 7.1-Right are larger due to the big scaling factor (22.16) of the Rockbox SM neutrino sample. From the original distributions the final uncertainty is taken as:

$$\sigma_i = \sqrt{N_i} \times \mathrm{S_F} \tag{7.2}$$

with $\mathrm{S_F}$ the scaling factor of the samples (see Appendix B) and N_i the original counts in bin i before the scaling. Statistical uncertainties dominate the background uncertainty as the generated MC sample of SM neutrinos from the BNB corresponds to roughly 450,000 neutrino interactions the biggest sample available as the MC is under development. For a complete three-year data taking of SBND (10^{21} POT), around 10 million neutrino interactions are expected.

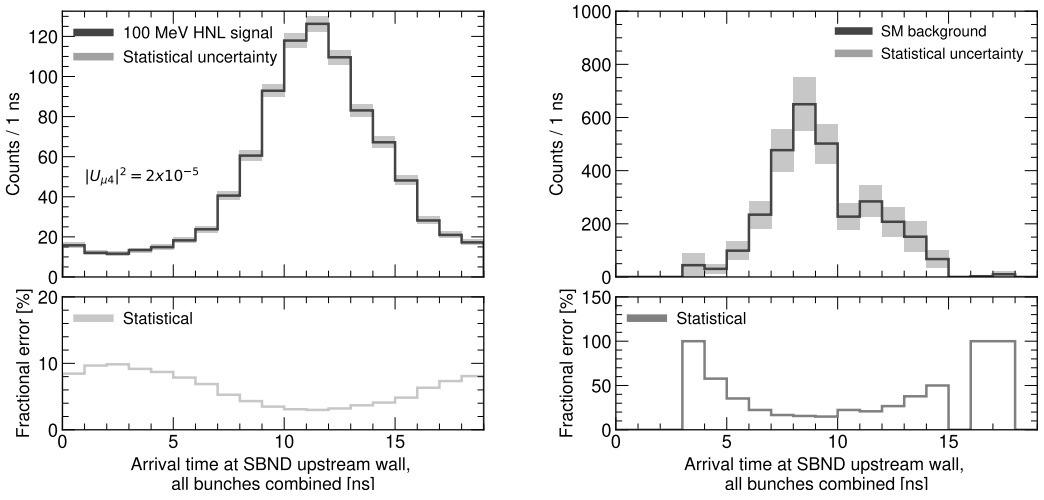

Figure 7.1: Uncertainties considered for the HNL signal (left) and SM backgrounds (right). In both cases, the size of the generated MC samples (with a large statistical uncertainty associated) is the main limitation.

Figure 7.1 shows the statistical uncertainty in the arrival time distribution for the HNL signal and SM backgrounds in the conservative selection. While the signal uncertainty oscillates between 5%–10%, the background uncertainty varies from 20% up to 100% in

the bins with fewer events. In bins with no entries the statistical uncertainty is set as the Poisson standard deviation of ±1.148.

In future analyses, not limited by the samples sizes, a careful treatment of the uncertainties (beam flux, detector systematics, neutrino-argon cross section ...) must be taken into account. For example, the signal suffer mainly from the uncertainties on the kaon flux: the POT counting, the intensity and fluctuations of the magnetic horn... Other HNL analysis have quantified the systematic uncertainties from the BNB flux between 5% and 10%. For the background case, in addition to the flux there are uncertainties that arise from the modeling of the neutrino interactions with the argon from the active volume and are estimated using the GENIE software.

7.2 Limit setting

The exclusion limits are estimated using a likelihood-based hypothesis test. The observable used to perform the test is the expected arrival time distribution at the SBND upstream wall. For a given exposure of the detector, the expectation value of the number of events or slices (see Chapter 6) in each time bin i is given by:

$$E[N_i] = \mu s_i + b_i \tag{7.3}$$

where s_i and b_i are the number of entries from the signal and background distributions in that bin. The *parameter of interest* (μ) is proportional to the number of signal events and thus to $|U_{\mu 4}|^4$. In general, other parameters may affect the number of signal and background events. For example, the uncertainty in the amount of delivered protons by the BNB or the value of the magnetic field of the focusing horn changes the total flux of neutrino events. Noting these *nuisance parameters* with $\boldsymbol{\theta}$, the two hypotheses for an exclusion test can be written as:

$$\text{Null hypothesis: } H_{s+b} = H(\mu = 1, \boldsymbol{\theta}) \tag{7.4}$$

$$\text{Test hypothesis: } H_b = H(\mu = 0, \boldsymbol{\theta}). \tag{7.5}$$

Following a frequentist approach and specifying a confidence level (CL) we can reject the null hypothesis, that is, that the observed data is compatible with a signal of HNL over the neutrino and cosmic backgrounds. In the absence of significative signal (the data is compatible with the SM prediction) this method allows μ to be constrained under a

limit value (μ_{exc}) as bigger values than μ_{exc} would have introduced significant differences between the background-only model and the observed data.

For SBND, no data is yet available and the estimated exclusion limits in Section 7.3 are performed assuming no HNL signal is found for three years of data equivalent to an exposure of 10^{21} POT.

7.2.1 Likelihood-based tests

In particle physics, a common practice for computing test statistics from multi-binned histograms of data is the use of likelihood-based functions [200]. In a general case, the likelihood function, $L(\mu, \boldsymbol{\theta})$, is built assuming each bin in the histogram follows a Poisson distribution:

$$L(\mu, \boldsymbol{\theta}) = \underbrace{\prod_{i=1}^{N} \frac{(\mu s_i + b_i)^{n_i}}{n_i!} e^{-(\mu s_i + b_i)}}_{\text{Poisson product}} \underbrace{\prod_{\theta \in \boldsymbol{\theta}} c_\theta(a_\theta|\theta)}_{\text{Nuisance parameters}} . \tag{7.6}$$

The first term in Equation 7.6 is the product of the Poisson distribution in each bin while the second are the constraint terms $c_\theta(a_\theta|\theta)$ with a measurement a_θ on the nuisance parameter $\theta \in \boldsymbol{\theta}$. Constraint terms can parametrize the systematic uncertainties, for example, the uncertainty in the POT counting from the BNB. Then, the profile likelihood ratio [200] is taken as:

$$\lambda(\mu) = \frac{L(\mu, \hat{\hat{\boldsymbol{\theta}}}(\mu))}{L(\hat{\mu}, \hat{\boldsymbol{\theta}})} \tag{7.7}$$

with $\hat{\hat{\boldsymbol{\theta}}}(\mu)$ the value of $\boldsymbol{\theta}$ that maximizes L for a given μ, and $L(\hat{\mu}, \hat{\boldsymbol{\theta}})$ the *unconditional* maximized likelihood for the best fit of the parameters $(\hat{\mu}, \hat{\boldsymbol{\theta}})$ to the observed data. Since the presence of HNLs can only increase the expected number of events, a slightly modified version of the ratio is defined for cases where numerical solutions with $\hat{\mu} < 0$ may appear:

$$\bar{\lambda}(\mu) = \begin{cases} \frac{L(\mu, \hat{\hat{\boldsymbol{\theta}}}(\mu))}{L(0, \hat{\hat{\boldsymbol{\theta}}}(0))} & \hat{\mu} < 0 \\ \frac{L(\mu, \hat{\hat{\boldsymbol{\theta}}}(\mu))}{L(\hat{\mu}, \hat{\boldsymbol{\theta}})} & \hat{\mu} \geq 0 \end{cases} \tag{7.8}$$

Following Equation 7.8, a test statistic for upper limits can be derived [200]:

$$\bar{q}_\mu = \begin{cases} -2\ln\bar{\lambda}(\mu) & \hat{\mu} \leq \mu \\ 0 & \hat{\mu} > \mu \end{cases} = \begin{cases} -2\ln\frac{L(\mu,\hat{\hat{\boldsymbol{\theta}}}(\mu))}{L(0,\hat{\hat{\boldsymbol{\theta}}}(0))} & \hat{\mu} < 0. \\ -2\ln\frac{L(\mu,\hat{\hat{\boldsymbol{\theta}}}(\mu))}{L(\hat{\mu},\hat{\boldsymbol{\theta}})} & 0 \leq \hat{\mu} \leq \mu, \\ 0 & \hat{\mu} > \mu \end{cases} \tag{7.9}$$

and the associated probability density function (PDF) $f(\bar{q}_\mu|\mu)$ for a given pair of $\mu, \hat{\mu}$.

7.2.2 CL$_s$ Method

Once the PDFs are estimated, the probabilities (in a frequentist interpretation) of the signal + background and background only hypotheses can be obtained by integrating:

$$p_{s+b} = \int_{\hat{q}}^{\infty} f(\bar{q}_\mu|s+b)d\bar{q}_\mu \tag{7.10}$$

$$p_b = \int_{-\infty}^{\hat{q}} f(\bar{q}_\mu|b)d\bar{q}_\mu \tag{7.11}$$

where p_{s+b} represents the probability of the signal + background hypothesis to produce a more background-like result than the data, and p_b the probability of the only-background hypothesis producing a more signal-like result. This is depicted in Figure 7.2 where the shaded areas correspond to the respective probabilities of only-background and background plus signal hypothesis.

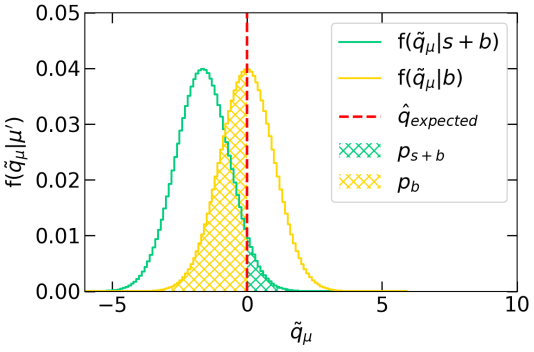

Figure 7.2: Example of $\bar{q}_\mu$ distributions using the asymptotic approximation. The distribution is shown for an expected signal strength μ corresponding to a CL$_s$ < 0.1. The expected $\bar{q}$ value is shown in red.

Finally, a criteria is needed to associate probabilities or p-values of the hypotheses with the physical parameters of interest. Historically, the approach developed for Higgs searches at LEP [201] assumes the experiment is close to the discovery limit with a

significant background present and a (potentially) small signal. To reduce the effects of statistical fluctuation the ratio CL_s is defined as:

$$CL_s = \frac{CL_{s+b}}{CL_b} = \frac{p_{s+b}}{1 - p_b}. \tag{7.12}$$

Because the denominator will always be smaller or equal to one, the $CL_s \geq CL_{s+b}$ relation holds, making CL_s a conservative estimation. The upper limit is the value $\mu_{\mathrm{exc}} = \mu_\alpha$ such as that $1 - \mathrm{CL}_s < \alpha$ with $\alpha = 0.1$ corresponding to a confidence level of 90%. Similarly, variations from the central value CL_s can be computed. They provide an estimation of how sensitive the result is to a small variation in the observed data.

To estimate the PDFs and compute the exclusion limits the **pyhf** package was used [202, 203]. The module provides a Python interface for the HistFactory software implemented in ROOT [204]. To find the closest μ value to the CL required, **pyhf** scans a range of μ values, calculating the PDFs for each one using asymptotic approximations. To validate the performance, the results of the package were compared with analytical formulas finding good agreement ([205] and references therein). In particular, the results merging and splitting the signal and backgrounds in multiple bins were compared to the exclusion formula under the Asimov approximation for a counting experiment.

Once the exclusion limit μ_{exc} has been found, the corresponding $|U_{\mu 4}|^2$ coupling is derived from the number of signal events (S) following $S \propto |U_{\mu 4}|^4$ (see Appendix B). For the determination of the HNL exclusion limits presented in the next section, the background and signal histograms obtained in Section 6.7 are employed. The background-only distribution contains only cosmic and BNB-neutrino events, while the background + signal hypothesis consist of the sum of both the SM and the HNL distributions.

7.3 Results

Table 7.1 summarizes the expected exclusion limits of SBND to a μ-coupled Majorana HNL produced from kaon two body decays for different mass points: 10, 35, 50, 75, 100, 125, 150 MeV and three years of data (10^{21} POT). The three selections considered are detailed in Section 6.7:

- The conservative selection: corresponding to a BDT score cut of 0.3. Distributions for each mass point are shown in Appendix D.
- The aggressive selection: corresponding to a BDT score cut of 0.5. Distributions for each mass point are shown in Appendix E.

- The projected sensitivity, assuming an enhancement of both reconstruction and time resolution of the SBND subsystems. Distributions input to **pyhf** can be found in Appendix F.

	Mass [MeV]	Expected $\|U_{\mu 4}\|^2$ Limit	+1σ	-1σ	+2σ	-2σ
Conservative	10	3.95×10^{-3}	5.79×10^{-3}	2.8×10^{-3}	7.95×10^{-3}	2.0×10^{-3}
	35	7.71×10^{-5}	1.11×10^{-4}	5.38×10^{-5}	1.54×10^{-4}	3.95×10^{-5}
	50	2.46×10^{-5}	3.55×10^{-5}	1.72×10^{-5}	4.92×10^{-5}	1.26×10^{-5}
	75	6.65×10^{-6}	9.58×10^{-6}	4.64×10^{-6}	1.33×10^{-5}	3.39×10^{-6}
	100	2.28×10^{-6}	3.28×10^{-6}	1.59×10^{-6}	4.51×10^{-6}	1.16×10^{-6}
	125	9.87×10^{-7}	1.42×10^{-6}	6.89×10^{-7}	1.97×10^{-6}	5.04×10^{-7}
	150	4.4×10^{-7}	6.35×10^{-7}	3.07×10^{-7}	8.79×10^{-7}	2.23×10^{-7}
Aggressive	10	3.3×10^{-3}	4.84×10^{-3}	2.33×10^{-3}	6.68×10^{-3}	1.66×10^{-3}
	35	6.57×10^{-5}	9.48×10^{-5}	4.58×10^{-5}	1.32×10^{-4}	3.36×10^{-5}
	50	2.11×10^{-5}	3.05×10^{-5}	1.47×10^{-5}	4.24×10^{-5}	1.08×10^{-5}
	75	5.69×10^{-6}	8.22×10^{-6}	3.97×10^{-6}	1.14×10^{-5}	2.9×10^{-6}
	100	2.02×10^{-6}	2.92×10^{-6}	1.41×10^{-6}	4.01×10^{-6}	1.03×10^{-6}
	125	8.86×10^{-7}	1.28×10^{-6}	6.19×10^{-7}	1.77×10^{-6}	4.54×10^{-7}
	150	4.32×10^{-7}	6.25×10^{-7}	3.02×10^{-7}	8.64×10^{-7}	2.19×10^{-7}
Smeared True	10	1.61×10^{-3}	2.19×10^{-3}	1.18×10^{-3}	2.96×10^{-3}	8.96×10^{-4}
	35	2.94×10^{-5}	4.03×10^{-5}	2.19×10^{-5}	5.29×10^{-5}	1.68×10^{-5}
	50	9.36×10^{-6}	1.28×10^{-5}	6.92×10^{-6}	1.68×10^{-5}	5.29×10^{-6}
	75	2.45×10^{-6}	3.29×10^{-6}	1.82×10^{-6}	4.31×10^{-6}	1.41×10^{-6}
	100	8.03×10^{-7}	1.10×10^{-6}	5.92×10^{-7}	1.45×10^{-6}	4.54×10^{-7}
	125	3.38×10^{-7}	4.59×10^{-7}	2.50×10^{-7}	6.01×10^{-7}	1.93×10^{-7}
	150	1.60×10^{-7}	2.22×10^{-7}	1.17×10^{-7}	2.97×10^{-7}	8.90×10^{-8}

Table 7.1: Summary of expected limits on the coupling $|U_{\mu 4}|^2$ of Majorana HNLs at 90% C.L. predicted for three years of SBND data or 10^{21} POT.

Figure 7.3 shows the exclusion limits at 90% confidence level for the conservative and aggressive selections with the 1σ and 2σ bands. The results are similar between the aggressive and conservative (less affected by statistical uncertainties of the background) selections. The sensitivity is driven mainly by the side-band bins away from the beam bunch which are background free in both cases for this selection. For the conservative selection this represents values of $|U_{\mu 4}|^2$ varying from 3.3×10^{-3} for the lower mass up to 4.4×10^{-7} for a 150 MeV HNL signal. The aggressive selection, with a superior background suppression ($\times 4$ factor) improves the results by $\sim$10%. Both selections are compatible within the uncertainties considered.

Figure 7.4 presents the central values obtained for the conservative and aggressive selections as well as the estimation with truth information assuming an increasing factor of two in the timing resolution and the signal selection efficiency. For the estimation using truth information, both enhancements play a significant role. The increase of signal

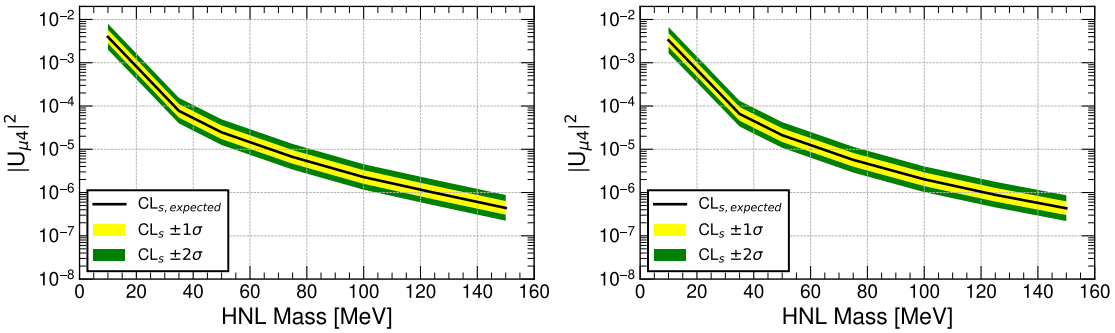

Figure 7.3: Plots showing the upper limits at 90% CL on the mixing element $|U_{\mu 4}|^2$ for different Majorana HNL masses for both the conservative (left) and aggressive (right) selections in three years of SBND data or 10^{21} POT.

selection efficiency represents a factor of $\times 1.55$ in the $|U_{\mu 4}|^2$ limit, while the increase in the time resolution improves the result by a factor of $\times 1.6$. This shows SBND capabilities to achieve better results in the near future, when more sophisticated reconstruction techniques are employed.

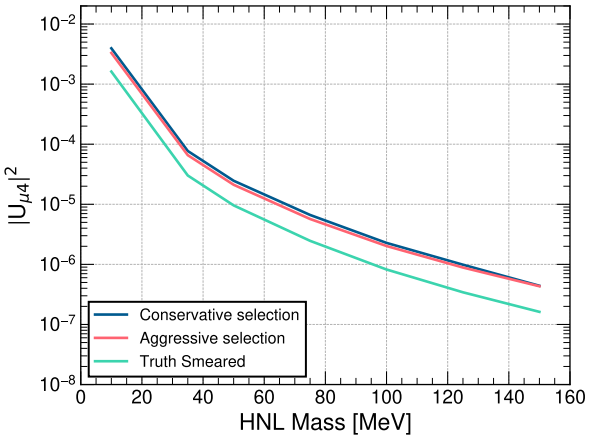

Figure 7.4: $|U_{\mu 4}|^2$ upper limits at 90% CL comparison between the reconstructed and the truth approach for the νee final state for different Majorana HNL masses in three years of SBND data or 10^{21}.

Additional features could be exploited such as the angular dependence of the energy spectra of SM neutrinos. For the NCπ^0 background in the case where both showers are reconstructed, an estimation of the invariant mass may allow to separate both populations. If the electron-positron pair is reconstructed in a single shower, a precise determination of the dE/dx is key to distinguish HNL events from the the CCν_e backgrounds as CCν_e events are started by a single electron. Thus, this search could benefit from specific tunings of the shower clustering algorithms that identify forward-focused showers. Different approaches such as convolutional neural networks could be applied to improve the clustering of both shower and track topologies [206, 207]. Finally, specific selections for each HNL mass can improve the signal selection efficiency as both the

opening angle between the electrons and the angle of the leading shower and the beam increase with the HNL mass.

For the timing resolution, the current optical hit-finding of the PMT reconstruction uses a single point of each PMT waveform (the rise time) to determine the time of the optical hit. A fit to the complete rising profile à la MicroBooNE [83] will increase the hit timing resolution and thus, the flash time resolution. To better estimate the photon propagation, the drift coordinate can be determined with TPC information. For example, the Pandora vertex of the slice (cm resolution) could be used once the flash and TPC info has been *matched*. In addition, time studies with raw waveforms may prevent the artifacts and smearing effects caused by the deconvolution workflow.

7.3.1 Comparison with other experiments

The results obtained in this analysis for the aggressive selection are compared with reported values from different experiments [65, 67–69, 208] in Figure 7.5. The projected result assuming a factor of $\times 2$ increase in SBND timing resolution and signal selection efficiency is also shown. The current SBND reconstruction chain is capable of producing a competitive first result using ns-timing for a physics analysis in this channel assuming three years of data (10^{21}).

Both aggressive and conservative selections improve the result obtained by MicroBooNE, the leading experiment in the 30–175 MeV range. In both cases there is a kinematic variable that separates the SM neutrino backgrounds from the signal. In SBND, that variable is the absolute arrival time at SBND, which is delayed for the HNLs. In MicroBooNE, the analysis assumes HNLs are produced by the NuMI absorber, approaching the detector in almost the opposite direction compared to the neutrinos from the NuMI beam target. For this reason, both searches can produce comparable results if the expected number of HNLs in both detectors is similar. For comparison, the MicroBooNE analysis after a minimal preselection predicts approximately 1300 HNL events in the detector from the NuMI beam for an HNL mass of 100 MeV and a $|U_{\mu 4}|^2 = 2 \times 10^{-5}$ [65]. For the same coupling and mass, a total 2644 HNL events are expected in SBND's fiducial volume from the BNB with three years of data applying the preselection described in Section 6.7.

The searches in the low mass range are led by the SIN [208] and PIENU [68] results. In both cases, the decay from positive stopping pions was measured with high statistics looking for peaks in the energy spectrum of the outgoing muon. Although SBND's result is not competitive in the low mass range, the HNL production from pion decays has not

been included in this work and will improve the limit presented in Figure 7.5 for HNL events with a mass below 30 MeV.

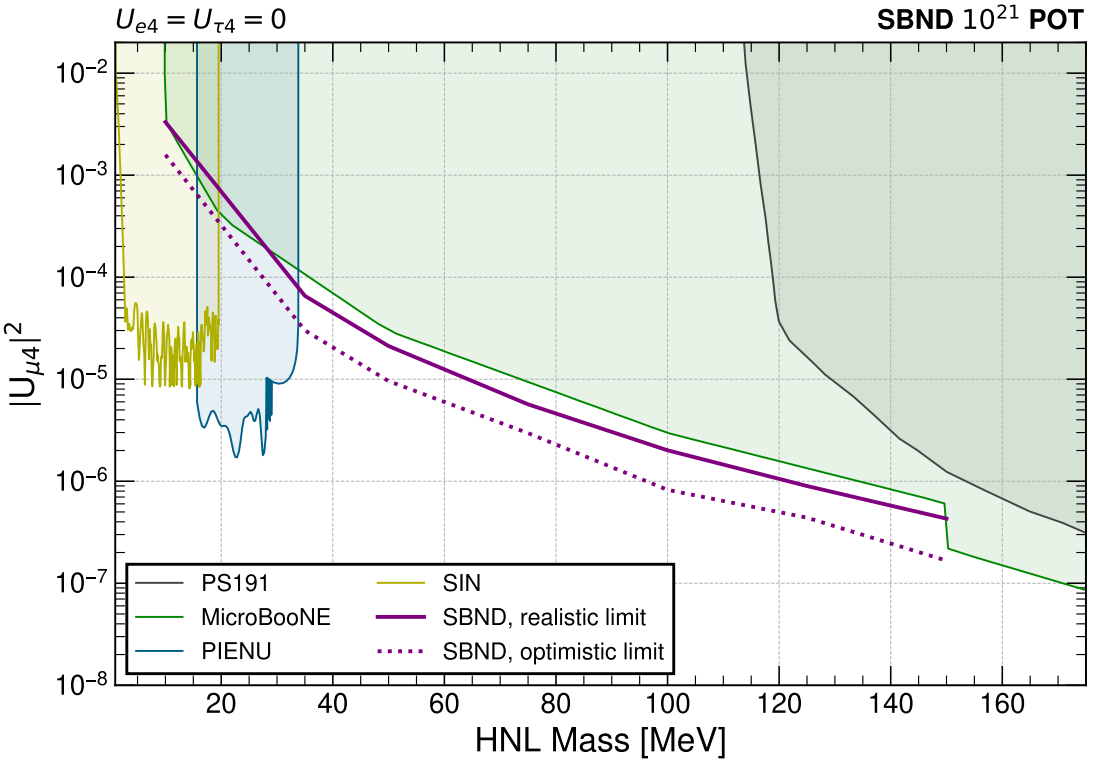

Figure 7.5: Upper limits on the coupling $|U_{\mu 4}|^2$ at the 90% confidence level for Majorana HNLs in the mass range of $1 < m_N < 175$ MeV. SBND expected limits for an exposure of 10^{21} POT are compared with existing experimental results, including SIN [208], PIENU [68], MicroBooNE [65] and PS191 [67].

In the next decade, DUNE, using its gaseous near detector (NDGAr), will be able to explore beyond the limits of these MeV-scale HNLs by an order of magnitude for HNL masses up to 490 MeV thanks to its superior statistics and a reduced neutrino background due to the lower density of the target [209]. Above the kaon mass, the SHiP experiment at CERN will look for μ-coupled HNLs with masses up to 5 GeV [210].

Conclusions

The Short-Baseline Near Detector (SBND) at Fermilab has been installed and filled with liquid argon. The experiment is being commissioned and early physics runs have begun. In the upcoming years, SBND and the Short-Baseline Neutrino (SBN) program will test the light sterile neutrino ($\sim$ 1 eV) hypothesis and perform other Beyond Standard Model (BSM) searches measuring with high precision the neutrino flux of the Booster Neutrino Beam (BNB).

Novel photon detection systems will be tested in SBND. 192 X-ARAPUCA photo-sensor modules, a new technology that traps the incoming photons in a highly reflective box equipped with silicon photo-multipliers (SiPMs), have been installed. They will operate for three years in cryogenic conditions capturing liquid argon scintillation photons and the visible light produced by the TPB-coated reflective foils placed in the middle of the detector.

To better understand and characterize SBND's X-ARAPUCA system, two pTP-coated units have been tested in liquid argon at CIEMAT. A complete suite of tools to analyze the laboratory data was also developed. Measurements of the X-ARAPUCAs photon detection efficiency (PDE) to the vacuum ultraviolet (VUV) scintillation light were performed using the light produced by alpha particles from a radioactive source. Thanks to the use of four reference Hamamatsu VUV4 SiPMs in the setup whose efficiency is known, the measurements are independent of the purity of the liquid argon. X-ARAPUCAs equipped with Hamamatsu S13360-6050-VE SiPMs and Glass to Power Blue wavelength-shifter bar showed PDE values to VUV light between 1.99% and 2.29% for overvoltages in the 2–3 V range. The VUV efficiency of X-ARAPUCAs with Onsemi MICROFC-30050-SMT SiPMs and Eljen EJ-286 wavelength-shifter bar was a bit lower than previous configuration in the 1.27%–2.20% range for overvoltages of 3.25 V and 5.75 V due to the lower efficiency of the Onsemi SiPMs and Eljen WLS bar.

The transmittance of the dichroic filters in the low-visible range ($\sim$ 400 nm) highly depends on the angle of incidence (AOI) of the light. For this reason, part of the visible light emitted by the TPB is captured unintendedly by the coated X-ARAPUCAs.

A laser centered at 420 nm (close to the TPB emission peak) was used to measure the X-ARAPUCA PDE to the 420 nm visible light. A PDE to the visible light as a function of the AOI was estimated. Taking into account the angular distributions at the CIEMAT setup and SBND, an average PDE to visible light at SBND was estimated. The PDE_{420nm} values were found to be in the 0.3%–0.45% range for both X-ARAPUCA units.

From calibration data runs, the correlated crosstalk was estimated. The measured crosstalk values of the Onsemi X-ARAPUCA (20.5%–42.4%) are consistently higher than the ones of the Hamamatsu X-ARAPUCA (6%–10%), as expected based on the SiPM performance reported by manufacturers. Data taken with the 420 nm laser at high intensity showed no deviation of the X-ARAPUCA from the linear regime up to 800 PEs, above the charge range expected at SBND.

Several developments were added to the SBND X-ARAPUCA signal simulation and reconstruction. The measured PDE and crosstalk values were included in the simulations. A realistic response of the X-ARAPUCA sensors was derived using data from a cryogenic test-stand at Fermilab. The detector simulation was also updated to better reproduce the continuous behavior of the pulses. A deconvolution and Gauss filtering was applied to remove the undershooting of the detector response and recover the original photon distribution. The optical hit and flash reconstruction algorithms were optimized to increase the reconstruction efficiency and the timing resolution.

The performance of the light detection system was evaluated using a sample of simulated Standard Model (SM) neutrinos from the BNB with a cosmic-muon overlay. The overall reconstruction efficiency of interacions with the X-ARAPUCA system is 92.2%. On average, the detected light yield by the X-ARAPUCA system was estimated in 7.7 PE/MeV, varying with the energy deposition distance to the photon detection system (PDE). The three spatial coordinates of the interaction were reconstructed with a resolution between 19–27 cm using only light information, which serves as a crosscheck to the TPC system. Selecting neutrino events with more than 200 MeV of deposited energy, an interaction time resolution of 3.05 ± 0.04 ns was obtained using only the X-ARAPUCA system, sufficient to resolve the BNB bunch structure. This is of particular importance in the search of massive BSM particles that can be produced by the BNB, as they propagate slower due to their heavier mass and arrive at SBND after the SM neutrinos. A precise timing allows searches between the BNB bunches in regions free of backgrounds from the SM neutrinos produced by the beam.

I performed the first sensitivity estimation of the search for μ-coupled heavy neutral leptons (HNLs) produced in kaon two-body decays from the BNB, and decaying into

an electron-positron pair and a neutrino in SBND. To simulate the HNL events, I incorporated the complete BNB meson flux to MeVPrtl, the BSM Monte Carlo (MC) generator of the SBN program. I participated in the validation and integration of the simulated channel in SBND's simulation framework, and generated the HNL samples between 10 and 150 MeV used in the analysis. The simulated signal and background events underwent a complete detector simulation. I used the results from the current SBND reconstruction chain combining information from the photon detection system, the TPC and the cosmic-ray tagger systems to train a dedicated boosted decision tree that selects HNL events. The HNL selection efficiency is 12.5% suppressing the contamination from SM events by more than a factor of 10^3. In addition, future sensitivity assuming an enhancement of the signal selection efficiency and the timing resolution was estimated. The obtained selections were used to produce exclusion limits to μ-coupled HNLs in this channel assuming no signal is observed after three years of data. The resulting limits to the $|U_{\mu 4}|^2$parameter, with values in the $[3.30 \times 10^{-3}$–$4.32 \times 10^{-7}]$ range, are world-leading surpassing MicroBooNE's results in the 30–150 MeV range. This demonstrates SBND's capabilities in this type of search.

In my firsts years I participated in the data taking and analysis of different prototypes of the DUNE X-ARAPUCA models. The light reconstruction developments applied in SBND have also been shared with the DUNE PDS group. During my stays at Fermilab I participated in the installation and commissioning of the SBND PDS. Thanks to the grant received from the Fermilab Neutrino Physics Center, I was able to stay at Fermilab developing the calibration software tools for the SBND X-ARAPUCAs using the late light pulses from scintillation signals (not included in this thesis).

In the upcoming years, SBND and the SBN program will record millions of neutrino events allowing the search for physics beyond the Standard Model, improving our understanding of the neutrino interactions, and paving the way for the next generation of LArTPC experiments.

Bibliography

[1] Wolfgang Pauli. Pauli's letter of the 4th of december 1930, 1930.

[2] J. Chadwick. The intensity distribution in the magnetic spectrum of β particles from radium (B + C). *Verh. Phys. Gesell.*, 16:383–391, 1914.

[3] J. Chadwick. Possible Existence of a Neutron. *Nature*, 129:312, 1932. doi: 10.1038/129312a0.

[4] J. Chadwick. The Existence of a Neutron. *Proc. Roy. Soc. Lond. A*, 136(830): 692–708, 1932. doi: 10.1098/rspa.1932.0112.

[5] W. Heisenberg. On the structure of atomic nuclei. *Z. Phys.*, 77:1–11, 1932. doi: 10.1007/BF01342433.

[6] Dmitri Iwanenko. The neutron hypothesis. *Nature*, 129(3265):798–798, 1932.

[7] E. Fermi. An attempt of a theory of beta radiation. 1. *Z. Phys.*, 88:161–177, 1934. doi: 10.1007/BF01351864.

[8] F. Reines and C. L. Cowan. Detection of the free neutrino. *Phys. Rev.*, 92:830–831, 1953. doi: 10.1103/PhysRev.92.830.

[9] Frederick Reines and Clyde L. Cowan. The neutrino. *Nature*, 178:446–449, 1956. doi: 10.1038/178446a0.

[10] G. Danby, J. M. Gaillard, Konstantin A. Goulianos, L. M. Lederman, Nari B. Mistry, M. Schwartz, and J. Steinberger. Observation of High-Energy Neutrino Reactions and the Existence of Two Kinds of Neutrinos. *Phys. Rev. Lett.*, 9:36–44, 1962. doi: 10.1103/PhysRevLett.9.36.

[11] K. Kodama et al. Observation of tau neutrino interactions. *Phys. Lett. B*, 504: 218–224, 2001. doi: 10.1016/S0370-2693(01)00307-0.

[12] S. Navas et al. Review of particle physics. *Phys. Rev. D*, 110(3):030001, 2024. doi: 10.1103/PhysRevD.110.030001.

[13] Kai Zuber. *Neutrino Physics*. Taylor & Francis, Boca Raton, 2020. ISBN 978-1-351-76458-2, 978-1-315-19561-2, 978-1-032-24220-0, 978-1-138-71889-0. doi: 10.1201/9781315195612.

[14] S. Schael et al. Precision electroweak measurements on the Z resonance. *Phys. Rept.*, 427:257–454, 2006. doi: 10.1016/j.physrep.2005.12.006.

[15] A. G. Adame et al. DESI 2024 VI: Cosmological Constraints from the Measurements of Baryon Acoustic Oscillations, 4 2024.

[16] M. Aker et al. Direct neutrino-mass measurement based on 259 days of KATRIN data, 6 2024. URL https://arxiv.org/abs/2406.13516.

[17] Matteo Agostini, Giovanni Benato, Jason A. Detwiler, Javier Menéndez, and Francesco Vissani. Toward the discovery of matter creation with neutrinoless $\beta\beta$ decay. *Rev. Mod. Phys.*, 95(2):025002, 2023. doi: 10.1103/RevModPhys.95.025002.

[18] S. Abe et al. Search for Majorana Neutrinos with the Complete KamLAND-Zen Dataset, 6 2024. URL https://arxiv.org/abs/2406.11438.

[19] M. Aker et al. Direct neutrino-mass measurement with sub-electronvolt sensitivity. *Nature Phys.*, 18(2):160–166, 2022. doi: 10.1038/s41567-021-01463-1.

[20] R. Davis. A review of the Homestake solar neutrino experiment. *Prog. Part. Nucl. Phys.*, 32:13–32, 1994. doi: 10.1016/0146-6410(94)90004-3.

[21] K. S. Hirata et al. Real time, directional measurement of B-8 solar neutrinos in the Kamiokande-II detector. *Phys. Rev. D*, 44:2241, 1991. doi: 10.1103/PhysRevD.44.2241. [Erratum: Phys.Rev.D 45, 2170 (1992)].

[22] K. S. Hirata et al. Observation of B-8 Solar Neutrinos in the Kamiokande-II Detector. *Phys. Rev. Lett.*, 63:16, 1989. doi: 10.1103/PhysRevLett.63.16.

[23] P. Anselmann et al. Solar neutrinos observed by GALLEX at Gran Sasso. *Phys. Lett. B*, 285:376–389, 1992. doi: 10.1016/0370-2693(92)91521-A.

[24] D. Casper et al. Measurement of atmospheric neutrino composition with IMB-3. *Phys. Rev. Lett.*, 66:2561–2564, 1991. doi: 10.1103/PhysRevLett.66.2561.

[25] K. S. Hirata et al. Experimental Study of the Atmospheric Neutrino Flux. *Phys. Lett. B*, 205:416, 1988. doi: 10.1016/0370-2693(88)91690-5.

[26] C. V. Achar et al. Detection of muons produced by cosmic ray neutrinos deep underground. *Phys. Lett.*, 18:196–199, 1965. doi: 10.1016/0031-9163(65)90712-2.

[27] F. Reines, M. F. Crouch, T. L. Jenkins, W. R. Kropp, H. S. Gurr, G. R. Smith, J. P. F. Sellschop, and B. Meyer. Evidence for high-energy cosmic ray neutrino interactions. *Phys. Rev. Lett.*, 15:429–433, 1965. doi: 10.1103/PhysRevLett.15.429.

[28] F. Reines, W. R. Kropp, H. W. Sobel, H. S. Gurr, J. Lathrop, M. F. Crouch, J. P. F. Sellschop, and B. S. Meyer. Muons produced by atmospheric neutrinos: Experiment. *Phys. Rev. D*, 4:80–98, 1971. doi: 10.1103/PhysRevD.4.80.

[29] Y. Fukuda et al. Evidence for oscillation of atmospheric neutrinos. *Phys. Rev. Lett.*, 81:1562–1567, 1998. doi: 10.1103/PhysRevLett.81.1562.

[30] Q. R. Ahmad et al. Direct evidence for neutrino flavor transformation from neutral current interactions in the Sudbury Neutrino Observatory. *Phys. Rev. Lett.*, 89:011301, 2002. doi: 10.1103/PhysRevLett.89.011301.

[31] D. S. Ayres et al. The NOvA Technical Design Report. Technical report, Fermilab, 10 2007.

[32] K. Abe et al. The T2K Experiment. *Nucl. Instrum. Meth. A*, 659:106–135, 2011. doi: 10.1016/j.nima.2011.06.067.

[33] K. Eguchi et al. First results from KamLAND: Evidence for reactor anti-neutrino disappearance. *Phys. Rev. Lett.*, 90:021802, 2003. doi: 10.1103/PhysRevLett.90.021802.

[34] M. H. Ahn et al. Measurement of Neutrino Oscillation by the K2K Experiment. *Phys. Rev. D*, 74:072003, 2006. doi: 10.1103/PhysRevD.74.072003.

[35] B. Pontecorvo. Mesonium and anti-mesonium. *Sov. Phys. JETP*, 6:429, 1957.

[36] B. Pontecorvo. Inverse beta processes and nonconservation of lepton charge. *Zh. Eksp. Teor. Fiz.*, 34:247, 1957.

[37] Ziro Maki, Masami Nakagawa, and Shoichi Sakata. Remarks on the unified model of elementary particles. *Prog. Theor. Phys.*, 28:870–880, 1962. doi: 10.1143/PTP.28.870.

[38] Martin L. Perl et al. Evidence for Anomalous Lepton Production in e+ - e- Annihilation. *Phys. Rev. Lett.*, 35:1489–1492, 1975. doi: 10.1103/PhysRevLett.35.1489.

[39] Nicola Cabibbo. Unitary Symmetry and Leptonic Decays. *Phys. Rev. Lett.*, 10:531–533, 1963. doi: 10.1103/PhysRevLett.10.531.

[40] Makoto Kobayashi and Toshihide Maskawa. CP Violation in the Renormalizable Theory of Weak Interaction. *Prog. Theor. Phys.*, 49:652–657, 1973. doi: 10.1143/PTP.49.652.

[41] Hiroshi Nunokawa, Stephen J. Parke, and Renata Zukanovich Funchal. What fraction of boron-8 solar neutrinos arrive at the earth as a nu(2) mass eigenstate? *Phys. Rev. D*, 74:013006, 2006. doi: 10.1103/PhysRevD.74.013006.

[42] S. N. Ahmed et al. Measurement of the total active B-8 solar neutrino flux at the Sudbury Neutrino Observatory with enhanced neutral current sensitivity. *Phys. Rev. Lett.*, 92:181301, 2004. doi: 10.1103/PhysRevLett.92.181301.

[43] I. Esteban et al. Nufit5.2 at nufit webpage, 2024. http://www.nu-fit.org.

[44] R. Acciarri et al. Long-Baseline Neutrino Facility (LBNF) and Deep Underground Neutrino Experiment (DUNE): Conceptual Design Report, Volume 2: The Physics Program for DUNE at LBNF, 2015. URL https://arxiv.org/abs/1512.06148.

[45] K. Abe et al. Hyper-Kamiokande Design Report, 5 2018.

[46] Basudeb Dasgupta and Joachim Kopp. Sterile Neutrinos. *Phys. Rept.*, 928:1–63, 2021. doi: 10.1016/j.physrep.2021.06.002.

[47] A. Aguilar et al. Evidence for neutrino oscillations from the observation of $\bar{\nu}_e$ appearance in a $\bar{\nu}_\mu$ beam. *Phys. Rev. D*, 64:112007, 2001. doi: 10.1103/PhysRevD.64.112007.

[48] A. A. Aguilar-Arevalo et al. Significant Excess of ElectronLike Events in the MiniBooNE Short-Baseline Neutrino Experiment. *Phys. Rev. Lett.*, 121(22):221801, 2018. doi: 10.1103/PhysRevLett.121.221801.

[49] A. A. Aguilar-Arevalo et al. Updated MiniBooNE neutrino oscillation results with increased data and new background studies. *Phys. Rev. D*, 103(5):052002, 2021. doi: 10.1103/PhysRevD.103.052002.

[50] P. Abratenko et al. Search for an Excess of Electron Neutrino Interactions in MicroBooNE Using Multiple Final-State Topologies. *Phys. Rev. Lett.*, 128(24):241801, 2022. doi: 10.1103/PhysRevLett.128.241801.

[51] R. Acciarri et al. A Proposal for a Three Detector Short-Baseline Neutrino Oscillation Program in the Fermilab Booster Neutrino Beam, 3 2015.

[52] Pedro AN Machado, Ornella Palamara, and David W Schmitz. The Short-Baseline Neutrino Program at Fermilab. *Ann. Rev. Nucl. Part. Sci.*, 69:363–387, 2019. doi: 10.1146/annurev-nucl-101917-020949.

[53] Joel Kostensalo, Jouni Suhonen, Carlo Giunti, and Praveen C. Srivastava. The gallium anomaly revisited. *Phys. Lett. B*, 795:542–547, 2019. doi: 10.1016/j.physletb.2019.06.057.

[54] G. Mention, M. Fechner, Th. Lasserre, Th. A. Mueller, D. Lhuillier, M. Cribier, and A. Letourneau. The Reactor Antineutrino Anomaly. *Phys. Rev. D*, 83:073006, 2011. doi: 10.1103/PhysRevD.83.073006.

[55] C. Giunti, Y. F. Li, C. A. Ternes, and Z. Xin. Reactor antineutrino anomaly in light of recent flux model refinements. *Phys. Lett. B*, 829:137054, 2022. doi: 10.1016/j.physletb.2022.137054.

[56] N. Aghanim et al. Planck 2018 results. VI. Cosmological parameters. *Astron. Astrophys.*, 641:A6, 2020. doi: 10.1051/0004-6361/201833910. [Erratum: Astron.Astrophys. 652, C4 (2021)].

[57] P. Adamson et al. Improved Constraints on Sterile Neutrino Mixing from Disappearance Searches in the MINOS, MINOS+, Daya Bay, and Bugey-3 Experiments. *Phys. Rev. Lett.*, 125(7):071801, 2020. doi: 10.1103/PhysRevLett.125.071801.

[58] Samoil M. Bilenky, C. Giunti, W. Grimus, and T. Schwetz. Four neutrino mass spectra and the Super-Kamiokande atmospheric up - down asymmetry. *Phys. Rev. D*, 60:073007, 1999. doi: 10.1103/PhysRevD.60.073007.

[59] M. Maltoni, T. Schwetz, and J. W. F. Valle. Cornering (3+1) sterile neutrino schemes. *Phys. Lett. B*, 518:252–260, 2001. doi: 10.1016/S0370-2693(01)01068-1.

[60] Asli M. Abdullahi et al. The present and future status of heavy neutral leptons. *J. Phys. G*, 50(2):020501, 2023. doi: 10.1088/1361-6471/ac98f9.

[61] Nicolò Foppiani. *Testing explanations of short baseline neutrino anomalies*. PhD thesis, Harvard U. (main), Harvard U., 8 2022.

[62] Evgeny Kh. Akhmedov and Alexei Yu. Smirnov. Paradoxes of neutrino oscillations. *Phys. Atom. Nucl.*, 72:1363–1381, 2009. doi: 10.1134/S1063778809080122.

[63] P. Abratenko et al. Search for Heavy Neutral Leptons Decaying into Muon-Pion Pairs in the MicroBooNE Detector. *Phys. Rev. D*, 101(5):052001, 2020. doi: 10.1103/PhysRevD.101.052001.

[64] P. Abratenko et al. Search for long-lived heavy neutral leptons and Higgs portal scalars decaying in the MicroBooNE detector. *Phys. Rev. D*, 106(9):092006, 2022. doi: 10.1103/PhysRevD.106.092006.

[65] P. Abratenko et al. Search for Heavy Neutral Leptons in Electron-Positron and Neutral-Pion Final States with the MicroBooNE Detector. *Phys. Rev. Lett.*, 132 (4):041801, 2024. doi: 10.1103/PhysRevLett.132.041801.

[66] K. Abe et al. Search for heavy neutrinos with the T2K near detector ND280. *Phys. Rev. D*, 100(5):052006, 2019. doi: 10.1103/PhysRevD.100.052006.

[67] Carlos A. Argüelles, Nicolò Foppiani, and Matheus Hostert. Heavy neutral leptons below the kaon mass at hodoscopic neutrino detectors. *Phys. Rev. D*, 105:095006, May 2022. doi: 10.1103/PhysRevD.105.095006. URL https://link.aps.org/doi/10.1103/PhysRevD.105.095006.

[68] A. Aguilar-Arevalo et al. Search for heavy neutrinos in $\pi \to \mu\nu$ decay. *Phys. Lett. B*, 798:134980, 2019. doi: 10.1016/j.physletb.2019.134980.

[69] A. V. Artamonov et al. Search for heavy neutrinos in $K^+ \to \mu^+\nu_H$ decays. *Phys. Rev. D*, 91(5):052001, 2015. doi: 10.1103/PhysRevD.91.052001.

[70] Alexey Boyarsky, Maksym Ovchynnikov, Oleg Ruchayskiy, and Vsevolod Syvolap. Improved big bang nucleosynthesis constraints on heavy neutral leptons. *Phys. Rev. D*, 104(2):023517, 2021. doi: 10.1103/PhysRevD.104.023517.

[71] C. Rubbia. The Liquid Argon Time Projection Chamber: A New Concept for Neutrino Detectors. Technical report, CERN, 5 1977.

[72] R. Acciarri et al. Design and Construction of the MicroBooNE Detector. *JINST*, 12(02):P02017, 2017. doi: 10.1088/1748-0221/12/02/P02017.

[73] P. Abratenko et al. Search for Neutrino-Induced Neutral-Current Δ Radiative Decay in MicroBooNE and a First Test of the MiniBooNE Low Energy Excess under a Single-Photon Hypothesis. *Phys. Rev. Lett.*, 128:111801, 2022. doi: 10.1103/PhysRevLett.128.111801.

[74] C. A. Argüelles, I. Esteban, M. Hostert, Kevin J. Kelly, J. Kopp, P. A. N. Machado, I. Martinez-Soler, and Y. F. Perez-Gonzalez. MicroBooNE and the νe Interpretation of the MiniBooNE Low-Energy Excess. *Phys. Rev. Lett.*, 128(24):241802, 2022. doi: 10.1103/PhysRevLett.128.241802.

[75] S. Amerio et al. Design, construction and tests of the ICARUS T600 detector. *Nucl. Instrum. Meth. A*, 527:329–410, 2004. doi: 10.1016/j.nima.2004.02.044.

[76] C. Rubbia et al. Underground operation of the ICARUS T600 LAr-TPC: first results. *JINST*, 6:P07011, 2011. doi: 10.1088/1748-0221/6/07/P07011.

[77] L. Bagby et al. Overhaul and Installation of the ICARUS-T600 Liquid Argon TPC Electronics for the FNAL Short Baseline Neutrino Program. *JINST*, 16(01): P01037, 2021. doi: 10.1088/1748-0221/16/01/P01037.

[78] P. Abratenko et al. ICARUS at the Fermilab Short-Baseline Neutrino program: initial operation. *Eur. Phys. J. C*, 83(6):467, 2023. doi: 10.1140/epjc/s10052-023-11610-y.

[79] P. Abratenko et al. Search for long-lived heavy neutral leptons and Higgs portal scalars decaying in the MicroBooNE detector. *Phys. Rev. D*, 106(9):092006, 2022. doi: 10.1103/PhysRevD.106.092006.

[80] Vladimir Shiltsev. Fermilab Proton Accelerator Complex Status and Improvement Plans. *Mod. Phys. Lett. A*, 32(16):1730012, 2017. doi: 10.1142/S0217732317300129.

[81] A. A. Aguilar-Arevalo et al. The Neutrino Flux Prediction at MiniBooNE. *Phys. Rev. D*, 79:072002, 2009. doi: 10.1103/PhysRevD.79.072002.

[82] M. Backfish. MiniBooNE Resistive Wall Current Monitor. Technical report, Fermilab, 2013.

[83] P. Abratenko et al. First demonstration of O(1 ns) timing resolution in the MicroBooNE liquid argon time projection chamber. *Phys. Rev. D*, 108(5):052010, 2023. doi: 10.1103/PhysRevD.108.052010.

[84] Supraja Balasubramanian. Beyond the Standard Model New Physics Searches with SBND †. *Phys. Sci. Forum*, 8(1):68, 2023. doi: 10.3390/psf2023008068.

[85] S. Agostinelli et al. GEANT4–a simulation toolkit. *Nucl. Instrum. Meth. A*, 506: 250–303, 2003. doi: 10.1016/S0168-9002(03)01368-8.

[86] G. Cheng et al. Measurement of K^+ production cross section by 8 GeV protons using high-energy neutrino interactions in the SciBooNE detector. *Phys. Rev. D*, 84:012009, 7 2011. doi: 10.1103/PhysRevD.84.012009. URL https://link.aps.org/doi/10.1103/PhysRevD.84.012009.

[87] Tadayoshi Doke, Kimiaki Masuda, and Eido Shibamura. Estimation of absolute photon yields in liquid argon and xenon for relativistic (1 MeV) electrons. *Nucl. Instrum. Meth. A*, 291:617–620, 1990. doi: 10.1016/0168-9002(90)90011-T.

[88] Lancaster University. Dune uk: experimental setup, 2022. https://wp.lancs.ac.uk/dune/dune-uk/experimental-setup/.

[89] M. Babicz et al. A measurement of the group velocity of scintillation light in liquid argon. *JINST*, 15(09):P09009, 2020. doi: 10.1088/1748-0221/15/09/P09009.

[90] D. Caratelli. Neutrino identification with scintillation light in MicroBooNE. *JINST*, 15(03):C03023, 2020. doi: 10.1088/1748-0221/15/03/C03023.

[91] A. Bettini et al. A Study of the factors affecting the electron lifetime in ultrapure liquid argon. *Nucl. Instrum. Meth. A*, 305:177–186, 1991. doi: 10.1016/0168-9002(91)90532-U.

[92] Adam Abed Abud et al. Scintillation light detection in the 6-m drift-length ProtoDUNE Dual Phase liquid argon TPC. *Eur. Phys. J. C*, 82(7):618, 2022. doi: 10.1140/epjc/s10052-022-10549-w.

[93] B. Abi et al. First results on ProtoDUNE-SP liquid argon time projection chamber performance from a beam test at the CERN Neutrino Platform. *JINST*, 15(12):P12004, 2020. doi: 10.1088/1748-0221/15/12/P12004.

[94] Yichen Li et al. Measurement of Longitudinal Electron Diffusion in Liquid Argon. *Nucl. Instrum. Meth. A*, 816:160–170, 2016. doi: 10.1016/j.nima.2016.01.094.

[95] A. Abed Abud et al. Design, construction and operation of the ProtoDUNE-SP Liquid Argon TPC. *JINST*, 17(01):P01005, 2022. doi: 10.1088/1748-0221/17/01/P01005.

[96] Liquid argon properties (tables and calculators), 2021. https://lar.bnl.gov/properties/#refs.

[97] T. Doke. Fundamental Properties of Liquid Argon, Krypton and Xenon as Radiation Detector Media. *Portugal. Phys.*, 12:9–48, 1981.

[98] Krishan VJ Mistry. *Exploring Electron-neutrino–argon Interactions*. Springer, 2023.

[99] M. A. Hernandez-Morquecho et al. Measurements of Pion and Muon Nuclear Capture at Rest on Argon in the LArIAT Experiment, 2024. URL https://arxiv.org/abs/2408.05133.

[100] R. Acciarri et al. First Observation of Low Energy Electron Neutrinos in a Liquid Argon Time Projection Chamber. *Phys. Rev. D*, 95(7):072005, 2017. doi: 10.1103/PhysRevD.95.072005.

[101] P. Abratenko et al. Measurement of the flux-averaged inclusive charged-current electron neutrino and antineutrino cross section on argon using the NuMI beam and the MicroBooNE detector. *Phys. Rev. D*, 104(5):052002, 2021. doi: 10.1103/PhysRevD.104.052002.

[102] Yiwen Xiao. Purity monitoring for ProtoDUNE-SP. *J. Phys. Conf. Ser.*, 2156: 012211, 2021. doi: 10.1088/1742-6596/2156/1/012211.

[103] P. Abratenko et al. Measurement of space charge effects in the MicroBooNE LArTPC using cosmic muons. *JINST*, 15(12):P12037, 2020. doi: 10.1088/1748-0221/15/12/P12037.

[104] Norman Gee, M Antonio Floriano, Toshinori Wada, Sam S-S Huang, and Gordon R Freeman. Ion and electron mobilities in cryogenic liquids: Argon, nitrogen, methane, and ethane. *Journal of applied physics*, 57(4):1097–1101, 1985.

[105] Gray Putnam and D. W. Schmitz. Effect of diffusion on the peak value of energy loss observed in a LArTPC. *JINST*, 17(10):P10044, 2022. doi: 10.1088/1748-0221/17/10/P10044.

[106] T. Heindl, T. Dandl, M. Hofmann, R. Krucken, L. Oberauer, W. Potzel, J. Wieser, and A. Ulrich. The scintillation of liquid argon. *EPL*, 91(6):62002, 2010. doi: 10.1209/0295-5075/91/62002.

[107] J. Soto-Oton. Impact of xenon doping in the scintillation light in a large liquid-argon TPC. *J. Phys. Conf. Ser.*, 2374:012164, 2022. doi: 10.1088/1742-6596/2374/1/012164.

[108] Akira Hitachi, Tan Takahashi, Nobutaka Funayama, Kimiaki Masuda, Jun Kikuchi, and Tadayoshi Doke. Effect of ionization density on the time dependence of luminescence from liquid argon and xenon. *Phys. Rev. B*, 27:5279–5285, 1983. doi: 10.1103/PhysRevB.27.5279.

[109] P. Agnes et al. DarkSide-50 532-day Dark Matter Search with Low-Radioactivity Argon. *Phys. Rev. D*, 98(10):102006, 2018. doi: 10.1103/PhysRevD.98.102006.

[110] Emily Grace and James A. Nikkel. Index of refraction, Rayleigh scattering length, and Sellmeier coefficients in solid and liquid argon and xenon. *Nucl. Instrum. Meth. A*, 867:204–208, 2017. doi: 10.1016/j.nima.2017.06.031.

[111] Shinzou Kubota, Masahiko Hishida, Masayo Suzuki, and Jian-zhi Ruan(Gen). Dynamical behavior of free electrons in the recombination process in liquid argon, krypton, and xenon. *Phys. Rev. B*, 20(8):3486, 1979. doi: 10.1103/PhysRevB.20.3486.

[112] W. Foreman et al. Calorimetry for low-energy electrons using charge and light in liquid argon. *Phys. Rev. D*, 101(1):012010, 2020. doi: 10.1103/PhysRevD.101.012010.

[113] C. Brizzolari et al. Enhancement of the X-Arapuca photon detection device for the DUNE experiment. *JINST*, 16(09):P09027, 2021. doi: 10.1088/1748-0221/16/09/P09027.

[114] R. Álvarez-Garrote et al. Measurement of the absolute efficiency of the X-ARAPUCA photon detector for the DUNE Far Detector 1. *Eur. Phys. J. C*, 84(10):1004, 2024. doi: 10.1140/epjc/s10052-024-13393-2.

[115] R. Acciarri et al. Construction of precision wire readout planes for the Short-Baseline Near Detector (SBND). *JINST*, 15(06):P06033, 2020. doi: 10.1088/1748-0221/15/06/P06033.

[116] Shanshan Gao. Low Noise Cold Electronics System for SBND LAr TPC. In *Meeting of the Division of Particles and Fields of the American Physical Society*, 10 2019.

[117] Hucheng Chen and Veljko Radeka. Cryogenic electronics for noble liquid neutrino detectors. *Nucl. Instrum. Meth. A*, 1045:167571, 2023. doi: 10.1016/j.nima.2022.167571.

[118] H. Chen et al. Lifetime Study of COTS ADC for SBND LAr TPC Readout Electronics. In *21st IEEE Real Time Conference*, 6 2018.

[119] Analog Devices. Ad7274, 2005. https://www.analog.com/en/products/ad7274.html#part-details.

[120] C. Adams et al. Measurement of the atmospheric muon rate with the MicroBooNE Liquid Argon TPC. *JINST*, 16(04):P04004, 2021. doi: 10.1088/1748-0221/16/04/P04004.

[121] R. Acciarri et al. Cosmic Ray Background Removal With Deep Neural Networks in SBND. *Front. Artif. Intell.*, 4:649917, 2021. doi: 10.3389/frai.2021.649917.

[122] M. Bahmanabadi. A method for determining the angular distribution of atmospheric muons using a cosmic ray telescope. *Nucl. Instrum. Meth. A*, 916:1–7, 2019. doi: 10.1016/j.nima.2018.11.010.

[123] Martin Auger, Marco Del Tutto, Antonio Ereditato, Bonnie T Fleming, Damian Goeldi, Elena Gramellini, Roxanne Guenette, Wesley Ketchum, Igor Kreslo, Ann Laube, et al. A novel cosmic ray tagger system for liquid argon tpc neutrino detectors. *Instruments*, 1(1):2, 2017.

[124] HAMAMATSU Datasheet - R5912. https://www.hamamatsu.com/resources/pdf/etd/LARGE_AREA_PMT_TPMH1376E.pdf, 2021. Accessed: September 2021.

[125] A.A. Machado, E. Segreto, D. Warner, A. Fauth, B. Gelli, R. Máximo, A. Pissolatti, L. Paulucci, and F. Marinho. The x-arapuca: an improvement of the arapuca device. *Journal of Instrumentation*, 13(04):C04026, apr 2018. doi: 10.1088/1748-0221/13/04/C04026. URL https://dx.doi.org/10.1088/1748-0221/13/04/C04026.

[126] W. M. Burton and B. A. Powell. Fluorescence of Tetraphenyl-Butadiene in the Vacuum Ultraviolet. *Appl. Opt.*, 12(1):87–89, 1973. doi: 10.1364/AO.12.000087.

[127] P. Abratenko et al. Scintillation Light in SBND: Simulation, Reconstruction, and Expected Performance of the Photon Detection System. *Eur. Phys. J. C*, 84:1046, 2024. doi: 10.1140/epjc/s10052-024-13306-3.

[128] C. Brizzolari et al. Cryogenic front-end amplifier design for large SiPM arrays in the DUNE FD1-HD photon detection system. *JINST*, 17(11):P11017, 2022. doi: 10.1088/1748-0221/17/11/P11017.

[129] C Green, J Kowalkowski, M Paterno, M Fischler, L Garren, and Q Lu. The art framework. *Journal of Physics: Conference Series*, 396(2):022020, dec 2012. doi: 10.1088/1742-6596/396/2/022020. URL https://dx.doi.org/10.1088/1742-6596/396/2/022020.

[130] Timothy A. DeVol, David K. Wehe, and Glenn F. Knoll. Evaluation of p-terphenyl and 2,2" dimethyl-p-terphenyl as wavelength shifters for barium fluoride. *Nuclear Instruments and Methods in Physics Research Section A: Accelerators, Spectrometers, Detectors and Associated Equipment*, 327, 1993. URL https://doi.org/10.1016/0168-9002(93)90701-I.

[131] C. Brizzolari et al. Enhancement of the X-Arapuca photon detection device for the DUNE experiment. *JINST*, 16(09):P09027, 2021. doi: 10.1088/1748-0221/16/09/P09027.

[132] Wavelength shifting plastics ej-280, ej-282, ej-284, ej-286. https://eljentechnology.com/products/wavelength-shifting-plastics/ej-280-ej-282-ej-284-ej-286, 2023. Accessed: October 2023.

[133] Silicon photomultipliers (sipm), low-noise, blue-sensitive c-series sipm sensors. https://www.onsemi.com/download/data-sheet/pdf/microc-series-d.pdf, 2023. Accessed: October 2023.

[134] Mppc (multi-pixel photon counter) s13360-2050ve/-3050ve/-6050ve. https://www.hamamatsu.com/content/dam/hamamatsu-photonics/sites/documents/99_SALES_LIBRARY/ssd/s13360-2050ve_etc_kapd1053e.pdf, 2023. Accessed: October 2023.

[135] Mppc (multi-pixel photon counter) s14160/14161 series. https://www.hamamatsu.com/content/dam/hamamatsu-photonics/sites/documents/99_SALES_LIBRARY/ssd/s14160_s14161_series_kapd1064e.pdf, 2023. Accessed: October 2023.

[136] Rodrigo Álvarez-Garrote et al. Measurement of the photon detection efficiency of Hamamatsu VUV4 SiPMS at cryogenic temperature. *Nucl. Instrum. Meth. A*, 1064:169347, 2024. doi: 10.1016/j.nima.2024.169347.

[137] G. Gallina et al. Characterization of the Hamamatsu VUV4 MPPCs for nEXO. *Nucl. Instrum. Meth. A*, 940:371–379, 2019. doi: 10.1016/j.nima.2019.05.096.

[138] H. V. Souza et al. Liquid argon characterization of the X-ARAPUCA with alpha particles, gamma rays and cosmic muons. *JINST*, 16(11):P11002, 2021. doi: 10.1088/1748-0221/16/11/P11002.

[139] PicoQuant. Picoquant,. https://www.picoquant.com/, 2016.

[140] E. Calvo Alamillo et al. Validation of electrodeposited 241Am alpha-particle sources for use in liquified gas detectors at cryogenic temperatures. *Applied Radiation and Isotopes*, 3 2024. doi: 10.1016/j.apradiso.2023.110913.

[141] C. Brizzolari et al. Cryogenic front-end amplifier design for large SiPM arrays in the DUNE FD1-HD photon detection system. *JINST*, 17(11):P11017, 2022. doi: 10.1088/1748-0221/17/11/P11017.

[142] CAEN tools for discovery. Caen, 2024. https://www.caen.it/.

[143] Sergey Vinogradov, T Vinogradova, V Shubin, Dmitry Shushakov, and Konstantin Sitarsky. Probability distribution and noise factor of solid state photomultiplier signals with cross-talk and afterpulsing. In *2009 IEEE Nuclear Science Symposium Conference Record (NSS/MIC)*, pages 1496–1500. IEEE, 2009.

[144] L. Gruber, S. E. Brunner, J. Marton, and K. Suzuki. Over saturation behavior of SiPMs at high photon exposure. *Nucl. Instrum. Meth. A*, 737:11–18, 2014. doi: 10.1016/j.nima.2013.11.013.

[145] Chiara Filomena Lastoria. *Analysis of the scintillation light production and propagation in the WA105 Dual-Phase demonstrator*. PhD thesis, UCM, Madrid, Dept. Phys., Madrid U., 2020.

[146] P. Nakarmi et al. Reflectivity and PDE of VUV4 Hamamatsu SiPMs in Liquid Xenon. *JINST*, 15(01):P01019, 2020. doi: 10.1088/1748-0221/15/01/P01019.

[147] Thor labs. CCSA1 Cosine Corrector. https://www.thorlabs.com/thorproduct.cfm?partnumber=CCSA1, 2014.

[148] Emily Grace and James A. Nikkel. Index of refraction, Rayleigh scattering length, and Sellmeier coefficients in solid and liquid argon and xenon. *Nucl. Instrum. Meth. A*, 867:204–208, 2017. doi: 10.1016/j.nima.2017.06.031.

[149] M. Babicz et al. A measurement of the group velocity of scintillation light in liquid argon. *JINST*, 15(09):P09009, 2020. doi: 10.1088/1748-0221/15/09/P09009.

[150] Ruth Pordes and Erica Snider. The Liquid Argon Software Toolkit (LArSoft): Goals, Status and Plan. *PoS*, ICHEP2016:182, 2016. doi: 10.22323/1.282.0182.

[151] E.L. Snider and G. Petrillo. Larsoft: toolkit for simulation, reconstruction and analysis of liquid argon tpc neutrino detectors. *Journal of Physics: Conference Series*, 898(4):042057, oct 2017. doi: 10.1088/1742-6596/898/4/042057. URL https://dx.doi.org/10.1088/1742-6596/898/4/042057.

[152] C. Andreopoulos et al. The GENIE Neutrino Monte Carlo Generator. *Nucl. Instrum. Meth. A*, 614:87–104, 2010. doi: 10.1016/j.nima.2009.12.009.

[153] Julia Tena-Vidal et al. Neutrino-nucleus CC0π cross-section tuning in GENIE v3. *Phys. Rev. D*, 106(11):112001, 2022. doi: 10.1103/PhysRevD.106.112001.

[154] Dieter Heck, Johannes Knapp, JN Capdevielle, G Schatz, T Thouw, et al. *CORSIKA: A Monte Carlo code to simulate extensive air showers*. Forschungszentrum Karlsruhe Karlsruhe, 1998.

[155] E. Segreto. Evidence of delayed light emission of TetraPhenyl Butadiene excited by liquid Argon scintillation light. *Phys. Rev. C*, 91(3):035503, 2015. doi: 10.1103/PhysRevC.91.035503.

[156] P. Abratenko et al. Cosmic Ray Background Rejection with Wire-Cell LArTPC Event Reconstruction in MicroBooNE. *Phys. Rev. Applied*, 15(6):064071, 2021. doi: 10.1103/PhysRevApplied.15.064071.

[157] Diego Garcia-Gamez, Patrick Green, and Andrzej M. Szelc. Predicting Transport Effects of Scintillation Light Signals in Large-Scale Liquid Argon Detectors. *Eur. Phys. J. C*, 81(4):349, 2021. doi: 10.1140/epjc/s10052-021-09119-3.

[158] Thomas K Gaisser and A Michael Hillas. Reliability of the method of constant intensity cuts for reconstructing the average development of vertical showers. In *In: International Cosmic Ray Conference, 15th, Plovdiv, Bulgaria, August 13-26, 1977, Conference Papers. Volume 8.(A79-37301 15-93) Sofia, B'lgarska Akademiia*

na Naukite, 1978, p. 353-357. NSF-supported research., volume 8, pages 353–357, 1977.

[159] Leif Lonnblad. CLHEP: A project for designing a C++ class library for high-energy physics. *Comput. Phys. Commun.*, 84:307–316, 1994. doi: 10.1016/0010-4655(94)90217-8.

[160] M. Bonesini et al. An innovative technique for TPB deposition on convex window photomultiplier tubes. *JINST*, 13(12):P12020, 2018. doi: 10.1088/1748-0221/13/12/P12020.

[161] Laura Paulucci, Franciole Marinho, Ana Amélia Machado, and Ettore Segreto. A complete simulation of the X-ARAPUCA device for detection of scintillation photons. *JINST*, 15(01):C01047, 2020. doi: 10.1088/1748-0221/15/01/C01047.

[162] sbndcode. https://github.com/SBNSoftware/sbndcode, 2024. Accessed: September 2024.

[163] F. Marinho, L. Paulucci, A. A. Machado, and E. Segreto. Numerical characterization of the ARAPUCA: a new approach for LAr scintillation light detection. *J. Phys. Conf. Ser.*, 1056(1):012036, 2018. doi: 10.1088/1742-6596/1056/1/012036.

[164] R. Fitzpatrick J. Mousseau, D. Mishins. Summary of X-TDB Cryocooler Tests. https://sbn-docdb.fnal.gov/cgi-bin/sso/ShowDocument?docid=21723, 2019. SBN Document 21723. Accesed: September 2024.

[165] L. Bartoszek et al. Mu2e Technical Design Report. Technical report, Fermilab, 10 2014.

[166] Bruce Baller. Liquid argon TPC signal formation, signal processing and reconstruction techniques. *JINST*, 12(07):P07010, 2017. doi: 10.1088/1748-0221/12/07/P07010.

[167] Henri J Nussbaumer and Henri J Nussbaumer. *The fast Fourier transform*. Springer, 1982.

[168] Jingdong Chen, Jacob Benesty, Yiteng Huang, and Simon Doclo. New insights into the noise reduction wiener filter. *IEEE Transactions on audio, speech, and language processing*, 14(4):1218–1234, 2006.

[169] W. Tang, X. Li, X. Qian, H. Wei, and C. Zhang. Data Unfolding with Wiener-SVD Method. *JINST*, 12(10):P10002, 2017. doi: 10.1088/1748-0221/12/10/P10002.

[170] SBN Software organization. sbndcode github repository, *v*09_82_02_01, 2023. URL https://github.com/SBNSoftware/sbncode/tree/v09_82_02_01.

[171] Jeffrey M. Berryman, Andre de Gouvea, Patrick J Fox, Boris Jules Kayser, Kevin James Kelly, and Jennifer Lynne Raaf. Searches for Decays of New Particles in the DUNE Multi-Purpose Near Detector. *JHEP*, 02:174, 2020. doi: 10.1007/JHEP02(2020)174.

[172] Anupama Atre, Tao Han, Silvia Pascoli, and Bin Zhang. The search for heavy majorana neutrinos. *Journal of High Energy Physics*, 2009(05):030, 2009.

[173] Peter Ballett, Silvia Pascoli, and Mark Ross-Lonergan. Mev-scale sterile neutrino decays at the fermilab short-baseline neutrino program. *Journal of High Energy Physics*, 2017(4):1–38, 2017.

[174] Pilar Coloma, Enrique Fernández-Martínez, Manuel González-López, Josu Hernández-García, and Zarko Pavlovic. GeV-scale neutrinos: interactions with mesons and DUNE sensitivity. *Eur. Phys. J. C*, 81(1):78, 2021. doi: 10.1140/epjc/s10052-021-08861-y.

[175] André de Gouvêa, Patrick J. Fox, Boris J. Kayser, and Kevin J. Kelly. Characterizing heavy neutral fermions via their decays. *Physical Review D*, 105(1), jan 2022. doi: 10.1103/physrevd.105.015019. URL https://doi.org/10.1103%2Fphysrevd.105.015019.

[176] André de Gouvêa, Patrick J. Fox, Boris J. Kayser, and Kevin J. Kelly. Three-body decays of heavy dirac and majorana fermions. *Physical Review D*, 104(1), jul 2021. doi: 10.1103/physrevd.104.015038. URL https://doi.org/10.1103%2Fphysrevd.104.015038.

[177] C. Adams et al. First measurement of ν_μ charged-current π^0 production on argon with the MicroBooNE detector. *Phys. Rev. D*, 99(9):091102, 2019. doi: 10.1103/PhysRevD.99.091102.

[178] Yung-Su Tsai. Pair Production and Bremsstrahlung of Charged Leptons. *Rev. Mod. Phys.*, 46:815, 1974. doi: 10.1103/RevModPhys.46.815. [Erratum: Rev.Mod.Phys. 49, 421–423 (1977)].

[179] S. Amoruso et al. Study of electron recombination in liquid argon with the ICARUS TPC. *Nucl. Instrum. Meth. A*, 523:275–286, 2004. doi: 10.1016/j.nima.2003.11.423.

[180] R. Acciarri et al. A Study of Electron Recombination Using Highly Ionizing Particles in the ArgoNeuT Liquid Argon TPC. *JINST*, 8:P08005, 2013. doi: 10.1088/1748-0221/8/08/P08005.

[181] C. Adams et al. A method to determine the electric field of liquid argon time projection chambers using a UV laser system and its application in MicroBooNE. *JINST*, 15(07):P07010, 2020. doi: 10.1088/1748-0221/15/07/P07010.

[182] Simon Ramo. Currents induced by electron motion. *Proc. Ire.*, 27:584–585, 1939. doi: 10.1109/JRPROC.1939.228757.

[183] O Bunemann, TE Cranshaw, and JA Harvey. Design of grid ionization chambers. *Canadian journal of research*, 27(5):191–206, 1949.

[184] C. Adams et al. Ionization electron signal processing in single phase LArTPCs. Part I. Algorithm Description and quantitative evaluation with MicroBooNE simulation. *JINST*, 13(07):P07006, 2018. doi: 10.1088/1748-0221/13/07/P07006.

[185] B. Viren et al. Wirecell toolkit, 2016. https://github.com/wirecell/.

[186] Lynn Tung and Moon Jung Jung. Signal Processing with WireCell in SBND, 2023.

[187] GausHitFinder. https://github.com/LArSoft/larreco/blob/86b7154f11685e67d424b40fe1be97a41bb87473/larreco/HitFinder/GausHitFinder_module.cc, Dec. 2021. Accessed: October 2024.

[188] Edward Tyley. *Reconstructing and selecting electron neutrino and anti-neutrino interactions on argon in the Short-Baseline Near Detector*. PhD thesis, University of Sheffield, Sheffield U., 5 2023.

[189] J. S. Marshall and M. A. Thomson. The Pandora Software Development Kit for Pattern Recognition. *Eur. Phys. J. C*, 75(9):439, 2015. doi: 10.1140/epjc/s10052-015-3659-3.

[190] R. Acciarri et al. The Pandora multi-algorithm approach to automated pattern recognition of cosmic-ray muon and neutrino events in the MicroBooNE detector. *Eur. Phys. J. C*, 78(1):82, 2018. doi: 10.1140/epjc/s10052-017-5481-6.

[191] Babak Abi et al. Deep underground neutrino experiment (dune), far detector technical design report, volume ii: Dune physics, 2020. URL https://arxiv.org/abs/2002.03005.

[192] Byron P. Roe, Hai-Jun Yang, Ji Zhu, Yong Liu, Ion Stancu, and Gordon McGregor. Boosted decision trees, an alternative to artificial neural networks. *Nucl. Instrum. Meth. A*, 543(2-3):577–584, 2005. doi: 10.1016/j.nima.2004.12.018.

[193] Pandora TrackShowerIdFeatureTool. https://github.com/PandoraPFA/LArContent/tree/master/larpandoracontent/LArTrackShowerId, Dec. 2022. Accessed: October 2024.

[194] Donald E. Groom and S. R. Klein. Passage of particles through matter: in Review of Particle Physics (RPP 2000). *Eur. Phys. J. C*, 15:163–173, 2000. doi: 10.1007/BF02683419.

[195] Andreas Hocker et al. Tmva - toolkit for multivariate data analysis, 2009. URL https://arxiv.org/abs/physics/0703039.

[196] Tianqi Chen, Tong He, Michael Benesty, Vadim Khotilovich, Yuan Tang, Hyunsu Cho, Kailong Chen, Rory Mitchell, Ignacio Cano, Tianyi Zhou, et al. Xgboost: extreme gradient boosting. *R package version 0.4-2*, 1(4):1–4, 2015.

[197] Gérard Biau and Erwan Scornet. A random forest guided tour. *Test*, 25:197–227, 2016.

[198] William S Noble. What is a support vector machine? *Nature biotechnology*, 24 (12):1565–1567, 2006.

[199] Thomas Gabriel Rentoul Brooks. *Selecting charged current muon neutrino interactions on argon with the short-baseline near detector*. PhD thesis, University of Sheffield, Sheffield U., 2020.

[200] Glen Cowan, Kyle Cranmer, Eilam Gross, and Ofer Vitells. Asymptotic formulae for likelihood-based tests of new physics. *Eur. Phys. J. C*, 71:1554, 2011. doi: 10.1140/epjc/s10052-011-1554-0. [Erratum: Eur.Phys.J.C 73, 2501 (2013)].

[201] Alexander L. Read. Presentation of search results: The CL_s technique. *J. Phys. G*, 28:2693–2704, 2002. doi: 10.1088/0954-3899/28/10/313.

[202] Lukas Heinrich, Matthew Feickert, and Giordon Stark. pyhf: v0.7.6, 2024. URL https://doi.org/10.5281/zenodo.1169739. https://github.com/scikit-hep/pyhf/releases/tag/v0.7.6.

[203] Lukas Heinrich, Matthew Feickert, Giordon Stark, and Kyle Cranmer. pyhf: pure-python implementation of histfactory statistical models. *Journal of Open Source Software*, 6(58):2823, 2021. doi: 10.21105/joss.02823. URL https://doi.org/10.21105/joss.02823.

[204] Kyle Cranmer, George Lewis, Lorenzo Moneta, Akira Shibata, and Wouter Verkerke. HistFactory: A tool for creating statistical models for use with RooFit and RooStats. Technical report, New York U., New York, 2012. URL https://cds.cern.ch/record/1456844.

[205] Nilanjana Kumar and Stephen P. Martin. Vectorlike leptons at the large hadron collider. *Phys. Rev. D*, 92:115018, Dec 2015. doi: 10.1103/PhysRevD.92.115018. URL https://link.aps.org/doi/10.1103/PhysRevD.92.115018.

[206] C. Adams et al. Deep neural network for pixel-level electromagnetic particle identification in the MicroBooNE liquid argon time projection chamber. *Phys. Rev. D*, 99(9):092001, 2019. doi: 10.1103/PhysRevD.99.092001.

[207] Adam Abed Abud et al. Separation of track- and shower-like energy deposits in ProtoDUNE-SP using a convolutional neural network. *Eur. Phys. J. C*, 82(10): 903, 2022. doi: 10.1140/epjc/s10052-022-10791-2.

[208] M. Daum, P.-R. Kettle, B. Jost, R. M. Marshall, R. C. Minehart, W. A. Stephens, and K. O. H. Ziock. Search for admixtures of massive neutrinos in the decay $\pi^+ \to \mu^+ + \nu$. *Phys. Rev. D*, 36:2624–2632, Nov 1987. doi: 10.1103/PhysRevD.36.2624. URL https://link.aps.org/doi/10.1103/PhysRevD.36.2624.

[209] Peter Ballett, Tommaso Boschi, and Silvia Pascoli. Heavy Neutral Leptons from low-scale seesaws at the DUNE Near Detector. *JHEP*, 03:111, 2020. doi: 10.1007/JHEP03(2020)111.

[210] C. Ahdida et al. Sensitivity of the SHiP experiment to Heavy Neutral Leptons. *JHEP*, 04:077, 2019. doi: 10.1007/JHEP04(2019)077.

[211] P. Abratenko et al. Search for Heavy Neutral Leptons in Electron-Positron and Neutral-Pion Final States with the MicroBooNE Detector. *Phys. Rev. Lett.*, 132 (4):041801, 2024. doi: 10.1103/PhysRevLett.132.041801.

List of Figures

1.1 Standard Model of elementary particles. . . . 3
1.2 Feynman diagrams for the neutrino charged and neutral currents 4
1.3 Normal and inverted hierarchy current status. Values taken from [43]. . . 10
1.4 Excess of electron-like events observed by LSND and MiniBooNE experiments. . . . 12
1.5 Global constraints to a 3+1 oscillation model from short-baseline experiments. . . . 12
1.6 Cartoon depicting propagation of the neutrino wave packets. . . . 14
1.7 Current experimental and projected limits on electron, muon and tau coupled HNL searches. . . . 15

2.1 Map of the SBN program at Fermilab. . . . 16
2.2 Oscillation probabilities for a light sterile neutrino at SBN. . . . 17
2.3 SBN exclusion and allowed-region sensitivities to $\nu_e(\nu_\mu)$ appearance (disappearance) under the (3+1) sterile neutrino hypothesis. . . . 18
2.4 Scheme of the Booster facilities at Fermilab in colors. . . . 20
2.5 Time structure of the BNB spills. . . . 20
2.6 Scheme of the BNB target and magnetic horn. . . . 21
2.7 Predicted BNB flux at SBND front face. . . . 22
2.8 Working principle of a LArTPC 23
2.9 Neutrino event candidate with showers (white) and tracks (orange). . . . 26
2.10 Scheme of different shower types if the starting particle is an electron (Left) or a photon (Right). . . . 26
2.11 dE/dx versus residual range for stopping protons and muons. . . . 27
2.12 dE/dx distribution for electrons and gammas from ArgoNeuT. . . . 27
2.13 Cartoon showing the ambiguity in the t_0 determination. . . . 28
2.14 Diagram of the scintillation photon production in liquid argon. . . . 29
2.15 Scheme of the SBND detector. . . . 32
2.16 Photos of the SBND TPC. . . . 32
2.17 Scheme of SBND TPC readout electronics. . . . 33
2.18 Example of a recorded CCν_μ candidate event in SBND. . . . 34
2.19 Working principle of the CRT system. . . . 34
2.20 Photos of the SBND CRT. . . . 35
2.21 Installation and first results of the CRT system. . . . 36
2.22 Scheme of the SBND PDS. . . . 36
2.23 Photos of the SBND PDS components. . . . 37
2.24 PDS calibration waveform and combined results with beam data 39
2.25 SBND hardware trigger components: MTC/A (Left) and PTB (Right). . . . 39

3.1 Working principle and scheme of SBND X-ARAPUCA sensors. 42
3.2 Transmittance curves of the pTP-coated 400-nm dichroic filter for different angles of incidence (AOI) light as a function of the wavelength. 43
3.3 Left (Right): absorption and emission spectra of the 286 (280) Eljen WLS bars, used in Onsemi coated (uncoated) units. 44
3.4 Photo and scheme of the experimental setup at CIEMAT. 45
3.5 Photo and schemes of the cryogenic vessel and the components submerged in liquid argon. 46
3.6 Scheme of the data acquisition system at the CIEMAT setup [114]. 47
3.7 Event displays of a calibration run for the Onsemi coated X-ARAPUCA and the reference SiPMs. 48
3.8 Example of charge estimation in a calibration run. 50
3.9 Charge histograms from calibration data of the Hamamatsu (Left) and Onsemi (Center) X-ARAPUCA and the reference SiPM 289 (Right) in blue. 50
3.10 Calibration curves for both coated X-ARAPUCA configurations tested at CIEMAT with Onsemi and Hamamatsu SiPMs, and the reference Hamamatsu-VUV4 SiPMs. 51
3.11 Probability distribution following Equation 3.4 for the same mean primary number of PE $\mu = 3$ and different crosstalk values. 53
3.12 Crosstalk determination procedure. 53
3.13 Average charge and dispersion (STD) for the different intensities as seen by the reference SiPM 289 and the Onsemi X-ARAPUCA. 56
3.14 X-ARAPUCA average waveforms for the different laser intensities tested in absolute (Top) and normalized amplitude (Bottom) with a closer zoom to the peak. 56
3.15 Examples of the G4 simulations carried out to estimate the number of photons arriving at each sensor for VUV (Left) and visible (Right) light. . 58
3.16 X-ARAPUCA signal processing with a VUV scintillation pulse. Small secondary pulses from the slow component are visible. 58
3.17 Left: event distribution detected by the coated Onsemi X-ARAPUCA in fast vs total ratio (F90) and total charge for an alpha source run with the applied cuts. Right: total charge distribution before and after cuts, 90 % of the events pass the cuts. 59
3.18 Average waveforms for a calibration run with the laser (blue), an alpha run (orange) and a muon run (green). 59
3.19 CCSA1 cosine corrector normalized intensity (blue) with respect to the angular aperture. 61
3.20 Sigmoid fit to the 420 nm points modeling the transmittance as a function of the AOI. 63
3.21 Angular distribution of visible photons arriving at the X-ARAPUCA window at SBND (blue) and CIEMAT setup (orange). 63
3.22 PDE at the CIEMAT setup (orange square) for the coated Onsemi X-ARAPUCA at an over-voltage of 5.75 V, extrapolation as a function of the angle of incidence (black) and expected mean value at SBND (blue square). The error band is extrapolated from the values obtained at CIEMAT setup. 64

4.1 Luminescence intensity (L) and collected charge (Q) as a function of the applied electric field for liquid xenon, argon and krypton. 66
4.2 Relation between the number of Geant4 simulated photons on the PDS and a pure geometrical estimation of the photons based on the solid angle subtended by each PD sensor for different offset angles. 68
4.3 Left (Right): measured PMT (X-ARAPUCA) single electron response (SER). The amplitude fluctuations 22% (10%) are also shown in gray. . . 71
4.4 Left: cold test setup with two SiPM boards at Fermilab. In the final setup, one SiPM board was connected, and the LED (top of the frame) was repositioned to point directly to the board. Right: Zoom-in of board-copper connection. 72
4.5 Left: Amplitude spectrum of calibration data from Fermilab test-stand and Gaussian fit to the first photo-electron. Right: average waveforms from consecutive peaks. 73
4.6 Raw simulated X-ARAPUCA waveform of scintillation light in liquid argon. 74
4.7 Scheme of the different stages in the light reconstruction chain, starting from the measured raw waveforms and finishing with the optical hits and optical flashes (clusters). 74
4.8 Left: Wiener filter and fitted Gaussian filter for the simulated noise distribution in SBND X-ARAPUCA channels in the frequency domain. Right: Filters response function in the time domain. 76
4.9 Left (Right): True simulated photon distribution, raw simulated waveform and deconvolved signal at a PMT (X-ARAPUCA) channel. 76
4.10 Performance of the optical hit finder algorithm on a simulated and deconvolved X-ARAPUCA waveform. Four optical hits are identified. The fast and part of the slow component are merged in the first hit. 77
4.11 Time difference between the optical hit time and the first arriving photon in that X-ARAPUCA channel. 78
4.12 Scheme of the OpFlash finder algorithm [127]. 79
4.13 Left: Saturated X-ARAPUCA channel distribution for the simulated BNB and cosmic sample. Right: saturated waveform before (black) and after (blue) signal processing. The shape of the filtered waveform is visibly distorted. 80
4.14 Reconstruction efficiency of X-ARAPUCA optical flashes for the sample of BNB neutrino interactions with cosmic rays overlaid as a function of the deposited energy (Left) and averaged drift distance (Right). 81
4.15 Left (Right): Reconstructed number of PEs from all OpHits within an OpFlash, and fractional bias and resolution (≡ StdDev), as a function of the total number of simulated PEs within one PMT (X-ARAPUCA) channel. 82
4.16 Distribution of the number of PEs per X-ARAPUCA channel within a neutrino flash and zoom to the low PEs region: a mean of 36 PEs per channel and flash is expected. 82
4.17 X-ARAPUCA system detected light yield maps for the lateral–PDS plane (Left) and top (Right) views of the detector. 83
4.18 Left (Right): Total PMT (X-ARAPUCA) light yield as a function of the averaged drift distance in blue. The contribution from uncoated units is shown in red. 84

4.19 Resolution (gray triangles) and bias (blue circles) of the X-ARAPUCA system in the Z (Left) and Y (Right) directions for simulated BNB neutrino interactions. . . . 84
4.20 Calibration curve (black markers) for the $\eta_{\text{X-ARAPUCA}}$ parameter. The vertical lines represent the dispersion in the vertical axis. . . . 85
4.21 Bias (blue circles) and resolution (gray triangles) of the drift distance estimation using the $\eta_{\text{X-ARAPUCA}}$ parameter. . . . 86
4.22 Time difference between the reconstructed optical flash time and the true interaction time, as a function of the drift distance. . . . 87
4.23 Cartoon depicting the time of flight of an interacting neutrino (dashed blue), and the produced photons (dashed black) to the PDS sensors (green). . . . 88
4.24 Time bias (blue) and resolution (gray) of the X-ARAPUCA system as a function of the drift distance (Left) and deposited energy (Right) after correcting for the photon time of flight. . . . 88
4.25 BNB neutrinos time of flight from the creation to the interaction inside SBND as a function of the beam (Z) direction for the first five bunches. . . . 89
4.26 True neutrino arrival time at SBND upstream wall (gray) and interaction time in the detector volume (blue) using X-ARAPUCA optical flashes. . . . 89
4.27 Neutrino interaction times of the BNB bunches merged into a single peak after correcting for both the photon propagation and the time of flight of the neutrinos inside the detector. . . . 90

5.1 Feynman diagram of the SM ν_μ (Left) and HNL (Right) production from positive kaon decay. . . . 92
5.2 Workflow diagram of the MeVPrtl generator. . . . 93
5.3 Kinematic ρ factor and branching ratios for HNL production as a function of the HNL mass. . . . 95
5.4 Arrival time at the SBND upstream wall of SM neutrinos and HNL signals with different masses. . . . 96
5.5 Truth time distributions of the SM neutrino background and a 300 MeV HNL at the SBND upstream wall. . . . 97
5.6 Fraction of HNL events in background free regions as a function of the HNL mass. . . . 97
5.7 HNL Branching ratios (Left) and decay widths (Right) of the channels simulated in the MeVPrtl generator. . . . 98
5.8 Density of the events at the SBND upstream wall in the perpendicular plane for SM neutrinos produced from the decays of kaons and pions. . . . 100
5.9 Density of the events at the SBND upstream wall in the perpendicular plane (XY) for an HNL signal of 300 MeV and the SM backgrounds. . . . 100
5.10 Energy spectrum of HNL events decaying into an electron-positron pair and a neutrino at SBND for different masses. . . . 101
5.11 Example of a simulated HNL event inside the SBND TPC. An overlaid crossing muon can be seen on the right side. . . . 101
5.12 Energy distribution of the leading electron or positron for the $N \to e^+e^-\nu$ decay channel for different HNL parent masses. . . . 103
5.13 Distribution of the angle between the electron and positron pair for the $N \to e^+e^-\nu$ decay channel for different HNL parent masses. . . . 104

5.14 Distribution of the angle of the leading electron/positron with the beam direction for the $N \to e^+e^-\nu$ decay channel for different HNL parent masses. . . . 104
5.15 Boundaries of the GENIE generator in SBND. . . . 105
5.16 NCπ^0 (Left) and CCν_e (Right) interactions with an argon nucleus. . . . 105
5.17 TPC image of simulated e^+e^- pairs for different angles between them. . . . 106

6.1 Workflow of SBND simulation. . . . 108
6.2 Example of electron drift paths with two induction planes and a collection plane at x=0. Picture taken from [184]. . . . 109
6.3 Wire response function for a single electron in the two induction planes (red and blue) and the collection plane (black) including (a) no neighboring wires or (b) [-10,+10] neighboring wires. . . . 110
6.4 Scheme of the different stages in the TPC reconstruction chain, starting from the raw waveforms and finishing with the TPC hits and Pandora clustering algorithms. . . . 110
6.5 Left: TPC image of a shower induced by a 1.23 GeV electron in the first induction plane. Right: simulated raw waveform as seen in a particular wire of the induction plane. . . . 111
6.6 GausHitFinder algorithm applied to deconvolved TPC waveforms (black) from an electron event. . . . 111
6.7 Representation of the two Pandora reconstruction paths. . . . 112
6.8 Example of a CCν_μ interaction with an outgoing muon (red), a proton (blue) and the two showers (blue and green) produced by the decay of a π^0. Image taken from [190]. . . . 113
6.9 Measured SiPM waveform from real data. . . . 115
6.10 Example of a crossing muon (green) leaving hits in two different CRT strips (blue) of the CRT walls (black). The TPC volume is shown in gray. 116
6.11 Left (Right): Confusion matrices of the Razzled BDT normalized such as the sum of each row (column) equals 1. . . . 118
6.12 CRUMBS score distributions for signal (SM ν, blue) and background slices (cosmic rays, red) in both the training and validation samples. . . . 119
6.13 Summary of the preselection applied to cosmic, BNB and HNL simulated events for the $N \to e^+e^-\nu$ search. The number of HNL slices corresponds to a coupling of $|U_{\mu 4}|^2 = 2 \times 10^{-4}$. . . . 122
6.14 Distribution of arrival time for signal and backgrounds for an HNL mass of 100 MeV after the preselection. . . . 123
6.15 Normalized distributions of the razzle-dazzle and razzled combined variables representing the total number of showers minus the total number of tracks in a given slice. . . . 124
6.16 Normalized distributions of the x,y and z coordinates of the primary vertex in the slice. . . . 125
6.17 Left and Right: Normalized distributions of the energy and opening angle of the shower cone (θ_{cone}) of the most energetic shower in the slice. . . . 126
6.18 Normalized distributions of the conversion gap (Left) and dE/dx (Right) of the most energetic shower in the slice. . . . 126
6.19 Left: distribution of the Opt0 fraction for background and signal slices. Center and right: total charge and amplitude collected in the first 100 ns of the matched flash. . . . 127

6.20 Fraction of signal and background events as a function of the BDT score for the train and validation samples. . . . 128
6.21 Left: distribution of signal and background slices by type as a function of the BDT score for three years of data. The normalized distributions are shown on the right. . . . 128
6.22 Time distribution of signal and background slices (all bunches combined) with a BDT score greater than 0.5. . . . 129
6.23 Efficiency and purity curves for a HNL mass of 100 MeV and different values of $|U_{\mu 4}|^2$ as a function of the BDT score cut. Preselection cuts are already applied. . . . 130
6.24 Left and right: truth (σ = 1.3 ns) and smeared truth (σ1.7 ns) arrival distributions at SBND for an HNL signal of 100 MeV and $|U_{\mu 4}|^2 = 2\times10^{-5}$ and the SM backgrounds. . . . 132

7.1 Uncertainties considered for the HNL signal (left) and SM backgrounds (right). . . . 134
7.2 Example of $\bar{q}_\mu$ distributions using the asymptotic approximation. . . . 137
7.3 Plots showing the upper limits at 90% CL on the mixing element $|U_{\mu 4}|^2$ for different Majorana HNL masses for both the conservative (left) and aggressive (right) selections in three years of SBND data or 10^{21} POT. . . . 140
7.4 $|U_{\mu 4}|^2$ upper limits at 90% CL comparison between the reconstructed and the truth approach for the νee final state for different Majorana HNL masses in three years of SBND data or 10^{21}. . . . 140
7.5 Upper limits on the coupling $|U_{\mu 4}|^2$ at the 90% confidence level for Majorana HNLs in the mass range of $1 < m_N < 175$ MeV. SBND expected limits for an exposure of 10^{21} POT are compared with existing experimental results, including SIN [208], PIENU [68], MicroBooNE [65] and PS191 [67]. . . . 142

A.1 Charge spectrum of alpha runs for the coated Onsemi X-ARAPUCA (Left) and the sum of the reference SiPMs 289 and 290 placed in front of the α source (Right) before (blue) and after the event selection using the F90 ratio (orange). . . . 172
A.2 Monte Carlo simulation computing the solid angle following Eq A.2 for 50,000 points randomly distributed on the α source surface (Left). The solid angle distribution is shown on the right. The left plot shows the simulated points with a color that corresponds to their respective solid angle. . . . 173

D.1 Conservative arrival time distributions in the mass range 10 - 75 MeV . . . 181
D.2 Conservative arrival time distributions in the mass range 100 - 150 MeV . 182

E.1 Aggressive arrival time distributions in the mass range 10 - 75 MeV . . . 184
E.2 Strict arrival time distributions in the mass range 100 - 150 MeV 185

F.1 Smeared True Arrival Time Distributions in the Mass Range 140 - 200 MeV . . . 187
F.2 Smeared True Arrival Time Distributions in the Mass Range 220 - 260 MeV . . . 188

List of Tables

1.1 Neutrino oscillation parameters: best values and confidence intervals from the global fit to the available experimental data. All values taken from [43]. 10

2.1 Summary of the three detectors of the SBN program. 19
2.2 Relevant physical properties of liquid argon. 25

3.1 Different X-ARAPUCA units in SBND by technical components. 44
3.2 Relevant properties of the different SiPM models in the SBND X-ARAPUCAs at room temperature provided by the manufacturers. All quantities taken from [133–135]. 44
3.3 Summary of the obtained gains for both X-ARAPUCA units tested. . . . 51
3.4 Summary of the obtained gains for all four reference SiPMs for a typical calibration run. 51
3.5 Summary of the obtained crosstalk values for both X-ARAPUCA units and the reference Hamamatsu VUV4 SiPMs in liquid argon. 54
3.6 Mean charge measured from the α source events for the two X-ARAPUCA configurations tested and the reference SiPM 289 and 290 in front of the α source that calibrate the light flux. 60
3.7 Summary of the obtained PDE values at 127 nm for both X-ARAPUCA units in liquid argon. For comparison, an X-ARAPUCA prototype for DUNE far detectors with different SiPMs but similar size is included. . . 60
3.8 Mean charge measured from the laser high intensity runs for the two X-ARAPUCA configurations tested and the reference SiPM 378 and 379 in front of the diffuser that calibrate the light flux. 62
3.9 Summary of the obtained PDE values at 420 nm for both X-ARAPUCA units in liquid argon. 64

4.1 Scintillation (VUV) light parameters used in SBND simulations taken from [87, 89, 108, 155]. τ_{fast} ratio is defined following equation 2.5 as the fraction of total light emitted in the fast component: τ_{fast} ratio = $A_{\text{fast}}/(A_{\text{fast}} + A_{\text{slow}})$ 67
4.2 Characteristic TPB decay times. Values taken from [155]. 69
4.3 Photon detection efficiencies for the different optical sensors used in SBND simulations. 70
4.4 Parameters for the simulation of PMT and X-ARAPUCA sensors. Values taken from the official SBND MC simulation [162], sbndcode v09_88_00_02. 71
4.5 List of OpFlash parameters used in the SBND reconstruction workflow. All the parameters but one, the time interval of the starting flash window, are shared by PMTs and X-ARAPUCAs. 80

4.6 Overall geometric resolution for the three space coordinates using X-ARAPUCA light flashes. 86

5.1 Particle lifetimes and branching ratios of neutrino-producing decays in the BNB simulation. 94
5.2 Coefficients determining the angular anisotropy in HNL decays. 102
5.3 Most common problems that cause the NCπ^0 and CCν_e backgrounds to be miss-reconstructed as an HNL signal. 105

6.1 Number and fraction of remaining slices after each cut of the preselection applied to cosmic, BNB and HNL simulated events for the $N \to e^+e^-\nu$ . . 122
6.2 Number of signal and background events left after different cuts in the BDT score for the validation sample with an HNL mass of 100 MeV and a $|U_{\mu 4}|^2$coupling of 2×10^{-5}. 130

7.1 Summary of expected upper Limits on the Coupling $|U_{\mu 4}|^2$ of Majorana HNLs 139

A.1 Values for the mean solid angle for both reference sensors in front of the alpha source and the X-ARAPUCA. The geometric VUV factor is the ratio between them, as the α source emission is isotropic. The methods agree within 1% level. 174

B.1 Masses and couplings of the produced samples for the $N \to e^+e^-\nu$ channel. 175

Appendix A

Analytical toy-model for the VUV PDE study

In the setup described in Chapter 3 the charge spectra from LAr scintillation light produced by alpha particles from a radioactive source, and measured by two SBND X-ARAPUCA modules and four reference Hamamatsu VUV4 SiPMs is analyzed.

The charge distributions of light signals detected by the sensors followed a Gaussian distribution in all cases except for the X-ARAPUCA (see Figure A.1). To explain the shape of this spectrum I developed an analytic model under a simple assumption: the flux seen by the X-ARAPUCA (and the other light sensors) is proportional to the solid angle subtended by their surfaces at the point where the α particle was emitted from the ^{241}Am source:

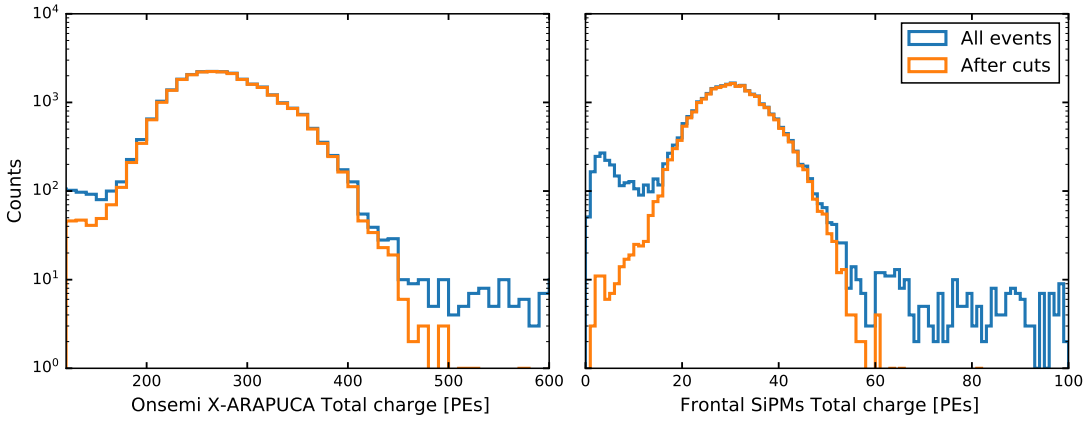

Figure A.1: Charge spectrum of alpha runs for the coated Onsemi X-ARAPUCA (Left) and the sum of the reference SiPMs 289 and 290 placed in front of the α source (Right) before (blue) and after the event selection using the F90 ratio (orange).

$$\Omega \equiv \int\int_S \frac{\hat{\mathbf{n}} \cdot d\,\hat{\mathbf{a}}}{r^2}. \tag{A.1}$$

with r the distance from the α particle to the surface patch, $\hat{n}$ is the unitary vector from the origin and $d\hat{a}$ is is the differential area of a surface patch. This is equivalent to assume an isotropic, point-like emission of the photons with negligible propagation effects. Since the length traveled by the alpha particle is O(μm) we can assume the αs stop immediately and photons are produced in the surface of the ^{241}Am source. Because the sensor's surfaces are rectangles, it is convenient to write Eq A.1 in Cartesian coordinates:

$$\Omega = \int_{y_0}^{y_1}\int_{x_0}^{x_1} \frac{z dx dy}{(x^2+y^2+z^2)^{3/2}} = \arctan\left(\frac{xy}{z(x^2+y^2+z^2)^{1/2}}\right)_{x_0,y_0}^{x_1,y_1} \tag{A.2}$$

where z is the distance from the light production point to the sensor plane and $x_{0,1}, y_{0,1}$ the corners of the sensor surface rectangle. The emission point is assumed to be at (0,0,0). The probability density function of the ^{241}Am events as a function of the solid angle (Ω_0) relates to the points in the alpha source surface (S_α) that meet the requirement:

$$P(\Omega_0) = \int\int_{S_{\alpha\ source}} \delta[\Omega_0 - \Omega(\theta, r \in S_{\alpha\ source})] r d\theta dr \tag{A.3}$$

No analytic solution to Eq A.3 with Eq A.2 as input was found, hence it was solved numerically with Monte Carlo methods.

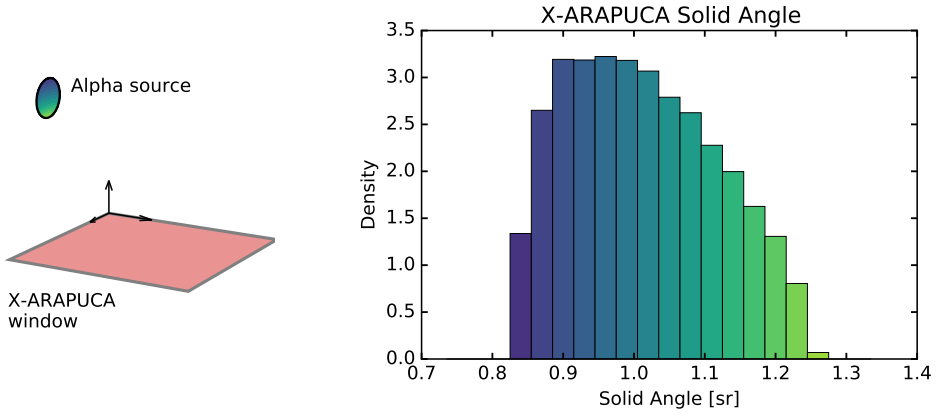

Figure A.2: Monte Carlo simulation computing the solid angle following Eq A.2 for 50,000 points randomly distributed on the α source surface (Left). The solid angle distribution is shown on the right. The left plot shows the simulated points with a color that corresponds to their respective solid angle.

The effect that drives the charge distribution shape then becomes clear: the alpha source has a diameter $\varnothing$=2.2 cm. The SiPMs are small enough (6×6 mm^2) to appear as

Method	**Sensor**	**Solid angle [sr]**
Analytic	X-ARAPUCA	1.029
	Frontal SiPMs	0.0242
G4	X-ARAPUCA	1.02 ± 0.02
	Frontal SiPMs	0.0242 ±0,0006

Table A.1: Values for the mean solid angle for both reference sensors in front of the alpha source and the X-ARAPUCA. The geometric VUV factor is the ratio between them, as the α source emission is isotropic. The methods agree within 1% level.

point-like and are placed symmetrically with respect to the alpha source perpendicular axis. On the other hand, the alpha source and the X-ARAPUCA window surfaces are orthogonal and their sizes are comparable to the distance between them. The photons produced by α particles closer to the X-ARAPUCA see a bigger Ω_{XA} than the ones far from it as depicted in Fig A.2.

The solid angles for the X-ARAPUCA and the reference SiPMs for both the analytic and G4 methods are presented on Table A.1. Both methods agree within the errors considered, and thus, the ratio between the SiPMs and X-ARAPUCA solid angles is taken as the geometrical ratio between them, used in Chapter 3 to compute the X-ARAPUCA PDE to the VUV light.

Appendix B

Monte Carlo samples produced for the HNL analysis

B.1 Signal samples

For the analysis carried out, a total of 50,000 HNL events in the $N \rightarrow \nu e^+ e^-$ decay channel with cosmic rays overlaid were produced per HNL mass point. The samples were processed through the complete SBND simulation and reconstruction workflow. The mass points and couplings are summarized in Table B.1. The couplings are chosen as such their values are close to the sensitivity limits set by MicroBooNE in this mass region [211]. The number of equivalent POT (protons on target) for each mass is also indicated. Using this information the signal and background samples can be scaled to the expected SBND three years dataset (10^{21} POT).

HNL_{mass} [MeV]	$\lvert U_{\mu 4}\rvert^2$	POT
10	3.32×10^{-3}	1.54×10^{19}
35	3.82×10^{-4}	5.38×10^{17}
50	2.96×10^{-4}	9.42×10^{16}
75	2.96×10^{-4}	6.51×10^{15}
100	2.00×10^{-5}	1.90×10^{17}
125	2.00×10^{-5}	3.80×10^{16}
150	5.99×10^{-7}	1.07×10^{19}

Table B.1: Masses and couplings of the produced samples for the $N \rightarrow e^+ e^- \nu$ channel.

The HNL sample at each mass point can be scaled to different couplings $|U_{\mu 4}|^2$. This is because the HNL production (Equation 5.2) depends at first order on $|U_{\mu 4}|^2$ and decay widths (Equations 5.5, 5.7 and 5.8) also depend on the square of the mixing $|U_{\mu 4}|^2$.

Thus, the number of HNLs at SBND is, at first order, proportional to the 4th power of the mixing coupling and the following relation holds:

$$N_{\text{HNLs}}/|U_{\mu 4}|^4 = N'_{\text{HNLs}}/|U'_{\mu 4}|^4 \tag{B.1}$$

where N is the number of HNLs at the reference and final couplings. Equation B.1 can be used to re-scale samples produced at the same HNL mass for a different coupling ($U'_{\mu 4}$):

$$N'_{\text{HNLs}} = N_{\text{HNLs}} \times \left(\frac{|U'_{\mu 4}|^2}{|U_{\mu 4}|^2} \right)^2 . \tag{B.2}$$

As it only approximates the complete decay probability, Equation B.2 has been verified numerically with variations in the number of HNLs below the percent level for HNL samples generated with different couplings in the range $|U_{\mu 4}|^2 = [10^{-3}\text{–}10^{-9}]$.

B.2 Background samples

To model the backgrounds, four Monte Carlo samples have been generated: a sample containing SM neutrinos with cosmic rays overlaid, a sample of only cosmic muons to count for the events that are not triggered by a neutrino but with a cosmic ray in time with the beam window, and two enriched samples for the backgrounds that can mimic a $N \to e^+e^-\nu$ signal (NCπ^0 and CCν_e events). A complete simulation of the trigger is not performed. A 100% trigger efficiency is assumed given the PMT trigger thresholds will be low enough to trigger most of the neutrino and HNL events. The properties and the normalization factors (weights) to the expected 10^{21} POT are described below for each MC sample.

1. **The Rockbox sample** consists of neutrino interactions with cosmic rays occurring within the readout windows. The statistics of the sample is 527,437 events, equivalent to 4.51×10^{19} POT and 3.00×10^6 beam spills. A scale factor is calculated to normalize the sample to the target POT as

$$\textit{Rockbox Scale Factor} = \frac{\textit{Target POT}}{\textit{Rockbox Sample POT}} = \frac{1 \times 10^{21}}{4.51 \times 10^{19}} = 22.16 \tag{B.3}$$

   The target neutrino beam spills after normalization are 6.64×10^7.

2. **The cosmic-only sample** accounts for in-time cosmic events. The statistics of the sample is 115,557 events, equivalent to 9.85×10^6 beam spills. The target cosmic beam spills are the number of beam spills that do not produce neutrino-triggered events, and assuming that HNL-triggered beam spills are negligible. The target total beam spills expected for the target POT is

$$Target\ Total\ Beam\ Spills = \frac{Target\ POT}{Averaged\ POT\ Per\ Spill} = \frac{1 \times 10^{21}}{5 \times 10^{12}} = 2.00 \times 10^8 \tag{B.4}$$

The target cosmic beam spills are calculated by subtracting the neutrino triggered beam spills:

$$\begin{aligned} Target\ Cosmic\ Beam\ Spills &= Target\ Total\ Beam\ Spills \\ &\quad - Target\ Neutrino\ Beam\ Spills \\ &= 2.00 \times 10^8 - 6.64 \times 10^7 \\ &= 1.34 \times 10^8 \end{aligned} \tag{B.5}$$

The scale factor to normalize the cosmic-only sample the target POT is

$$Cosmic\ Scale\ Factor = \frac{Target\ Cosmic\ Beam\ Spills}{Sample\ Cosmic\ Beam\ Spills} = \frac{1.34 \times 10^8}{9.85 \times 10^6} = 13.57 \tag{B.6}$$

3. **The enriched $NC\pi^0$ sample** has a filter applied to keep $NC\pi^0$ interactions inside the active volume at the generation stage, and an additional filter to keep only events inside the fiducial volume at the analysis stage. The enriched sample contains 56,525 $NC\pi^0$ events in the SBND fiducial volume (FV) after filtering. The same filtered events are completely removed from the Rockbox sample, equivalent to 12,932 events. The events from the enriched sample and Rockbox are combined into a single sample, adding to a total of

$$\begin{aligned} Total\ NC\pi^0\ Events &= Enriched\ Sample\ NC\pi^0\ Events \\ &\quad + Rockbox\ Sample\ NC\pi^0\ Events \\ &= 56,525 + 12,932 \\ &= 69,457 \end{aligned} \tag{B.7}$$

The scale factor to normalize to the target POT for this sample is calculated as

$$\begin{aligned} NC\pi^0\ Scale\ Factor &= \frac{Rockbox\ Sample\ NC\pi^0\ Events}{Total\ NC\pi^0\ Events} \times Rockbox\ Scale\ Factor \\ &= \frac{12,932}{69,457} \times 22.16 \\ &= 4.13 \end{aligned} \tag{B.8}$$

4. **The enriched $CC\nu_e$ sample** has similar filters described as above, to keep only CCν_e interactions in the FV. The enriched sample contains 22,562 FV $CC\nu_e$ events after filtering. The same filtered events are completely removed from the Rockbox sample, equivalent to 1,399 events. The combined sample from the enriched and the Rockbox samples contains a total number of events of

$$\begin{aligned} Total\ CC\nu_e\ Events &= Enriched\ Sample\ CC\nu_e\ Events \\ &\quad + Rockbox\ Sample\ CC\nu_e\ Events \\ &= 22,562 + 1,399 \\ &= 23,961 \end{aligned} \tag{B.9}$$

The scale factor to normalize to the target POT for this sample is calculated as

$$\begin{aligned} CC\nu_e\ Scale\ Factor &= \frac{Rockbox\ Sample\ CC\nu_e\ Events}{Total\ CC\nu_e\ Events} \times Rockbox\ Scale\ Factor \\ &= \frac{1,399}{23,961} \times 22.16 \\ &= 1.29 \end{aligned} \tag{B.10}$$

Appendix C

XGBoost BDT model

The following model was trained on half the HNL signal and the SM (BNB neutrinos and cosmic-ray muons) background data samples. The HNL selection is explained in detail in Chapter 6.

```

    # Booster parameters
    param['eta']              = 0.02 # learning rate
    param['max_depth']        = 10  # maximum depth of a tree
    param['subsample']        = 0.6 # fraction of events to train tree on
    param['colsample_bytree'] = 0.8 # fraction of features to train tree
    on

    # Learning task parameters
    param['objective']   = 'binary:logistic' # objective function
    param['objective']   = 'reg:squaredlogerror' # objective function

    num_trees = 200  # number of trees to make
    booster = xgb.train(param,train,num_boost_round=num_trees)
```

Listing C.1: BDT chosen parameters

Appendix D

Arrival time distributions in the conservative selection

Arrival time distributions of HNLs, SM neutrinos and cosmic muons passing the conservative selection are presented. Details of the selection of HNL events are provided in Chapter 6. They correspond to a BDT score cut of 0.3.

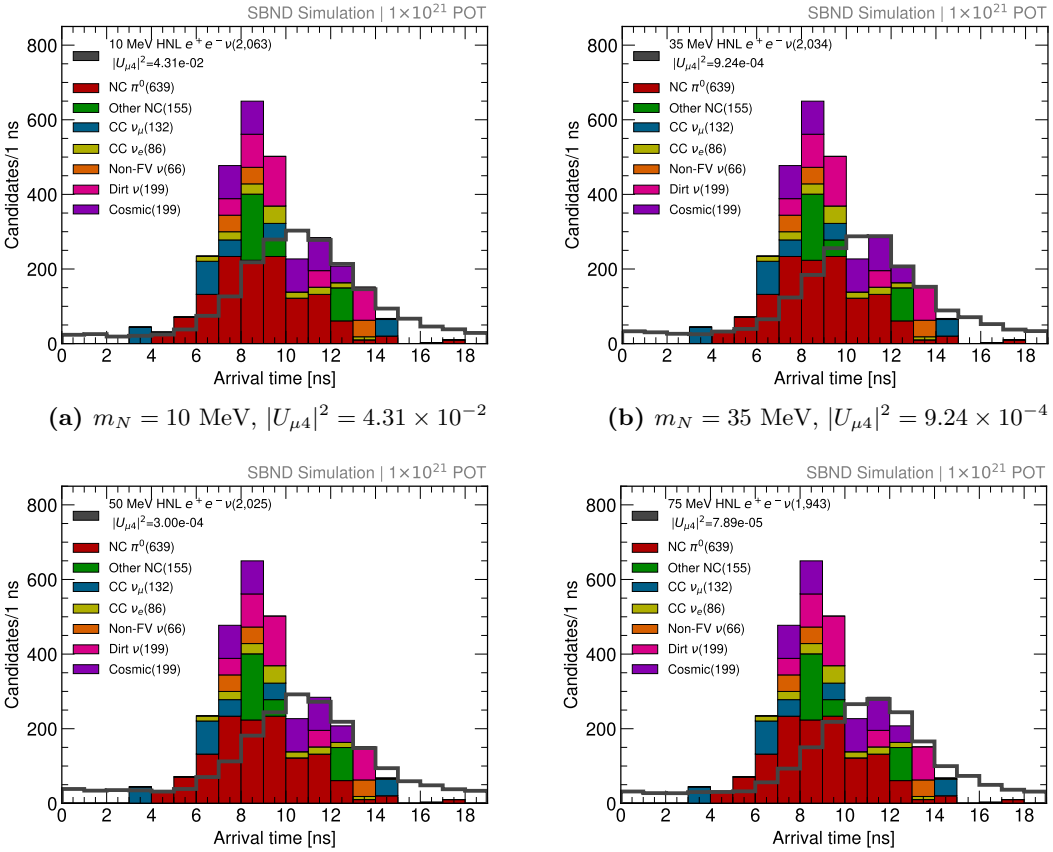

(a) $m_N = 10$ MeV, $|U_{\mu 4}|^2 = 4.31 \times 10^{-2}$

(b) $m_N = 35$ MeV, $|U_{\mu 4}|^2 = 9.24 \times 10^{-4}$

(c) $m_N = 50$ MeV, $|U_{\mu 4}|^2 = 3.00 \times 10^{-4}$

(d) $m_N = 75$ MeV, $|U_{\mu 4}|^2 = 7.89 \times 10^{-5}$

Figure D.1: Arrival time distributions of HNLs, SM neutrinos and cosmic muons passing the conservative selection, normalized to the exposure of 1×10^{21} POT. HNLs of mass m_N: [10, 35, 50, 75] MeV are normalized to the listed coupling $|U_{\mu 4}|^2$.

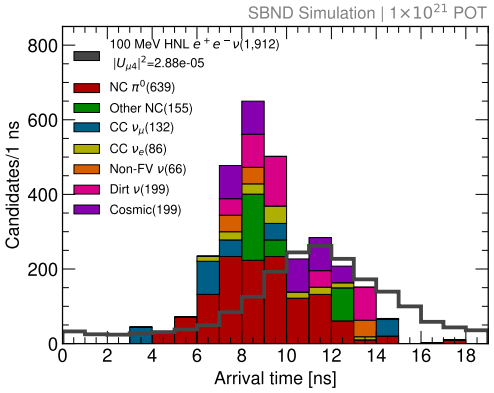

(a) $m_N = 100$ MeV, $|U_{\mu 4}|^2 = 2.88 \times 10^{-5}$

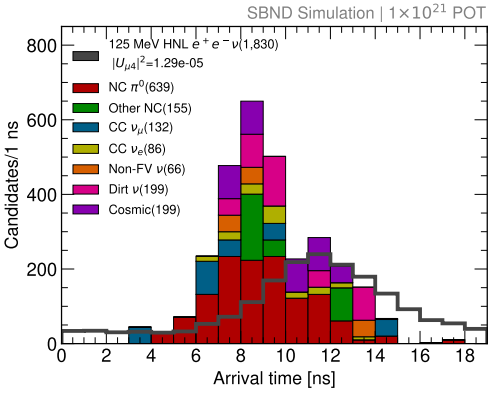

(b) $m_N = 125$ MeV, $|U_{\mu 4}|^2 = 1.29 \times 10^{-5}$

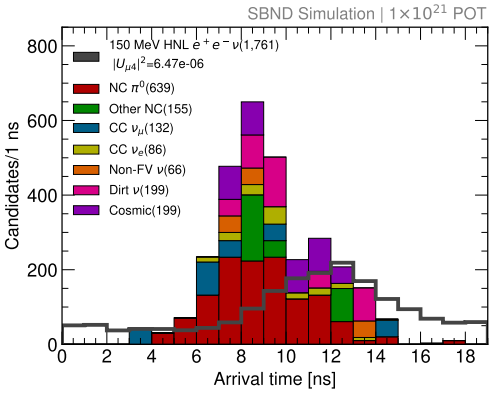

(c) $m_N = 150$ MeV, $|U_{\mu 4}|^2 = 6.47 \times 10^{-6}$

Figure D.2: Arrival time distributions of HNLs, SM neutrinos and cosmic muons passing the conservative selection, normalized to the exposure of 1×10^{21} POT. HNLs of mass m_N: [100, 125, 150] MeV are normalized to the listed coupling $|U_{\mu 4}|^2$.

Appendix E

Arrival time distributions in the aggressive selection

Arrival time distributions of HNLs, SM neutrinos and cosmic muons passing the aggressive selection are presented. Details of the selection of HNL events are provided in Chapter 6. They correspond to a BDT score cut of 0.5.

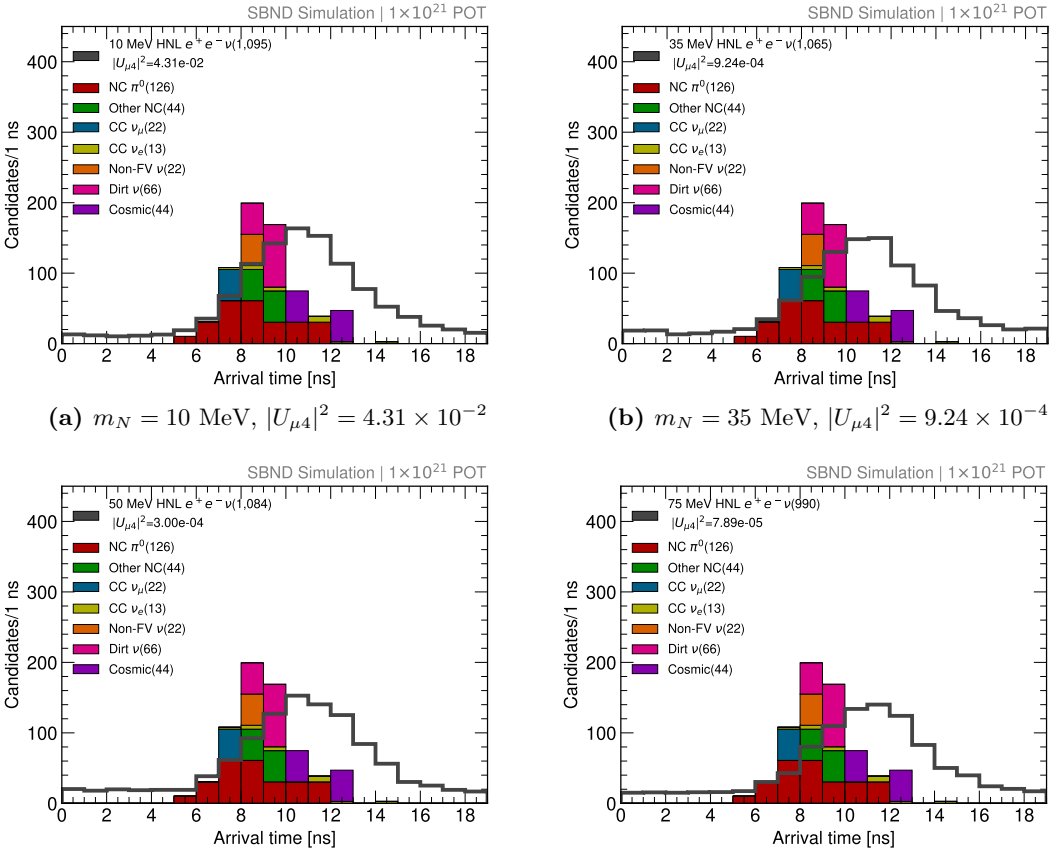

(a) $m_N = 10$ MeV, $|U_{\mu 4}|^2 = 4.31 \times 10^{-2}$

(b) $m_N = 35$ MeV, $|U_{\mu 4}|^2 = 9.24 \times 10^{-4}$

(c) $m_N = 50$ MeV, $|U_{\mu 4}|^2 = 3.00 \times 10^{-4}$

(d) $m_N = 75$ MeV, $|U_{\mu 4}|^2 = 7.89 \times 10^{-5}$

Figure E.1: Arrival time distributions of HNLs, SM neutrinos and cosmic muons passing the aggressive selection, normalized to the exposure of 1×10^{21} POT. HNLs of mass m_N: [10, 35, 50, 75] MeV are normalized to the listed coupling $|U_{\mu 4}|^2$.

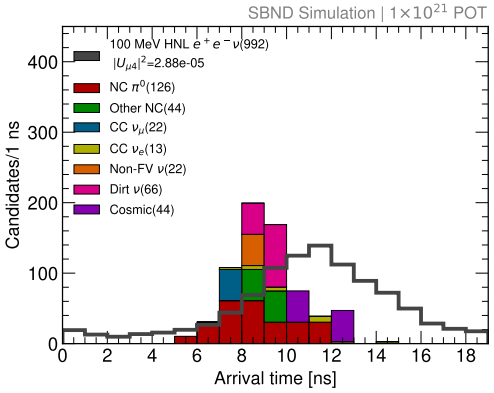

(a) $m_N = 100$ MeV, $|U_{\mu 4}|^2 = 2.88 \times 10^{-5}$

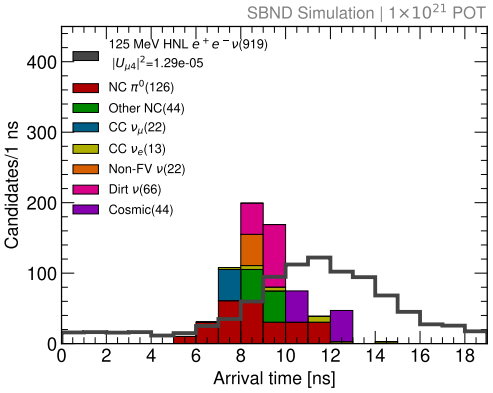

(b) $m_N = 125$ MeV, $|U_{\mu 4}|^2 = 1.29 \times 10^{-5}$

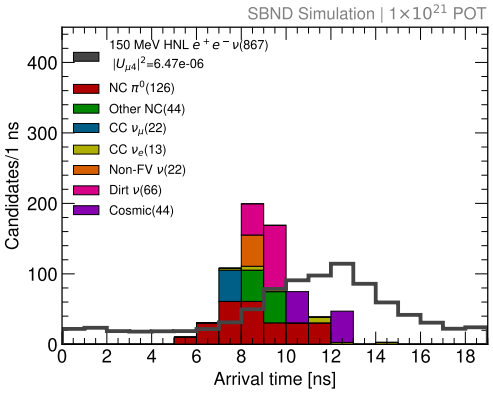

(c) $m_N = 150$ MeV, $|U_{\mu 4}|^2 = 6.47 \times 10^{-6}$

Figure E.2: Arrival time distributions of HNLs, SM neutrinos and cosmic muons after the aggressive selection, normalized to the exposure of 1×10^{21} POT. HNLs of mass m_N: [100, 125, 150] MeV is normalized to the listed coupling $|U_{\mu 4}|^2$.

Appendix F

Arrival time distributions in the smeared true selection

Arrival time distributions of HNLs, SM neutrinos and cosmic muons acquired by smearing true variables under the assumption of a timing resolution improvement are presented. Descriptions of the arrival time distribution and details of the smearing process are provided in Chapter 6. For displaying purposes, a coupling corresponding to approx. 1500 HNL events after selection is computed.

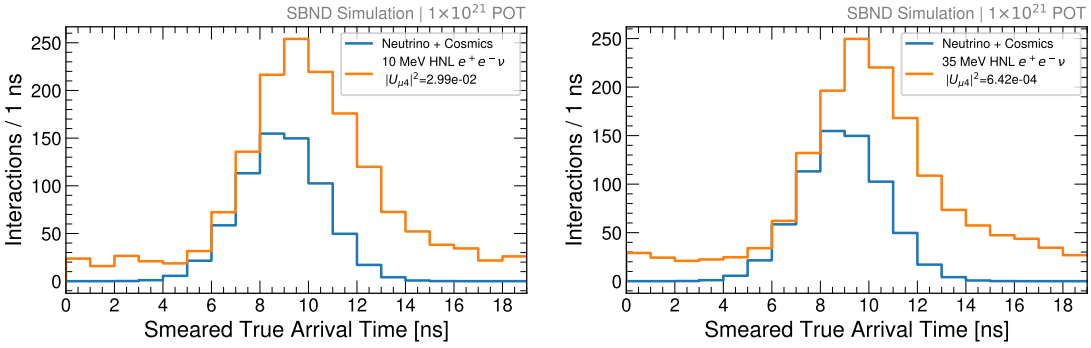

(a) $m_N = 10$ MeV, $|U_{\mu 4}|^2 = 2.99 \times 10^{-2}$

(b) $m_N = 35$ MeV, $|U_{\mu 4}|^2 = 6.42 \times 10^{-4}$

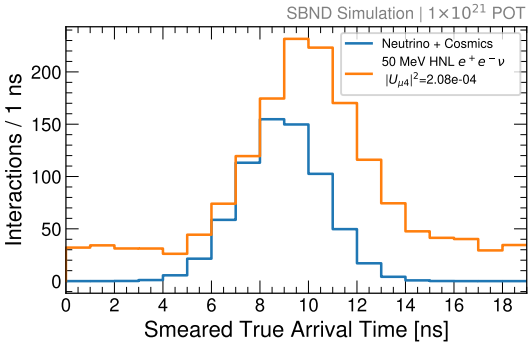

(c) $m_N = 50$ MeV, $|U_{\mu 4}|^2 = 2.08 \times 10^{-4}$

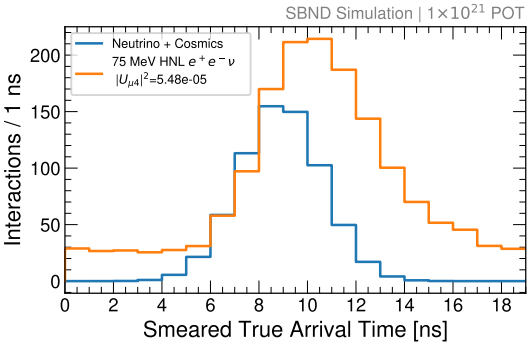

(d) $m_N = 75$ MeV, $|U_{\mu 4}|^2 = 5.48 \times 10^{-5}$

Figure F.1: Arrival time distributions of HNLs, SM neutrinos and cosmic muons under the assumption of a timing resolution improvement, normalized to the exposure of 1×10^{21} POT. HNLs of mass m_N: [10, 35, 50, 75] MeV are normalized to the listed coupling $|U_{\mu 4}|^2$.

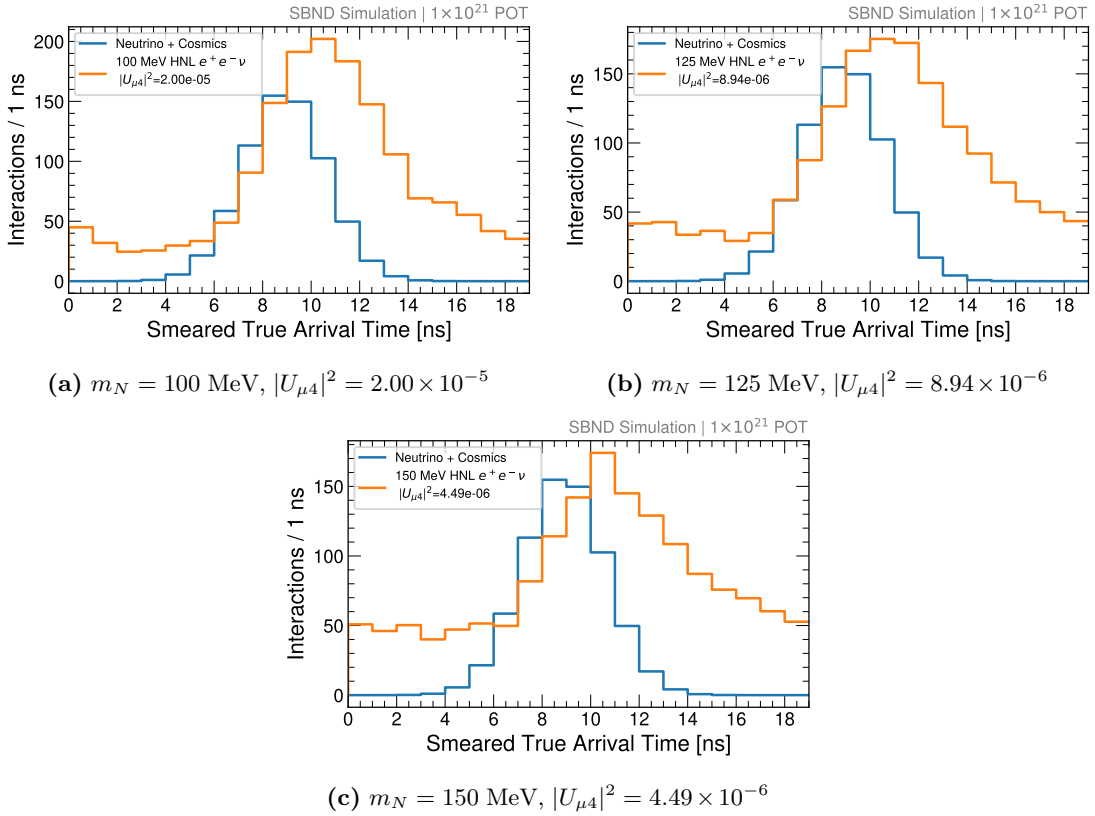

(a) $m_N = 100$ MeV, $|U_{\mu 4}|^2 = 2.00 \times 10^{-5}$

(b) $m_N = 125$ MeV, $|U_{\mu 4}|^2 = 8.94 \times 10^{-6}$

(c) $m_N = 150$ MeV, $|U_{\mu 4}|^2 = 4.49 \times 10^{-6}$

Figure F.2: Arrival time distributions of HNLs, SM neutrinos and cosmic muons under the assumption of a timing resolution improvement, normalized to the exposure of 1×10^{21} POT. HNLs of mass m_N: [100, 125, 150] MeV are normalized to the listed coupling $|U_{\mu 4}|^2$.